The Role of Ocean Dynamics in Shaping Exoplanetary Climate and Habitability

A thesis submitted to the School of Engineering, Mathematics & Physics at the University of East Anglia in partial fulfilment of the requirements for the degree of Doctor of Philosophy

Maria Di Paolo

January 2026

Abstract

Characterising terrestrial exoplanets requires physically consistent climate modelling, including ocean dynamics, often neglected despite its dominant role in shaping climate. This is especially relevant for planets orbiting low-mass stars, the primary targets for habitability studies, whose climatic complexity remains underexplored and for which oceans cannot be assumed to be Earth-like.

Tidal interactions can substantially modify ocean mixing and the heat-transport mechanisms operating on Earth-like aquaplanets. The climatic response to different tidal mixing, represented in a fully coupled atmosphere-ocean general circulation model through the vertical diffusion coefficient, is nonlinear and nonmonotonic: moderate diffusivities enhance ocean heat transport and reduce meridional temperature gradients, peaking at values about 100 times those of Earth, whereas stronger mixing reverses these effects. Consequently, certain tidal forcing regimes can widen the habitable zone by enabling temperate climates under reduced instellation, indicating that ocean tides are a key factor in assessing the habitability of planets affected by strong tidal forcing, such as planets orbiting low-mass stars.

In this context, the climate dynamics of terrestrial exoplanets in 3:2 spin-orbit resonances is examined, a configuration that remains understudied relative to synchronous rotation, characterised by fixed day and night hemispheres. Two tidal regimes and two rotation states are analysed, and simulations with both dynamic and thermodynamic oceans assess the role of ocean processes in climate and observability. Periodic stellar forcing shapes both mean climate and variability, producing migrating temperature and precipitation patterns. These result in distinctive thermal emission phase-curve signatures that differentiate asynchronous from synchronous rotators.

Overall, this thesis provides an assessment of terrestrial planets climates highlighting the importance of fully coupled ocean dynamics in shaping their climatic and observational properties. The findings contribute to clarifying the diversity of climates permitted by asynchronous rotation and offer a framework for interpreting future observations of nearby terrestrial exoplanets.

Acknowledgements

I would like to thank the Engineering and Physical Sciences Research Council (grant EP/W524074/1) for funding my PhD studentship. I am grateful to my supervisors, Dave Stevens and Manoj Joshi, for providing constant guidance and feedback throughout this project. I also wish to acknowledge the HPC and IT-Linux teams for their invaluable technical assistance. Special thanks to Davide for his support and encouragement.

The past years have offered a generous selection of challenges, but also unexpected gifts including a broken ankle and a slipped disc. These riveting experiences would have been far less entertaining if not shared with the friends who accompanied me through this four-year endeavour: Kristina, Tommy, Arthur, Anna, and Jordan. Life in this fine city has also been brightened by a cast of vibrant personalities who turned it into home: Conni at the Sportspark, Minty and Rudy at Edwina's, Joleen at Planted, and Sylvester at UEA. To friends scattered across the world who came for a visit and remained long-distance constants: thanks to Federico, Fabiola, and Micol. Most importantly, I want to express my gratitude and appreciation to my family: mamma, papà, zio Gek, zio Beppe, and Lilli.

As I write this, the launch date for Artemis II is currently targeted for just over a week from now. I wish the crew a successful mission and a smooth trip; leaving the US seems increasingly sensible these days.

“[...] perchè quando gli uomini si quietassero ugualmente nel vero,
non saria differenza tra letterati e altri ignoranti,
già che tutti sarebbero letterati a un modo
perchè altro non è l’esser ignorante,
che il non si quietar nel vero.”

Galileo Galilei
Errori di Giorgio Coresio, 1613

Contents

Abstract **i**

Acknowledgements **iii**

Contents **vii**

List of Figures **xi**

Aim and structure of the thesis **1**

1 Introduction **3**

1.1 Context . . . 4

1.1.1 The path to exoplanetary science . . . 4

1.1.2 Towards a definition . . . 8

1.1.3 Exoplanet detection . . . 10

1.1.4 Exoplanet characterisation . . . 14

1.2 Exoplanetary climate and habitability . . . 17

1.2.1 The concept of habitability . . . 17

1.2.2 Habitable Zone . . . 19

1.2.3 Climate models . . . 22

1.2.4 The impact of the ocean . . . 25

1.2.5 M stars and tidal locking . . . 28

2 Methodology 33

2.1 Analysis of the Global Meridional Overturning Circulation . . . 34

2.1.1 Theory . . . 34

2.1.2 Validation via control dataset . . . 35

2.2 MOMA . . . 38

2.2.1 Brief model description . . . 38

2.2.2 Experiments . . . 39

2.3 FORTE 2.0 . . . 46

2.3.1 Brief model description . . . 46

2.3.2 Experiments . . . 49

2.4 Concluding remarks . . . 52

3 Nonlinear and nonmonotonic effect of ocean tidal mixing on climate 57

3.1 Abstract . . . 58

3.2 Introduction . . . 58

3.3 Methods . . . 60

3.3.1 Model description . . . 60

3.3.2 Tidal mixing parameterization . . . 61

3.3.3 Planet configuration . . . 63

3.3.4 System architecture . . . 64

3.4 Results . . . 64

3.4.1 Effect of vertical diffusion: circulation and temperature structure . . . 64

3.4.2 Effect of vertical diffusion: ocean temperature and heat transport . . . 67

3.4.3 Effect of change in instellation . . . 69

3.5 Discussion and Conclusions . . . 70
3.6 Supplementary material . . . 73
3.6.1 Mean climate state . . . 73
3.6.2 Heat transport . . . 78
3.6.3 Decrease in instellation . . . 83
3.7 Further Investigation . . . 86
3.7.1 No evidence of climate bistability under different ocean initial temperatures . . . 86
3.7.2 Alternative land configurations . . . 89
3.8 Concluding remarks and motivation for Chapter 4 . . . 102

4 Climate Patterns of Spin-Orbit Resonant Exoplanets 105

4.1 Abstract . . . 106
4.2 Introduction . . . 106
4.3 Methods . . . 110
4.3.1 Model description . . . 110
4.3.2 System architecture . . . 111
4.3.3 Planet configuration . . . 113
4.4 Results . . . 114
4.4.1 Ocean . . . 114
4.4.2 Atmosphere . . . 117
4.4.3 Observables . . . 122
4.5 Discussion and Conclusions . . . 128
4.6 Supplementary material . . . 132
4.6.1 Phase curves computation . . . 132
4.6.2 Ocean-driven modulation of phase curves . . . 135

4.6.3 Mean climate state 141

4.6.4 Ocean dynamical waves 147

4.7 Concluding remarks 150

5 Conclusions and Perspectives **151**

5.1 Conclusions 152

5.2 Perspectives 155

Bibliography **159**

List of Figures

1.1.1 Postcards from exoplanets 8

1.1.2 Cumulative number of confirmed exoplanets by year of discovery 11

1.1.3 Perryman Tree 12

1.1.4 Scatter plot of M_p or $M_p\sin(i)$ vs orbital periods for confirmed exoplanets 15

1.2.1 Conservative circumstellar habitable zones around main-sequence stars . . 21

1.2.2 Factors affecting habitability 23

1.2.3 Confirmed exoplanets as a function of host star temperature and received instellation 30

2.1.1 Control data set: mean heat flux time series 36

2.1.2 Control data set: GMOC time series 37

2.1.3 Control data set: mean GMOC and AMOC streamfunctions 37

2.2.1 MOMA Arakawa-B grid in 3D 39

2.2.2 MOMA - Standard Earth, simple Earth, varying κ experiments: GMOC time series 41

2.2.3 MOMA - Standard Earth, simple Earth: year 1 surface salinity maps . . . 41

2.2.4 MOMA - Varying κ: GMOC streamfunction 42

2.2.5 MOMA - Varying γ_s with standard and enhanced Atlantic salinity: GMOC time series 43

2.2.6 MOMA - Enhanced Atlantic salinity: year 1 and year 100 surface salinity maps . . . 43

2.2.7 MOMA - Wide enhanced Atlantic salinity: year 1 and year 100 surface salinity maps . . . 45

2.2.8 MOMA - Wide enhanced Atlantic salinity and standard salinity with relaxation to initial fields: year 1 surface salinity maps . . . 45

2.2.9 MOMA - Varying enhanced Atlantic salinity and relaxation conditions: GMOC time series . . . 46

2.2.10 MOMA - Varying enhanced Atlantic salinity and relaxation conditions: GMOC streamfunction . . . 47

2.3.1 FORTE - Varying $fkph$: κ_{stab} vertical profiles . . . 50

2.3.2 FORTE - Varying $fkph$: GMOC time series . . . 51

2.3.3 FORTE - Varying $fkph$: surface temperature and salinity time series . . . 51

2.3.4 FORTE - Varying κ: GMOC time series . . . 53

2.3.5 FORTE - Varying κ: surface temperature and salinity time series . . . 53

2.3.6 FORTE - Varying κ: mean GMOC streamfunction . . . 54

2.3.7 FORTE - Varying κ: mean surface temperature maps . . . 55

3.4.1 Ocean temperature and overturning streamfunction, atmospheric temperature and zonal wind for varying κ. . . . 65

3.4.2 Total rainfall latitudinal profile for varying κ . . . 67

3.4.3 Mean climatic properties as a function of κ . . . 68

3.4.1 Table summarizing mean climate states for varying κ and different values of instellation . . . 71

3.4.4 Surface temperature for varying κ for different values of instellation . . . 72

3.6.1 Additional ocean temperature and overturning streamfunction, atmospheric temperature and zonal wind for varying κ. . . . 75

3.6.2 Additional mean climatic properties as a function of κ . . . 76

3.6.3 Surface- and volume-averaged temperature, total rainfall and zonal winds latitudinal profiles for varying κ 77

3.6.4 Mean sea surface temperature maps for varying κ. 79

3.6.5 Total, ocean and atmosphere heat transport latitudinal profiles for varying κ 80

3.6.6 Total, AQMOC and gyre advective heat transport latitudinal profiles for varying κ 83

3.6.7 Advective ocean heat transport mechanisms 84

3.6.8 Sea surface temperature and ice latitude time series for the reduced instellation cases. 85

3.7.1 Heat flux time series for warm and cold start simulations 88

3.7.2 Volume-averaged oceanic temperature time series for warm and cold start simulations 89

3.7.3 Temperature and overturning streamfunction for warm start simulations and difference with cold start simulations. 90

3.7.4 Ocean heat transport for warm start simulations and difference with cold start simulations 91

3.7.5 Surface temperature maps for warm start simulations and difference with cold start simulations. 92

3.7.6 Ridgeworld and Waterworld continental configurations 93

3.7.7 Ocean surface currents and sea surface height for Ridgeworld and Waterworld configurations 94

3.7.8 Ocean temperature and overturning streamfunction for Waterworld configuration, difference with the Ridgeworld configuration 96

3.7.9 Mean sea surface temperature maps for Waterworld configuration, difference with the Ridgeworld configuration 96

3.7.10 Splitridge and Fourridges continental configurations 97

3.7.11 Ocean temperature and overturning streamfunction for Splitridge and Fourridges configurations, difference with the Ridgeworld configuration . . 98

3.7.12 Mean sea surface temperature maps for Splitridge and Fourridges configurations, difference with the Ridgeworld configuration 99

3.7.13 Latitudinal profiles of ocean heat transport, surface temperature, volume-averaged temperature and volume-averaged salinity for all analysed configurations 101

4.2.1 Observing configuration of simulated 3:2 SOR planets orbiting low-mass stars 109

4.4.1 Ocean cross section at longitude 120° and averaged over the equatorial band for dynamic ocean simulations 115

4.4.2 Ocean temperature profiles at longitude 120° and averaged over the equatorial band for each of the analysed scenarios 116

4.4.3 Hovmöller diagram showing density anomaly at 482 m of depth averaged over the equatorial band for each of the analysed scenarios - details of $\kappa = 1.5\ \kappa_{\oplus}$, $T_{orbital} = 30$ days 117

4.4.4 Hovmöller diagrams showing surface temperature and total rainfall averaged over the equatorial band for each of the analysed scenarios . . . 118

4.4.5 Variability of total rainfall at longitude 120° and averaged over the equatorial band for each of the analysed scenarios 120

4.4.6 Hovmöller diagrams showing zonal winds at 850 hPa for each of the analysed scenarios, both as a function of longitude and of latitude 121

4.4.7 Hovmöller diagrams showing TOA upward shortwave and longwave radiation averaged over the equatorial band for each of the analysed scenarios and highlighting visible portions of the planet 124

4.4.8 Hovmöller diagram showing convective cloud amount averaged over the equatorial band for each of the analysed scenarios 125

4.4.9 Emitted and reflected light phase curves for each analysed scenario 127

4.5.1 Thermal emission phase curve schematics for idealised 1:1 SOR and our 3:2 SOR scenarios. 130

4.6.1 Geometry of the system for an exoplanet observed from Earth. 133

4.6.2 Observing geometry for the $T_{orb} = 9$ days scenario 134

4.6.3 Hovmöller diagram of composite surface temperature averaged over all latitudes for each of the analysed scenarios 137

4.6.4 TOA upward longwave flux for light curve peaks of the $\kappa = 150\ \kappa_{\oplus}$, $T_{orb} = 30$ days scenario 138

4.6.5 TOA upward longwave flux for light curve troughs of the $\kappa = 150\ \kappa_{\oplus}$, $T_{orb} = 30$ days scenario 139

4.6.6 Surface temperature latitudinal profile for each of the analysed scenarios . 141

4.6.7 Heat flux latitudinal profile for each of the analysed scenarios 142

4.6.8 Volume-averaged temperature latitudinal profile for each of the analysed scenarios 143

4.6.9 Ocean, atmosphere and total heat transport latitudinal profiles for each of the analysed scenarios 144

4.6.10 Mean sea surface temperature maps for each of the analysed scenarios . . 146

4.6.11 Hovmöller diagram showing density anomaly at 482 m of depth averaged over the equatorial band for each of the analysed scenarios - details of $\kappa = 1.5\ \kappa_{\oplus}$, $T_{orbital} = 9$ days 147

4.6.12 Hovmöller diagram showing density anomaly at 0.15 m of depth averaged over the equatorial band for each of the analysed scenarios 148

Aim and structure of the thesis

The characterisation of terrestrial exoplanets represents one of the central challenges in contemporary astrophysics. As observational capabilities advance, physically consistent climate modelling becomes essential for interpreting forthcoming measurements and for assessing the potential habitability of nearby worlds. Most studies of exoplanetary climate have relied on simplified ocean representations, despite oceans exerting a dominant influence on climate, as demonstrated by Earth's system. Understanding ocean dynamical processes is therefore a crucial component of modelling terrestrial exoclimates, since neglecting fully dynamic oceans, although computationally convenient, can lead to incomplete or misleading assessments of climate states.

Planets orbiting M stars are widely regarded as the most promising candidates for hosting potentially habitable environments, and consequently much of the current research effort is directed towards them. Close-in planets around low-mass stars experience strong tidal interactions capable of altering their rotational state, yet their spin states are not currently constrainable observationally. Although most previous studies have focused on synchronous rotation, tidal theory predicts that a range of asynchronous configurations - including higher-order spin-orbit resonances - are dynamically plausible. The climatic implications of these states, particularly when fully coupled oceans are considered, remain insufficiently explored. On Earth, tides are a major driver of vertical mixing that sustains the large-scale overturning circulation and associated heat transport, but Earth's tidal regime is unlikely to be representative of all aquaplanets.

This thesis addresses these largely unexplored scenarios by simulating the climates of terrestrial exoplanets across a range of tidal and rotational regimes. Using a fully coupled atmosphere-ocean general circulation model, it provides original perspectives to the topic of planetary habitability and provides new insights into the potential observability of terrestrial planets orbiting low-mass stars. The thesis is structured as follows:

- **Chapter 1: Introduction**
  This chapter traces the intellectual and scientific development of ideas about other

worlds, framing exoplanet research as the culmination of centuries of evolving thought and observational progress and providing a concise overview of current observational techniques. The importance of climate modelling for interpreting planetary environments and assessing habitability is established. After introducing the concept of the habitable zone and the hierarchy of climate models, particular emphasis is placed on the role of oceans in shaping climate and on terrestrial exoplanets around low-mass stars, considered prime targets for climate studies.

- **Chapter 2: Methodology**
  This chapter focuses on oceanic dynamical processes such as the meridional overturning circulation, which governs large-scale oceanic heat and mass transport and can differ substantially from Earth's in exoplanetary contexts. A validation procedure based on a published Earth control run is outlined. The models used to run the simulations are introduced, followed by a suite of experiments designed to assess model sensitivity.

- **Chapter 3: Nonlinear and nonmonotonic effect of ocean tidal mixing on exoplanet climates and habitability**
  This chapter investigates how tidal-driven ocean vertical mixing, which can reach values thousands of times larger than on Earth when strong travelling tides move across the planetary surface, influences climate and habitability in a coupled atmosphere-ocean model. The nonlinear and nonmonotonic climatic responses that arise across several orders of magnitude in diffusivity are highlighted. Further investigations strengthen the analysis by examining different initial conditions and alternative land configurations.

- **Chapter 4: Climate Patterns of Spin-Orbit Resonant Exoplanets Around Low-Mass Stars**
  This chapter investigates climate patterns on planets in 3:2 spin-orbit resonances around low-mass stars using a coupled atmosphere-ocean model configured with both dynamic and thermodynamic ocean setups. Across different tidal and rotational regimes, the emergence of periodic climate behaviour and its observational signatures in thermal emission phase curves is highlighted. Particular attention is given to the influence of ocean dynamical processes on specific features of the phase curve.

- **Chapter 5: Conclusions and Perspectives**
  This chapter provides a synthesis of the main findings and discusses their broader implications. Possible avenues for extending the work, both by increasing the complexity of the modelling framework and by exploring applications of the concepts developed throughout the thesis are outlined. Specifically, the relevance of this study and its future improvements is discussed in the context of potential contributions to climate model intercomparison efforts.

1

Introduction

The search for alien worlds is strongly motivated by an attempt to find astronomical environments that feature the chemical and physical characteristics that can allow and support the origin and evolution of life. Among these characteristics, climate plays a pivotal role in determining whether a planet can maintain conditions conducive to habitability. Climate modelling provides a framework for probing the critical processes and complex interplay of factors that govern a planet's ability to bolster or hinder habitable conditions. Furthermore, climate models help interpret observational data, bridging the gap between raw measurements and theoretical simulations, thus providing meaningful insights about planetary environments. As our detection capabilities improve and the catalogue of detected exoplanets expands, robust climate modelling becomes increasingly vital for prioritising targets in the search for life beyond Earth.

1.1 Context

1.1.1 The path to exoplanetary science

Exoplanetary science, though formally established only in the last few decades, has roots that trace back over two millennia. Throughout history and across cultures, humans have gazed at the night sky and questioned whether our planet, with its rich biosphere, exists in isolation in the cosmos. This enduring curiosity has shaped philosophical thought, and with a transition from metaphysical speculation to empirical investigation, now drives the scientific search for planets beyond our Solar System.

The debate over cosmic pluralism can be traced to Anaximander (c. 610 - 546 BCE), who argued that infinite worlds arise from and return to the ápeiron, the boundless and eternal source of all things [Kočandrle, 2019]. His work laid fundamental ideas that anticipated the atomists, with Leucippus (c. 480 - 420 BCE) and Democritus (c. 460 - 370 BCE), who reasoned that infinite atoms moving in infinite space combine in countless ways, leading to the formation of innumerable worlds differing in size, structure, and the presence or absence of life[1]. The Democritean scholar Epicurus (341-270 BCE) expanded this into a materialist and non-teleological framework, rejecting divine creation and emphasizing that natural laws govern all phenomena, including the formation of worlds[2]. These doctrines were later popularised by Lucretius (c. 99 - 55 BCE) in his *De Rerum Natura* [Lucretius, 1924] divulging the fundamental principles of the Epicurean doctrine to a Roman audience. Though philosophical rather than empirical, these early conjectures on cosmic plurality resonate with the planetary diversity revealed by modern exoplanetary science.

In contrast to Epicurus' conception of infinite worlds, opposition to cosmic pluralism was articulated by Plato (428 - 348 BCE) and his student Aristotle (384 - 322 BCE). Plato maintained that the uniqueness of the creator implied the uniqueness of creation, while Aristotle advanced a finite, geocentric cosmology in which Earth lay immobile at the centre, surrounded by nested spheres of aether carrying the planets, Sun, Moon, and fixed stars. The outermost sphere defined the universe's boundary, leading Aristotle to conclude that no other worlds could exist[3]. Aristotelian cosmology became dominant in the Greco-Roman world and was later integrated into Christian theology, entrenching the notion of a singular, purposefully created cosmos and suppressing atomist and pluralist views until

[1] "In some worlds there is no sun and moon, in others they are larger than in our world, and in others more numerous. The intervals between the worlds are unequal. [...] There are some worlds devoid of living creatures or plants or any moisture." [Siegfried, 2019]

[2] In a letter addressed to the historian Herodotus, Epicurus reaffirmed "There is an infinite number of worlds, some like this world, others unlike it. [...] And further, we must not suppose that the worlds have necessarily one and the same shape. For nobody can prove that in one sort of world there might not be contained, whereas in another sort of world there could not possibly be, the seeds out of which animals and plants arise and all the rest of the things we see." [Laertius, 1925].

[3] "It follows that there cannot be more worlds than one. [...] It is plain, too, from the following considerations that the universe must be one." [Aristotle, 1939]

their revival nearly two millennia later.

By the Renaissance, thinkers such as Nicholas of Cusa and Giordano Bruno challenged Aristotelian physics and Christian orthodoxy. Drawing on Copernican heliocentrism, Bruno (1548 - 1600) in *De l'infinito, universo e mondi* argued that the stars were not fixed points embedded in a celestial sphere, but rather distant suns, each potentially hosting planetary systems, and that the universe was infinite and populated by innumerable worlds, some capable of harboring life. He even anticipated the observational challenges of detecting dark, small planets orbiting other stars, decades prior to the invention of the telescope and centuries before the development of observational technologies capable of detecting exoplanets[4]. By rejecting Earth's centrality and uniqueness, Bruno advanced a metaphysical pluralistic cosmology that laid intellectual groundwork for later scientific inquiry, foreshadowed modern exoplanetary science, and preceded observational detection by centuries. Condemned as heretical, his refusal to recant led to his execution, symbolizing the clash between emerging scientific thought and religious dogma.

At the time of Bruno's assertions, planetary knowledge was limited to the five bodies visible to the unaided eye - Mercury, Venus, Mars, Jupiter, and Saturn - recognised since antiquity as "wandering stars" due to their apparent motion against the fixed stellar background. The invention of the "spyglass" in the early 17th century marked a revolutionary turning point: Galileo Galilei's telescopic observations revealed the moons of Jupiter and the phases of Venus [Galilei, 1610], provided evidence for the Copernican heliocentric model [Galilei, 1632], demonstrated that celestial bodies were neither flawless nor immutable through discoveries of lunar craters [Galilei, 1610] and solar sunspots [Galilei, 1613], and revealed that the Milky Way comprised innumerable stars expanding the perceived scale of the universe [Galilei, 1610]. This led to a shift from philosophical speculation to empirical evidence and experimentation, sparking the birth of modern astronomy.

Like Bruno a century earlier, Newton considered that stars beyond the Sun might host planetary systems, yet in the appendix to the *Principia* he attributed the orderly structure of the cosmos to the counsel of an intelligent being[5]. Although framed within divine design, his laws of motion and universal gravitation established the mathematical foundation of celestial mechanics and enabled predictions of planetary motion.

[4] "There are countless suns and countless earths all rotating round their suns in exactly the same way as the seven planets of our system. [...] We see only the suns because they are the largest bodies and are luminous, but their planets remain invisible to us because they are smaller and non-luminous." [Bruno, 1830]. The inherent difficulty in imaging exoplanets was reiterated one century later by Huygens: "For let us fancy our selves placed at an equal distance from the Sun and fixed Stars; we would then perceive no difference between them. For, as for all the Planets that we now see attend the Sun, we should not have the least glimpse of them, either that their Light would be too weak to affect us, or that the Orbs in which they move would make up one lucid point with the Sun." [Huygens, 1698].

[5] "This most beautiful System [...] could only proceed from the counsel and dominion of an intelligent and powerful being." [Newton, 1729]

The discovery of Uranus by William Herschel in 1781, initially mistaken for a comet, marked the first planetary identification with a telescope [Herschel, 1912], expanding the Solar System beyond Saturn and demonstrating the power of telescopic instrumentation. Neptune's discovery in 1846 introduced a new paradigm of indirect detection: orbital residuals of Uranus, inconsistent with Newtonian predictions, led Le Verrier [Le Verrier, 1846] and Adams [Adams, 1846] to calculate its location, enabling Galle's observational confirmation [Galle, 1846]. This validated gravitational perturbations as a method of planetary discovery and exemplified the potential of indirect inference over direct observation. The notion that similar indirect methods could infer planets beyond the Solar System gained traction shortly after. In discussing periodic variable stars, Lardner suggested that variability in stellar brightness could arise from planetary transits, although planets capable of inducing such an effect would necessarily be large and Solar System planets would not be observable from afar[6].

Early exoplanet claims arose in the 19th century, when astrometric anomalies in stellar motions were attributed to gravitational perturbations of unseen companions, hypothetically presumed to be planets. In 1855, the binary 70 Ophiuchi was proposed to host a third planetary-mass body [Jacob, 1855], a claim later reinforced [See, 1896] but ultimately rejected on orbital stability grounds [Moulton, 1899]. Similar assertions persisted through the 20th century, involving 70 Ophiuchi [Berman, 1932; Reuyl & Holmberg, 1943], 61 Cygni [Strand, 1943], Lalande 21185 [van de Kamp & Lippincott, 1951], and Barnard's star [van de Kamp, 1963]. Subsequent re-analyses attributed these signals to observational or instrumental errors [Hershey, 1973; Gatewood, 1974; Heintz, 1978]. Modern detections have since confirmed planets in some of these systems, albeit with properties distinct from earlier predictions - for example, Barnard's star hosts a system of four rocky planets rather than a gas giant [Basant et al., 2025].

Beyond astrometry, other indirect detection methods were explored theoretically. Belorizky[7] propounded a detailed evaluation of the transit method first suggested a century earlier [Belorizky, 1938], dismissing its feasibility due to the planet's faint magnitude at stellar distances and extreme star-planet luminosity contrast[8], and noting that only systematic monitoring of dense stellar fields could reveal the rare case of a transit under nearly edge-on orbital alignment. He also considered radial velocity detection - detecting Doppler shifts in the spectrum of an observed star induced by an orbiting companion - already routinely used for binaries, but concluded that planetary signals were far below the precision of contemporary spectrographs.

[6] "Periodical obscuration or total disappearance of the star, may arise from transits of the star by its attendant planets." [Lardner, 1851]

[7] Interestingly, he was sheltered at the Haute Provence Observatory to escape persecution as a Jew amid the Nazi occupation in France. Remarkably, this same observatory later became the site of the discovery of 51 Peg b, the first known extrasolar planet.

[8] "The only way that we see at the moment to possibly detect existence of planets in other worlds is the photometry with a precision of 1/100 magnitude, which is the precision of current photo-cells." [Belorizky, 1938]

In 1952 Struve, a pioneer of modern astrophysics, argued that advances in instrumentation would render exoplanet detection via radial velocity and transits feasible [Struve, 1952]. Close-in giant planets[9] could induce Doppler shifts marginally detectable with existing Coudé spectrographs (200 m s^{-1}), while transits might produce measurable light losses with photoelectric methods, though spectroscopy offered greater accuracy[10]. Struve thus advocated extensive spectrographic surveys as the next step for exoplanet detection. These proposals faced skepticism, as prevailing models assumed planetary systems resembled the Solar System, with gas giants at wide separations producing weak velocity signals. Similarly, the low geometric probability of transits implied that only long-term monitoring of vast stellar samples could yield detections.

By the 1980s, radial velocity precision reached 15 m s^{-1} [Campbell & Walker, 1979], and transit theoretical framework and instrumentation design were refined [Rosenblatt, 1971; Borucki & Summers, 1984]. Several candidate exoplanet detections were reported in the late 1980s and early 1990s (see Figure 1.1.1), primarily via radial velocity, but most failed to achieve consensus or definitive confirmation. A companion to Gamma Cephei A was announced in 1988 [Campbell et al., 1988], withdrawn four years later when the signal was attributed to periodic changes in the star's magnetic activity, yet ultimately confirmed a decade afterward [Hatzes et al., 2003]. In 1989, Doppler spectroscopy revealed a massive companion to HD 114762 A [Latham et al., 1989], confirmed in 1991 [Cochran et al., 1991] but later reclassified as a red dwarf in a binary system [Kiefer, 2019; Winn, 2022]. In 1991, pulsar timing - measurements of the variations in the arrival times of regular radio pulses from the pulsar - of PSR B1257+12 uncovered two Earth-mass planets [Wolszczan & Frail, 1992]. The detection of planets in such a hostile environment challenged prevailing expectations, which had been shaped by theories and observational efforts focused primarily on main-sequence stars.

The first detection of an exoplanet orbiting a Sun-like star via radial velocity was announced in 1995 by Mayor and Queloz [Mayor & Queloz, 1995]. They identified a Jupiter-mass companion in a close orbit around 51 Pegasi, overturning long-standing assumptions about planetary architectures and inaugurating the class of "hot Jupiters". The importance of 51 Pegasi b was later recognised with the 2019 Nobel Prize in Physics. This landmark discovery triggered rapid growth in exoplanetary science, propelled by advances in observational techniques and multidisciplinary collaboration. Rooted in millennia of speculation but only recently grounded in empirical evidence, the field continues to progress swiftly, reshaping our understanding of planetary systems.

[9] "There is no compelling reason why the hypothetical stellar planets should not, in some instances, be much closer to their parent stars than is the case in the solar system." [Struve, 1952]

[10] "loss of light in stellar magnitudes [...] should be ascertainable by modern photoelectric methods, though the spectrographic test would probably be more accurate." [Struve, 1952]

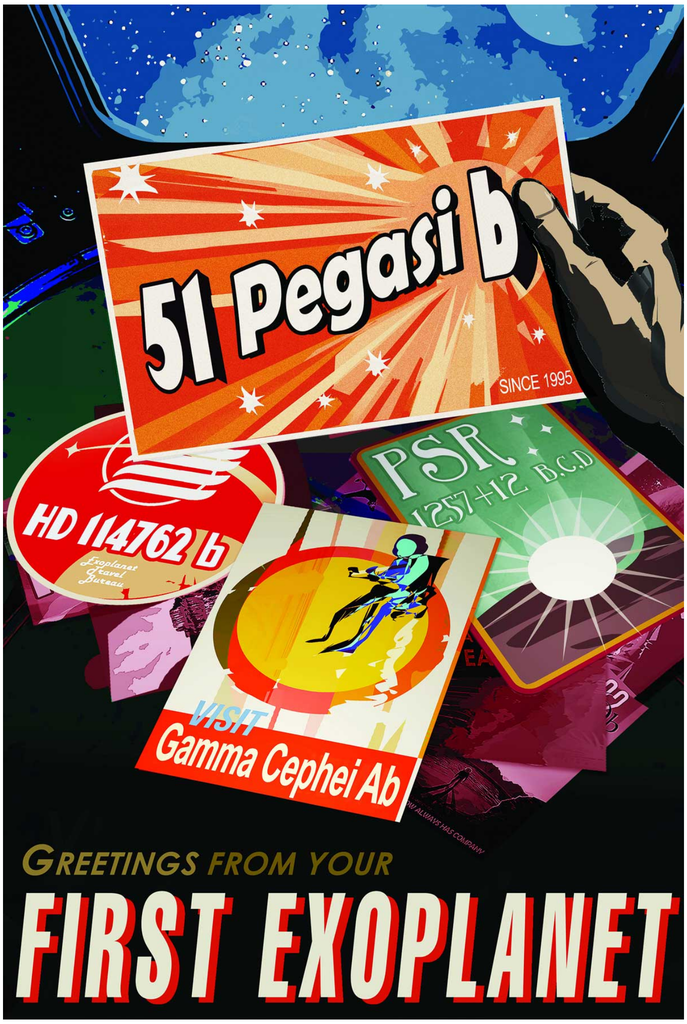

Figure 1.1.1: Postcards from exoplanets: claimed "first exoplanet" detections around Gamma Cephei A, HD 114762, PSR B1257+12, and 51 Pegasi (1988 - 1995). Image credit: NASA - Jet Propulsion Laboratory, California Institute of Technology [2020].

1.1.2 Towards a definition

The first discovery of an exoplanet around a main-sequence star, just over thirty years ago, revolutionised our anthropocentric view of the Universe: planets can differ radically from those in the Solar System, reside in systems with disparate architectures, and orbit stars unlike the Sun. Since then, exoplanet research has seen an unstoppable development, with 6080 planets confirmed to date (January 2026, NASA Exoplanet Archive [Christiansen et al., 2025]). Although now firmly established - underscored by the 2019 Nobel Prize in Physics - the field's early development was marked by considerable scepticism. Until the late 1990s, the community remained cautious, shaped by premature claims later dismissed as false positives, which underscored the methodological challenges of distinguishing planetary signals from stellar or instrumental noise[11].

Following the first confirmed detections, a formal definition of "planet" became necessary to establish clear criteria amid growing detections and ambiguities surrounding brown dwarfs, free-floating planetary-mass objects, and binary companions. In the early 2000s, the International Astronomical Union (IAU) Working Group on Extrasolar Planets (WGESP) issued and later amended a provisional definition of the term "planet" specifically for application to extrasolar bodies, stating that "We can expect this definition to evolve as our knowledge improves." [Boss et al., 2003]. By 2018, confirmed exoplanets had increased by a factor of forty, revealing wide diversity in masses, radii, orbital configurations, and host environments. This expanded dataset enabled population-level analyses of occurrence rates and parameter distributions, providing essential constraints that refined - and in many cases redefined - theoretical paradigms of planet formation, evolution, and classification.

The previous definition needed to be reassessed and, if needed, updated. In 2018, The Organizing Committee (OC) of IAU Commission F2 "Exoplanets and the Solar System" established that [Lecavelier des Etangs & Lissauer, 2022]:

The current working definition of an exoplanet is as follows:

1. *Objects with true masses below the limiting mass for thermonuclear fusion of deuterium (currently calculated to be 13 Jupiter masses for objects of solar metallicity) that orbit stars, brown dwarfs or stellar remnants and that have a mass ratio with the central object below the L4/L5 instability* ($M/M_{central} < 2/(25+\sqrt{621}) \approx 1/25$) *are "planets" (no matter how they formed). The minimum mass/size required for an extrasolar object to be considered a planet should be the same as that used in our Solar System.*

2. *Substellar objects with true masses above the limiting mass for thermonuclear fusion of deuterium are "brown dwarfs", no matter how they formed nor where they are located.*

3. *Free-floating objects in young star clusters with masses below the limiting mass for thermonuclear fusion of deuterium are not "planets", but are "sub-brown dwarfs" (or whatever name is most appropriate).*

[11] In the late 1980s, while searching for exoplanetary signals via Doppler observations at the University of British Columbia, the team leader emphasized the need for greater support from the Telescope Time Allocation Committee: "It is quite hard nowadays to realize the atmosphere of skepticism and indifference in the 1980s to proposed searches for [extrasolar] planets. Some people felt that such an undertaking was not even a legitimate part of astronomy." [Murphy, 2022]. Notably, his team led to the detection of Gamma Cephei Ab [Campbell et al., 1988], but the claim, although ultimately true, was later recanted due to supposed data ambiguity.

This current definition remains a working definition and may be subject to amendment or complete revision as our knowledge and understanding continue to advance, particularly in view of the anticipated growth in detections and the increasingly sophisticated characterisation of exoplanets enabled by both space- and ground-based observations.

1.1.3 Exoplanet detection

As outlined previously, multiple observational techniques have been developed for exoplanet detection, each subject to intrinsic biases and yielding only partial information regarding planetary physical and orbital characteristics. Figure 1.1.2 provides a visual representation of the cumulative number of confirmed exoplanets by year and discovery method, while the Perryman Tree (Figure 1.1.3) complements this by synthetically detailing current and prospective methods, organised hierarchically to show both the number of detections and the logarithmic mass range accessible to measurements achieved today (solid lines) or anticipated within the next 10-20 years (dashed lines). Recognising these methodological limitations is essential for appreciating the complementary role of theoretical modelling in interpreting and characterising exoplanetary systems.

In the following, the principal detection techniques are briefly reviewed, with particular attention to their respective strengths and constraints in the context of current-generation astronomical instrumentation.

- **Astrometry**
  As noted previously, small periodic shifts in a star's position relative to background references led to the earliest, later refuted, claims of exoplanet detection. This periodic anomalous motion, caused by the gravitational pull of a companion, appears as a helical stellar trajectory when stellar positions are measured precisely over time. Astrometric detection requires multi-year campaigns and, with current instrumentation, is limited to Jupiter-mass bodies orbiting low-mass stars. To date, the method has yielded six confirmed planets, four of which with ESA's Gaia spacecraft designed for astrometry [Christiansen et al., 2025]. Astrometry is proving valuable as a follow-up for further characterising known exoplanets, enabling inference of planetary masses and orbital parameters (e.g. [Snellen & Brown, 2018; Wallace et al., 2025]) and refining knowledge of host stars. Gaia Data Release 3 (DR3) includes about 60 astrometry candidates [Gaia Collaboration et al., 2016], while DR4 (to be released in December 2026) is expected to yield a substantially larger set.

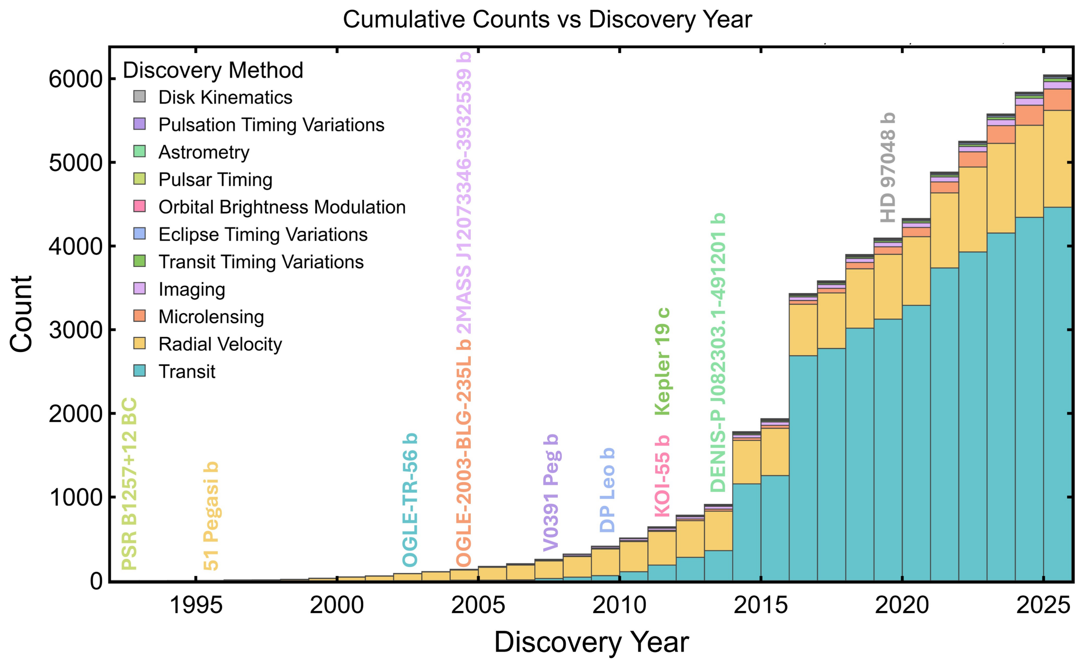

Figure 1.1.2: Cumulative number of confirmed exoplanets by year of discovery, obtained using the data from the NASA Exoplanet Archive [Christiansen et al., 2025] (accessed on 27 January 2026). The total number of exoplanets is 6080. The displayed names correspond to the first confirmed discoveries obtained with each listed method. The sharp increases in 2014 and 2016 corresponds to Kepler data releases, respectively, consisting of the announcement of 715 and 1284 detections via transit.

- **Radial velocity**
  The radial velocity method, responsible for the first exoplanet discovery around a main-sequence star [Mayor & Queloz, 1995] and for the majority of the first few hundred detections, relies on high-resolution spectroscopy to measure periodic Doppler shifts in stellar spectra caused by planet-induced motion of the host star around the system's centre of mass. These shifts yield stellar radial velocities and, in turn, lower-limit constraints on planetary masses. To date, 1158 exoplanets have been identified via radial velocimetry [Christiansen et al., 2025]. The technique is most sensitive to massive planets in close, edge-on orbits around their parent stars, as these produce larger Doppler shifts. Detecting terrestrial planets in the habitable zones of Sun-like stars remains challenging, as their signals approach the sensitivity threshold of current instruments ($\sim$10 cms^{-1} for the Echelle Spectrograph for Rocky Exoplanets and Stable Spectroscopic Observations, ESPRESSO [Pepe et al., 2014]) and are strongly affected by stellar activity, oscillations, and granulation [Netto et al., 2021]. By contrast, due to the closer-in habitable zones of low-mass stars, terrestrial panets in such configurations yield stronger radial velocity signals, enabling detections of potentially habitable terrestrial planets around nearby hosts (e.g. Proxima Centauri b [Anglada-Escudé et al., 2016], Ross 128b [Bonfils et al., 2018], Teegarden's Star b and c [Zechmeister

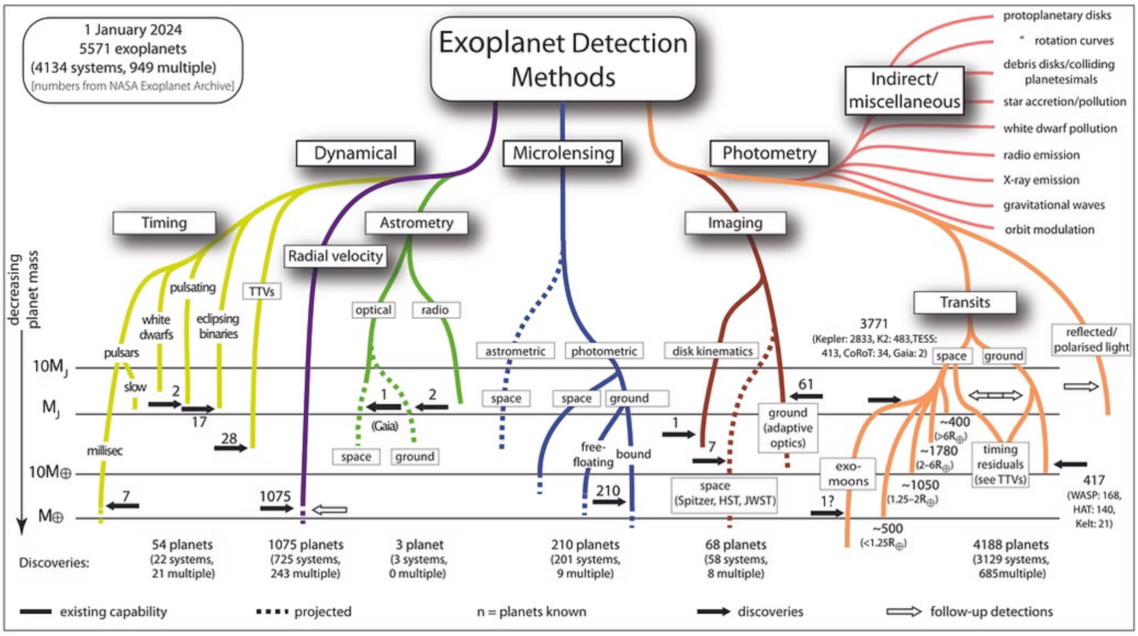

Figure 1.1.3: The Perryman Tree: first published in 2000 in a review of the then embryonic field of exoplanet science [Perryman, 2000] and subsequently updated, this diagram gives a schematic overview of the present and future methods of detecting exoplanets and their capabilities. The diagram pictured here is an updated version from January 2024. Image credit: Perryman [2024].

et al., 2019], and Wolf 1069b [Kossakowski et al., 2023]).

- **Transits**
  The vast majority of confirmed exoplanets (∼74% at the time of writing [Christiansen et al., 2025]) have been detected via the transit method, which measures periodic stellar dimming as a planet traverses in front of the target star. First applied to HD 209458 b, already detected via radial velocity [Charbonneau et al., 2000; Henry et al., 2000] and the first planet observed with multiple methods, the transit method has been successfully carried out as a means to discover transiting exoplanets. Dedicated space missions have since surveyed large portions of the sky over extended periods of time, including Kepler (2783 confirmed, 1979 candidates), its extended mission K2 (549 confirmed, 976 candidates), and TESS (733 confirmed, 4686 candidates) [Christiansen et al., 2025]. Transits require near edge-on orbital alignment with the observer, with larger planets in smaller orbits around low-mass stars producing more frequent and bigger fractional reduction in observed flux. Notwithstanding this bias, terrestrial planets around Sun-like stars yield ∼100 ppm signals, well within the sensitivity of the aforementioned facilities (e.g. ∼20 ppm for Kepler [Koch et al., 2010]). Transit photometry directly yields orbital periods and planetary radii, while further characterisation is possible through light-curve analysis and transmission spectroscopy (see Section 1.1.4).

- **Direct imaging**
  Direct detection spatially resolves the planet and host star separately, thereby directly observing the target exoplanet through reflected or emitted radiation. Despite technical challenges posed by high star-planet contrast and small star-planet angular separations, the method can be successfully employed with the use of highly sensitive detectors, the aid of coronagraphs and adaptive optics, and the use of techniques such as speckle imaging or nulling interferometry. Direct imaging favours wide-orbit planets or isolated planetary-mass objects (iPMOs) with high intrinsic flux, for example from residual accretion heat in young planets. Although relatively successful in identifying massive bodies (91 confirmed exoplanets to date [Christiansen et al., 2025]), the direct detection of terrestrial planets remains beyond current capabilities, but promises valuable constraints on orbital parameters and emission spectra.

- **Gravitational microlensing**
  First proposed in the 1990s [Mao & Paczynski, 1991; Gould & Loeb, 1992], gravitational microlensing detects exoplanets through the temporary relativistic magnification of a background star's light caused by a foreground star-planet system acting as a lens. The method favours large planet-star mass ratios - though Earth-mass planets remain detectable - and intermediate semi-major axes, and dense background stellar fields such as the Galactic Bulge maximise the probability of alignments with the foreground systems. Microlensing can also reveal iPMOs, although these events are unpredictable [Mróz et al., 2019] and is sensitive to Earth- and Neptune-sized planets in wide orbits beyond the snow line [Sumi et al., 2010; Vandorou et al., 2025]. This method has been relatively successful in identifying massive objects (263 confirmed exoplanets at the time of writing [Christiansen et al., 2025]).

- **Other methods**
  The techniques discussed above account for the overwhelming majority of exoplanet detections, while additional methods have yielded 76 confirmed cases at the time of writing [Christiansen et al., 2025].
  Timing variation methods detect exoplanets by measuring deviations in the expected timing of periodic astronomical events, caused by the gravitational influence of an orbiting planet. These include *pulsar timing* (variations in the regular pulses of radio waves) - responsible for the first exoplanet detections in 1992 [Wolszczan & Frail, 1992] - and *pulsation timing* (variations in the stable oscillations of pulsating variable stars). Planetary perturbations can also alter the periodicity or duration of transits, leading to *transit timing* (variations in known transit signals) and *eclipse timing* (variations in binary star eclipses).
  Orbital brightness modulations detect non-transiting planets with high reflectivity or thermal emission through phase-dependent variations in star-planet system

brightness. *Disk kinematics* has yielded one detection by analysing localised deviations in gas velocity patterns within protoplanetary discs caused by young planets. For completeness, the first extragalactic candidate - around a high-mass X-ray binary in the M51 Whirlpool Galaxy, ∼28 million light-years from Earth - has been reported via the novel *X-ray transit* method but remains unconfirmed [Di Stefano et al., 2021]. Whether planets in other galaxies can be detected thus remains an open question.

1.1.4 Exoplanet characterisation

Exoplanet science has advanced dramatically since the first confirmed detections, with recent efforts shifting from discovery to detailed characterisation. Current scientific objectives have evolved to encompass a comprehensive investigation of planetary interiors and atmospheric properties to elucidate formation pathways and migration histories, thereby informing the architecture and evolution of planetary systems. A central focus also lies in probing physical processes - such as climate states and star-planet interactions - that govern habitability and long-term stability (see Section 1.2).

The integration of multiple detection techniques advances the physical characterisation of exoplanets, as illustrated by the mass-period distribution in Figure 1.1.4, which highlights the observational biases inherent in different methods. Transit measurements yield planetary radii by quantifying flux dips during occultation, while radial velocity provides mass estimates from spectral Doppler shifts. Combined, these methods enable bulk density determinations, essential for inferring internal composition and distinguishing between rocky, gaseous, and icy bodies. Signal periodicity constrains the semi-major axis and orbital period, while joint analyses of transit timing and radial velocity refine eccentricity and inclination, offering insights into dynamical histories and system architectures.

Beyond characterisation through a combination of multiple detection techniques, methods exist to observe and characterise exoplanetary atmospheres, as they provide critical insights into planetary composition, evolution, and habitability [Kreidberg, 2018; Madhusudhan, 2019]. Spectrometry enables inferences regarding composition, revealing chemical species in the form of gases, condensates, and aerosols, while also constraining thermal structure and dynamical processes such as circulation and heat redistribution. Spectra encode signatures of disequilibrium phenomena, including vertical mixing, photochemistry, and atmospheric escape. These phenomena can be linked to surface interactions, internal conditions, and formation pathways. Detecting atmospheres is far more challenging than detecting planets themselves, requiring sensitivities orders of magnitude higher. Nonetheless, remote sensing has become a central tool for probing

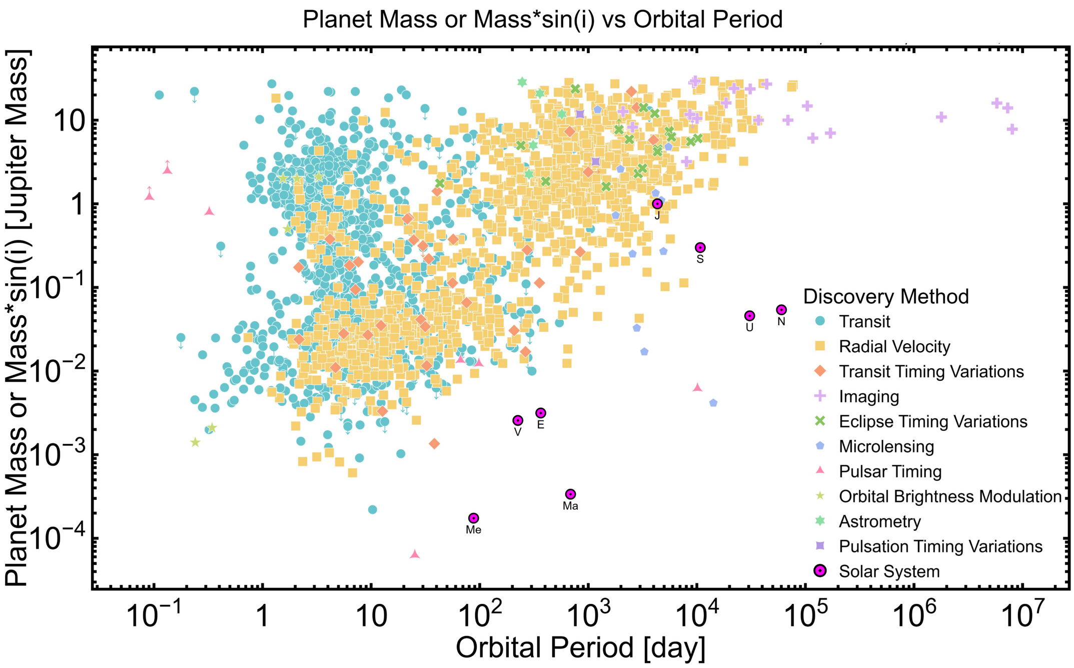

Figure 1.1.4: Scatter plot of known exoplanets M_p [or $M_p\sin(i)$] and orbital periods, coloured according to detection method. The Solar System planets are overlaid for comparison. The data used is from the NASA Exoplanet Archive [Christiansen et al., 2025] (accessed on 27 January 2026).

both Solar System and extrasolar planets. Several techniques have been developed, each addressing specific questions about atmospheric composition, dynamics, and climate.

Brief outlines of the main observational approaches for exoplanet atmosphere characterisation, along with their key inferences, are presented below.

- **Transmission spectroscopy**
  During a primary transit, a fraction of the starlight filters through the planet's terminator region - the boundary between the planet's dayside and nightside - where atmospheric molecules and atoms absorb at specific wavelengths, imprinting characteristic spectral signatures onto the transmitted light. Comparing in-transit and out-of-transit spectra reveals the sources of extinction underlying these features. Transit spectroscopy, first proposed in 1994 [Schneider, 1994] and demonstrated nearly a decade later for HD 209458 b with the detection of Na absorption at 589 nm [Charbonneau et al., 2002], is most effective for hotter, larger planets due to its dependence on atmospheric scale height, while cooler, smaller planets remain more challenging to characterise.

- **Eclipse spectroscopy**
  Eclipse spectroscopy probes the dayside atmosphere of exoplanets by comparing spectra obtained shortly before the secondary eclipse, containing both stellar and

planetary dayside contributions, with those during eclipse, when the planet is fully obscured by the star. Isolating the planet's contribution yields the thermal emission from the atmosphere alongside reflected starlight. The resulting spectra may exhibit absorption and/or emission features depending on the atmospheric vertical temperature profile and wavelength-dependent opacity of atmospheric constituents. Thermal emission spectra studies predominantly target the infrared range, where planetary emission is maximised, while the optical range is valuable for detecting starlight reflected off the planet, revealing the presence of reflective clouds or hazes. Eclipse depth depends on the relative radii and temperatures of the planet and its host star, making the technique particularly sensitive to large, hot planets orbiting comparatively smaller, cooler stars. HD 209458 b yielded one of the earliest multi-wavelength eclipse depth measurements, obtained with the photometric channels of the Infrared Array Camera (IRAC) aboard the Spitzer Space Telescope [Knutson et al., 2008].

- **High resolution Doppler spectroscopy**
  By observing the spectrum of a star-planet system in sufficiently high resolution, planetary spectral features can be separated from those of the host star, as they are Doppler shifted due to the planet's radial velocity while stellar lines appear stationary. High resolution spectroscopy typically requires ground-based high-resolution spectrographs and can be applied to non-transiting exoplanets, differently from transit and eclipse spectroscopy. This technique enables inference of atmospheric composition via cross-correlation with synthetic template spectra [Birkby, 2018], and can constrain atmospheric thermal profiles through planetary emission. Additional Doppler shifts reveal dynamical processes such as $\mathrm{km\,s^{-1}}$ winds [Snellen et al., 2010], while rotational broadening of spectral features constrains planetary spin [Snellen et al., 2014]. Moreover, sharper lines at high resolution allow characterisation of cloudy atmospheres that appear featureless at lower resolution [de Kok et al., 2013].

- **Phase curve**
  Observations of the planet-star flux ratio as a function of orbital phase can be performed for both transiting and non-transiting exoplanets. As different regions of the illuminated and dark planetary hemispheres rotate in and out of the observer's field of view, phase curves enable atmospheric characterisation as a function of longitude. Photometric phase curves provide insights into planetary temperature maps, heat redistribution efficiency, and cloud coverage, often revealed through shifts of the hotspot relative to the substellar point [Cowan & Agol, 2011; Komacek et al., 2017; Parmentier & Crossfield, 2018]. Spectroscopic phase curves, analogous to eclipse spectroscopy, constrain atmospheric composition, temperature profiles, and cloud/haze properties, but uniquely allow these quantities to be mapped longitudinally and tracked over time, thereby probing circulation patterns

[Stevenson et al., 2014]. As with other techniques, phase curve studies favour large, strongly irradiated planets. The first photometric phase curves of hot Jupiters obtained in the infrared [Harrington et al., 2006; Knutson et al., 2007] and optical [Snellen et al., 2009; Demory et al., 2013], revealed eastward hotspots and inhomogeneous high-altitude reflective clouds respectively.

- **Direct imaging spectroscopy**
  While the techniques discussed so far primarily target highly irradiated close-in giants such as hot Jupiters, direct imaging is instead sensitive to wide-orbit, recently-formed exoplanets, where large separations allow the planetary signal to be disentangled from stellar features. Direct imaging spectroscopy constrains atmospheric composition, thermal structure, and cloud properties, and has been conducted with both ground- and space-based facilities. Current efforts focus on emission spectra, while reflected-light spectra are a key goal for next-generation telescopes. The first direct low-resolution infrared spectra were obtained from two gas giants in the same system, HR 8799b [Bowler et al., 2010] and HR 8799c [Janson et al., 2010], revealing thick photospheric dust clouds.

1.2 Exoplanetary climate and habitability

1.2.1 The concept of habitability

It is often assumed that the debate on extraterrestrial life began in the last century. Historical research, however, shows this view is misleading: discussions of the possibility of intelligent life, deeply connected to the concept of the plurality of worlds (see Section 1.1.1), date back to Greek and Latin antiquity. An interesting comprehensive survey of this debate in Western tradition from antiquity to the twentieth century is provided by Crowe & Dowd [2013]. The search for life beyond Earth represents one of the most compelling scientific endeavours of our time. Over the past several decades, advances in both theoretical and observative science have transformed this pursuit from speculation into a rigorous field of inquiry. Identifying extraterrestrial life, within and beyond the Solar System, would provide critical insights into the origin and evolution of biology and the potential diversity of life forms, as well as having profound implications for understanding Earth's uniqueness and the prevalence of habitable environments.

Over the past three decades, exoplanet detection and characterisation have advanced dramatically, revealing a Universe teeming with a fascinating assortment of exoplanets. Many of these worlds lack Solar System analogues and broaden our understanding of planetary systems, yet particular attention is given to terrestrial planets, which - despite their detection challenges - have been found in reasonable numbers. Notable examples include Proxima Centauri b, orbiting our nearest star [Anglada-Escudé et al., 2016], and the close-by TRAPPIST-1 system of seven transiting Earth-sized planets [Gillon et al., 2017]. Next-generation telescopes will enable precise atmospheric characterisation of rocky temperate planets, our best opportunity to search for biosignatures given Earth as the sole inhabited reference. Habitability, the degree to which a global environment can support life, is therefore a central focus of astrobiology and a cornerstone of strategic roadmaps such as NASA's Astrobiology Strategy [Hays et al., 2017] and the European AstRoMap project [Horneck et al., 2016].

Earth remains the only known inhabited planet, and its properties inform the search for habitable environments elsewhere. Although no consensus exists on the origin of life - its timing, location, or mechanisms - its fundamental requirements are well established. All known life depends on four conditions: an energy source (light or chemical energy), essential biogenic elements (C, H, N, O, P, S), a suitable solvent (liquid water), and physicochemical environments that permit molecular synthesization, stability and interaction (specific ranges of temperature, pH, salinity, and pressure) [Cockell et al., 2016]. Habitable conditions exist where these requirements are simultaneously met. The *surface liquid water criterion* is based on the premise that life as we know it requires a liquid environment, specifically water, and that only planets with stable surface water could be equipped with the physical and chemical conditions supportive of biospheres robust enough to be detected remotely. The requirement for liquid water constrains the temperature-pressure regime in which it is stable, thereby specifying the orbital range where a planet's radiation budget permits such conditions. This range constitutes the *circumstellar habitable zone* (see Section 1.2.2), within which the probability of life as a planetary process is enhanced, increasing the observational value of these targets.

Additional concepts analogous to those of the classic habitable zone have been developed regarding specific habitability requirements. On galactic scales, the *galactic habitable zone* is the region at a suitable distance from the Galactic centre where four conditions for complex life are satisfied: the presence of a host star, sufficient heavy elements to form terrestrial planets, adequate time for biological evolution, and protection from life-extinguishing supernovae [Lineweaver et al., 2004]. The position of the *photosynthetic habitable zone* permits both liquid water and oxygenic photosynthesis, making it the region where biosignatures of photosynthetic life are most likely to occur [Hall et al., 2023]. The *ultraviolet habitable zone* is bounded by a minimum UV flux that drives photochemical synthesis of life's building blocks and a maximum flux that erodes atmospheres and damages essential biomolecules [Spinelli et al., 2023]. Beyond the planetary context, the *circumplanetary* or *exomoon habitable zone* encompasses the potential for satellites and minor bodies to sustain habitability even at large orbital distance from the host star, supported by tidal heating and illumination from the host planet in addition to instellation [Heller & Barnes, 2013; Forgan & Kipping, 2013; Dobos et al., 2017; Martínez-Rodríguez et al., 2019; Forgan, 2019].

Residence within the habitable zone offers only a binary assessment of habitability, whereas proposed habitability indices - based on climatological metrics such as thermal and aridity thresholds for microbial and macroscopic life - can capture patterns of surface habitability and provide a foundation for more comprehensive evaluations of life-supporting environments on other planets [Silva et al., 2017; Woodward et al., 2025]. Even so, they are predictions based on our knowledge and understanding of Earth-based processes, and therefore they do not serve as a universal and definitive way of identifying environments that could potentially host life. Extraterrestrial life may employ biochemistries subject to requirements and constraints distinct from those of Earth biology. The properties of terrestrial life may represent a single manifestation of a broader set of biological possibilities, and environments habitable to Earth organisms may constitute only a subset of potential habitats. Alternative chemistries, solvents, and energy sources remain plausible [Schulze-Makuch & Irwin, 2006], and the potential presence of habitable environments beyond the planetary surface, such as in subterranean environments [Möhlmann, 2012; McMahon & Parnell, 2014], in cloud decks [Stark et al., 2014; Seager et al., 2021], and in subsurface oceans [Quick et al., 2023] is contemplated in a few studies.

1.2.2 Habitable Zone

Although the concept of the "habitable zone of a star" may be traced back to ideas developed well before the 20th century[12], one of the first scientific definitions found in literature was proposed by Huang [1959], and places the concept against the backdrop of exoplanetary habitability and extraterrestrial carbon-based life, assuming a universal chemistry of organic substances. This definition of habitable zone states that the energy provided by the luminosity L of a star supplies necessary heat to the living organisms on a planet, but said heat must be "neither too large nor too small. [...] Otherwise they will perish.". Huang therefore defined the circumstellar habitable zone as the region such that the energy received per unit area at a distance d, $L/(4\pi d^2)$, lies between an upper and a lower limit, that determine the inner and outer edges of said region. Thus, a planet is habitable if its distance d from the host star satisfies the condition $d_{inner} < d < d_{outer}$. Moreover, if all planets orbiting a certain star are formed approximately in a single fundamental plane, as is true for the Solar System, the habitable zone takes the shape of a concentric circular ring around the star.

[12]For example, Richard Bentley (1662 - 1742) "praised God's wisdom in placing our planet at just such a distance from the sun that we are neither too cold nor too hot", and subsequently William Whewell (1858) mentioned the "temperate zone of the solar system" [Perryman, 2018].

Dole [1964] refers to an analogous concept with the term "ecosphere", a "region in space, in the vicinity of a star, [... that] lies between two spherical shells centered on the star. Inside the inner shell, illuminance levels are too high; outside the outer shell, they are too low" for allowing not only the origin, evolution and continuous existence of complex life forms, but also for providing conditions suitable specifically for human beings. According to this definition, at least 10% of the surface must maintain a mean annual temperature between 0°C and 30°C, with seasonal mean daily temperatures remaining within the range of -10°C to 40°C.

Based on the aforementioned "liquid water criterion", the classical habitable zone is defined as the circumstellar region in which the combination of stellar flux and orbital parameters allow a planet to be characterised by surface properties compatible with the existence of liquid water on its surface. Establishing the inner and outer edges of the habitable zone is a complex task, and different approaches can be employed to estimate this range. The simplest way of estimating the position of habitable zone boundaries involves zero-dimensional (0-D) energy balance models, which treat the planet as a single point to calculate its average temperature based on the energy balance between the incoming and outgoing radiation.

The classic definition of the *circumstellar habitable zone* around main-sequence stars was established by Kasting et al. [1993] using one-dimensional (1-D) radiative-convective climate models of an Earth-like planet with a $CO_2/H_2O/N_2$ atmosphere and an active carbonate-silicate cycle regulating carbon exchange between atmosphere, surface, and interior (Figure 1.2.1a). The atmosphere was treated as a single vertical column divided into layers for radiative transfer calculations, with clouds excluded at the microphysical level but their macroscopic effects, such as their reflectance, parametrised by increasing the surface albedo. As stellar luminosity increases over main sequence evolution, the boundaries of the habitable zone shift outward. As a result, the *continuously habitable zone* (Figure 1.2.1b) is defined as the circumstellar region within which a planetary body can sustain surface liquid water over geologically significant timescales, thereby providing the temporal stability necessary for long-term climatological equilibrium and potential biospheric development [Hart, 1979; Kasting et al., 1993; Rushby et al., 2013].

The width of the habitable zone is determined by inner and outer boundaries set by extreme climate conditions that limit surface liquid water, primarily governed by atmospheric properties regulating feedbacks. The conservative inner edge corresponds to stratospheric water vapour saturation, water loss via photolysis, and hydrogen escape (*moist greenhouse*), while the conservative outer edge is defined by CO_2 cloud formation that increases albedo and cools the surface (*maximum greenhouse*). A less conservative inner edge, more violent and catastrophic, reflects complete vaporisation of surface water on short geological timescales (*runaway greenhouse*). A more optimistic empirical habitable zone is inferred from the supposed past habitability of the planets

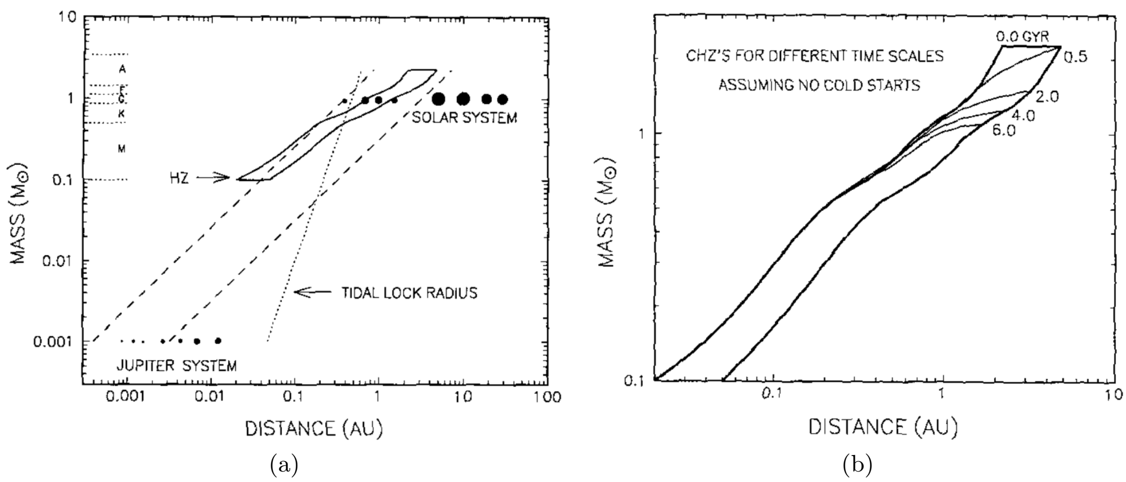

Figure 1.2.1: (a) Solid line: position of the conservative circumstellar habitable zone around host stars with different masses. Dotted line: position of the tidal lock radius around stars with different masses. Dashed lines: position of the region of terrestrial planet formation around stars with different masses. (b) Conservative continuous circumstellar habitable zone around host stars with different masses for different planetary habitability times. In this plot, no "cold starts" are permitted, meaning that a planet initially beyond the outer edge of the habitable zone will not be able to warm up once the stellar luminosity increases. Image credit: Kasting et al. [1993].

neighbouring Earth: the inner edge from Venus, whose surface has lacked liquid water for at least 1 Gyr according to observations from the Magellan radar system (*recent Venus*) [Solomon & Head, 1991], and the outer edge from Mars, whose surface hosted liquid water 3.8 Gyr ago (*early Mars*) [Pollack et al., 1987].

The classical definition of the habitable zone is continually revised in parallel with the refinement of climate models used to compute its boundaries, as well as the incorporation of additional factors influencing planetary climate, in order to achieve a more precise determination of the location of these boundaries. Therefore, the boundaries of the habitable zone are not rigorous barriers, but intrinsically depend on the adopted climate model and the consideration of factors that have an impact on climate (see Figure 1.2.2).

Kopparapu et al. [2013] proposed adjourned estimates of the inner and outer edges, ultimately adopting a model based on Kasting et al. [1993] with updated atomic and molecular databases. Kopparapu et al. [2014] expanded this work to provide estimates for planet masses within the range 0.1 - 5 $M_\oplus$ (with $M_\oplus$ denoting the mass of Earth) and generally found wider habitable zones for larger planets. Further refinements obtained with similar models take into account more comprehensive choices of atmospheric compositions, including molecular gases such as dihydrogen [Ramirez & Kaltenegger, 2017] and methane [Ramirez & Kaltenegger, 2018], or contemplating the possibility of primordial, H-He dominated atmospheres [Mol Lous et al., 2022].

Habitable zone boundary estimates, and in a broader sense habitability assessments, obtained with 1-D single atmospheric column models were naturally followed by those obtained with more sophisticated models that could simulate the effect of atmospheric features (such as clouds [Kitzmann et al., 2010; Yang et al., 2013] and hazes [Marley et al., 2013], varying atmospheric pressure [Vladilo et al., 2013], CO_2 outgassing [Abbot, 2016]), surface features (such as land/ocean fraction and distribution [Spiegel et al., 2009; Lewis et al., 2018; Kodama et al., 2019], surface type [Madden & Kaltenegger, 2020], ice and snow albedo feedbacks dependent on stellar spectral energy distribution [Joshi & Haberle, 2012; Shields et al., 2013], radiogenic and primordial heat [Lingam & Loeb, 2020], internal tidal heating [Jackson et al., 2008a], oceanic heat transport [Cullum et al., 2014; Hu & Yang, 2014], ocean salinity [Cullum et al., 2016; Batra & Olson, 2024], ocean tides [Si et al., 2022], salt-albedo feedback [Shields & Carns, 2018]), orbital characteristics (such as eccentricity [Williams & Pollard, 2002; Dressing et al., 2010; Palubski et al., 2020], obliquity [Ferreira et al., 2014; Vervoort et al., 2022], rotation rate [Yang et al., 2014a], long-term Milankovitch-type cycles [Spiegel et al., 2010], planetary companions [Menou & Tabachnik, 2003; Jones et al., 2006], orbital evolution due to tides [Jackson et al., 2008b]) and stellar effects (such as space weather and host star activity [Airapetian et al., 2017, 2020; Ridgway et al., 2023], stellar magnetism [Atkinson et al., 2024], stellar evolution [Gallet et al., 2017], stellar X-ray irradiation and consequent photoionisation and Compton scattering [Cecchi-Pestellini et al., 2006], stellar UV flux [Spinelli et al., 2023], stellar multiplicity [Simonetti et al., 2020; Eggl et al., 2020]).

The concept of habitable zone constitutes a useful preliminary tool to discern habitable planets from observable characteristics, providing a first-order assessment of habitability potential. This definition is ultimately oversimplified, as it neglects a range of factors influencing planetary climate. Although primarily controlled by the star-planet separation, the climate, and hence potential habitability of a planet, depend crucially on several factors.

1.2.3 Climate models

The habitable zone serves as a navigational tool for assessing planetary habitability, marking the region where surface liquid water is most likely to persist, yet its definition remains under scrutiny and continues to evolve with the search for a universal framework of habitability. Habitability assessment is a multi-parameter, interdisciplinary process, affected by numerous factors that may be intrinsic of the considered planet, may regard stellar inherent features or may refer to the system's architecture (see Figure 1.2.2). To refine these assessments, climate models of varying complexity - adapted from Earth studies and parametrising processes often unconstrained by observations - are employed

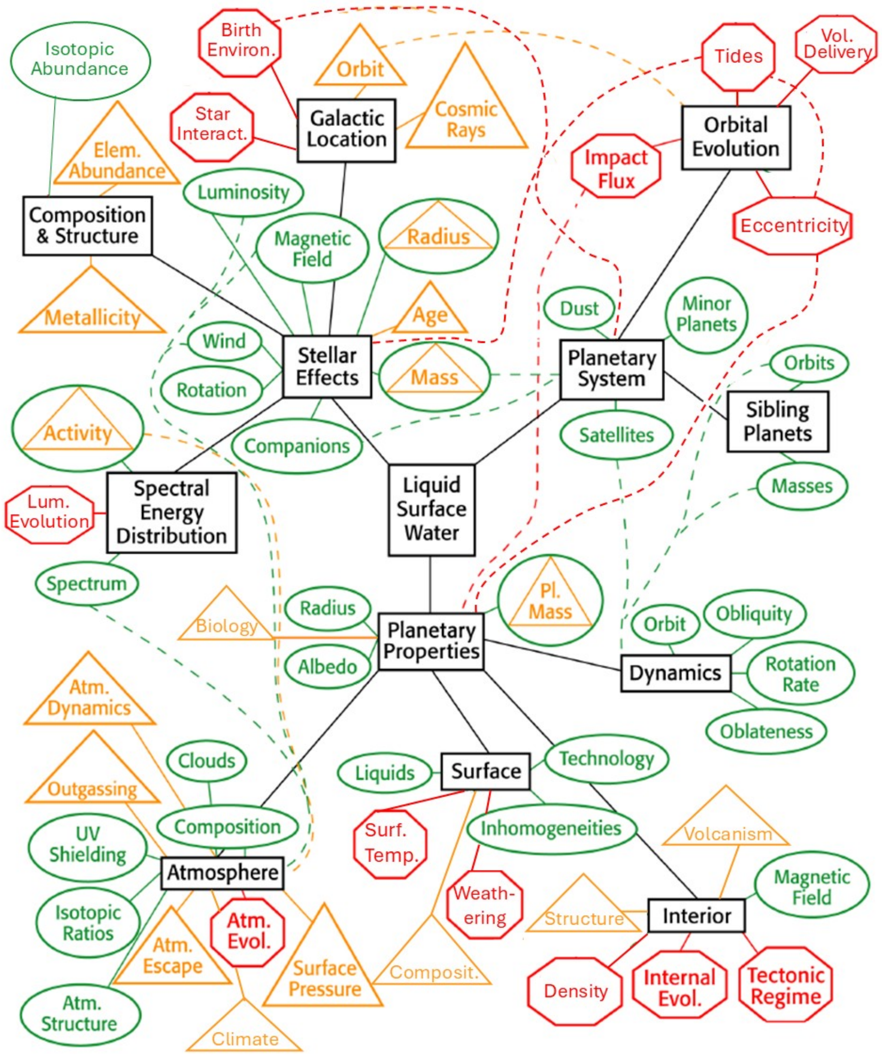

Figure 1.2.2: Planetary, stellar, and system properties and processes influencing habitability are shown, with font colours denoting observability: directly detectable with sufficiently powerful telescopes (green), requiring model interpretation possibly constrained by observations (orange), or accessible primarily through theoretical modelling (red). Adapted from Meadows & Barnes [2018].

to evaluate planetary habitability across diverse scenarios.

General Circulation Models (GCMs) are three-dimensional (3-D) mathematical tools solving geophysical fluid dynamics governing planetary climate. Atmospheric (AGCMs) and oceanic (OGCMs) models address individual components of the climate systems, while coupled Atmosphere-Ocean GCMs (AOGCMs) are the most comprehensive of the physical processes involved in determining planetary climate. State-of-the-art AOGCMs enable both large scale and local climate predictions and can incorporate modules for biogeochemistry, cloud chemistry, aerosols microphysics, carbon cycling, dynamic vegetation, human activity, and cryosphere dynamics, thereby capturing multiple feedbacks beyond atmosphere-ocean interactions. When these coupled physical models are further extended to include interactive biogeochemical cycles, they are referred to as Earth System Models (ESMs), which enable the simulation of climate-carbon-biosphere feedbacks beyond the scope of AOGCMs. These frameworks are specifically designed for Earth and are not directly applicable to other planets without substantial modification. Increasing model complexity requires extensive input parameters - many unconstrained for exoplanets - and imposes heavy computational demands. As GCMs are computationally intensive and time-consuming, they are not particularly suited for broad parameter space explorations typical of exoplanet climate studies. Simplified versions, often AGCMs with basic ocean representations, are therefore commonly employed.

Just below GCMs in the hierarchy of complexity are global models of intermediate complexity (ICMs), which adopt a simplified description of certain physical processes to allow faster calculations on more modest hardware compared to more sophisticated GCMs, while still delivering a reasonably accurate representation of the simulated scenarios. Compared to fully coupled GCMs, ICMs are more suitable for long-term integrations, sensitivity studies, and exploration of broad parameter spaces.

Low-complexity models are particularly well suited to rapid climate simulations, enabling preliminary habitability assessments and broad explorations of parameter space. Single atmospheric column calculations feature a simplified treatment of the vertical energy transport within a single column of atmosphere, taking into consideration how the atmospheric chemical composition and the stratification affect the radiative-convective equilibrium. This type of model has been adopted to derive analytical prescriptions of the habitable zone (e.g. Kasting et al. [1993]; Kopparapu et al. [2013], see Section 1.2.2). Energy Balance Models (EBMs) analytically describe the global energy balance of the planet, and can be adapted to include the longitudinal or latitudinal variations of physical quantities along the planetary surface, as well as to incorporate results from single atmospheric column calculations. Moreover, upgraded versions can adopt treatments of physical processes validated with three-dimensional experiments conducted with models of higher complexity.

Simulating planetary climates is inherently complex, and models differ widely in capability. Thus, the full hierarchy of climate models should be employed for cross-validation. With advancing observational capabilities, it is vital that exoplanet models reliably predict observability, enable robust data retrieval, and support accurate interpretation of planetary environments. Model intercomparisons are therefore essential, and the CUISINES Working Group of NASA's Nexus for Exoplanet System Science (NExSS) has addressed this challenge by developing a framework for community-organised Model Intercomparison Projects (exoMIPs) [Sohl et al., 2024]. By comparing climates across diverse model types and planetary targets, they seek to establish a systematic approach for evaluating exoplanet model performance.

1.2.4 The impact of the ocean

The dynamics and physics of oceans on exoplanets remain largely unexplored, along with many other exoplanetary characteristics, since only a few of them can be inferred from observational studies. However, Earth's ocean has been extensively studied and its relevance in determining Earth's climate is well established. Without the mitigating influence of the oceans, surface temperatures would exhibit significantly greater geographic, seasonal, and diurnal variability, likely rendering vast regions of the planet inhospitable to advanced life forms [Read, 2014].

The ocean is the principal carbon reservoir in Earth's climate system, storing ∼50 times more CO_2 than the atmosphere. It currently absorbs a large fraction of anthropogenic emissions and has exerted a dominant influence on past climate variability through carbon storage and release processes [Fischer et al., 2010]. With a heat capacity over 1000 times that of the atmosphere and a relatively low albedo that allows efficient absorption of solar radiation, the ocean is Earth's primary thermal reservoir, having absorbed over 90% of the excess heat from CO_2-induced warming in recent decades [Schmitt, 2018]. Thermal inertia causes ocean surface temperatures to respond slowly to variations in solar radiation, thus buffering surface temperatures against fluctuations in the forcings. Ocean circulation redistributes heat globally, moderating temperature contrasts between the equator and high latitudes. In the tropics, poleward energy transport by the ocean is comparable to that of the atmosphere [Trenberth & Caron, 2001]. Eliminating ocean circulation and its heat transport would expand sea ice cover and lower high-latitude surface temperatures [Winton, 2003], as well as cool the global mean climate [Herweijer et al., 2005]. Apart from present-day Earth, several studies substantiate that ocean dynamics constitute a significant contribution to climate states across a variety of planetary contexts, encompassing Earth's paleoclimates [Yang et al., 2012a,b; Kienert et al., 2012; Brown et al., 2018; Ragon et al., 2024] as well as climates of planets orbiting the early Solar System [Way & Del Genio, 2020; Schmidt et al., 2022].

It is clear, therefore, that oceans play a vital role in keeping much of Earth comfortably habitable, and their central influence on climate makes modelling exoplanetary oceans essential for assessing planetary habitability. As key exoplanetary characteristics, such as land mass distribution, are generally unknown, exoplanets are often approximated as water worlds entirely covered by global oceans, rendering a realistic representation of ocean processes particularly critical.

Due to their high computational demands, AOGCMs are seldom employed, and the vast majority of exoplanet climate studies rely on AGCMs of varying complexity coupled to simplified slab oceans typically 30-100 m thick, that neglect ocean heat transport or prescribe meridional heat fluxes (Q-fluxes) [Kopparapu et al., 2016, 2017; Boutle et al., 2017; Hammond & Komacek, 2024]. Owing to their computational efficiency, these approaches have yielded valuable insights into planetary habitability, atmospheric processes and surface characteristics through parameter sweeps [Wang et al., 2016; Kilic et al., 2017; Adams et al., 2019; Lerner et al., 2025]. Approaches that refine ocean representation employ simplified variants of coupled full-depth dynamic oceans, such as a 2-layer model incorporating Ekman-driven heat fluxes [Codron, 2012; Charnay et al., 2013; Charnay et al., 2017] which can incorporate parametrisations of mesoscale eddies [Bhatnagar et al., 2025], slab oceans emulating heat transport through purely diffusive fluxes [Kilic et al., 2017], and coupled OGCMs with relatively shallow (∼100-2000 m), uniformly deep "bathtub" oceans that reach radiative equilibrium more rapidly than full-depth models [Way & Georgakarakos, 2017; Way et al., 2018; Del Genio et al., 2019b; Salazar et al., 2020; Olson et al., 2020, 2022; Way, 2025].

These studies inherently limit the accuracy of climate and habitability assessments by neglecting the complex interactions and feedbacks of fully dynamic oceans. Although such approaches yield valuable insights, the lack of coupling to a dynamic ocean model precludes accurate portrayals of circulation in the simulated scenario. Incorporating processes such as tides, currents, heat transport, and sea ice dynamics can produce substantial differences in simulated exoclimates. Consequently, AOGCMs are particularly advisable for scenarios where ocean dynamics are likely to exert a significant influence on planetary climate.

The primary influence of ocean processes on exoplanetary climate has been illustrated by several studies (synchronous rotation scenarios are detailed in Section 1.2.5). Ocean heat storage capacity is of primary importance for mitigating climate, and even preventing snowball states, of high-obliquity [Ferreira et al., 2014] and moderate- to high-eccentricity planets [Way & Georgakarakos, 2017; Ji & Abbot, 2025]. In aquaplanet configurations, ocean heat transport dominates in the tropics resulting in warmer global mean surface temperature and reduced meridional temperature gradients, whereas land distribution changes mainly affect regional climate with limited impact on overall heat transport or global climate [Smith et al., 2006; Marshall et al., 2007; Ferreira et al., 2010]. Ocean circulation can be reversed by high salinity, yielding warmer climates and reduction in sea ice cover, so much so that a saltier ocean is suggested as a possible solution to the Faint Young Sun Paradox (e.g. Cullum et al. [2016]; Olson et al. [2022]). An increase in the strength of the overturning circulation and poleward heat transport, driven by slower planetary rotation, reduces meridional temperature gradients. Depending on the rotational regimes, this can lead to modest high-latitude warming but an overall cooling of global surface temperatures, potentially allowing the inner edge of the habitable zone to shift inward, although atmospheric feedbacks can introduce additional complexity (e.g. Cullum et al. [2014]; Way et al. [2018]; Guzewich et al. [2020]). Enhanced upwelling, driven by slower planetary rotation and higher surface pressure than Earth, increases nutrient supply to the surface biosphere, making such planets favourable targets for remote biosignature detection [Olson et al., 2020]. A strengthened meridional heat transport, simulated by an increase of oceanic horizontal diffusivity, can completely melt the perennial equatorial sea ice belt that characterises uncapped cryoplanets arising under high obliquity and intermediate stellar irradiance [Kilic et al., 2018]. Tide-induced ocean mixing, parametrised through enhanced vertical diffusivity, strengthens overturning circulation and poleward heat transport, leading to surface warming, polar sea ice loss, and reduced planetary albedo [Si et al., 2022; Di Paolo et al., 2025].

Understanding how oceans operate and how they influence climate remains an open problem in planetary science, particularly when extending beyond Earth-like conditions to bodies spanning a wide range of radii, compositions, and thermal regimes. Even for terrestrial planets, the diversity of possible ocean properties requires further investigation, and systematic comparisons between different models applied to similar scenarios would help clarify the sensitivity of ocean dynamics to model assumptions. These challenges become even more pronounced in environments that diverge substantially from Earth's, where the simplifications that are valid in terrestrial ocean modelling no longer apply, and different and/or additional processes must be accounted for.

Within the Solar System, several moons and dwarf planets are now known or strongly suspected to host large liquid water oceans, mostly overlain by icy shells. Confirmed or candidate ocean worlds include satellites orbiting Jupiter (Europa, Ganymede, Callisto), Saturn (Enceladus, Titan, Mimas), and Neptune (Triton), with Pluto and Ceres also potentially harbouring liquid layers. Among these bodies, Europa and Enceladus are considered prime candidates for hosting subsurface oceans with astrobiological potential and have been the focus of recent efforts to develop simplified ocean-circulation models with ice-ocean coupling [Zeng & Jansen, 2021; Ashkenazy & Tziperman, 2021; Ames et al., 2025]. However, substantial uncertainties in salinity, internal heat fluxes, ice-shell thickness, and the behaviour of high-pressure ice phases still prevent the development of fully realistic ocean general circulation models.

A similar situation arises for sub-Neptunes. Ocean modelling for these planets is at an early stage, with most work focusing on interior structure and the phase behaviour of deep water layers rather than detailed ocean dynamics. Current models suggest that sub-Neptunes may host a wide range of internal configurations, typically involving a rocky core overlain by high-pressure water layers (liquid, supercritical, or icy) and a variable-mass H/He envelope [Nixon & Madhusudhan, 2021]. Alternative interpretations propose that strong stellar irradiation can drive water-rich envelopes into a supercritical state, producing inflated radii that mimic sub-Neptunes even in the absence of significant H/He envelopes [Mousis et al., 2020]. Conversely, other studies argue that sub-Neptunes may be far drier than previously assumed, with most primordial water destroyed or sequestered into the interior during early magma-ocean equilibration, resulting in final water fractions too small to sustain global oceans [Werlen et al., 2025].

Given this wide landscape of possible ocean-bearing environments, no single modelling framework can yet capture the full diversity of relevant physical regimes. Consequently, ocean modelling beyond Earth remains a rapidly developing field, in which efforts to constrain planetary properties and to identify the key physical processes operating in each context are essential for establishing the robust modelling approaches needed to interpret observations across diverse planetary settings.

1.2.5 M stars and tidal locking

Studies of habitability of planets orbiting cool stars, and more specifically M dwarfs, are compelling for several reasons. M dwarfs are the most numerous stars in the solar neighbourhood, comprising ∼70% of all stars in the Milky Way [Bochanski et al., 2010], thus offering the best chance of finding habitable planets through sheer numbers. Moreover, they present evident observational advantages: terrestrial planets yield larger spectroscopic Doppler shifts under radial velocity due to smaller star-planet mass ratios, as well as deeper photometric transits owing to smaller star-planet size ratios. Furthermore, their lower effective temperatures and luminosities place the habitable zone much closer to the host star (see Figure 1.2.1), increasing both transit geometric probability and frequency within observational windows. Lastly, the longevity of M dwarfs represents a benefit for the search of planets within their habitable zone and at the same time for the chances of such planets to be inhabited. Low-mass main-sequence stars consume nuclear fuel at slower rates than more massive stars and exhibit comparatively smaller luminosity variations over given timescales. Consequently, although the habitable zone around low-mass stars is narrower[13], its continuously habitable fraction is proportionally larger than that around hotter stars [Kasting et al., 1993]. Therefore, long-lived cold stars offer sufficiently long timescales conducive to planetary and possibly biological evolution.

The occurrence of small (0.75-1.5 $R_\oplus$, with $R_\oplus$ the radius of Earth) close-in ($T_{orb} < 100$ days) habitable zone planets, $\eta_\oplus$, increases with decreasing stellar mass from A to K stars [Mulders et al., 2014; Bergsten et al., 2022; Giacalone & Dressing, 2024], and even more for M dwarfs, where such planets may be ∼3.5 times more common than around FGK stars [Mulders et al., 2014; Hsu et al., 2020; Petigura et al., 2022]. Whether this trend extends to longer-period habitable zone planets remains unclear [Bergsten et al., 2023]. Early estimates of terrestrial planet occurrence in M dwarf habitable zones [Dressing & Charbonneau, 2015] were revised after Gaia reclassified many Kepler targets, yielding values in the range of $\eta_\oplus = 9^{+18}_{-8}$ - 33^{+10}_{-12} %, where $\eta_\oplus$ denotes the

[13] This is straightforward when considering the inverse-square relationship between flux (f) and distance (d) for a source of luminosity L: $f = L/(4\pi d^2)$.

fraction of stars expected to host at least one such planet [Hsu et al., 2020; Bergsten et al., 2023], depending on the adopted occurrence model. Ambiguities stem from the paucity of Earth-sized habitable zone candidates, Kepler's limited duration for secure detection of long-period candidates, variations in stellar models, uncertainties in host star properties. Detection around M dwarfs is further complicated by stellar activity - spots, convective inhomogeneities, and flares - which can mimic planetary signals [Barnes et al., 2011; Robertson et al., 2015; Suárez Mascareño et al., 2017; Yaptangco et al., 2025]. Current and future surveys aim to refine $\eta_\oplus$ constraints. The ongoing TESS mission focuses on relatively nearby, luminous stars, but its nonuniform observing strategy will introduce large variations in the completeness and reliability of the data. NASA's Nancy Grace Roman Space Telescope, scheduled for launch in 2026, will extend coverage to mid- to late-type M dwarfs. For Sun-like stars, upcoming missions include ESA's PLATO (scheduled for launch in January 2027) [Rauer et al., 2025] and China's Earth 2.0 (ET), proposed for the 2030s [Zhang et al., 2022].

Nevertheless, for rocky exoplanets in the habitable zone, host star temperatures peak near 3300 K, and ~60-70% of confirmed cases (about 70 in total as of January 2025, though estimates vary across studies [Planetary Habitability Laboratory, 2024; Bohl et al., 2025]) orbit M dwarfs (Figure 1.2.3). Thus, the majority of potentially habitable environments currently accessible for investigation are expected around M dwarfs, making them prime targets for observations with present and next-generation facilities. Despite these considerations, residence within the habitable zone of an M star does not ensure habitability, as such stars raise significant concerns as hosts of life-bearing planets, mainly focused on stellar activity and tidal locking.

M stars' intense activity, with flare frequency and amplitude increasing toward lower stellar masses and strong UV and X-ray emission during the first billion years of their evolution, exposes planets to conditions that can drive atmospheric and ocean loss, potentially sterilizing them before the star reaches the main sequence [Luger & Barnes, 2015; Rodríguez-Mozos & Moya, 2019; Tilley et al., 2019]. However, atmospheric column density and ozone concentration profile have been proven to play a dominant factor in reducing surface radiation dose, with planetary magnetic field shielding playing a secondary role against flares and stellar winds [Segura et al., 2010; Kay et al., 2016].

The habitable zone lies much closer to low-mass stars (Figure 1.2.1), subjecting planets within it to strong tidal interactions that generate torques altering rotational angular momentum and ultimately fixing the rotation rate at a specific frequency, a process known as tidal locking[14]. The most commonly studied outcome of such process is synchronous rotation, a 1:1 spin-orbit resonance in which a planet's rotational and orbital periods

[14]Finite-sized planets experience gravitational gradients across their dimensions as a result of tidal interactions with the host star. The strength of this gradient depends primarily on the orbital radius, with closer planets subject to stronger tidal effects [Murray & Dermott, 1999].

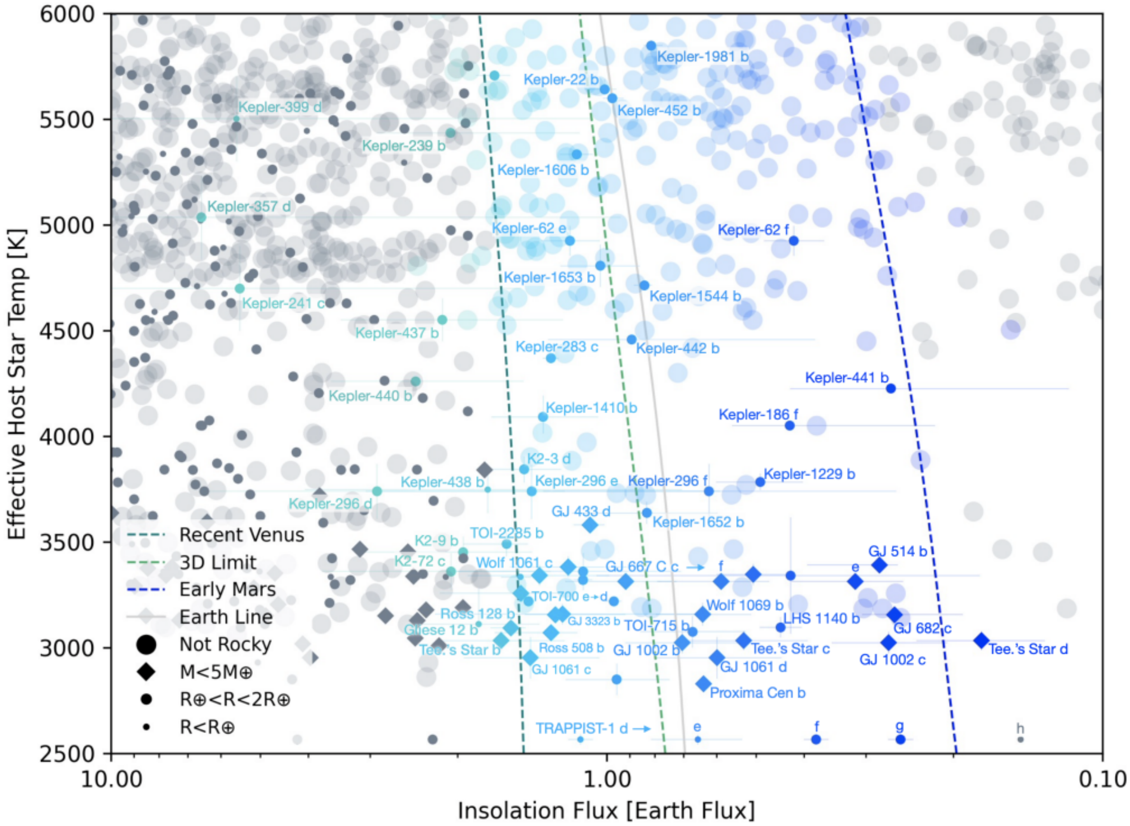

Figure 1.2.3: Confirmed exoplanets plotted by host star temperature and received instellation, with markers indicating planet radius. Dashed lines represent empirical habitable zone boundaries (teal: recent Venus; blue: early Mars), 3D-GCM habitable zone inner edge (green - the outer edge roughly coincides with the Early Mars boundary and is therefore omitted). The grey line denotes irradiation comparable to modern Earth across stellar temperatures. Image credit: Bohl et al. [2025].

coincide, resulting in permanent night and day hemispheres. Kasting et al. [1993] explicitly computed the *tidal lock radius*, the orbital distance at which a circularly orbiting Earth-like planet would become a synchronous rotator around main-sequence stars (dotted line in Figure 1.2.1a). Planets in M star habitable zones, and near the inner edge of late K star habitable zones, are therefore particularly prone to tidal locking.

As tidal braking is a complex process, close-in planets are not necessarily expected to be synchronous rotators, as demonstrated by examples in the Solar System. Mercury's 3:2 spin-orbit resonance has been interpreted through different evolutionary scenarios. A chaotic orbital history with rapid prograde rotation slowed by solar tides [Correia & Laskar, 2004, 2009] appears inconsistent with modern models of core-mantle friction, while an initial retrograde rotation captured into 1:1 resonance and later disrupted by large impacts is consistent with the distribution of surface basins and sublimation hollows [Wieczorek et al., 2012]. Venus' slow retrograde rotation arises from the torque exerted by solar gravitational forcing on its atmospheric tide, which counteracts the despinning effect of bodily tides [Dobrovolskis, 1980].

While tidal locking and its possible outcomes have been discussed since the 18th century in the context of Solar System planets and satellites [Kant, 1754; Kaula, 1964; MacDonald, 1964; Goldreich, 1965; Goldreich & Peale, 1966a; Goldreich, 1966; Goldreich & Peale, 1966b], tidal studies for exoplanets are challenging due to a combination of observational limitations - such as sparse constraints on the orbital architecture of the system and the presence of companions - and uncertainties in planetary properties - such as atmospheric structure, unknown internal and rheological variables, tidal deformation and dissipation parameters. Planetary systems around M dwarfs are often multiple and tightly dynamically packed [Fang & Margot, 2013; Ballard & Johnson, 2016]. Thus, planetary spin states might be significantly influenced by gravitational interactions between neighbouring planets [Correia & Delisle, 2019]. Possible outcomes of such tidal evolution in this scenario seem to be manifold, ranging from spin-orbit resonances to librations of different amplitude and even chaotic behaviour [Dobrovolskis, 2007; Correia et al., 2014; Leconte et al., 2015; Barnes, 2017; Vinson & Hansen, 2017; Correia & Delisle, 2019; Renaud et al., 2021; Chen et al., 2023; Valente et al., 2024; Yuan et al., 2025].

Habitability implications of synchronous rotation arising from the permanent day-night hemispheres configuration were first discussed by Dole [1964]: "It is evident that low rates of rotation are incompatible with human habitability requirements and also that tidal effects can cause a planet's rotation rate to slow down until one side always faces the primary and there is no longer an alternation of day and night on the planetary surface.". On the nightside, volatiles may freeze out, forming cold traps that deplete the dayside of water. Conversely, the dayside can drive atmospheric heating to levels that preclude the stability of water. Such dire inhospitable scenarios have been discredited by more comprehensive studies that account for atmospheric and oceanic heat transport between hemispheres, along with various stabilising mechanisms.

On the nightside, an atmosphere containing 1000-1500 mbar of CO_2 can prevent atmospheric collapse [Joshi et al., 1997], while including convective adjustment parametrisation warms the cold traps [Sergeev et al., 2020]. On the dayside, convection can generate thick substellar water clouds that increase albedo, cool the surface, and prevent a runaway greenhouse through stabilising feedbacks [Yang et al., 2013]. Additionally, airborne mineral dust can simultaneously cool the dayside and warm the nightside [Boutle et al., 2020]. In specific settings, drastic hemispheric temperature contrasts limit the regions suitable to hold liquid water, potentially forming *eyeball planets* - *cold* if water lies on the day side, *hot* if on the night side - or confining it to a narrow, ring-shaped eternal twilight zone along the terminator separating the two hemispheres [Pierrehumbert, 2011; Kite et al., 2011; Lobo et al., 2023]. In the first scenario, dynamic ocean heat transport extends equatorial melting and transforms the substellar melted pool into a lobster-like pattern, and in some cases proves more effective than atmospheric transport, enabling complete nightside deglaciation [Hu & Yang, 2014]. Ocean heat transport can effectively inhibit sea-ice expansion, preventing global snowball states and producing thinner nightside ice, indicating that nightside water trapping on aquaplanets is unlikely [Yang et al., 2014b; Checlair et al., 2019].

However, ocean heat transport might have different climatic results near the boundaries of the habitable zone. At low instellation near the outer habitable zone, zonal ocean heat transport cools the dayside and insufficiently warms the nightside, and can drive global glaciation except for limited open water at the substellar point. Thus, although ocean transport promotes deglaciation under moderate conditions, it can hinder habitability by narrowing the habitable zone around cold stars via an inward shift of its outer edge [Hu & Yang, 2014]. At high instellation near the inner habitable zone, day-night heat transport is dominated by the atmosphere, while oceanic influence weakens due to reduced wind stress and diminished surface shortwave energy absorption from enhanced absorption by water vapour and reflection by clouds. Consequently, unlike at the outer edge, the inner boundary of the habitable zone is largely insensitive to ocean dynamics [Yang et al., 2019].

For completeness, it is noted that considering dynamical oceans in this scenario may have observational implications, such as shifting the planetary hot spot relative to the substellar point and altering thermal emission phase curves, a topic further addressed in Chapter 4. The climatic effects discussed here might significantly depend on the assumed continental configuration, as all results were obtained for aquaplanets without barriers that could affect heat transport and circulation. This will be further expanded in Chapter 3 and 4.

2

Methodology

This chapter focuses on describing the modelling framework and validating it under Earth-like conditions. Two approaches are employed: an ocean general circulation model (MOMA) and a coupled atmosphere-ocean model (FORTE 2.0), both of which are briefly described. Tests are conducted using both models, with particular attention to analysing the global meridional overturning circulation in the ocean, a key diagnostic of large-scale ocean dynamics. Validation against a published control data set [Blaker et al., 2021], together with targeted sensitivity tests, provides the necessary benchmark for extending the analysis to exoplanetary scenarios. When configured in an Earth-like manner, and under specific setup choices, both models reproduce the principal features of Earth's large-scale ocean circulation with reasonable accuracy.

2.1 Analysis of the Global Meridional Overturning Circulation

2.1.1 Theory

As previously mentioned (see Section 1.2.4 and 1.2.5), the ocean plays a fundamental role in shaping planetary climate. Oceans store the heat received by solar radiation and currents redistribute that heat across the globe, in some cases more effectively than the atmosphere, thereby exerting strong control on climate regulation and, potentially, on planetary habitability. The meridional overturning circulation (MOC) denotes the large-scale vertical and meridional transport of ocean waters. It is often conceptualized as a global "conveyor belt" [Broecker, 1991], by which warm, buoyant surface waters are advected poleward, cooled, and rendered more dense before sinking at high latitudes to form dense deep waters. These deep waters subsequently flow equatorward and eventually upwell in other regions, completing the overturning loop.

The MOC is driven primarily by thermohaline forcing - buoyancy gradients arising from variations in temperature and salinity - as well as mechanical forcing by wind stress that contributes to upwelling and surface transport. The Atlantic Meridional Overturning Circulation (AMOC) constitutes the dominant contributor to the global MOC and is characterised by two principal cells. The upper cell involves northward transport of warm surface waters from the tropics via the Gulf Stream and North Atlantic Current, which cool and sink in the subpolar North Atlantic to form cold, relatively saline North Atlantic Deep Water (NADW). This water mass spreads southward at depth and eventually upwells in the south. Beneath this cell lies Antarctic Bottom Water (AABW), with sinking at high southern latitudes followed by a deep cross hemispheric circulation and upwelling again within the Antarctic Circumpolar Current (ACC). The AMOC delivers a substantial amount of heat and nutrients to colder latitudes and transfers carbon to the ocean depths, by moving 17 $\times 10^6$ m^3 of water northwards per second, and transporting 1.2 PW of heat [Johns et al., 2023].

The MOC is a fundamental component of Earth's climate system, coupling vertical and horizontal ocean transport processes. It is reasonable to expect that the MOC of exoplanetary oceans would also constitute a crucial component of the climate system and hence have direct implications for planetary habitability. The dynamics of the MOC on Earth is shaped by density gradients, wind forcing, basin geometry and specific parameter values. Modelling exoplanetary oceans may result in outcomes that present features that are vastly different from the ones that we are familiar with in the case of Earth, depending on the characteristics of the model set up. A potential exoplanetary MOC can be affected by a range of factors, including intrinsic planetary characteristics, stellar inherent features and the architecture of the planetary system. Since several planetary properties, and specifically ocean parameters, are largely unknown for exoplanets, the behaviour of their oceans and subsequent impact on climate cannot be assumed a priori.

2.1.2 Validation via control dataset

Initial tests were conducted using a control dataset of Blaker et al. [2021]. The dataset derives from a standard Earth control integration employed to evaluate the performance of FORTE 2.0, an intermediate-resolution global coupled atmosphere-ocean general circulation model (described in detail in Section 2.3.1). Specifically, it consists of ocean model output from the final 500 years of a 2000-year control integration.

To assess whether the system reached steady state, the time series of annual mean heat flux into the ocean averaged over the planetary surface was computed (Figure 2.1.1). Ascertaining that heat transfer across the ocean-atmosphere interface averaged over a suitably long period remains within a reasonable range of zero ensures that the run has reached equilibrium, implying that no substantial changes in the climate are expected. This diagnostic will be applied to subsequent runs, together with evaluation of the rate of change in surface- and volume-averaged ocean temperature.

The meridional overturning streamfunction at latitude θ, depth z and time t - $\Psi(\theta, z, t)$ - is computed by zonally integrating the meridional velocity (v) across the entire width of the ocean basin and consequently vertically integrating it from the bottom of the basin to a given depth (z):

$$\Psi(\theta, z, t) = -\int_{-H(\theta)}^{z} \int_{\lambda_w(\theta,z')}^{\lambda_e(\theta,z')} v(\lambda, \theta, z', t)\, a \cos\theta \, d\lambda \, dz' \quad , \tag{2.1.1}$$

where:

- $\Psi(\theta, z, t)$ is the streamfunction at latitude θ, depth z, and time t. Standard units of measurement for the volume of water transport in the ocean is the Sverdrup, $1\ \text{Sv} = 10^6\ \text{m}^3\text{s}^{-1}$,
- $v(\lambda, \theta, z', t)$ is the northward velocity component at longitude λ, latitude θ, depth z', and time t,
- a is the radius of Earth,
- $\lambda_w(\theta, z')$ and $\lambda_e(\theta, z')$ are the western and eastern boundaries of the ocean basin at latitude θ and depth z',
- $H(\theta)$ is the maximum ocean bottom depth at latitude θ,

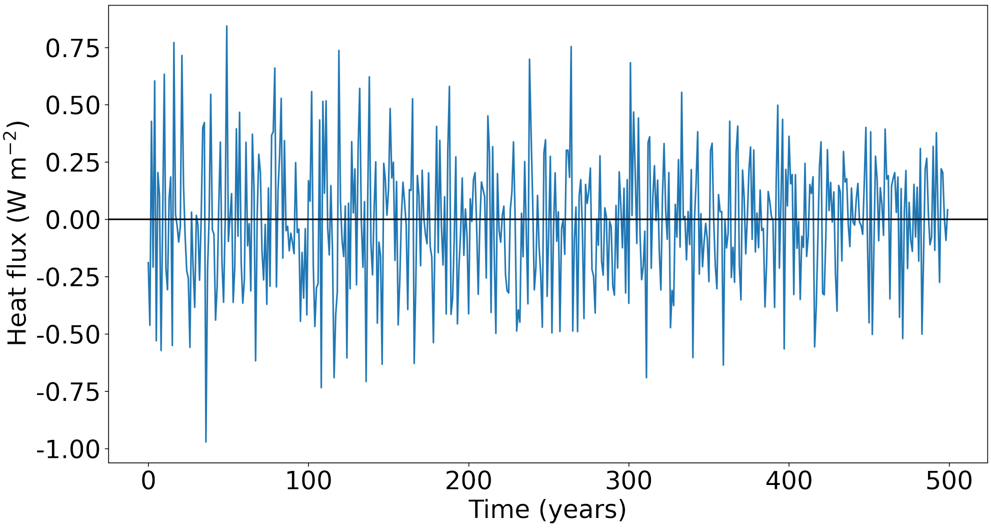

Figure 2.1.1: Time series of the annual mean heat flux (Wm^{-2}) into the ocean for the FORTE 2.0 control climate data set.

- z' is the vertical integration variable.

The global meridional overturning circulation (GMOC), analogous to the Atlantic meridional overturning circulation (AMOC) but computed for the entirety of the globe rather than a single basin, is derived following equation 2.1.1. The zonal boundaries are set to encompass the full globe ($\lambda_w(\theta, z') = 0°$, $\lambda_e(\theta, z') = 360°$), and the vertical integral is computed cumulatively from the ocean floor to the ocean surface[1]. The annual mean GMOC is evaluated over the final 500 years of the integration run at 26°N, a latitude commonly associated with the maximum heat transport by the overturning circulation (e.g., Hall & Bryden [1982]; Johns et al. [2011]; McCarthy et al. [2015]), and shown in Figure 2.1.2.

Although the calculation is not restricted to the Atlantic basin, the global overturning circulation remains dominated by the Atlantic, as illustrated in the following plots. Figure 2.1.3 presents the GMOC as a function of latitude and depth, averaged over the final 500 years of the control integration (left) and the meridional overturning circulation computed by limiting the domain to longitudes between 21°W and 97°E, and to latitudes within the North hemisphere (right). While this range does not precisely follow continental boundaries, it effectively isolates the North Atlantic contribution from the global circulation.

These result are consistent with the results presented by Blaker et al. [2021] and in overall

[1]Although the streamfunction is formally defined through continuous integrals, in practice the calculation is performed on the discretized model grid, where the integrals are approximated by finite sums over grid cells.

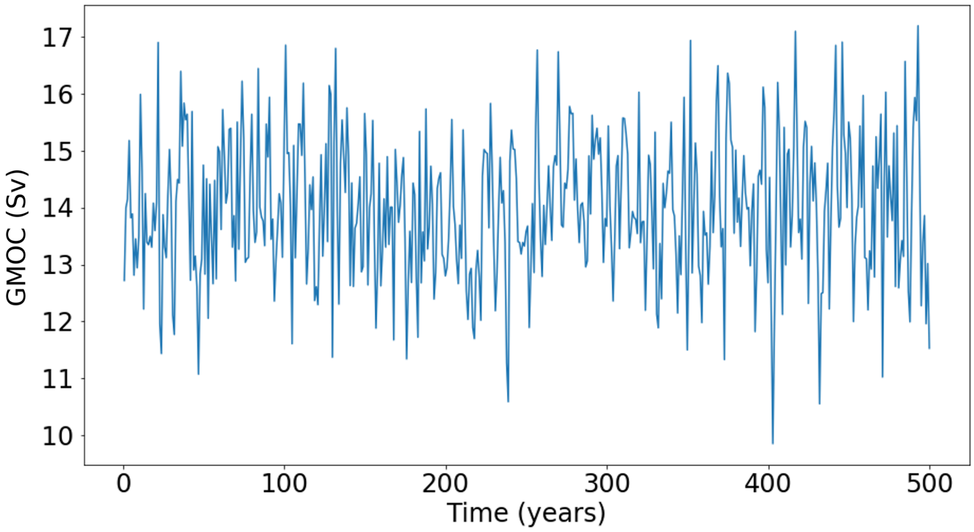

Figure 2.1.2: Time series of the annual mean GMOC (Sv) at 26°N for the control climate data set.

agreement with data-based estimates [Talley et al., 2003].

In the following sections, simulations are conducted first with the uncoupled ocean general circulation model MOMA and subsequently with the coupled atmosphere-ocean model FORTE2.0. We present attempts to reproduce the characteristics of the control dataset, followed by a series of experiments to evaluate model sensitivity to parameter choices and configurations. Both models are briefly described, and results from runs with varying

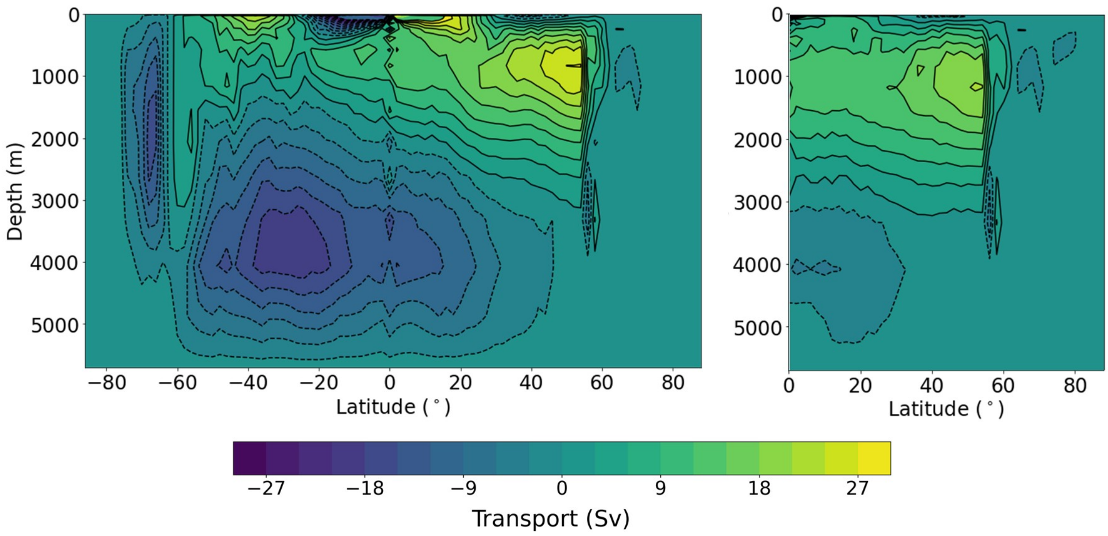

Figure 2.1.3: Left: GMOC (Sv) as a function of latitude and depth, averaged over the 500 years of the control climate data set. Right: AMOC (Sv), computed in the North Atlantic, as a function of latitude and depth, averaged over the 500 years of the control climate data set run.

parameter settings are presented.

2.2 MOMA

2.2.1 Brief model description

Historically, in order to study the physics, chemistry, and biology of the ocean and its overall effect on climate, different numerical models have been used. One of the most widely used types of ocean general circulation model is based on the Bryan-Cox-Semtner model. The model was first presented essentially as a standard primitive equation ocean model code [Bryan, 1969], but has since undergone a series of changes aimed at adapting it in order to provide improved diagnostics. The MOMA (Modular Ocean Model - Array) code, used here, is based on the Geophysical Fluid Dynamics Laboratory (GFDL) Modular Ocean Model or MOM code [Pacanowski et al., 1991], where the final 'A' of the acronym indicates that the code has been developed for use with array processor computers [Webb, 1996].

The Modular Ocean Model - Array processor version is an ocean general circulation model (OGCM) that solves equations for momentum, temperature and salinity by adopting some traditional approximations (thin shell assumption, the Boussinesq approximation, and hydrostatic balance) in order to render the computational expense manageable. By solving the primitive equations discretised using finite differences on an Arakawa-B grid [Arakawa, 1966] (Figure 2.2.1), MOMA simulates the large-scale physical processes that determine global ocean circulation. In the version here adopted (except when specified in the next section), the modelled ocean is characterised by a horizontal resolution of $2° \times 2°$ and by 15 z-levels, whose thickness increases progressively with depth, starting from 30 m at the surface and ending with a 836.10 m thick level.

In principle, a wide range of parameters can be adjusted within MOMA to investigate how the characteristics of exoplanetary oceans respond to different planetary conditions. This flexibility is particularly valuable given the uncertainties surrounding key properties of exoplanets which are often poorly constrained or entirely unknown. By allowing these variables to be modified, the model serves as a powerful tool for exploring hypothetical climate scenarios and assessing the sensitivity of oceanic behaviour.

To ensure the model's reliability, our initial approach focuses on reproducing the results of the control dataset. This validation step is essential for confirming that the model behaves consistently under known conditions. Once this baseline is achieved, we proceed with a series of targeted experiments, systematically altering individual parameters to observe how the model responds to different configurations. The outcomes of these trial runs are

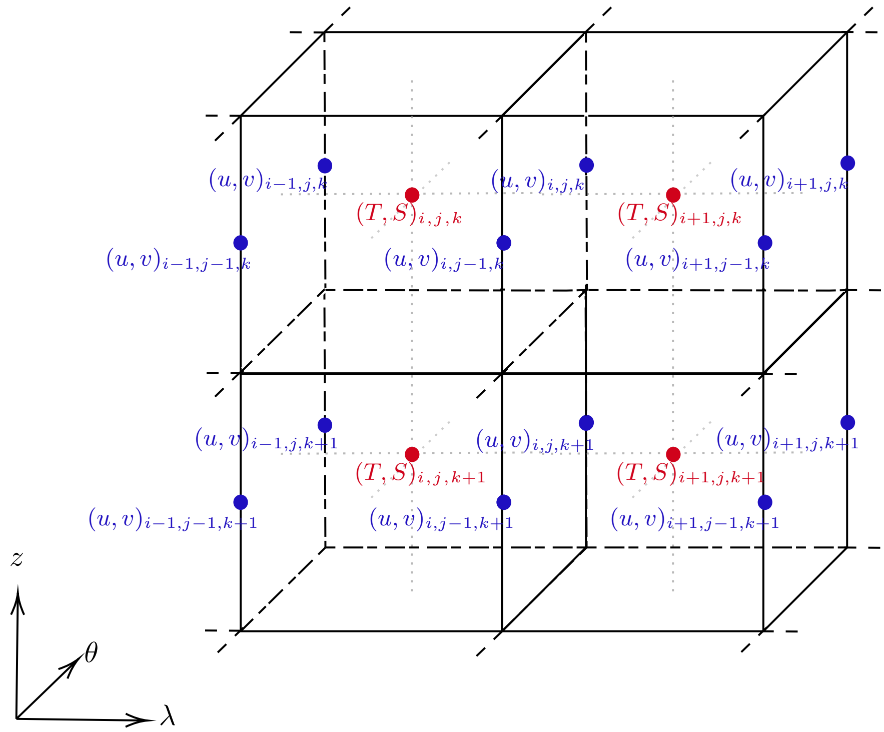

Figure 2.2.1: Configuration of potential temperature (T), salinity (S), northward velocity (v), and eastward velocity (u) points on the Arakawa-B grid in 3D.

presented in the following section.

2.2.2 Experiments

We obtain several different data sets by running MOMA for 200 years with different model setups, described below. The aim of the experiments is to become familiar with running the model and to explore sensitivity to some parameters and forcings. A particular focus is placed on the vertical diffusion coefficient κ, which enters the vertical diffusion term of the advection-diffusion equations for the tracers, potential temperature and salinity. The plots in this section show the analysis of the different data sets.

- Standard run
  We run the model using the following default settings: the vertical diffusion coefficient is set to a constant value $\kappa = 0.5 \times 10^{-4}\,\mathrm{m}^2\,\mathrm{s}^{-1}$ and the relaxation timescales of the tracers, temperature and salinity, are $\gamma_t = \gamma_s = 40$ days. Horizontal resolution is $2° \times 2°$.
  The ocean surface is forced by idealised profiles of momentum and tracers based on fits to observations: data are based on global, annual mean zonally-averaged values of windstress [Hellerman & Rosenstein, 1983], temperature, and salinity [Levitus, 1982].

The GMOC computed in this case (black curve in Figure 2.2.2a) rapidly collapses, contrary to what we aim to reproduce based on the control dataset analysis. The surface salinity map at the start of this run (after just after 1 year of integration) is shown in Figure 2.2.3a. The field is zonally uniform, in contrast to the real world distribution, which exhibits pronounced high salinity subtropical belts shaped by strong evaporation and weak precipitation. In particular, the North Atlantic subtropical gyre hosts the saltiest large scale surface waters on Earth, a feature that contributes to the density structure supporting the AMOC.

- Simple Earth run
  This simulation closely mirrors the configuration described above, with the key distinction that the modelled ocean employs a coarser horizontal resolution of $4°\times4°$. Figure 2.2.3b presents the surface salinity distribution at the start (year 1) for this run. A comparison with the corresponding output from the standard-resolution simulation (Figure 2.2.3a) highlights the reduced spatial detail: the representation of continental coastlines is notably less precise, reflecting the lower grid resolution.
  The resulting GMOC collapses at even smaller values with respect to the standard run (Figure 2.2.2a).

- Varying the vertical diffusion coefficient κ
  Vertical transport across density surfaces is critical for returning deep waters to the surface within the global overturning circulation, and is driven primarily by internal-wave breaking and boundary processes. Diapycnal mixing, quantified by the vertical diffusion coefficient κ, exerts strong control on overturning strength, with scaling studies indicating dependencies from $\kappa^{1/3}$ [Bryan, 1987] to $\kappa^{2/3}$ [Marotzke, 1997], and $\kappa^{1/2}$ in coupled models [Vallis & Farneti, 2009]. This set of simulations explores the sensitivity of the GMOC to variations in κ. In addition to the standard value, κ=$0.5\times10^{-4}\,\mathrm{m}^2\,\mathrm{s}^{-1}$, κ is also prescribed as $5.0\times10^{-4}\,\mathrm{m}^2\,\mathrm{s}^{-1}$ and $50\times10^{-4}\,\mathrm{m}^2\,\mathrm{s}^{-1}$, enabling an assessment of the impact of a three-order-of-magnitude variation in vertical diffusivity on the resulting circulation.
  Contrary to expectations, the GMOC weakens progressively with increasing κ, ultimately collapsing to smaller - and even negative - values (Figure 2.2.2b). However, a more detailed examination of the GMOC structure as a function of latitude and depth (Figure 2.2.4) suggests that the deeper Antarctic cell strengthens as κ increases, in line with theoretical predictions. Enhanced negative cells in the Northern hemisphere for increasing κ drive the net transport at 26°N into negative values.

- Varying the salinity relaxation timescale γ_s
  In this set of simulations, the vertical diffusion coefficient is fixed at the original

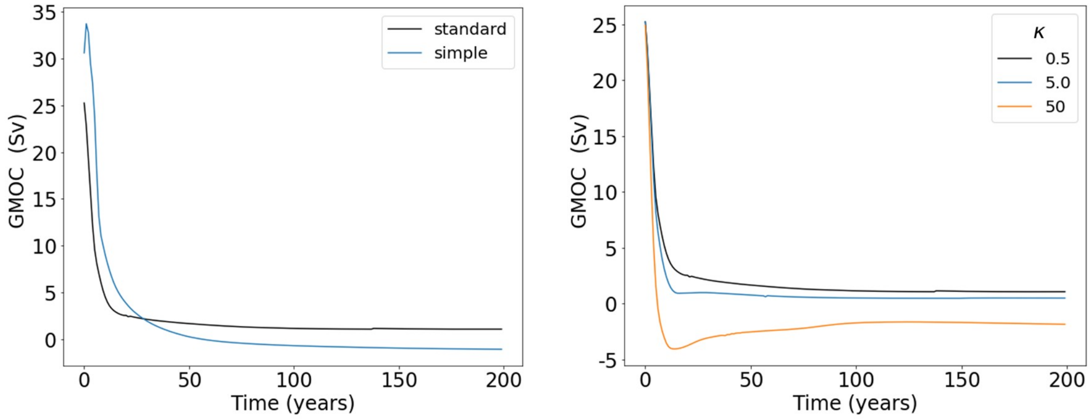

(a) (b)

Figure 2.2.2: Time series of the annual mean GMOC (Sv) at 26°N obtained by running MOMA. Standard configuration and simple Earth configuration (a), varying values of the vertical diffusion coefficient κ, with the legend showcasing values in $\times\, 10^{-4}\,\mathrm{m^2\,s^{-1}}$.

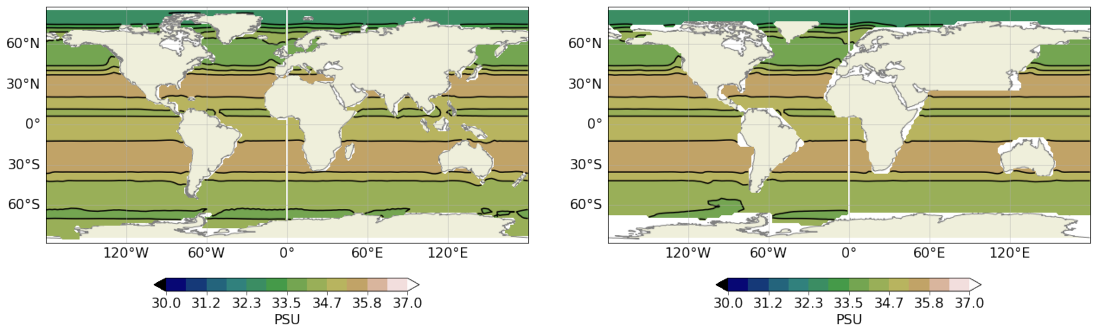

(a) (b)

Figure 2.2.3: Surface salinity map at the start (year 1) of the standard run (a) and the simple Earth configuration run (b).

default value, $\kappa = 0.5 \times 10^{-4}\,\mathrm{m^2\,s^{-1}}$. The relaxation timescale for temperature is held constant at $\gamma_t = 40$ days, while the salinity relaxation timescale is varied across four values: $\gamma_s = 40$ days (standard), 360 days, 900 days, and 1800 days. From a physical standpoint, the salinity relaxation time scale should be longer than that of temperature, as the latter adjusts rapidly through atmosphere-ocean interactions [Griffies et al., 2009].

The hypothesis that the GMOC might persist above a certain γ_s threshold is not supported: in all examined cases, the GMOC collapses to smaller values, albeit on slightly longer timescales, as γ_s increases (Figure 2.2.5a). This is in accordance with a decrease in the meridional overturning magnitude with increasing restoring timescales found in sensitivity studies [Cox & Bryan, 1984; Bryan, 1987].

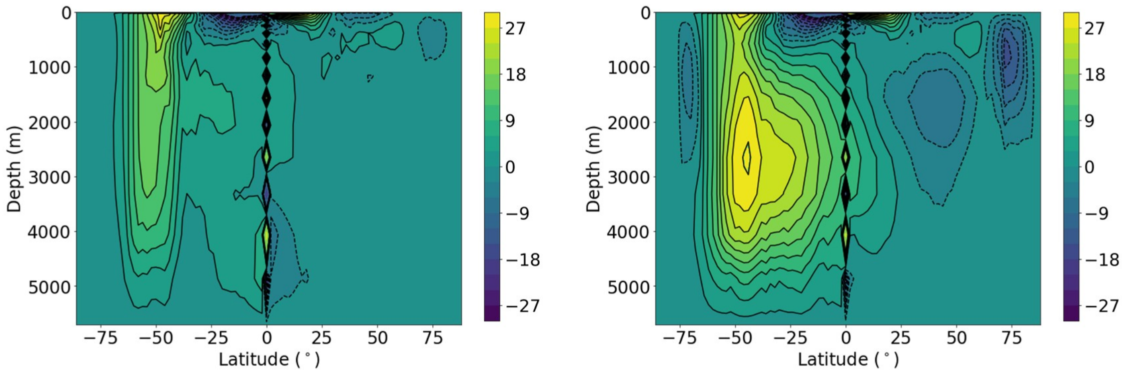

(a) (b)

Figure 2.2.4: GMOC (Sv) as a function of latitude and depth, averaged over 10 years at the midpoint of the model runs (year 100) with $\kappa = 5.0 \times 10^{-4}\,\mathrm{m^2\,s^{-1}}$ (a) and $\kappa = 50\times 10^{-4}\,\mathrm{m^2\,s^{-1}}$(b).

- Varying the surface salinity in the Atlantic Ocean

Salinity, together with temperature, governs thermohaline circulation and strongly influences ocean density structure. Increasing salinity raises seawater density, modifies the temperature-density relationship, and depresses the freezing point, thereby inhibiting sea ice formation [Fofonoff & Millard, 1983]. These combined effects shape overturning circulation, with the Atlantic Meridional Overturning Circulation strength shown to scale approximately linearly with mean salinity [Cael & Ferrari, 2017]. As an attempt to trigger the meridional overturning circulation, this set of runs is characterised by a change in the salinity term of the Atlantic Ocean. More specifically, we introduced an additional term in the surface salinity, so that the total salinity term S is given by:

$$S = S + \Delta S\; e^{-\left[\frac{(i-i_0)^2}{2\sigma_i^2} + \frac{(j-j_0)^2}{2\sigma_j^2}\right]} \tag{2.2.1}$$

with i and j the longitude and latitude indexes. The additional term results in a distribution of the salinity value peaked at coordinates (j_0, i_0) located at (25°N, 45°W) in the Atlantic and decreasing exponentially in latitude (modulated by the parameter σ_j) and in longitude (modulated by the parameter σ_i) with increasing distance from the peak position. We set $\sigma_i^2 = \sigma_j^2 = 50$, while the value of the coefficient ΔS=2 determines the “amplitude” of the peaked distribution. The different data sets are then characterised by varying salinity relaxation timescales γ_s = 40 days, 360 days, 900 days, 1800 days, 2700 days, 3600 days. Figure 2.2.6a displays the surface salinity distribution at the onset of the simulation characterised by a salinity relaxation timescale of γ_s = 40 days. A comparison with the standard configuration (Figure 2.2.3a) reveals a distinctly peaked salinity

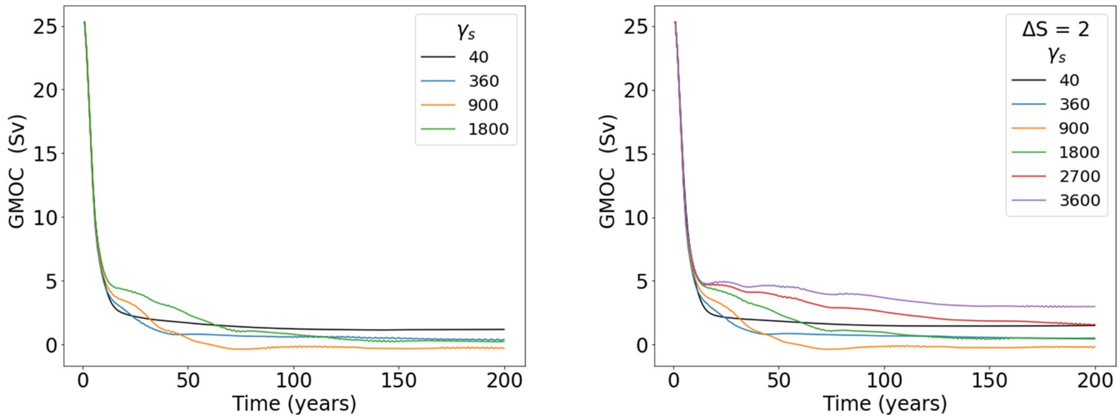

(a) (b)

Figure 2.2.5: Time series of the annual mean GMOC (Sv) at 26°N obtained by running MOMA with $\kappa = 0.5 \times 10^{-4}\,\mathrm{m^2\,s^{-1}}$ and varying values of the salinity relaxation timescale γ_s (days). Standard salinity term in the Atlantic Ocean (a), additional salinity term in the Atlantic Ocean with ΔS=2 PSU (b).

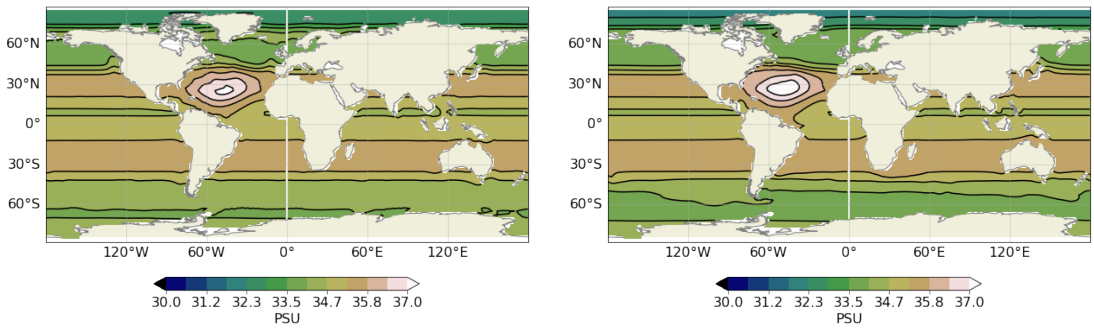

(a) (b)

Figure 2.2.6: Surface salinity maps of the run characterised by $\kappa = 0.5 \times 10^{-4}\,\mathrm{m^2\,s^{-1}}$, γ_s=40 days, ΔS=2 PSU, σ_j^2=50. Start - year 1 - of the simulation (a) and midpoint - year 100 - of the simulation (b).

pattern, attributable to the influence of the additional salinity forcing term.
Figure 2.2.5b demonstrates that the modification introduced in the salinity forcing does not yield the intended GMOC time series. When comparing the results to those presented in Figure 2.2.5a, it becomes evident that the adjustment to the salinity term does not produce a discernible change in the GMOC amplitude. As γ_s increases, the GMOC undergoes collapse on progressively longer timescales. For higher γ_s, the GMOC appears to stabilize to values that remain substantially lower than those observed in the reference simulation (Figure 2.1.2).

- Varying the spatial distribution of the additional surface salinity term in the Atlantic Ocean: change in ΔS, σ_j

  The peaked salinity distribution observed in the Atlantic Ocean does not lead to the desired GMOC response, likely due to the accumulation of high-salinity water within a subtropical gyre. This water remains largely isolated and is not effectively advected, thereby inhibiting the initiation of the overturning circulation. This interpretation is supported by comparing Figure 2.2.6b, which illustrates the surface salinity map midway through the simulation (at year 100) to the surface salinity snapshot at the start of the run represented in Figure 2.2.6a. The persistence of the high-salinity anomaly at the same location over time confirms that the water is not being transported meridionally, but instead remains trapped in the gyre circulation. To address this issue, modifications are introduced to the parameters appearing in Equation 2.2.1. Specifically, the latitudinal extent of the peaked salinity distribution is broadened by setting $\sigma_j^2 = 100$. This adjustment increases the spatial spread of the high-salinity anomaly, thereby promoting its transport and reducing the likelihood of confinement within the subtropical gyre. To further investigate the impact of the amplitude of the additional salinity term, two distinct data sets are generated with $\Delta S = 2$ and $\Delta S = 4$, respectively.

Figure 2.2.7a presents the surface salinity map at the start of the simulation characterised by $\Delta S = 2$, $\gamma_s = 3600$ days, and $\sigma_j^2 = 100$. In comparison with the case using $\sigma_j^2 = 50$ (Figure 2.2.6a), the additional salinity term produces a distribution that is spread across a broader latitudinal range, rather than being tightly concentrated around a single coordinate in the Atlantic Ocean. Figure 2.2.7b illustrates the evolution of this configuration at year 100, midway through the run. The results indicate that, under the adopted salinity distribution, the high-salinity anomaly in the Atlantic Ocean is effectively transported and contributes to the development of a circulation, rather than remaining confined within the subtropical gyre. Figure 2.2.8a is completely analogous to Figure 2.2.7a, but shows a more evident peak in the salinity, given that in this case the amplitude of the distribution is ΔS=4.

The GMOC results shown in Figure 2.2.9a are not fully satisfactory, yet they remain encouraging when compared to the pronounced collapse observed in previous simulations (see, for instance, the purple curve in the same figure). It should be emphasized, however, that the time series is truncated at 200 years, and the curves corresponding to the new data sets continue to exhibit a declining trend at the end of the integration period.

- Relaxation to the observed initial fields

  Instead of restoration to the initial idealised zonally-averaged surface standard state, the atmospheric forcing of ocean temperature and salinity at the surface is now represented through relaxation toward prescribed, annual mean values from observed climatologies [Levitus, 1982].

  With this setup and adopting standard parameter values, the GMOC stabilizes at approximately ∼5.6 Sv (green curve in Figure 2.2.9b), a value lower than that

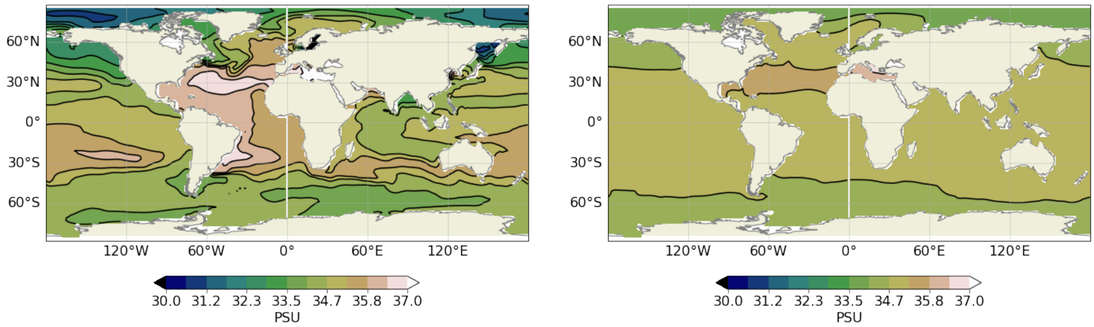

(a) (b)

Figure 2.2.7: Surface salinity maps of the run characterised by $\kappa = 0.5 \times 10^{-4}\,\mathrm{m}^2\,\mathrm{s}^{-1}$, γ_s=3600 days, ΔS=2 PSU, σ_j^2=100. Start - year 1 - of the simulation (a) and midpoint - year 100 - of the simulation (b).

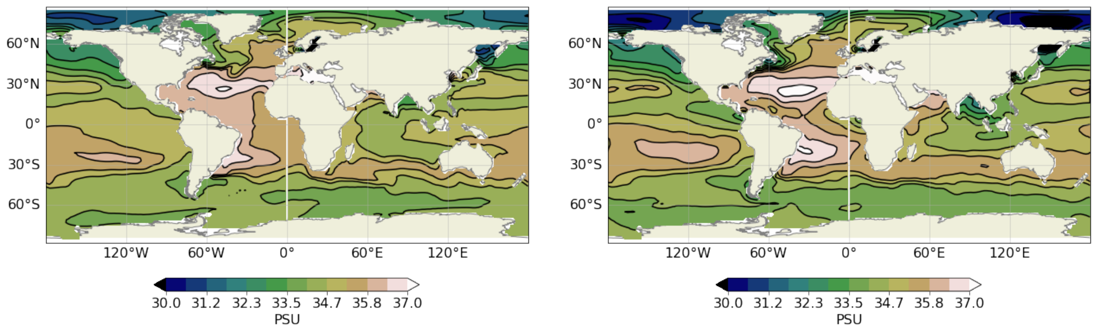

(a) (b)

Figure 2.2.8: Surface salinity map at the start - year 1 - of the run characterised by $\kappa = 0.5 \times 10^{-4}\,\mathrm{m}^2\,\mathrm{s}^{-1}$, γ_s=3600 days, ΔS=4, σ_j^2=100 (a) and the run characterised by $\kappa = 0.5 \times 10^{-4}\,\mathrm{m}^2\,\mathrm{s}^{-1}$, γ_s=40 days, ΔS=0 (standard salinity distribution) and relaxation to the observed initial fields (b).

achieved through the additional salinity input under idealised zonal mean forcing ($\sim$9.2 Sv, orange curve in the same Figure). However, the time limited plot fails to highlight an important distinction between these runs: the GMOC associated with the relaxation to observed climatology continues to increase gradually, whereas the one associated to the enhanced salinity distribution exhibits a declining trend. This comparatively more promising outcome may be attributed to the use of observed initial fields, which enable the model to incorporate features absent in idealised zonal mean configurations. The GMOC response therefore appears to reflect the influence of these specific, physically grounded features.

In summary, the analysis presented in this section yields reasonably acceptable values of the global meridional overturning circulation (GMOC) only for two specific model configurations: (i) the setup incorporating a latitudinally extended enhanced surface salinity distribution in the Atlantic Ocean, and (ii) the configuration characterised by

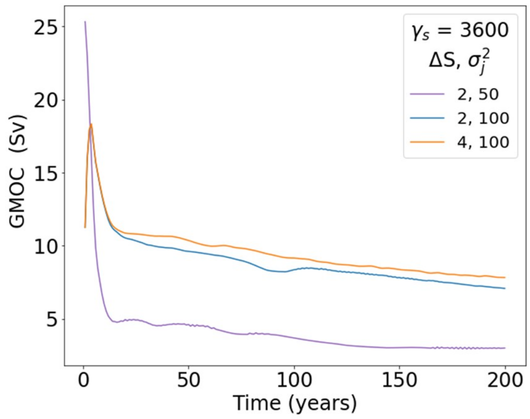

(a)

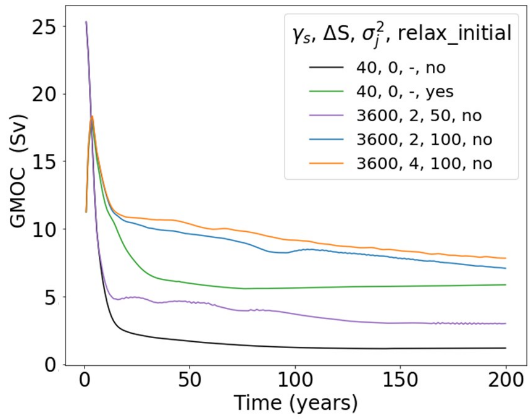

(b)

Figure 2.2.9: Time series of the annual mean GMOC (Sv) at 26°N obtained by running MOMA with $\kappa = 0.5 \times 10^{-4}\,\mathrm{m^2\,s^{-1}}$. Run with and γ_s=3600 days and varying values of the parameters ΔS and σ_j^2 of the additional salinity term in the Atlantic Ocean (a), comparison between runs with varying values of γ_s, ΔS, σ_j^2 and a run characterised by relaxation to the observed initial fields (b). In the legends, γ_s is expressed in days and ΔS in PSU.

relaxation to observed initial fields. To illustrate these outcomes, Figure 2.2.10 shows the global circulation streamfunction at the midpoint (year 100±5) of these two simulations. The detailed parameter choices for each run are provided in the figure caption. The decision to average the overturning transport over a shorter interval of time (10 years), rather than time-mean fields as in Figure 2.1.3 (500 years), is motivated by the substantial temporal variability of the GMOC throughout these simulations due to their short duration, i.e. only 200 years from the initial state to the end of the runs. The streamfunction plots reveal several similarities with the control dataset, particularly in the large-scale overturning patterns, although the overall circulation intensity remains weaker.

2.3 FORTE 2.0

2.3.1 Brief model description

As discussed in Chapter 1, the ocean and atmosphere form a highly complex coupled system. Coupled atmosphere-ocean general circulation models (AOGCMs) have become indispensable tools to investigate and explore different climate scenarios. A wide range of more or less complex coupled climate models have been developed. The presence of feedback mechanisms and processes that act on vastly different timescales determine the complexity of climate models. State-of-the-art, high-resolution models allow detailed

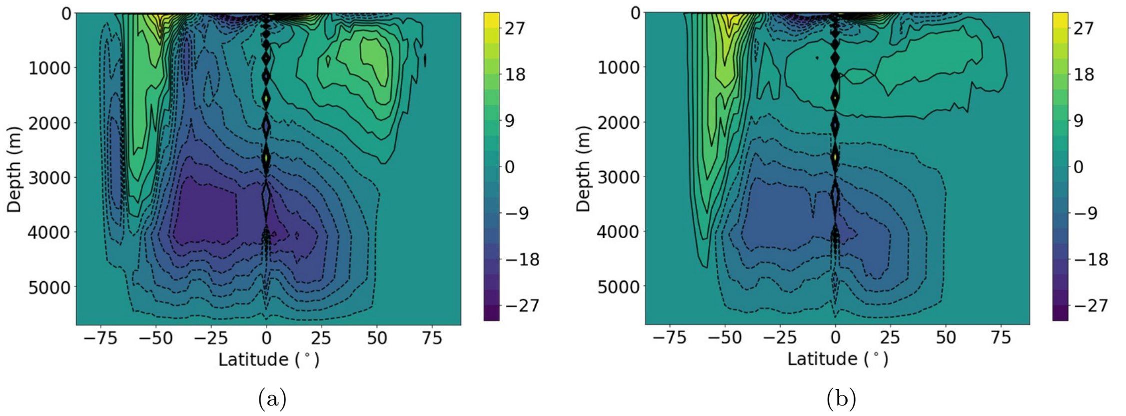

Figure 2.2.10: GMOC (Sv) as a function of latitude and depth, averaged over 10 years at the midpoint of the model runs (year 100): $\kappa = 0.5 \times 10^{-4}\,\mathrm{m}^2\,\mathrm{s}^{-1}$, γ_s=3600 days, ΔS=2, σ_j^2=50 (a), standard run with relaxation to the observed initial fields (b).

examination of Earth's climate but are usually computationally demanding and time intensive. Simpler, coarse-resolution models are less complex and cost effective, designed to run simulations relatively quickly at the expense of detail. The middle ground between these two different types of model is constituted by intermediate-resolution coupled atmosphere-ocean general circulation model, among which we find FORTE 2.0.

This model, thoroughly presented in Blaker et al. [2021], is an improved version of the Fast Ocean Rapid Troposphere Experiment (FORTE), a fast and flexible coupled climate model developed in the early 2000 [Sinha & Smith, 2002]. The ocean general circulation model Modular Ocean Model - Array Processor (MOMA), described in the previous section, is coupled to the atmospheric general circulation model Intermediate Global Circulation Model version 4 (IGCM4) [Joshi et al., 2015].

IGCM4 is a global spectral primitive equation climate model. It is characterised by a T42 spectral resolution, a grid spacing of approximately 2.8° and can be configured with either 35σ layers (troposphere and stratosphere) or 20σ layers (troposphere only) for a faster integration. The time step is adjustable, but commonly adopted choices are 72 or 96 time steps per day.

A modified version of the Morcrette radiation scheme is used to model the long and short wave radiative fluxes [Zhong & Haigh, 1995]. The convection scheme follows the formulation described by Forster et al. [2000], with some adjustments to better match observations of outgoing longwave radiation and downward surface shortwave radiation. Low, medium and high layer clouds and convective cloud amounts are based on a critical grid point relative humidity criterion.

Land grid boxes are classified into one of 24 surface types, each defined by specific albedo values (for both snow-free and snow-covered conditions) and a characteristic roughness length. FORTE 2.0 does not include a dynamic sea-ice model, thus sea ice is represented as a heat flux barrier at the interface between ocean and atmosphere when the sea surface temperature falls below 271 K. Surface albedo is set to 0.6 to mimic ice cover, and further increases linearly to 0.8 at 261 K to account for the enhanced reflectivity of snow-covered ice.

The ocean and atmosphere components of the model are coupled once per model day using the Ocean Atmosphere Sea Ice Soil (OASIS) coupler, version 2.3 [Terray et al., 1999], together with the Parallel Virtual Machine (PVM), version 3.4.6 [Geist et al., 1994], a software package that links heterogeneous networked computers into a single virtual parallel machine to enable distributed, cost-effective high-performance computing. Daily average quantities of the variables that are to be exchanged are passed to the coupler at the end of each model day. MOMA provides sea surface temperature, zonal and meridional velocities, IGCM4 provides heat flux, net freshwater flux, and zonal and meridional surface wind stress. Since the ocean and atmosphere employ different numerical grids, fluxes at the ocean surface must be interpolated to ensure accurate exchange between models at their interface. The interpolation at each location is performed using a pre-computed set of weights applied to the four surrounding grid points. This procedure ensures conservation and accounts for the fractional overlap between oceanic and atmospheric grid cells. To ensure water conservation, soil moisture in each land grid box is simulated using a 0.5 m deep bucket. When the water volume exceeds this capacity, the surplus is accumulated and transferred to the ocean as runoff at each coupling time step.

A tiling routine is employed to handle differences between the ocean and atmospheric grids. Ocean grid cells are classified as either land or ocean, whereas atmospheric grid cells may represent land, ocean, or partial coverage (when the atmosphere cell overlaps both land and ocean cells of the ocean model). Using the appropriate IGCM4 boundary layer scheme depending on the type of cell ensures conservation of atmospheric moisture and correct partitioning of precipitation between land and ocean. The tiling scheme thus enables a precise representation of coastlines within the model.

Integration is relatively fast, with $\sim$70-100 model years per wall-clock day on 24 cores of ADA - the University of East Anglia's High Performance Computing cluster - depending on the adopted configuration. FORTE 2.0 has been developed with an emphasis on flexibility, enabling straightforward configuration across a range of experimental setups, and is thus ideal for exoclimates simulations. The model supports variable resolution in both the ocean and atmosphere, which can be run either independently or in coupled mode. The ocean component includes switchable physical processes, enabling configurations that range from a simple mixed-layer slab ocean to a fully dynamical ocean, with corresponding differences in computational cost. The orbital configuration - such as orbital eccentricity, semi-major axis, inclination - and planetary characteristics - such as rotation rate, land–sea masks at the surface and at depth, orography, surface type, ice/snow albedo, atmospheric composition, and ocean salinity - are fully customizable. Parameterizations of individual processes can be easily toggled, facilitating controlled experimentation and sensitivity studies.

In this section, we aim to reproduce results comparable to those of the control data set, originally obtained with this coupled model. After establishing a sufficient degree of coherence between the simulation outputs and the reference case, attention is directed toward examining how variations in selected parameter values influence the behaviour of the climate system. The corresponding trial runs and the analysis of the resulting data sets are presented in the following section. Validation of the model for present-day Earth constitutes a necessary step before shifting focus toward simulating alternative scenarios. This initial exploration of the parameter space provides the foundation for more comprehensive and systematically structured investigation of exoplanetary climates in different configurations, that will constitute the core of the study presented in Chapters 3 and 4.

2.3.2 Experiments

The adopted configuration of the IGCM4 is characterised by a troposphere-only atmosphere which extends to around 25 km altitude and is subdivided in 20 σ-levels (L20), and by pre-industrial atmospheric concentrations of CO_2. Both in Blaker et al. [2021] and in this section, the model starts to run from an initial rest state. The initial state of the ocean is described by the temperature and salinity of the Levitus climatology [Levitus, 1982] adopted in the last experiment of the previous section, while the atmosphere is characterised by a standard globally-averaged Earth-like vertical profile of temperature.

We obtain several different data sets by running FORTE 2.0 with different model setups, described below. The plots in this section show the analysis of the different data sets.

- Varying the stability dependent ocean vertical diffusion κ_{stab}
  The background vertical diffusion is set to be stability dependent [Gargett, 1984] and varies between a fixed value of 0.4 $\times 10^{-4}\,\mathrm{m^2\,s^{-1}}$ and the chosen value $fkph$.

$$\kappa_s = \left(0.4 + 1.7e^{-(0.15[\max(T_s,T_b)-T_b])^2}\right) \times 10^{-4}\,\mathrm{m^2\,s^{-1}} \tag{2.3.1}$$

$$\kappa_{stab} = \kappa_s + \left(fkph \times 10^{-4} - \kappa_s\right)\frac{z}{H}\,\mathrm{m^2\,s^{-1}} \quad , \tag{2.3.2}$$

  where T_s and T_b are the surface and bottom potential temperatures, z is depth, and H the local total ocean depth.

We obtain three different data sets by running the model for a time of 200 years with $fkph$ = 0.5, 2.5, 5.0, while for the control climate data set $fkph$ = 2.0. Figure 2.3.1 shows the geographical variation of the vertical profiles of the stability-dependent diffusion coefficient $\kappa_{\rm stab}$ for the control run and for all simulations with different $fkph$ values. Representative low- and high-latitude locations were selected to capture the contrast between regions characterised by strong vertical temperature gradients in the tropics and weakly stratified conditions at high latitudes. At equilibrium, these profiles illustrate how the vertical diffusion parametrisation responds to local stratification: $\kappa_{\rm stab}$ generally attains larger values near the sea floor and at high latitudes, while remaining smaller in the upper ocean at low latitudes. The magnitude of $\kappa_{\rm stab}$ increases systematically with $fkph$, and in all simulations its maximum value approaches the imposed $fkph$, reflecting the upper bound set by the parametrisation.

Figure 2.3.2 shows the GMOC time series computed for this set of runs and for the control data set. As $fkph$ increases, the GMOC seems to stabilize at slightly higher values. Overall, the meridional overturning circulation seems to be comparable in order of magnitude to the one relative to the control climate data set (blue curve). The time series of the surface temperature and the surface salinity of the three runs and the control data set are shown in Figure 2.3.3a and Figure 2.3.3b, respectively. Differently from the three runs, the surface physical quantities of the control data set do not vary significantly in time, since the model is already spun up. In order to have a more accurate assessment of the equilibrium state of the analysed cases, the three simulations need to be run for a much longer time. Moreover, the curve

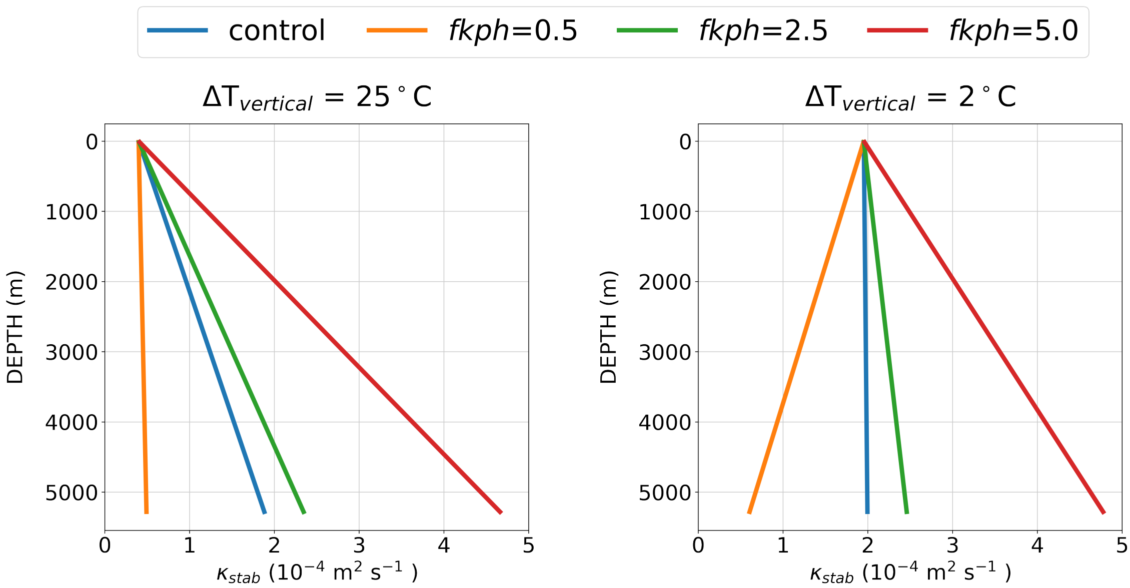

Figure 2.3.1: Vertical profiles of the stability-dependent vertical diffusion coefficient κ_{stab} at low (left) and high (right) latitudes for the control data set and for the FORTE 2.0 runs with different values of $fkph$, shown at the end of each run.

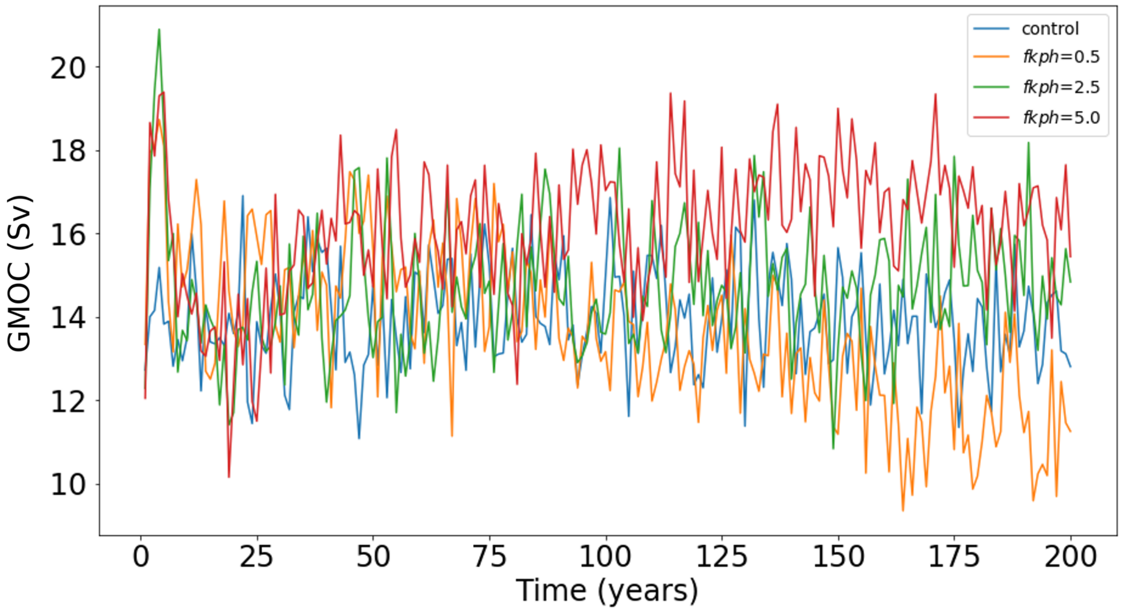

Figure 2.3.2: Time series of the annual mean GMOC (Sv) at 26°N obtained for the control data set and for the FORTE 2.0 runs with different values of $fkph$.

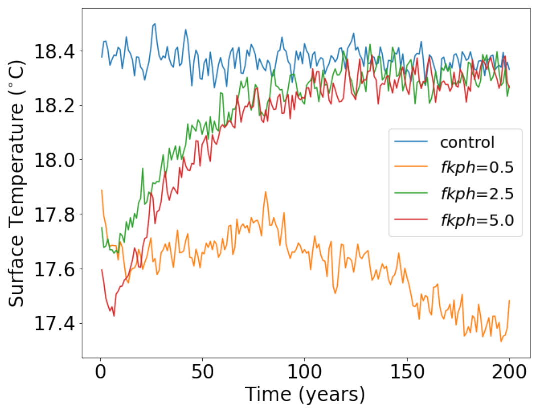

(a)

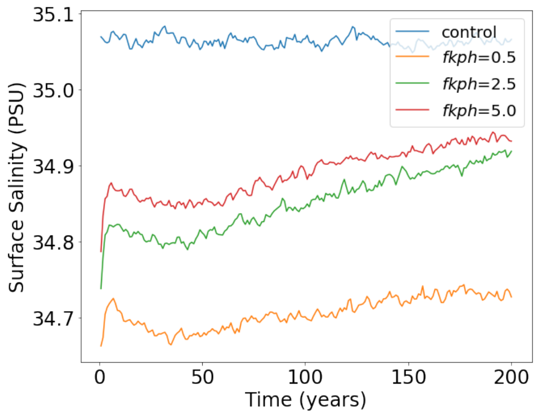

(b)

Figure 2.3.3: Time series of the globally averaged surface temperature (a) and surface salinity (b) for the control data set and for the FORTE 2.0 runs with different values of $fkph$.

corresponding to the simulation with $fkph = 0.5$ shows generally smaller values in surface temperature and salinity, while the two curves $fkph = 2.5$ and $fkph = 5.0$ - which differ only by a factor of 2 - generally exhibit similar trends. It is reasonable to expect that, over longer timescales, simulations with $fkph$ values exceeding that of the control case will eventually exhibit higher globally averaged surface temperatures than the control, as they show an increasing trend toward the end of the simulations while the control remains relatively stable.

- Varying the constant vertical diffusion κ

  In order to make a more direct comparison with the MOMA set of simulations with varying values of κ, FORTE 2.0 is adapted to run simulations with constant instead of stability dependent vertical diffusion coefficient. The range of explored values spans four order of magnitudes, $\kappa = 0.5,\ 5.0,\ 50,\ 500\ \times 10^{-4}\,\mathrm{m^2\,s^{-1}}$. Running the simulations for 500 years instead of the shorter timescale previously adopted enables a more accurate understanding of the GMOC trend in time. As a comparison, the control integrations analysed in Blaker et al. [2021] are run over a period of 2000 years to ensure a complete spin up.

  The annual mean GMOC time series (Figure 2.3.4) is in agreement to what observed with stability dependent κ_{stab}, with the GMOC strengthening as background vertical diffusivity increases. The time series of the surface temperature and the surface salinity of the four runs and the control data set are shown in Figure 2.3.5a and Figure 2.3.5b, respectively. Once again, longer run times are necessary for a more accurate assessment of the equilibrium state of the four analysed cases. In general, runs with increasing values of κ exhibit progressively stronger positive trends in globally averaged surface temperature, with the steepest gradient occurring for $\kappa = 500 \times 10^{-4}\,\mathrm{m^2\,s^{-1}}$. A strong resemblance to the structure of the time averaged GMOC as a function of latitude and depth for the control data set is observed for lower values of κ (Figure 2.3.6a and 2.3.6b). For $\kappa = 500\ \times 10^{-4}\,\mathrm{m^2\,s^{-1}}$ heat is efficiently diffused in the vertical direction, and the resulting structure of the streamfunction presents two distinct hemispheric cells that extend from the upper ocean to depth (Figure 2.3.6d), removing the asymmetry that is usually seen in Earth's GMOC. Maps of surface temperature for each simulated case (Figure 2.3.7) show progressively warmer high-latitude surface temperatures for increasing values of κ, consistent with the strengthening of the overturning circulation transporting heat poleward. The case with $\kappa = 500 \times 10^{-4}\,\mathrm{m^2\,s^{-1}}$, whose GMOC is by far the strongest - reaching values roughly seven times larger than in simulations with lower κ - also exhibits a markedly flattened meridional surface temperature profile, with cooler temperatures at low latitudes, warmer temperatures at high latitudes, and an approximately symmetric zonal structure across the midlatitudes.

2.4 Concluding remarks

The evaluation of the MOMA experiments highlights an important limitation of using the ocean model in forced mode. Representing a time-varying atmospheric forcing with an ocean-only configuration is inherently difficult: the imposed surface fields are highly

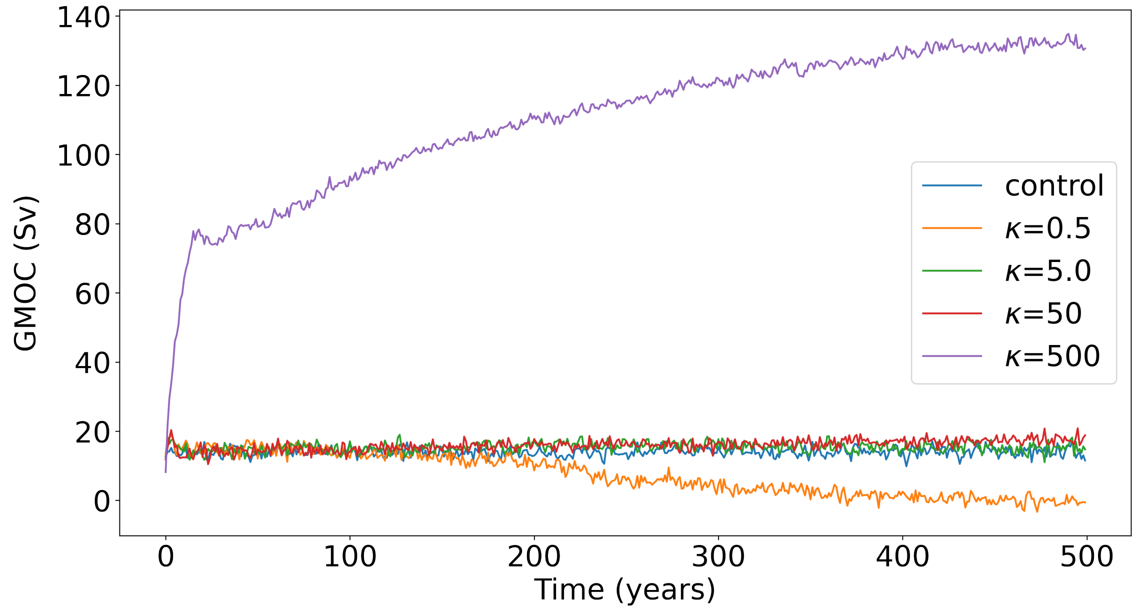

Figure 2.3.4: Annual mean GMOC (Sv) at 26°N 500-year time series obtained from the control data set (blue) and for FORTE 2.0 runs conducted with different values of the constant ocean vertical diffusion coefficient κ (in $\times\,10^{-4}\,\mathrm{m}^2\,\mathrm{s}^{-1}$ in the plot legend).

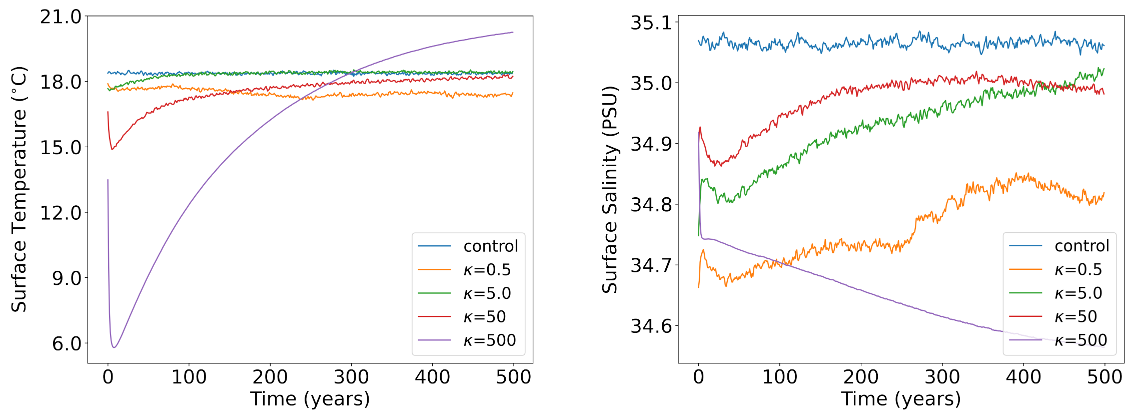

(a) (b)

Figure 2.3.5: Time series of the globally averaged surface temperature (a) and surface salinity (b) for the control run and the data sets corresponding to different values of the constant ocean vertical diffusion coefficient κ (in $\times\,10^{-4}\,\mathrm{m}^2\,\mathrm{s}^{-1}$ in the plot legends).

simplified compared to the complexity, variability, and feedbacks present in a fully interactive atmosphere. In our experiments, the prescribed forcing was unable to capture the spatial and temporal structure of real atmospheric variability, which led to a weak or poorly developed overturning circulation. Only when non-zonally averaged forcing was applied, or when an enhanced surface salinity was introduced in the Atlantic Ocean, MOMA produced a circulation resembling a GMOC-like structure.

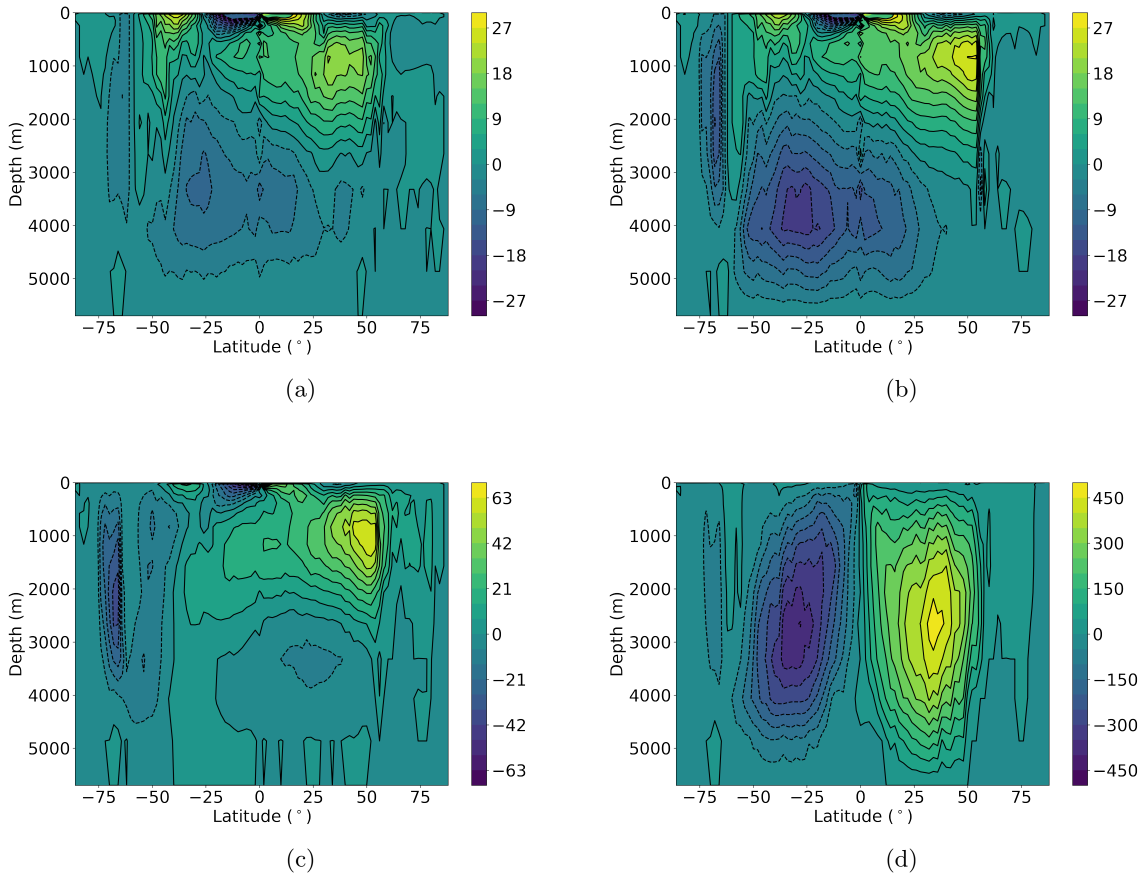

Figure 2.3.6: GMOC (Sv) as a function of latitude and depth, averaged over the last 100 years of the four data sets corresponding to different values of κ, respectively 0.5 $\times\,10^{-4}\,\mathrm{m}^2\,\mathrm{s}^{-1}$ (a), $5.0\times10^{-4}\,\mathrm{m}^2\,\mathrm{s}^{-1}$ (b), $50\times10^{-4}\,\mathrm{m}^2\,\mathrm{s}^{-1}$ (c), and $500\times10^{-4}\,\mathrm{m}^2\,\mathrm{s}^{-1}$ (d).

By contrast, when MOMA is coupled to the IGCM4 atmosphere, the system performs substantially better. The coupled configuration allows the ocean and atmosphere to exchange momentum, heat, and freshwater interactively, enabling the circulation to adjust dynamically to evolving atmospheric conditions. This leads to more realistic results and a more robust overturning circulation. These results justify the modelling choices adopted in the remainder of the thesis: all subsequent investigations rely on the fully coupled FORTE 2.0 model, with the coupled approach providing a more physically consistent framework for exploring planetary climates.

The model sensitivity study conducted in this chapter lays the groundwork for the more comprehensive analysis carried out in the following chapters. Investigating the physical processes driving enhanced vertical diffusion in exoplanetary scenarios will be the focus of Chapter 3. Particular attention is given to the observed trend of strengthening meridional overturning circulation with increasing values of the vertical diffusivity parameter κ, and its implications for climate regulation and planetary habitability. A detailed analysis is

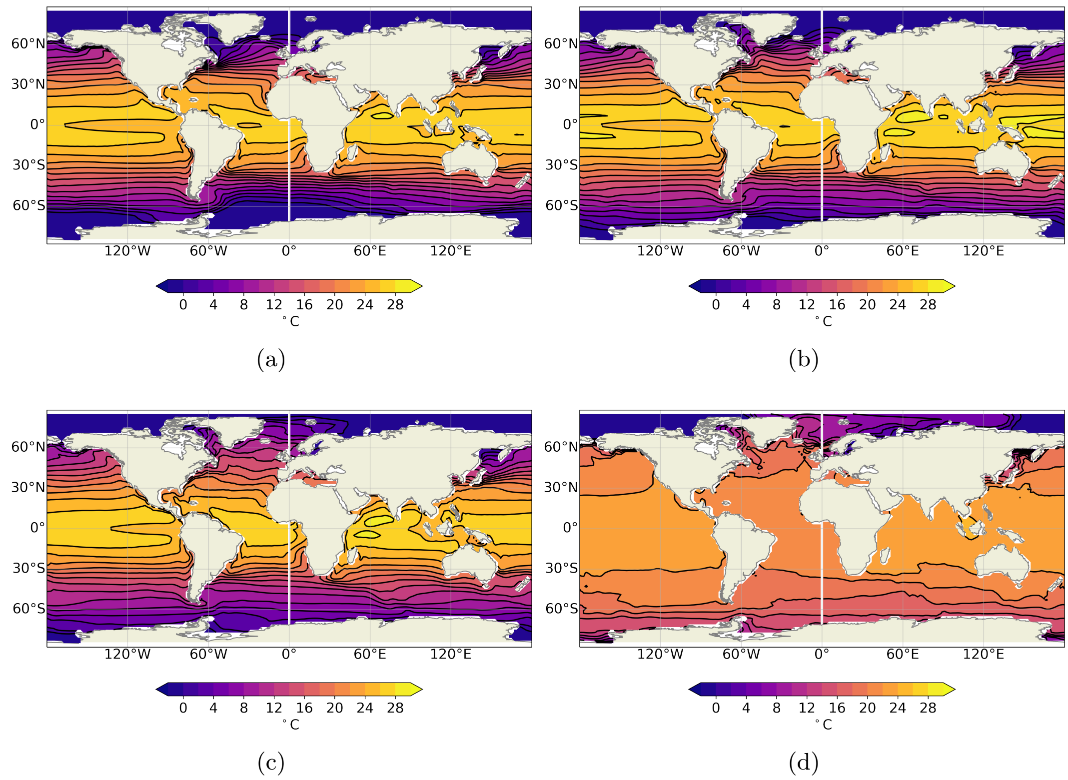

Figure 2.3.7: Surface temperature (°C) as a function of latitude and longitude, averaged over the last 100 years of the four data sets corresponding to different values of κ, respectively $0.5 \times 10^{-4}\,\mathrm{m^2\,s^{-1}}$ (a), $5.0 \times 10^{-4}\,\mathrm{m^2\,s^{-1}}$ (b), $50 \times 10^{-4}\,\mathrm{m^2\,s^{-1}}$ (c), and $500 \times 10^{-4}\,\mathrm{m^2\,s^{-1}}$ (d).

presented across a range of model configurations to assess how variations in κ influence large-scale ocean dynamics, heat transport and surface temperature gradients.

3

Nonlinear and nonmonotonic effect of ocean tidal mixing on exoplanet climates and habitability

---

This study was published in *The Astrophysical Journal Letters* in April 2025 under the same title by Maria Di Paolo, David P. Stevens, Manoj Joshi, and Rob A. Hall, and will hereafter be referred to as Di Paolo et al. [2025]. The text in this chapter is unchanged compared with the article, except for the section "Supplementary material" (3.6) and the section "Further investigation" (3.7) included at the end of the chapter. The former provides further detail to the analysis presented in the paper, with additional comments and plots not shown in the paper due to space limitations. The latter presents additional analyses and broader discussion that complement and contextualize the main study. The research presented in this chapter was carried out on the High-Performance Computing cluster ADA supported by the Research and Specialist Computing Support service at the University of East Anglia. M.D.P., D.S., and M.J. conceived the study. M.D.P. conducted the experiments. All authors contributed to the analysis and reviewed the paper manuscript. The FORTE 2.0 code Blaker et al. [2021], compilation instructions and example run scripts, together with all necessary ancillary files, are accessible at `doi.org/10.5281/zenodo.4108373`. The data that support the findings of this study are accessible at `doi.org/10.5281/zenodo.13961191`.

3.1 Abstract

Tides play an important role in the circulation and mean state of the Earth's oceans through inducing significant mixing. On other planets, tidal forcings could be highly amplified compared to Earth, such as planets orbiting relatively close to low-mass host stars, or planets having massive and/or close moons. The former scenario is especially important as, due to their abundance and their observational advantages, low-mass stars offer the best chance of finding habitable planets through sheer numbers. By varying the magnitude of tidal forcing over several orders of magnitude in a coupled atmosphere-ocean global circulation climate model, we find that key climatic quantities, such as heat transport intensity and both surface and deep ocean temperature, change with tidal strength in a nonlinear and nonmonotonic manner. We find an optimum value of tidal mixing, approximately 100 times that of Earth's oceans, which minimises climatic thermal gradients across the planet. In particular, we show that such planets are habitable for stellar flux values at which oceans with weaker or stronger tidal mixing freeze globally, suggesting an important role for ocean tidal mixing in planetary habitability.

3.2 Introduction

The oceans on exoplanets remain largely unknown, as are the vast majority of precise exoplanetary characteristics, since only a few of them can be inferred from observational studies. The ocean on our planet has been extensively studied and its importance in determining Earth's climate is well established. Earth's ocean is tightly coupled with the atmosphere and cryosphere, with which it exchanges considerable amounts of water, heat and biogeochemical tracers. For instance, the poleward transport of energy from the tropics carried out by ocean circulation has a significant impact on our planet's climate, so much so that the magnitude of oceanic heat transport can be considered comparable to that of the atmospheric heat transport within the tropics [Trenberth & Caron, 2001]. Moreover, switching off ocean circulations and consequently their heat transport would cause an expansion of the sea ice coverage, with a drop in surface temperatures at high latitudes [Winton, 2003]. Our planet would experience more extreme geographic, seasonal and diurnal variability in surface temperature, which could potentially render sizable areas uninhabitable for advanced forms of life [Read, 2014]. Given the key role of the ocean on Earth's climate and habitability, studies of exoplanetary oceans and their impact on climate are of great importance.

The vast majority of research focused on exoplanetary climate adopts atmospheric global circulation models (AGCM) of varying degrees of complexity, often coupled to simplified models of the ocean, such as slab oceans with a depth of 50 m or 100 m, and often rely on prescribed heat fluxes. While this type of study is certainly worthwhile and leads to important results, the lack of coupling to a dynamic ocean precludes an accurate treatment of ocean circulation. Including ocean tides, ocean currents, heat transport, and sea ice [Hu & Yang, 2014; Cullum et al., 2014, 2016; Olson et al., 2020] can lead to significant qualitative differences in the results of exoclimate studies. More specifically, adopting a coupled ocean-atmosphere general circulation model (AOGCM) is particularly advisable when considering scenarios in which the consideration of ocean dynamics can have an important impact on climate.

Studies of habitability of planets orbiting cool stars, and more specifically M dwarfs, are especially interesting for several reasons. Not only are M dwarfs the most numerous stars in the solar neighborhood, offering the best chance of finding habitable planets through sheer numbers, but they also present evident observational advantages. Moreover, the longevity of M-dwarfs represents a benefit for the chances of detecting potentially habitable planets, as these host stars provide a stable environment for the conditions required for the origin and the evolution of life [Shields et al., 2016].

The orbital distance of the circumstellar habitable zone around low-mass stars is significantly smaller compared to the case of Solar type stars, as a consequence of the lower luminosity of low-mass stars. Thus, planets orbiting low-mass stars are more strongly impacted by tidal interactions, causing frictional forces that result in torques that alter the planet's rotational angular momentum. Over time the tidal torques fix the rotation rate at a specific frequency: a process known as tidal locking. According to equilibrium tide theory [Murray & Dermott, 1999], tidally locked planets on circular orbits are destined to rotate synchronously (the periods for the completion of one rotation and one orbit around the central body become identical), always exposing the same face to the host star. However, due to a complex interplay of several factors, planets are not necessarily expected to be exact synchronous rotators, but rather to experience an imperfect tidal locking (see Methods). We choose to investigate the case of an asynchronously rotating planet, therefore characterised by a travelling tide that moves across the planetary surface, consequently affecting ocean tidal-driven vertical mixing. It is well known that oceanic meridional overturning circulation and meridional heat transport have a dependence on vertical mixing [Bryan, 1987; Vallis & Farneti, 2009].

A few studies have investigated the role of ocean heat transport by using fully coupled AOGCMs to carry out exoplanet climate simulations. These publications provided a demonstration of the relevance of exooceanography in studying the climate of exoplanets and in determining their potential habitability [Ferreira et al., 2014; Kilic et al., 2018; Del Genio et al., 2019a]. However, to our knowledge, only one recent study investigated the process of tidal-driven vertical ocean mixing [Si et al., 2022] - and that study assumed Earthlike continents and bathymetry. The authors investigated the effect of high vertical diffusivity (with a parameter 10 and 100 times greater the one of the Earth) on the ocean circulation and surface climate of asynchronously rotating Earth analogs. They found that higher vertical diffusivity strengthened the meridional overturning circulation, enhancing heat transport from the tropics to high latitudes and resulting in overall surface warming.

We conduct studies using the coupled atmosphere-ocean general circulation model FORTE 2.0 [Blaker et al., 2021] to investigate the effects of tidal mixing on climate and habitability. Since the continental configuration of exoplanets cannot be currently constrained from observational studies, we use a custom continental "Ridgeworld" configuration (see Methods), which stops the formation of unrealistically large zonal jets in the ocean which typically occur in aquaplanet models, and allows the formation of ocean gyres, while being more general than assuming the specific continental configuration of present-day Earth.

As strong tidal interactions are tightly linked to the ocean vertical mixing (which we parameterize as a vertical diffusivity κ) [Musgrave, 2021], we demonstrate how taking account of the impact of ocean tides can lead to significant effects on planetary climate. A higher ocean vertical diffusivity, associated to a stronger tidal forcing, is not intended to be necessarily due to the modelled planet orbiting a low-mass star, but can also be interpreted as linked to planets orbited by close and/or massive satellites. We intend to present a comparison of high diffusivity results and scenarios characterised by κ of the same order of magnitude of κ on Earth. In order to do so, we conduct an idealised study, focusing on varying a single parameter of the multidimensional parameter space. We vary the value of κ over a range of four orders of magnitude (see Methods), which reveals nonlinear climatic effects and consequently a nonmonotonic impact on the position of the outer edge of the habitable zone.

3.3 Methods

3.3.1 Model description

We adopt FORTE 2.0 [Blaker et al., 2021], a fast and flexible intermediate-resolution coupled AOGCM. The ocean general circulation model Modular Ocean Model - Array Processor (MOMA) [Webb, 1996] is coupled to the atmospheric general circulation model Intermediate Global Circulation Model version 4 (IGCM4) [Joshi et al., 2015]. The ocean and atmosphere components of the model are coupled once per model day.

In the version of MOMA adopted here, the modelled ocean is characterised by a horizontal resolution of $2° \times 2°$ and by 15 z-layer levels, whose thickness increases progressively with depth, starting from 30 m at the surface and ending with a 836.10 m layer at the bottom.

The ocean reaches a maximum depth of 5700 m, chosen to represent a deep ocean consistent with the 5000-6000 m depths characteristic of large abyssal plains outside major trenches on Earth, with the specific value reflecting a conventional choice made in the original model configuration rather than an attempt to reproduce an exact global mean.

The configuration of the IGCM4 is characterised by a T42 spectral resolution, a grid spacing of approximately 2.8° and a troposphere-only atmosphere which extends to around 25 km altitude and is subdivided in 20σ levels.

3.3.2 Tidal mixing parameterization

Planets in close orbit around their host star experience particularly strong tidal interactions. Thus, potentially habitable planets orbiting M dwarfs are often tidally locked. However, under some circumstances (e.g. eccentricity, spin-orbit resonances, interactions in multi planet systems) these planets may not be synchronously rotating [Barnes, 2017]. For instance, planets on eccentric orbits will not evolve to a state of synchronous rotation, but rather will rotate super-synchronously. For example, it is believed that an initially high orbital eccentricity of Mercury led to its capture into a 3:2 resonance [Correia & Laskar, 2004]. Furthermore, other phenomena can modify the rotational velocity of a planet and even counteract the effects of tidal damping. One example is given by the torque exerted by the Sun's gravitational field on Venus' atmospheric tide, which balances the despinning effect of tides raised in the body of the planet, resulting in its slow retrograde rotation [Dobrovolskis & Ingersoll, 1980]. Atmospheric tides have been shown to be a mechanism potentially capable of desynchronizing Earth-mass planets in the habitable zone of lower-mass stars with much sparser atmospheres than Venus [Leconte et al., 2015]. Therefore, asynchronously rotating potentially habitable planets around M stars can be subjected to large travelling tides, and are therefore characterised by enhanced oceanic vertical mixing and diffusion.

In order to estimate the magnitude of vertical diffusivity, κ, we need to quantitatively determine the orbital radius of an exoplanet residing in the habitable zone of an M star. The M spectral class is divided into nine different groups, numbered from 0 to 9, with 0 being hottest and 9 being coolest. The mass of an M star can therefore vary over a range of $M_\star \approx (0.08 - 0.6)\, M_\odot$, with $M_\odot$ being the solar mass [Pecaut & Mamajek, 2013]. Given that we aim to simulate Earth-like scenarios, we choose the instellation received by the modelled exoplanet to be equal to the insolation that Earth receives. The instellation $S_\star$, in terms of the solar constant $S_\odot$, received from the host star is given by

$$S_\star = \frac{L_\star}{{r_{p,\star}}^2} \quad , \tag{3.3.1}$$

with $L_\star$ the luminosity of the host star in solar units ($L_\odot$), and $r_{p,\star}$ the planetary orbital radius in AU units.

The luminosity and the mass of a main sequence star are linked by the traditional luminosity-mass relationship, that is often parameterized [Harwit, 1998] as

$$L_\star = {M_\star}^{3.5} \quad . \tag{3.3.2}$$

Combining Eq. 4.3.1 and Eq. 3.3.2 allows us to determine the distance between the exoplanet and its host star

$$r_{p,\star} = \sqrt{\frac{{M_\star}^{3.5}}{S_\star}} \quad . \tag{3.3.3}$$

By requiring $S_\star = S_\odot$, and by substituting the values of the M star mass, we obtain

$$r_{p,\star} \approx (0.01 - 0.4) \sqrt{\frac{{M_\odot}^{3.5}}{S_\odot}} = (0.01 - 0.4) \;\; AU \quad . \tag{3.3.4}$$

According to equilibrium tide theory, we can express the maximum potential height of the tidal bulge raised on the planetary surface by the star [Murray & Dermott, 1999] as

$$h_{p,\star,max} = \frac{M_\star}{m_p} \left(\frac{R_p}{r_{p,\star}} \right)^3 R_p \quad , \tag{3.3.5}$$

where R_p is the planetary radius and m_p is the mass of the planet. Therefore, by using the aforementioned stellar mass limits and the range of values of the planetary orbital radius obtained in Eq. 3.3.4, the maximum theoretical height of the tidal bulge in the scenario of an Earth-mass planet orbiting an M star would be:

$$h_{p,\star,max} \approx (80000 - 9) h_{\oplus,\odot,max} \quad , \tag{3.3.6}$$

where $h_{\oplus,\odot,max} \simeq 16$ cm is the maximum potential height of the equilibrium tide raised on Earth by the Sun.

We assume that the tidal potential energy, given by [Murray & Dermott, 1999]

$$V = h_{p,\star} \frac{G m_p}{{R_p}^2} \quad , \tag{3.3.7}$$

where G is the gravitational constant, is completely transferred into kinetic energy, meaning that the maximum energy flux from ocean tides to vertical mixing (through bottom friction, internal wave generation and breaking, etc.) is proportional to $h_{p,\star,max}$. Following the assumption that there is a linear relation between the vertical diffusion coefficient κ and said energy flux [Si et al., 2022], we can estimate the magnitude of κ, which is therefore proportional to $h_{p,\star,max}$. For instance, let us consider an example case of an M5 star with $M_\star = 0.21 M_\odot$ [Heath et al., 1999], then $r_{p,\star} \approx 0.07$ AU and therefore $h_{p,\star,max} \approx 800 \; h_{\oplus,\odot,max}$.

Given the average estimate for Earth $\kappa_\oplus = 1 \times 10^{-4}\mathrm{m}^2\mathrm{s}^{-1}$ [Munk & Wunsch, 1998], we let the value of the globally uniform vertical diffusion coefficient vary within a range $\kappa = (0.5 - 5000)\kappa_\oplus = 0.5, 1.5, 5.0, 15, 50, 150, 500, 1500, 5000 \times 10^{-4}\mathrm{m}^2\mathrm{s}^{-1}$, and carry out climatic simulations adopting these values. The low limit of this range of values corresponds to a vertical diffusion coefficient that is lower than Earth's, and a scenario characterised by especially weak tidal forcings. The upper limit would, in the case of a planet orbiting a low-mass star, correspond to a host star mass of approximately $0.13M_\odot$.

3.3.3 Planet configuration

Given that planetary climates are deeply impacted by the arrangement of land and ocean topography, the choice of planetary topography is particularly important [Macdonald et al., 2022]. In principle, an infinite number of continental configurations are possible for a terrestrial planet. Even though the possibility of extensively exploring realistic synthetic topographies of rocky exoplanetary bodies [Landais et al., 2019] is interesting, it is also very time consuming. Through investigating a limited number of simple configurations it is however possible to draw valid conclusions regarding planetary climate and to evaluate potential habitability in different scenarios.

For instance, when dealing with idealised climate models that consider the contribution of the ocean, two categories of land configurations are often adopted: the pure aquaplanet and the ridgeworld (for example Smith et al. [2006]; Ferreira et al. [2010]; Yang et al. [2019]; van de Velde et al. [2021]). In the first case, the ocean covers the entire globe and no topographic constraints are present. Here large zonal ocean currents can dominate, particularly at the equator. In addition, the zonal pressure gradients that can support a planetary scale overturning circulation are largely absent. In the second case, a number of strips of land extend in the meridional direction obstructing ocean flows, and can feature gaps at different latitudes. Such configurations are chosen as they provide simple representations of how ocean circulation can vary according to different more specific topographic configurations that include multiple continents distributed at different positions across the globe.

In this study, we consider an Earth-sized planet characterised by pre-industrial atmospheric concentrations of CO_2, covered by a single, global-scale ocean basin of uniform depth (5700 m) with limited and idealised hemispherically symmetric expanses of land. The land mass is characterised by two polar islands, that extend to 86°N/S, which prevent eventual numerical instabilities resulting from grid convergence to arise. The chosen configuration features a single, 2° wide, meridional ridge 145 m below the surface that connects the two polar islands and allows an overturning circulation. Because the ridge remains submerged, the atmosphere interacts only with the ocean surface, avoiding the need to prescribe additional land-surface properties or albedos and ensuring a more generalised scenario. The sub-surface placement of the ridge does not significantly affect the large-scale ocean circulation, while still providing the boundaries required to maintain the meridional circulation.

3.3.4 System architecture

We assume that the orbital and dynamical characteristics of the system (orbital semi-major axis, orbital eccentricity, planetary rotation period, planetary axial tilt, planetary mass, atmospheric composition, surface pressure) are the same as for the Earth-Sun system.

We adopt a solar spectral energy distribution and we assume an Earthlike stellar radiation forcing at the top of the atmosphere: $S_{\odot} = 1365$ Wm^{-2}. Once the simulated climates reach a quasi steady state after 2000 years, the instellation value is reduced to a fraction of the solar constant (0.90, 0.85, 0.80 $S_{\odot}$), and we let the simulations run until a new steady climate state is reached.

3.4 Results

3.4.1 Effect of vertical diffusion: circulation and temperature structure

The ocean meridional circulation is tightly linked to the value of κ. The Atlantic Meridional Overturning Circulation (AMOC) on Earth [Buckley & Marshall, 2016] is a particularly interesting analogue of the AQuaplanet Meridional Overturning Circulation (AQMOC).

The mechanisms driving the thermohaline currents that form this conceptual conveyor belt [Broecker, 1991] are the same as those on Earth. Here, this overturning circulation is of fundamental importance to establish the climate we experience today, since it distributes heat and salt around the globe and carries nutrients necessary to sustain biological activities and support ocean life [Buckley & Marshall, 2016]. Essentially, warm surface water near the equator moves northward, gradually losing heat to the atmosphere. Colder water is denser, especially if subjected to sea ice formation processes, since salt is left behind in the ocean water. Towards the poles water sinks, and flows equatorwards at depth. Eventually, the circulation is completed with a process called upwelling, when the water that has reached lower latitudes (or the Southern Ocean in the case of present-day Earth) is pulled towards the surface, and then proceeds to warm and start the cycle again.

The left panel of Figure 3.4.1 shows the zonally averaged ocean temperature (shading)

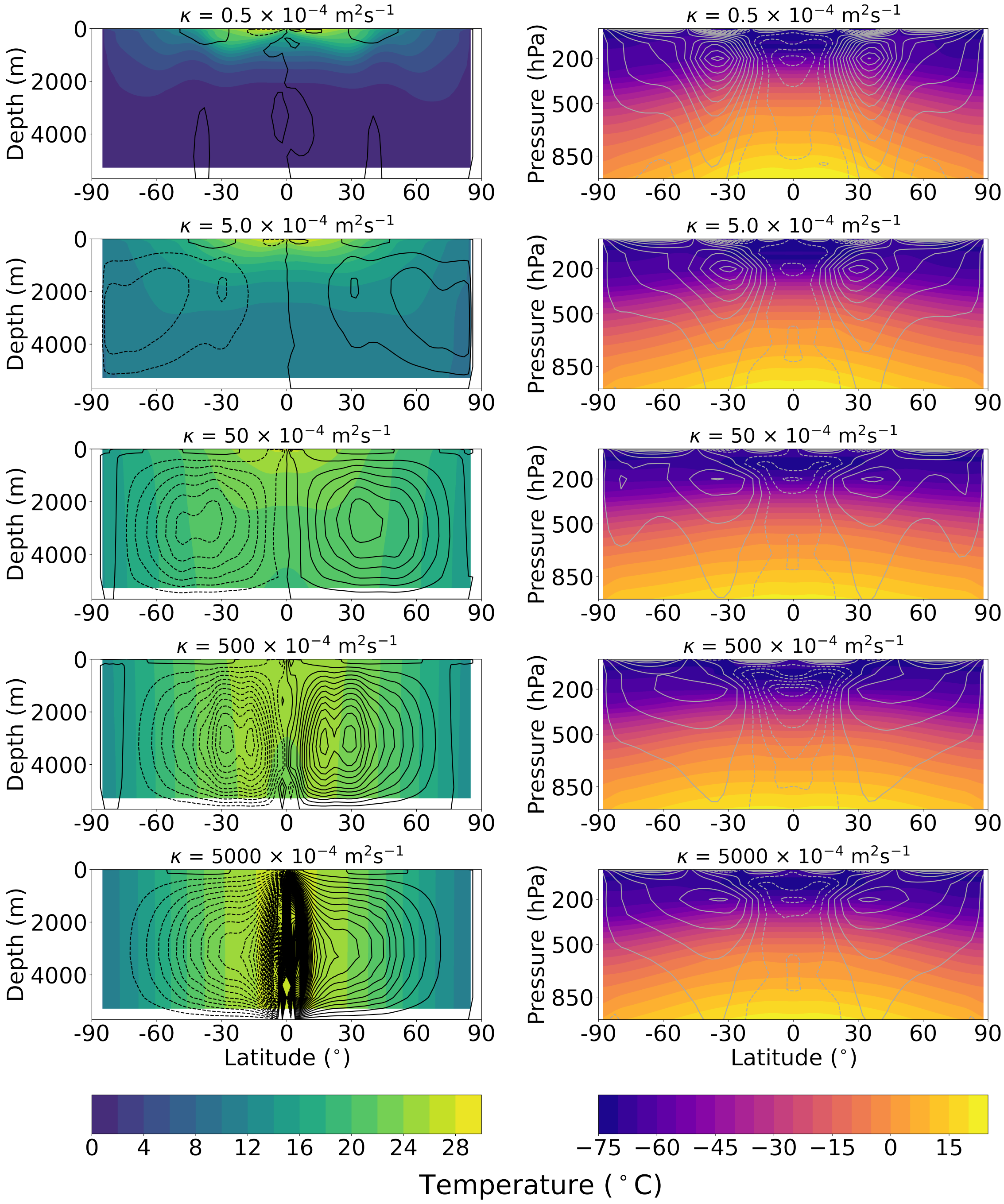

Figure 3.4.1: Shading shows zonally averaged values of temperature for the ocean (left) and the atmosphere (right). Black contours show the meridional overturning streamfunction. Contour interval is 50 Sv. Clockwise circulation is depicted by solid lines, anticlockwise circulation is depicted by dashed lines. Grey contours show the zonal wind. Contour interval is 3 ms^{-1} . Westerlies are depicted by solid lines, easterlies are depicted by dashed lines. Quantities are averaged over the last simulated 100 years for each case.

and the overturning streamfunction (black contours) as a function of depth and latitude for each of the analysed cases. In every figure, circulation cells exist that move water in a clockwise (anticlockwise) motion in the Northern (Southern) hemisphere, from the equator to higher latitudes at surface and in the opposite direction at depth. While the topographic configuration in every case is hemispherically symmetric, a few slight differences appear between the two hemispheres for both quantities shown here, because of the adoption of Earth's orbital characteristics, i.e. the planet is located at the orbit's periapsis during northern winter / southern summer, and at the apoapsis during northern summer / southern winter.

In general, the results show hemispheric AQMOC cells that envelope the whole planet, different from what happens on present-day Earth (the AMOC). Increasing values of κ result in an enhanced circulation, which is evident by an increasing number of black contours in Figure 3.4.1. As oceanic diffusion increases, the thermocline deepens progressively, and deep water at depths below 1-2 km becomes warmer, especially at low latitudes.

As κ increases and more efficient circulation, and thus redistribution of heat is achieved, temperature minima increase and temperature maxima decrease, resulting in a flattening of the meridional surface temperature profile. When a threshold value of $\kappa \approx$ 150-500 $\times 10^{-4}$ $\mathrm{m^2 s^{-1}}$ is reached, the opposite behaviour arises: for higher vertical diffusivities, the overturning cells become confined to lower latitudes, and water is effectively mixed in the vertical, but less efficiently moved in the meridional direction.

Sea surface temperature variations with κ have an impact on the atmosphere. The right panel of Figure 3.4.1 shows the zonally averaged atmospheric temperature and zonal winds for each of the analysed cases. Subtropical jet streams are more intense for lower values of κ, associated with a larger meridional gradient in surface temperature, and become progressively less intense as κ increases and the meridional temperature profile is flattened, as shown by the decreasing number of grey contours. This trend is reversed once the threshold value of κ is reached, and the differences between equatorial and polar temperatures become starker.

In association with the gradual flattening of the meridional surface temperature gradient as κ increases, the Intertropical Convergence Zone becomes less defined in shape. Figure 3.4.2 shows how rainfall bands, distinctly separated in the low κ scenarios, progressively weaken, broaden and merge as κ increases. Although only annual-mean precipitation is available for this analysis, the structure of the rainfall peaks in Figure 3.4.2 suggests that their behaviour may also exhibit pronounced seasonal modulation. In low-κ scenarios, where the meridional temperature gradient is strong and the ITCZ is well defined, the seasonal migration of the convergence zone is expected to produce distinct, seasonally separated rainfall maxima in the Northern/Southern hemispheres during boreal summer/winter. Conversely, as κ increases and the annual-mean ITCZ broadens and weakens, the corresponding seasonal peaks would likely become less coherent, with reduced amplitude and greater overlap between hemispheres, smearing out seasonal

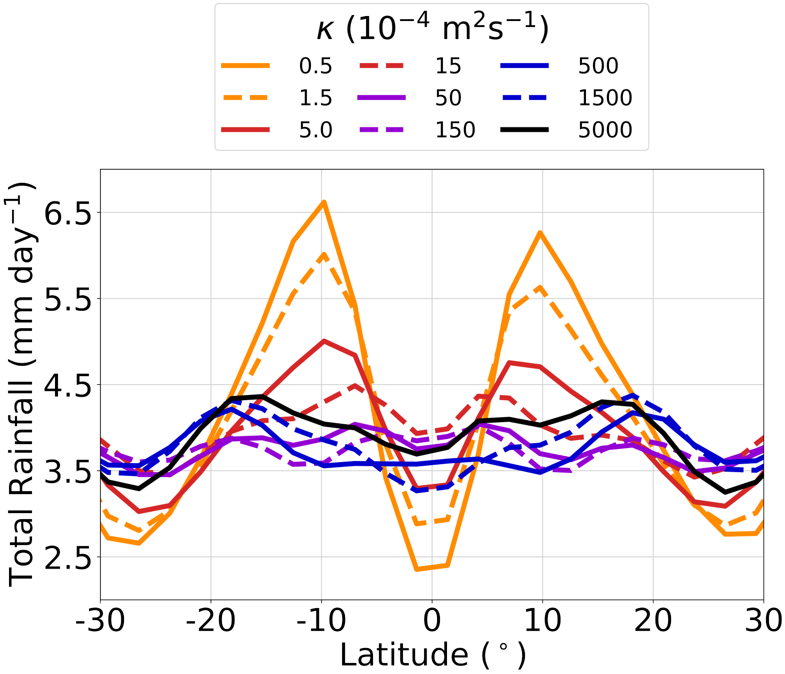

Figure 3.4.2: Zonal mean of the total rainfall as a function of latitude and κ. Quantities are averaged over the last 100 years for each simulation.

shifts of the rainfall bands. Exploring this behaviour with diagnostics from monthly outputs would therefore be a valuable extension of the present analysis.

Figure 3.4.1 shows, both for the ocean and the atmosphere, a behaviour that is qualitatively similar to the one presented in Si et al. [2022] (temperature shown in Figure 4 and circulation shown in Figure 1) for similar values of κ. Noticeable asymmetries, especially for the ocean, are due to the fact that the adopted topography presents Earth-like continents in Si et al. [2022]. Relying on these results to infer a trend from for high values of κ would however be misleading, as non linearities arise for $\kappa > 100 \times 10^{-4}$ m^{2}s^{-1}, with increasing κ leading to reduced total and ocean heat transport and to enhanced meridional temperature gradients.

3.4.2 Effect of vertical diffusion: ocean temperature and heat transport

The total poleward heat transport (combined atmospheric and oceanic components) at 35° N increases from 4.46 PW to 5.69 PW as κ increases from 0.5×10^{-4} m^{2}s^{-1} to 500×10^{-4} m^{2}s^{-1}, and then slowly decreases for even higher values of κ (Figure 3.4.3c). While the maximum value of the total heat transport is reached around 35-40° N for each value of κ, it is interesting to note that the ocean heat transport peaks at low latitudes for low values of vertical diffusion, starting from about 9° N for $\kappa = 0.5 \times 10^{-4}$ m^{2}s^{-1}, and then shifts towards higher latitudes, settling at about 30° N for higher values of κ (see Section

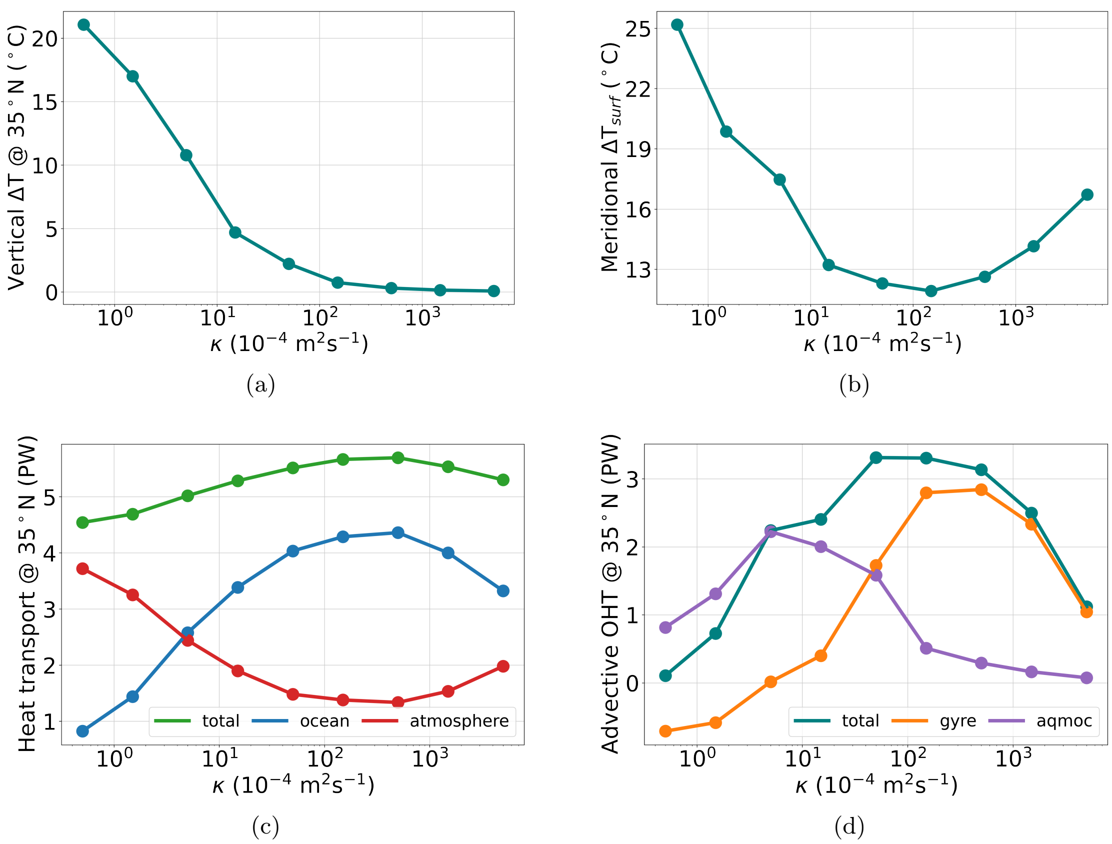

Figure 3.4.3: Mean climatic properties as a function of κ. Quantities are averaged over the last 100 years for each simulation. (a) Zonal mean vertical temperature difference (surface-bottom) at 35° N, (b) zonal mean meridional surface temperature difference (equator-pole), (c) total, ocean and atmosphere meridional heat transport at 35° N, (d) advective components of the meridional ocean heat transport at 35° N.

3.6.2 and Figure 3.6.5 for further details).

Although the total heat transport varies within a small range as κ varies, the changes in oceanic and atmospheric heat transport are much larger with a degree of compensation between these components. Low oceanic heat transport at low values of κ results in a higher atmospheric heat transport and conversely high oceanic heat transport at high values of κ results in a lower atmospheric heat transport.

Heat transport in the ocean is mainly carried out through two different circulation processes: the AQMOC and the horizontal gyres. Figure 3.4.3d shows the total advective ocean heat transport and its components due to the AQMOC and the gyre circulation, computed with monthly averaged data[1]. Unlike the oceanic heat transport shown in Figure 3.4.3c, the advective part of oceanic heat transport in Figure 3.4.3d does not take into account sub-monthly transient effects and diffusion processes. As a result of the

[1] Details on the calculations of the advective ocean heat transport components are provided in Section 3.6.2.

particularly efficient mixing associated with high values of κ, the temperature gradient between the top and the bottom layers of the ocean becomes progressively smaller, and vertical stratification disappears (Figures 3.4.1 and 3.4.3a). In this scenario, the heat transport associated with the gyre circulation becomes more important than the overturning component, as the vertical temperature gradient is eroded but the horizontal gradient remains.

Higher values of κ correspond to a more efficient oceanic vertical mixing, which consequently means that as the surface to ocean bottom temperature gradients decrease, the volume averaged temperatures steadily increase (Table 3.4.1). Meridional gradients of surface temperature reach a minimum between $\kappa \sim 150 - 500 \times 10^{-4}$ $\mathrm{m^2 s^{-1}}$, which corresponds to the peak in heat transport.

For comparison, the three values of the vertical diffusion coefficient adopted by [Si et al., 2022] are $\kappa = 1,\ 10,\ 100\ \kappa_\oplus = 1,\ 10,\ 100 \times 10^{-4}$ $\mathrm{m^2 s^{-1}}$ (see Figure 3.4.3). The behaviour shown in Figure 3.4.3c is qualitatively comparable to that presented in Figure 3 of Si et al. [2022], with increasing ocean heat transport and decreasing atmosphere heat transport as κ increases. The main differences in our results for similar values of κ consist in the latitude of the peak in heat transport and in overall lower values of heat transport, both ascribable to a different planetary configuration. Once again, taking into consideration higher values of κ allows us to unveil a nonmonotonic trend that would otherwise remain undetected.

3.4.3 Effect of change in instellation

Ocean diffusion plays an important role in determining the basic state of the planetary surface, and therefore in determining quantities that are tightly linked to the concept of habitability, such as surface temperatures. For instance, a low value of κ implies that less heat is transported away from the warmest regions at low latitudes and towards the coldest regions at high latitudes, increasing the temperature of the warmest regions and further cooling down the coldest regions - such a situation implies that an ocean with a low value of κ will completely freeze over at values of instellation that can support a non-frozen ocean with a higher value of κ.

In order to test the impact that ocean tidal mixing might have on the position of the outer edge of the habitable zone, we run a set of simulations with a reduced instellation ($S_\star = 0.90,\ 0.85,\ 0.80\ S_\odot$) for the cases $\kappa = 0.5,\ 5.0,\ 50,\ 500,\ 5000 \times 10^{-4}$ $\mathrm{m^2 s^{-1}}$. The new simulations are started from the steady climate state reached in the case of $S_\star = S_\odot$, and are run until a new equilibrium state was achieved. A reduced instellation causes a drop in temperatures and, in some cases, the formation of sea ice. A more efficient oceanic heat transport mitigates these effects. In some scenarios, the planets characterised by higher values of κ are spared from completely freezing over. An enhanced oceanic circulation can prevent the planet from freezing over. On the contrary, an inefficient heat redistribution can be associated with a quick global glaciation: once sea ice starts forming at high latitudes, a strong ice-albedo feedback causes its rapid expansion towards lower latitudes.

The results summarized in Table 3.4.1 and Figure 3.4.4 show a variety of scenarios: planets receiving the same amount of energy from their host star, but characterised by different values of κ, may eventually become completely frozen (Table 3.4.1 grey rows), their surface might be partially covered by some ice (light blue rows), or they might not form any sea ice at all (dark blue rows). In general, values of κ associated with efficient heat transport (see Figure 3.4.3c) result in warmer climates. More specifically, if we focus on the case $S_\star = 0.80\ S_\odot$, the scenario characterised by $\kappa = 500 \times 10^{-4}\ \mathrm{m^2 s^{-1}}$, associated with the peak in heat transport discussed in the previous section, is the only case in which the planet is not completely frozen, but rather features sea ice that extends from the poles to $\sim 50°$ N/S. These results demonstrate that the variation of tidal strength has an impact not just on climate, but also habitability in a nonmonotonic manner.

Ocean diffusion effectively plays a role in determining the position of the outer edge of the habitable zone, which presents an outwards shift in the scenarios characterised by efficient meridional heat transport. Referring to equation 3.3.3, a 20% decrease in instellation corresponds roughly to a 12% increase of the orbital radius of the habitable zone.

3.5 Discussion and Conclusions

In this paper we address the issue of estimating the impact of ocean tides on planetary climate, in the case of a water rich planet residing in the habitable zone of a low-mass star.

We demonstrate that enhancing tidally-driven vertically diffusivity in the ocean crucially influences the global circulation patterns and the strength of overturning cells in a "Ridgeworld" climate model, and dictates the amount of heat transported meridionally, therefore playing an important role in determining the temperature of the planetary surface. Concurrently, tidal energy dissipation has an impact on other quantities that characterise the planetary surface. For instance, given the strong interaction between the ocean and the atmosphere, lower values of κ result in larger latitudinal gradients of surface temperature, therefore resulting in more intense zonal winds.

The magnitude of κ has significant implications for the mechanisms at play in transporting heat in the ocean. Our findings suggest that a more efficient vertical diffusion, and the consequent reduction of vertical stratification, enables the horizontal gyres to become the predominant medium to transport heat.

$S_\star$ ($S_\odot$)	κ (10^{-4} m^{2}s^{-1})	**Mean annual climate state**		
		T_{surf} (°C)	T_{vol} (°C)	ϕ_{ice} (° N/S)
1.00	0.5	20.6	3.7	86.0
	5.0	21.6	13.0	86.0
	50	22.3	20.5	86.0
	500	22.1	22.1	86.0
	5000	21.9	22.2	86.0
0.90	0.5	6.6	-0.0	39.0
	5.0	14.8	7.0	86.0
	50	15.3	13.7	86.0
	500	15.5	15.5	86.0
	5000	15.0	15.3	86.0
0.85	0.5	-2.2	-1.9	0.0
	5.0	-2.2	-1.9	0.0
	50	10.7	9.3	86.0
	500	11.1	11.2	86.0
	5000	10.4	10.7	86.0
0.80	0.5	-2.2	-1.8	0.0
	5.0	-2.2	-1.9	0.0
	50	-2.2	-1.9	0.0
	500	4.1	4.2	51.2
	5000	-2.2	-1.9	0.0

Table 3.4.1: Values of sea surface temperature, volume averaged oceanic temperature and latitude reached by sea ice corresponding to different values of instellation and κ. The values represent the mean annual climate state and are computed at the end of each simulation, once the climate is considered stable, and averaged over 10 years. Climate stability was assessed from the trend of the globally volume-averaged and surface-averaged ocean temperature over the final 100 years of integration. Negligible residual drifts indicate that the simulated climate is approximately equilibrated.

Interestingly, the results point to a nonlinear and nonmonotonic effect of the vertical diffusion coefficient on several climatic variables. Having expanded the range of values of diffusivity previously considered [Si et al., 2022], here we argue for the existence of a threshold value of κ at which surface temperature and oceanic heat transport are maximised (see Figure 3.4.3c).

The effect of tidal mixing on climate is especially noteworthy if it is possible to distinguish different scenarios from observed surface features. In the case of reduced instellation, ice coverage of the planetary surface would be an especially effective observable. We find that, for a fixed instellation value (for example $S_\star = 0.85\ S_\odot$), sea ice changes from covering the entirety of the planetary surface to being completely absent depending on the choice of κ. In the case of a solar instellation, $S_\star = S_\odot$, cloud patterns could offer an insight into the climate dynamics of the observed planet. We find that planets characterised by different κ present different Intertropical Convergence Zone configurations, consistent with the surface temperature profile depicted in Figure 3.4.1. For low values of κ, the Intertropical Convergence Zone appears to be split in two bands separated by an evident

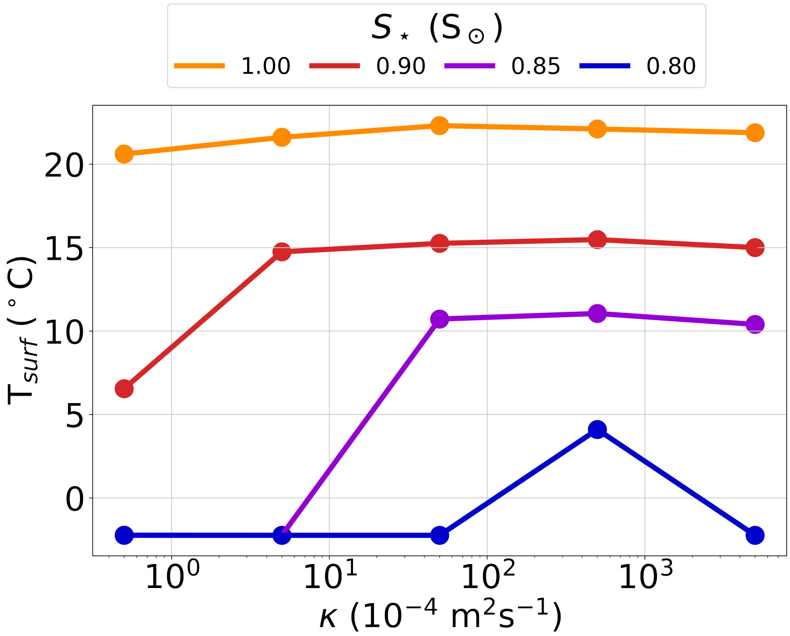

Figure 3.4.4: Globally averaged surface temperature as a function of κ for different values of instellation. Quantities are averaged over the last 10 years for each simulation.

equatorial cold tongue, and these two bands merge into a singular band across the equator as κ increases. This effect is seen on a regional scale, and therefore is not observable with the present technology that can at best characterise surface properties of exoplanets on a global scale. Advances in observational technologies might unveil such characteristics in the near future.

This study aims at highlighting how the climates of planets affected by significant tidal forces differ from the reference case of the Earth. Our simulations are based on several assumptions. We choose to simulate the case of a water rich planet characterised by a simple ridgeworld configuration and we focus on parameterizing the impact of ocean tides. We assume that our results are general enough for the case of any planet with oceans that features some kind of meridional barrier. To validate this statement, we run simulations where the pole to pole grid cell wide ridge is split into multiple sections spread over a range of longitudes. We find that the results from these runs do not present significant differences from the standard scenario analysed in this paper. By contrast, configurations with a much deeper meridional ridge - or an ocean world with no meridional barriers - would allow zonal currents to dominate the circulation, substantially weakening the meridional overturning and reducing poleward heat transport, subsequently leading to sharper equator-to-pole temperature gradients (see Section 3.7.2).

We do not take into account the different nature of the stellar spectrum of a low-mass star compared to the solar equivalent, nor do we factor in the effect of the host star spectral energy distribution on the ice-albedo feedback (in this study, the adopted ice albedo is

0.6). For instance, Shields et al. [2013] conducted a study regarding the ice latitude of exoplanets orbiting three different types of host stars, varying the amount of instellation and taking into account the wavelength-dependent reflectivity of ice and snow. Using the CCSM4, they found that an M-dwarf planet entered a snowball state at $S_\star = 0.73\ S_\odot$, compared to the instellation value necessary for a planet orbiting a G star to completely freeze over, that is $S_\star = 0.92\ S_\odot$.

Even though the adopted model is different from FORTE 2.0, we can safely assume that we would obtain a similar outcome in our case, which would mean that the outer edge of the habitable zone would be further outwardly shifted if we considered the ice and snow albedos to be lower for a host star colder than the Sun. Similarly, different levels of CO_2 would change the value of $S_\star$ at which the formation of sea ice, and ultimately global glaciation, occur.

An additional factor that is not taken into account in this study is the contribution of planetary tidal heating, which could provide an additional source of heat. Including this aspect of the tidal forcings exerted on the simulated planet would once again temper the onset of snowball scenarios and further extend the outer edge of the habitable zone. The above effects, as well as the cases of planetary rotation rates dissimilar to the Earth's, and specifically spin-orbit resonances, are topics that are left for future work.

In conclusion, we show how a nonlinear and nonmonotonic relationship exists between ocean circulation, climate, potential habitable zone width and ocean tidal mixing κ. The potential habitability of asynchronously rotating tidally locked planets implicitly depends on the stellar type through the effect of stellar size on star-planet distance and ocean tidal strength and hence κ. Our results apply to any case in which a terrestrial planet is subjected to strong non-stationary tidal forcings, which include those being orbited by either massive or close satellites. For example, on Earth the equilibrium lunar tide is more than twice as strong as the equilibrium solar tide. An appropriate choice of κ, associated with enhanced oceanic heat transport, can lead to planets being spared from entering a snowball state and completely freezing over, or equivalently to an outwards shift of the outer edge of the habitable zone, effectively widening the circumstellar region that can host potentially habitable planets.

3.6 Supplementary material

3.6.1 Mean climate state

This section includes additional plots and expanded discussion regarding the mean state of the climate of the analysed scenarios with varying κ. Further details deepen the interpretation of the study's findings and support its primary results.

Figure 3.6.1 complements Figure 3.4.1 by presenting the zonally averaged temperature (shading), overturning streamfunction (black contours), and zonal winds (grey contours) as functions of depth/pressure and latitude for the additional cases not shown previously. The mean state of the ocean and atmosphere are consistent with those in Figure 3.4.1: increasing values of κ associated with enhanced oceanic vertical diffusion strengthen the circulation, evident from the increasing number of streamfunction contours in the left panel, progressively deepen the thermocline and warm the deep ocean, particularly at low latitudes. These additional plots do not introduce new qualitative behaviour beyond that already illustrated, but complete the analysis presented in Di Paolo et al. [2025] by documenting all simulated scenarios.

Figure 3.6.2a further illustrates the progressive erosion of ocean vertical stratification as κ increases: the mean surface temperature, the volume-averaged temperature, and the temperature at the bottom of the basin converge toward similar values. Consistently, the zonally averaged surface temperature (Figure 3.6.3a) and volume-averaged temperature (Figure 3.6.3b) gradually acquire comparable meridional structures with increasing κ. The surface temperature profile becomes increasingly uniform as circulation strengthens, while the volume-averaged temperature develops sharper meridional gradients due to substantial warming of water at depth, particularly at lower latitudes.

Due to temperature-dependent weathering rates, the temperature at the bottom of the ocean has potential implications for habitability. The long-term climate stability of geologically active planets is regulated by temperature-dependent silicate weathering, with CO_2 removed by continental weathering and replenished by volcanic outgassing. Because weathering rates increase with temperature and cease below freezing, while outgassing is largely temperature-independent, this feedback stabilizes climate above freezing [Walker et al., 1981; Marshall et al., 1988; Berner, 1994; Lenton et al., 2018]. Seafloor weathering also removes CO_2 dissolved in seawater, lowering its atmospheric levels as the ocean absorbs excess CO_2. Like continental weathering, it depends on the local temperature - seafloor temperature instead of surface temperature [Coogan & Dosso, 2015] - but its stronger temperature dependence suggests seafloor weathering may have been more dominant for early Earth [Krissansen-Totton & Catling, 2017]. Crucially, while continental weathering halts under global glaciation, seafloor weathering can persist if the deep ocean remains unfrozen due to geothermal heat fluxes, with hydrothermal oases maintaining ocean-atmosphere CO_2 exchange [Le Hir et al., 2008; Nakayama et al., 2019]. By reducing CO_2 levels during glaciated states, seafloor weathering can prevent planets from attaining strong greenhouse conditions and instead stabilize globally or near-globally ice-covered climates, thereby introducing equilibrium regimes inaccessible through continental weathering alone, which ceases under full glaciation with no mechanism remaining to balance outgassing [Chambers, 2020]. As

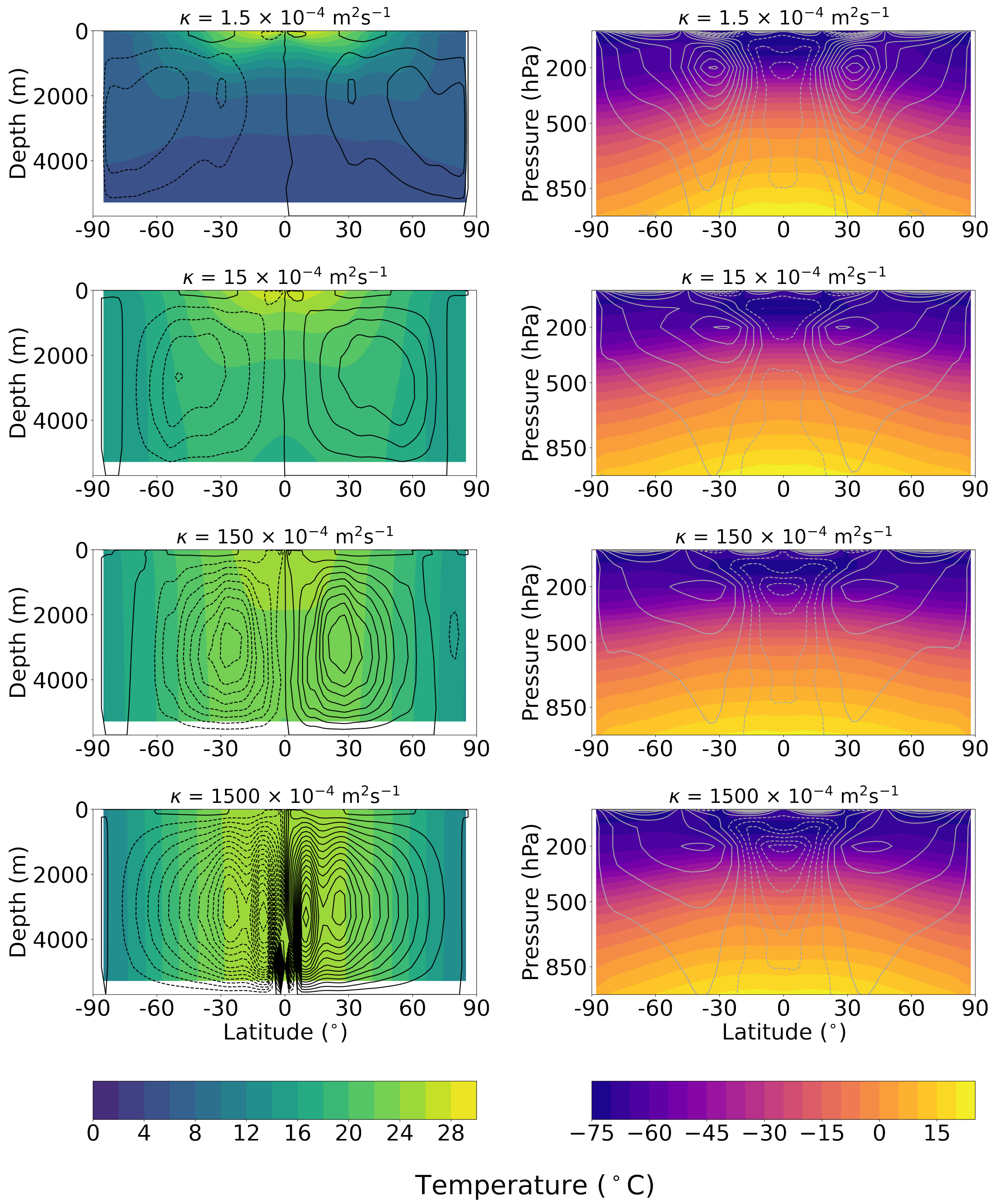

Figure 3.6.1: Supplementary plot complementary to Figure 3.4.1. Shading shows zonally averaged values of temperature for the ocean (left) and the atmosphere (right). Black contours show the meridional overturning streamfunction. Contour interval is 50 Sv. Clockwise circulation is depicted by solid lines, anticlockwise circulation is depicted by dashed lines. Grey contours show the zonal wind. Contour interval is 3 ms^{-1} . Westerlies are depicted by solid lines, easterlies are depicted by dashed lines. Quantities are averaged over the last simulated 100 years for each case.

seafloor temperatures rise with increasing κ (Figure 3.6.2a), seafloor weathering would be expected to become more efficient, potentially reducing atmospheric CO_2 and

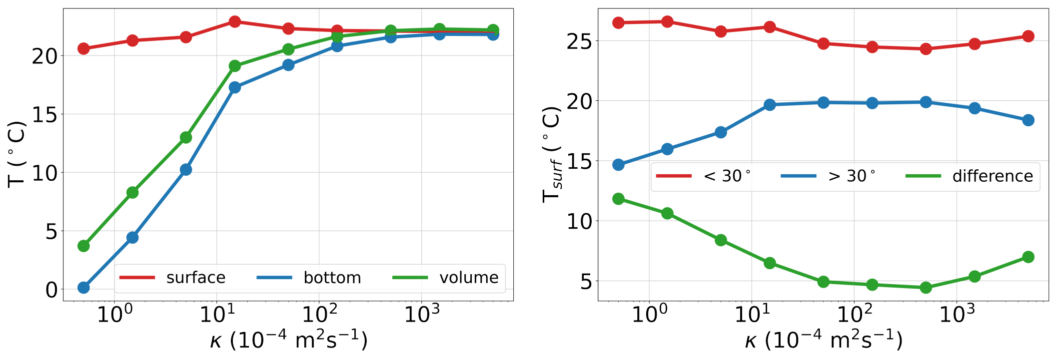

(a) (b)

Figure 3.6.2: Mean climatic properties as a function of κ. Quantities are averaged over the last 100 years for each simulation. Sea surface temperature, volume-averaged temperature, temperature at the bottom of the basin (a) zonally averaged surface temperature over the regions $\theta \leq 30°$ and $\theta \geq 30°$ and their difference (b).

counteracting the warming associated with enhanced ocean vertical diffusivity. This feedback is not captured in our analysis and would introduce additional complexities, such as assumptions about sedimentation rates, with lower sedimentation rates amplifying seafloor weathering by exposing a greater fraction of oceanic crust to alteration and vice versa [Coogan & Dosso, 2015; Coogan & Gillis, 2018].

Meridional temperature gradients are minimised for $\kappa = 150 \times 10^{-4}$ m^{2}s^{-1} (Figure 3.4.3b), whereas total heat transport at 35° N peaks for $\kappa = 500 \times 10^{-4}$ m^{2}s^{-1} (Figure 3.4.3c). In a purely diffusive system, both quantities would be minimised or maximised at the same value of κ, while using a more complex model introduces nonlinearities that result in the shift observed here. In this case, such non linearities are likely linked to changes in structure and position of the Intertropical Convergence Zone, which in turn affect the planet energy balance. The magnitude of this effect is relatively small in the context of exoplanetary studies, and therefore the shift of the value of κ that minimises/maximises meridional surface temperature gradients/heat transport is not of major significance. To confirm this, we computed the meridional surface temperature gradient using zonal averages over broader latitudinal bands (30°S–30° N for the tropics and 30°–90° for higher latitudes) rather than the equatorial and polar values shown in Figure 3.4.3c, thereby smoothing over the Intertropical Convergence Zone. In this formulation, high-latitude temperatures are maximised and tropical temperatures minimised at $\kappa = 500 \times 10^{-4}$ m^{2}s^{-1}, yielding a meridional gradient minimised at the same value of κ where total heat transport is maximised (Figure 3.6.2b).

Moreover, nonlinearities associated with the Intertropical Convergence Zone likely explain the slight increase in mean surface temperature at $\kappa = 15 \times 10^{-4}$ m^{2}s^{-1} (Figure 3.6.2a), driven primarily by warmer tropical temperatures (Figure 3.6.2b) with respect to the adjacent values of κ. In this case, warmer equatorial temperatures arise from suppressed

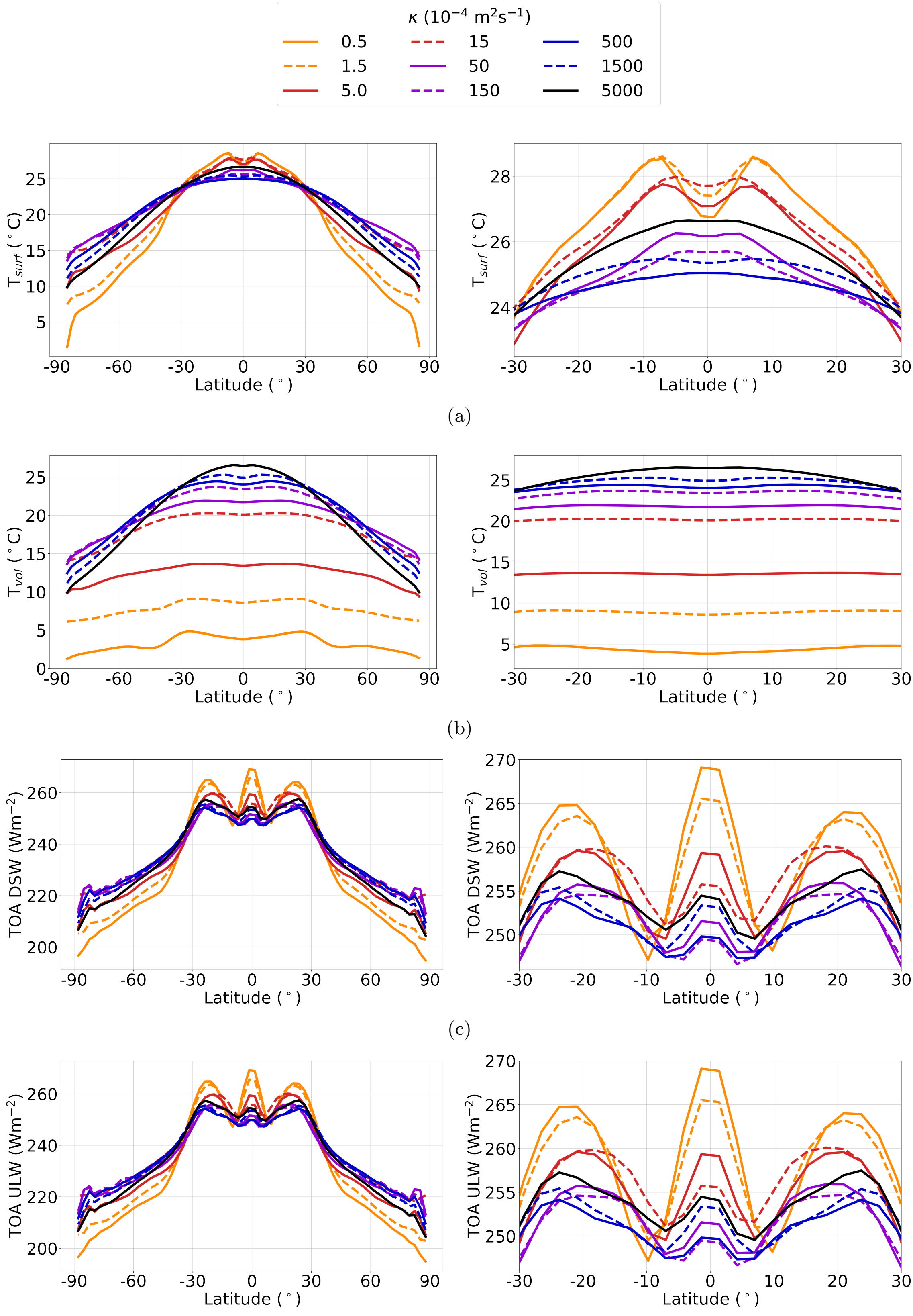

(a)

(b)

(c)

(d)

Figure 3.6.3: Zonal mean of the surface-averaged temperature (a), volume-averaged temperature (b), net downward shortwave flux (c), and top-of-atmosphere longwave flux (d) as a function of latitude (zoomed over 30°S-30° N on the right of each panel) and κ. Quantities are averaged over the last 100 years for each simulation.

upwelling relative to lower κ scenarios, and remain elevated due to less efficient poleward heat transport compared to higher κ cases (Figure 3.6.3a). Rainfall bands begin merging at equatorial latitudes: the $\kappa = 15 \times 10^{-4}$ m^{2}s^{-1} case no longer exhibits distinct peaks of a split Intertropical Convergence Zone, though the nearly merged bands have not yet weakened (Figure 3.4.2). At higher κ, these bands progressively weaken and flatten, reflecting a reduction in atmospheric circulation strength. Despite this variability of the Intertropical Convergence Zone across the investigated range of κ, cloud radiative forcing varies by only $\sim$3 Wm^{-2} (Figure 3.6.3c), representing a minor global effect in the context of exoplanetary climate studies and thus not particularly noteworthy.

Different latitudinal profiles of surface temperature (Figure 3.6.3a) lead to corresponding differences in planetary thermal emission and therefore in the top-of-atmosphere outgoing longwave radiation flux (Figure 3.6.3d). As expected, low values of κ are associated with higher outgoing longwave flux in the tropics and lower flux at high latitudes compared with scenarios characterised by larger κ. As κ increases up to the value that maximises poleward heat transport, the outgoing longwave flux decreases in the tropics and increases at higher latitudes. These variations in the meridional distribution largely compensate one another, resulting in a change of only $\sim$3 W m^{-2} in the globally averaged top-of-atmosphere outgoing longwave flux across all simulated scenarios.

While the figures presented thus far illustrate the mean climate state, they omit details of the longitudinal distribution of key quantities. To address this, latitude-longitude maps of surface temperature are presented in Figure 3.6.4 for all analysed scenarios. These maps not only capture variability associated with the meridional barrier at longitude 240°, but also provide a basis for comparison with the cases discussed in Section 3.7. The maps show a progressive reduction in meridional temperature gradients as the vertical diffusion coefficient increases up to $\kappa = 500 \times 10^{-4}$ m^2 s^{-1}, beyond which the trend reverses. The temperature distribution in all scenarios reflects the structure of the surface gyres: the western side of the basin, just east of the barrier, is consistently warmer than other longitudes at any given latitude due to the poleward flowing western boundary currents east of the barrier. The horizontal extent of the gyres expands with increasing κ and reaches a maximum at $\kappa = 500 \times 10^{-4}$ m^2 s^{-1}, consistent with the behaviour shown in Figure 3.4.3d. Moderate equatorial upwelling in the $\kappa = 0.5 \times 10^{-4}$ m^2 s^{-1} case produces cooler equatorial temperatures relative to adjacent latitudes.

3.6.2 Heat transport

Figure 3.6.5 illustrates the latitudinal distribution of the different components of heat transport across the analysed cases. The northward ocean heat transport (OHT) is computed by integrating the zonal mean surface energy balance from the South to the North Pole. Similarly, the total heat transport (THT) is computed by subtracting the

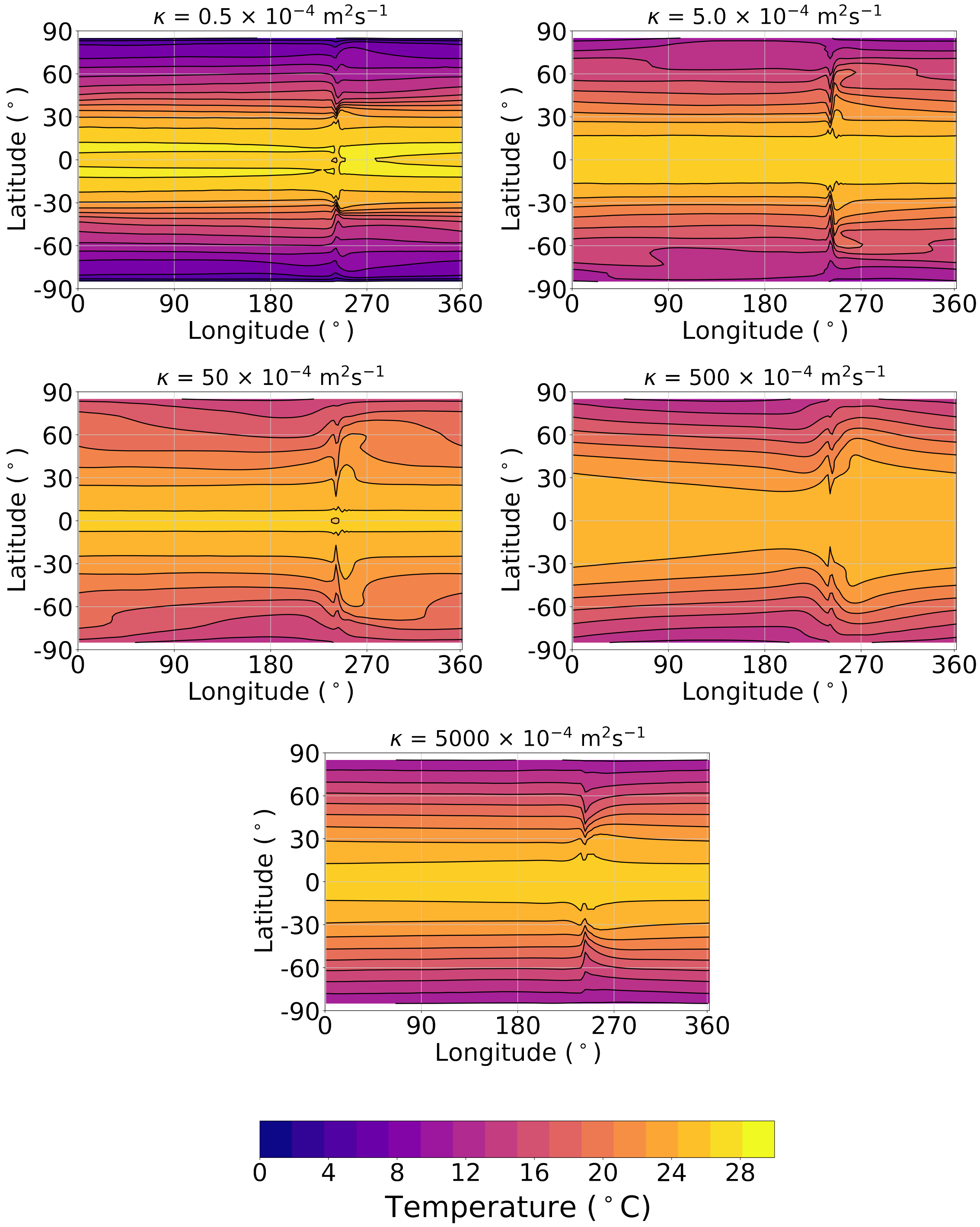

Figure 3.6.4: Surface temperature averaged over the last 100 years for analysed κ scenario. The meridional barrier is positioned at longitude 240°.

top-of-atmosphere upward longwave flux from the top-of-atmosphere net downward shortwave flux, thus taking into account the net radiative energy imbalance at the top of the atmosphere. The atmosphere heat transport (AHT) is computed by subtracting the ocean heat transport from the total heat transport.

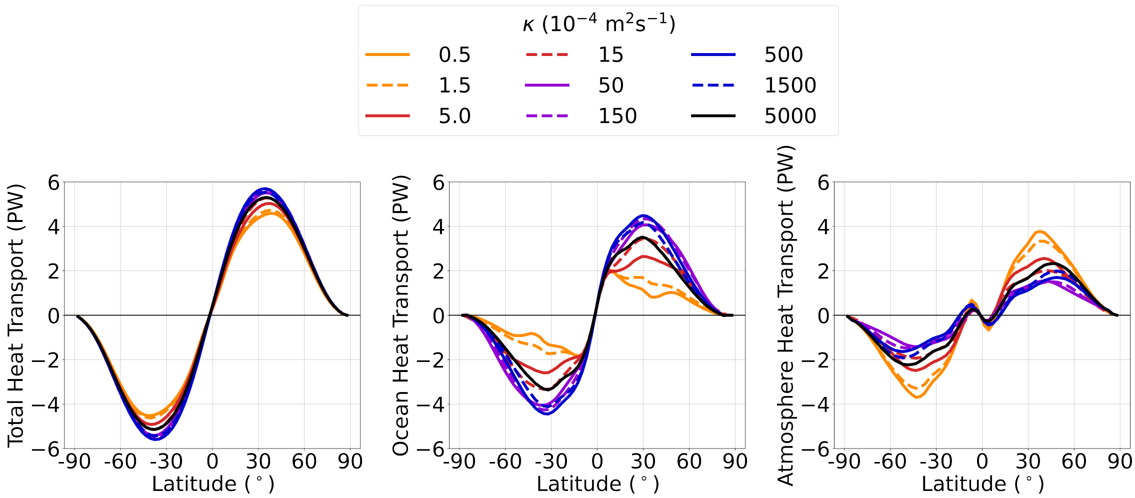

Figure 3.6.5: Total (left), ocean (centre) and atmosphere (right) heat transport as a function of latitude and κ. Quantities are averaged over the last 100 years for each simulation.

As discussed in Section 3.4.2, the maximum total heat transport consistently occurs around 35-40° N for all values of κ. A comparison of the centre and right panels of Figure 3.6.5 highlights a certain degree of compensation between oceanic and atmospheric contributions: not only in their magnitudes, but also in such a way that the latitude of the THT peak remains invariant across scenarios with different κ. For example, in the $\kappa = 0.5 \times 10^{-4}$ m^{2}s^{-1} case, OHT diminishes with increasing latitude, reaching its maximum at only 9° N. Correspondingly, the atmospheric component strengthens poleward, culminating in a peak at 38° N.

The compensatory adjustment between AHT and OHT, such that their sum remains approximately constant under any changes in forcings in the system, is referred to as the “Bjerknes compensation” [Bjerknes, 1964]. Given the constraint of global energy conservation, a stable climate requires that large variations in AHT and OHT balance each other, with variations of equal magnitudes but opposite signs. Stone [1978] provided the theoretical foundation for this principle, arguing that the strength and structure of meridional energy transports are governed primarily by astronomical and planetary parameters such as the planet’s size, rotation rate, axial tilt, the received instellation, and the mean albedo. The total planetary heat transport is therefore largely insensitive to the relative partitioning between AHT and OHT, as an increase in OHT must be associated to a compensating decrease in AHT, and vice versa, to preserve equilibrium. Recognition of this mechanism has been reproduced with both simplified models [Bjerknes, 1964; Manabe, 1969] and in modern coupled GCMs [Yang et al., 2015].

However, such compensation is often incomplete or imperfect, with the relative contributions of AHT and OHT varying in both magnitude and structure with a degree of over- or undercompensation. Imperfect compensation has been demonstrated in several studies of Earth's climate system. For example, Singh et al. [2022] found that changes in AHT typically compensate only about two-thirds of OHT variations across most latitudes, with the resuting THT consequently presenting a reduced amplitude of roughly one-third. Similarly, Yang et al. [2015] showed that AHT may either overcompensate or undercompensate OHT variations depending on latitude, with some experiments reproducing cases of AHT compensation ranging from 20% to 300% of the OHT signal depending on the simulated scenario. In addition, Farneti & Vallis [2013] demonstrated that compensation breaks down when oceanic heat transport variability is driven by surface winds - such as the case of wind-driven gyres - with OHT varying in phase with AHT rather than in opposition, and concluded that the extent of compensation thus depends on the efficiency of the atmospheric response to altered surface temperatures and is unlikely to be perfect.

In non-Earth contexts, Smith et al. [2006] demonstrated that the hypothesis of constant system heat transport holds under several scenarios - including three distinct planetary continental configurations - when OHT variations are small. However, the hypothesis fails when OHT is substantially suppressed, with AHT increasing modestly but not fully compensating for extreme reductions in OHT. In aquaplanet configurations, Rencurrel & Rose [2018] showed that increasing OHT out of the tropics induces an incomplete compensating decrease in AHT, thus resulting in a THT increase up to 1 PW, while the latitude of THT maximum remains fixed.

In the simulations analysed here, the latitude of the THT maximum appears insensitive to changes in the partitioning between oceanic and atmospheric contributions, with peaks consistently located between 35-40° N. Although the variability of THT across scenarios is considerably smaller than that of either AHT (∼2.3 PW) or OHT (∼2.5 PW) individually, the overall difference of ∼1.1 PW in THT between the $\kappa = 0.5 \times 10^{-4}$ m^{2}s^{-1} and $\kappa = 500 \times 10^{-4}$ m^{2}s^{-1} cases is significant. This difference is particularly relevant for habitability assessment under reduced instellation, as it can determine whether the system resides in a globally glaciated state or maintains a temperate climate.

It is noteworthy that substantial climatic differences can arise even when the THT remains virtually identical, with different partitioning of heat transport between the ocean and atmosphere significantly influencing surface climate. Marotzke [1997] demonstrated that significant differences in the mean state of the climate do not necessarily require large differences in THT by using a coupled AOGCM to simulate climates under two distinct continental configurations: differences of only 0.5 PW in the peak THT result in climates being markedly different, with one exhibiting extensive ice caps and the other a substantially warmer, ice-free state.

Figure 3.6.6 shows the total oceanic advective heat transport (Q_{tot}), which can be split into a component carried out by the AQMOC (Q_{AQMOC}) and a component associated with gyres (Q_{gyre}).

These advective quantities are computed over the entire extent of the basin from monthly data as follows (e.g. Böning & Herrmann [1994]; Ferrari & Ferreira [2011]):

$$Q_{tot}(\theta) = \rho_0\ C_p \overline{\int_{-H}^{\eta} \int_{0}^{\Lambda(\theta)} v(\lambda,\theta,z,t)\ T(\lambda,\theta,z,t)\ a\cos\theta\ d\lambda\ dz}, \tag{3.6.1}$$

$$Q_{AQMOC}(\theta) = \rho_0\ C_p L(\theta) \overline{\int_{-H}^{\eta} [v(\lambda,\theta,z,t)][T(\lambda,\theta,z,t)]\ dz}, \tag{3.6.2}$$

$$Q_{gyre}(\theta) = \rho_0\ C_p \overline{\int_{-H}^{\eta} \int_{0}^{\Lambda(\theta)} v'(\lambda,\theta,z,t) T'(\lambda,\theta,z,t)\ a\cos\theta\ d\lambda\ dz} \quad , \tag{3.6.3}$$

where ρ_0 is an ocean water reference density, C_p is its heat capacity, a is the planetary radius, v is its northward velocity, T is the potential temperature, H is the depth of the basin, η is the free surface, L is the width of the basin, spanning from 0 to $\Lambda(\theta)$. The overbar denotes the time average. Square brackets in Equation 3.6.2 indicate the zonal average over the width of the basin, such that

$$[v(\lambda,\theta,z,t)] = \frac{1}{L(\theta)} \int_{0}^{\Lambda(\theta)} v(\lambda,\theta,z,t)\ a\cos\theta\ d\lambda \quad ,$$

$$[T(\lambda,\theta,z,t)] = \frac{1}{L(\theta)} \int_{0}^{\Lambda(\theta)} T(\lambda,\theta,z,t)\ a\cos\theta\ d\lambda \quad ,$$

while deviations from the zonal mean are expressed in Equation 3.6.3 as

$$v'(\lambda,\theta,z,t) = v(\lambda,\theta,z,t) - [v(\lambda,\theta,z,t)] \quad ,$$

$$T'(\lambda,\theta,z,t) = T(\lambda,\theta,z,t) - [T(\lambda,\theta,z,t)] \quad .$$

For low values of κ (0.5, 1.5 and 5.0×10^{-4} m^2s^{-1}), the low latitude gyre component of the OHT (right panel of Figure 3.6.6) though much weaker than the overturning component, carries heat equatorward rather than poleward. This behaviour arises from the upwelling of cold deep water at low latitudes, leading to relatively cooler temperatures in those regions (Figure 3.6.3a, left panels of Figures 3.4.1 and 3.6.1). Such equatorward transport is in agreement with previous findings for the ridgeworld scenario [Smith et al., 2006; Enderton & Marshall, 2009]. At mid and high latitudes, all κ scenarios feature poleward gyre heat transport.

A schematic representation of the mechanisms governing the partitioning of ocean advective heat transport between AQMOC and gyre components is provided in Figure 3.6.7. As κ increases, the enhanced vertical mixing progressively reduces the temperature contrast between the upper and lower ocean layers, ultimately eroding

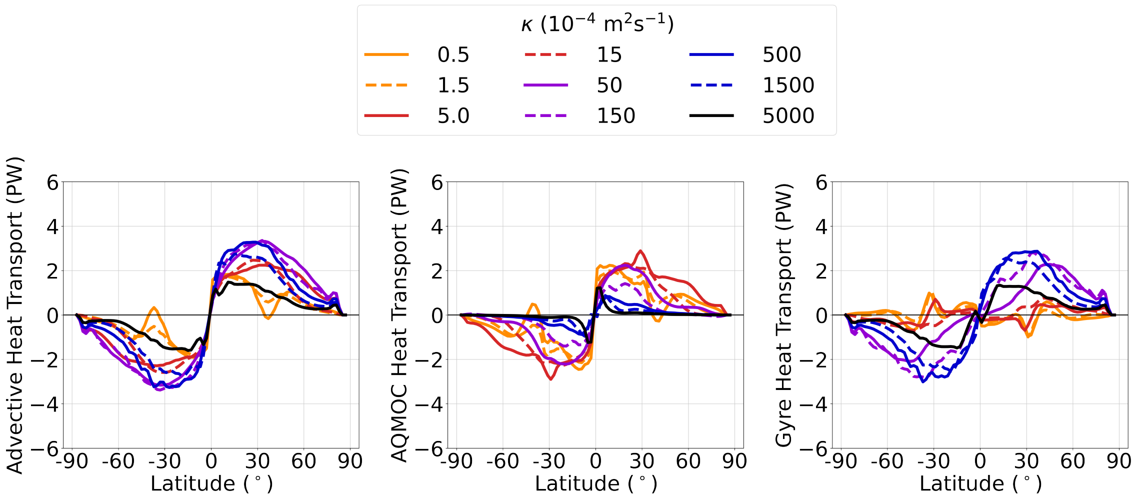

Figure 3.6.6: Total (left), AQMOC (centre) and gyre (right) advective heat transport as a function of latitude and κ. Quantities are averaged over the last 100 years for each simulation.

vertical stratification. Under these conditions, the overturning circulation loses efficiency because the vertical temperature gradient is diminished, whereas the horizontal gradient persists. As a consequence, the gyre circulation assumes a more prominent role in the redistribution of heat, and its relative contribution to the total advective heat transport increases with κ.

3.6.3 Decrease in instellation

The temporal evolution of the mean sea surface temperature and the latitude reached by sea ice under reduced instellation, corresponding to the values listed in Table 3.4.1, is presented in Figure 3.6.8. In general, the time series shown in the right column of Figure 3.6.8 reveal a common feature across scenarios characterised by different values of $S_\star$: there appears to be a critical ice-line latitude, around 35°, beyond which the simulated planet undergoes a rapid transition into a globally glaciated state. Scenarios with more efficient heat transport exhibit a comparatively slower progression toward this threshold, with the ice edge advancing equatorward more gradually than in cases with κ values associated with less efficient transport. The sharp transition is evident in the cases with $\kappa = 0.5$ and 5.0×10^{-4} m^{2}s^{-1} for $S_\star = 0.85\,S_\odot$, as well as in the cases with $\kappa = 0.5$, 5.0, 50, and 5000×10^{-4} m^{2}s^{-1} for $S_\star = 0.80\,S_\odot$. In these simulations, the ice-latitude time series curves exhibit a distinct change in curvature - from concave upward to concave downward - which marks the onset of a sharp transition to a snowball state. By contrast, the case with $\kappa = 0.5 \times 10^{-4}$ m^{2}s^{-1} at $S_\star = 0.90\,S_\odot$, in which the ice advances to 39°N and then stabilizes, is spared from global glaciation.

This behaviour is consistent with previous studies that identified a critical ice-line latitude

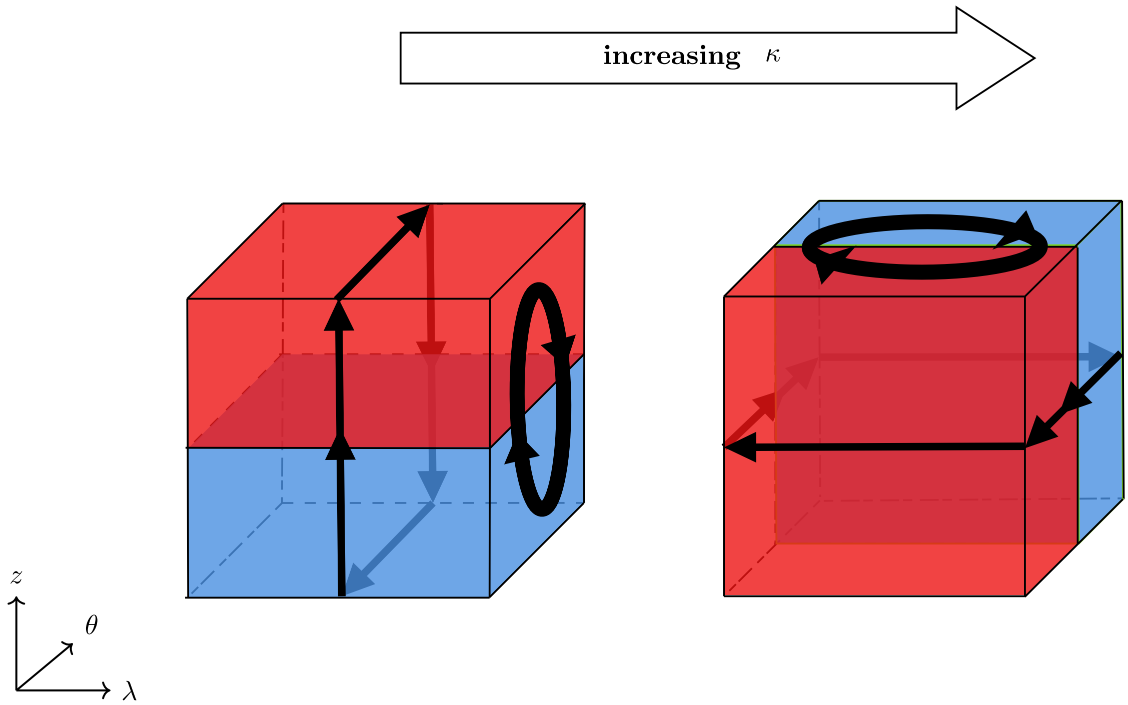

Figure 3.6.7: At low values of κ vertical stratification - depicted by the different colours of vertically stacked ocean portions - drives strong overturning circulation. At high values of κ vertical stratification is eroded, and horizontal gradients - depicted by the different colours of horizontally stacked ocean portions - results in dominating gyre heat transport.

beyond which the ice-albedo feedback dominates, driving the climate system into a sudden transition toward global glaciation. Both EBMs and GCMs can reproduce multiple stable climate states for terrestrial exoplanets, including configurations with large polar ice caps extending into mid-latitudes around 50° [Ferreira et al., 2011; Kilic et al., 2018], as further discussed in Section 3.7.1. Once the ice edge advances equatorward into lower latitudes, however, the strong positive ice-albedo feedback triggers sharp transitions to snowball states.

For ancient Earth, climate models consistently show that once the ice line advances to latitudes of approximately 30°-40°, the system crosses a critical equilibrium threshold and nonlinear feedbacks drive a system collapse into global glaciation. When approximately half of Earth's surface becomes ice covered, the positive ice-albedo feedback dominates: surface temperatures plummet and pack ice quickly engulfs the tropical oceans [Hyde et al., 2000; Baum & Crowley, 2001]. Neoproterozoic climate studies corroborate this picture by consistently identifying the ice-line latitude as the critical tipping point [Caldeira & Kasting, 1992; Hoffman & Schrag, 2002], while more recent work highlights the sensitivity of Snowball Earth inceptions to continental configuration, orbital geometry, and volcanic forcing; nevertheless, across scenarios the critical ice-line latitude of 30°-40° emerges as a robust threshold [Eberhard et al., 2023].

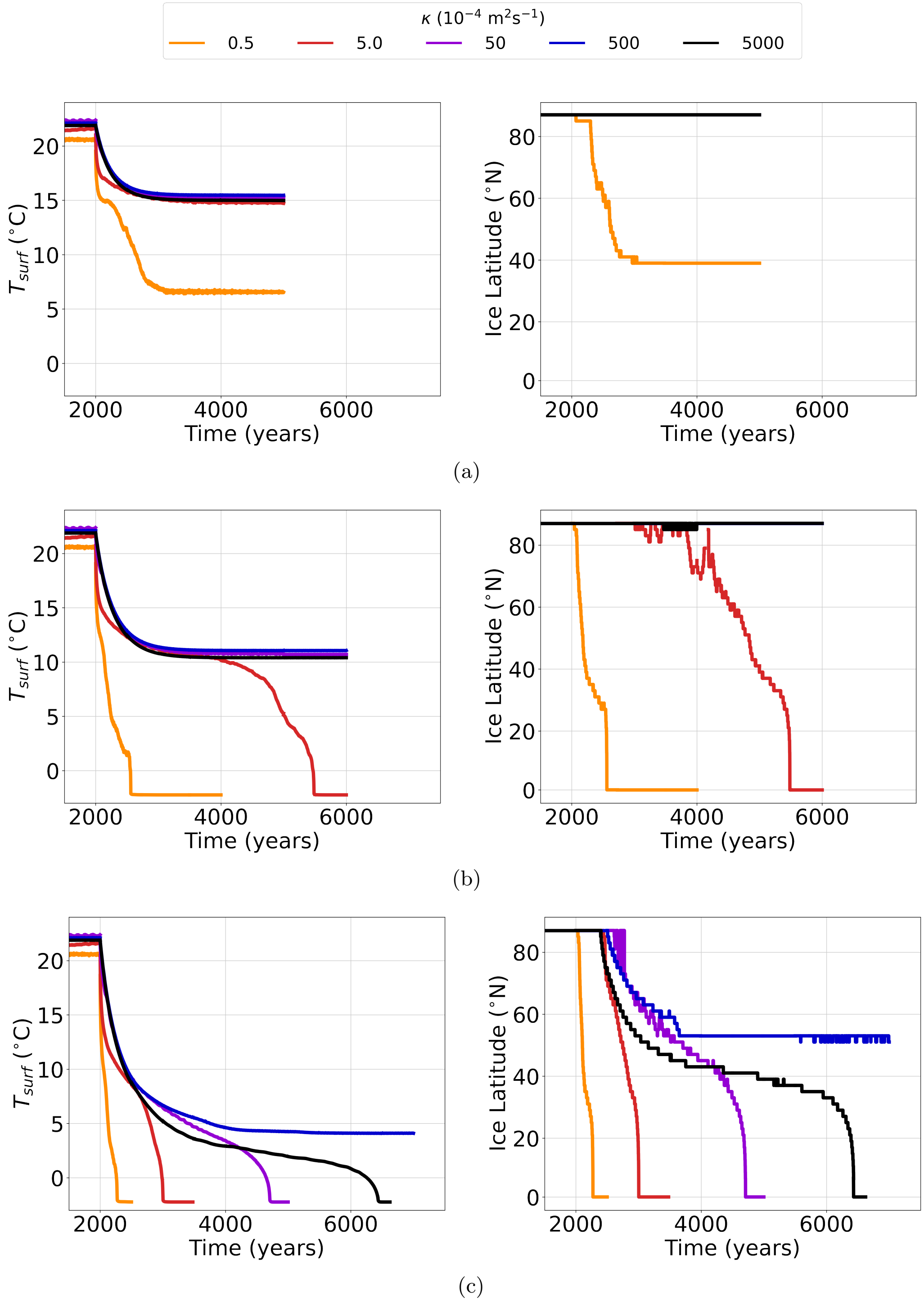

Figure 3.6.8: Mean annual sea surface temperature (left panels) and latitude reached by sea ice (right panels) corresponding to different values of instellation and κ. Reduced instellation values: 0.90 $S_\odot$ (a), 0.85 $S_\odot$ (b), 0.80 $S_\odot$ (c).

Overall, this is consistent with the behaviour illustrated in Figure 3.6.8. Variations in the precise value of the critical ice-line latitude reported by different studies can largely be attributed to differences in the adopted surface ice albedo, the treatment of meridional heat transport, and the underlying continental configuration. Despite these model-dependent sensitivities, the onset of global glaciation is governed primarily by the latitude of the ice edge, with collapse triggered once a critical threshold is crossed.

3.7 Further Investigation

3.7.1 No evidence of climate bistability under different ocean initial temperatures

Snowball Earth events are a series of periods during the Neoproterozoic (ca. 1000 - 541 million years ago) when Earth was nearly or entirely ice-covered, with ice sheets extending to low latitudes for millions of years. Habitability was severely constrained, with photosynthetic life restricted to refugia such as hydrothermal vents, subglacial meltwater pools, or equatorial ice margins in the case of the alternative *slushball Earth* hypothesis, which posits thin equatorial ice-free zones. These global glaciations profoundly influenced evolution, with their termination coinciding with rising atmospheric oxygen and the diversification of multicellular life, potentially fuelling the Cambrian explosion. Selective pressures during glaciations favoured larger sizes in motile heterotrophs, conferring an evolutionary advantage to multicellular eukaryotes, such that transient Snowball Earth conditions may have been a prerequisite for the emergence of metazoans with elevated energetic demands [Ward & Brownlee, 2000; Crockett et al., 2024].

Transitions into and out of snowball states likely reflected bifurcations driven by runaway ice-albedo feedbacks, for which proposed triggers include rapid reductions in solar input from higher aerosols concentrations due to volcanic and impact events [Arnscheidt & Rothman, 2020; Fu et al., 2024], enhanced continental weathering and magmatism accelerating CO_2 drawdown [Macdonald & Swanson-Hysell, 2023], oxygenic photosynthesis collapsing the methane greenhouse [Kopp et al., 2005], and historically low volcanic CO_2 emissions [Dutkiewicz et al., 2024]. Beyond nearly or completely glaciated states, the geological record reveals ice-free conditions, notably in the Late Cretaceous (100.5 - 66 Ma), when volcanic activity elevated atmospheric CO_2 to $\sim$1000 ppm, driving a strong greenhouse effect [Zachos et al., 2001; MacLeod et al., 2013]. Today, Earth's climate state is relatively moderate, characterised by persistent ice caps at both poles.

Such evidence of multiple equilibria under identical values of external forcing (i.e. solar radiation) is understood within the framework of climate bistability for Earth's climate. Numerical climate models capture this multiplicity, with the system settling on one specific equilibrium state determined by initial conditions and subject to transitions driven by external perturbations or internal variability. In the case of exoplanets, both EBMs and

GCMs of varying complexity can reveal three climate states - a warm de-glaciated climate, a moderate climate with stable ice caps, and a fully glaciated snowball - arising from nonlinear feedbacks [Rose & Marshall, 2009; Ferreira et al., 2011; Leconte et al., 2013; Linsenmeier et al., 2015; Kilic et al., 2017; Murante et al., 2020].

Beyond the ice-albedo feedback, numerous processes influence climate stability and bistability, with stabilizing (negative) feedbacks dampening perturbations and promoting resilience, whereas destabilizing (positive) feedbacks amplifying disturbances, therefore often producing multiple equilibria [Ghil & Lucarini, 2020]. Vegetation feedbacks with both surface albedo and hydrology cycle can generate bifurcations on both a regional and a global scale, potentially generating hysteresis between hot, arid states and cooler, vegetated regimes [Charney, 1975; D'Andrea et al., 2006; Janssen et al., 2008; Bathiany et al., 2012; Aleina et al., 2013]. Atmospheric circulation regime bifurcations have been extensively studied across contexts ranging from Earth to terrestrial exoplanets and hot Jupiters, revealing strong sensitivity to model setup and initial conditions [Edson et al., 2011; Arnold et al., 2012; Showman et al., 2015; Noda et al., 2017; Haqq-Misra et al., 2018; Sergeev et al., 2022]. Similarly, the oceanic meridional overturning circulation exhibits bistability, with a *halothermal* regime that may have operated in past geological times, when equatorial deep-water formation produced an overturning circulation opposite in sign to the *thermohaline* regime prevailing today [Stommel, 1961; Broecker et al., 1985; Rahmstorf et al., 2005; Hawkins et al., 2011].

As discussed in Section 3.4.3, multiple equilibrium climate states are identified for the same level of instellation but different values of the ocean vertical diffusion coefficient κ, yielding fully glaciated, partially glaciated, or ice-free conditions. Climate sensitivity to initial conditions is further examined using the setup described in Section 3.3, with $\kappa = 0.5$, 5.0, and 50×10^{-4} m^2 s^{-1}. Initial conditions correspond to distinct isothermal latitudinal ocean temperature profiles: a warm start (uniform 10°C) and a cold start (uniform 1°C), the latter being the configuration adopted in Di Paolo et al. [2025]. In both cases, the ocean was ice-free at the beginning of the simulations.

Quasi-steady states of these simulations are reached after 2000 years, when the net heat flux into the ocean is near-zero (with a maximum variation of $\pm$ 0.9 Wm^{-2} for $\kappa = 0.5 \times 10^{-4}$ m^2 s^{-1} in the warm start case), indicating equilibrium between incoming and outgoing energy within a reasonable range (Figure 3.7.1). The persistent oscillatory behaviour of the annual mean ocean heat flux time series in the high-diffusivity simulations is linked to self-sustained multicentennial GMOC oscillations. Enhanced vertical diffusivity weakens stratification and accelerates vertical adjustment, increasing the sensitivity of the overturning to density anomalies and enabling an advective feedback that produces sustained variability [Li & Yang, 2022]. These oscillations manifest as alternating phases in which the overturning strengthens first at low latitudes and subsequently at high latitudes, leading to corresponding periods of reduced and then

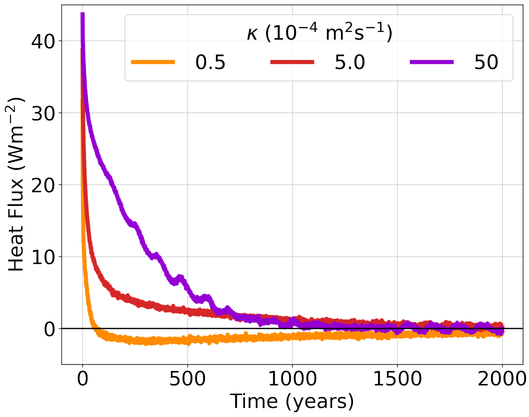

(a)

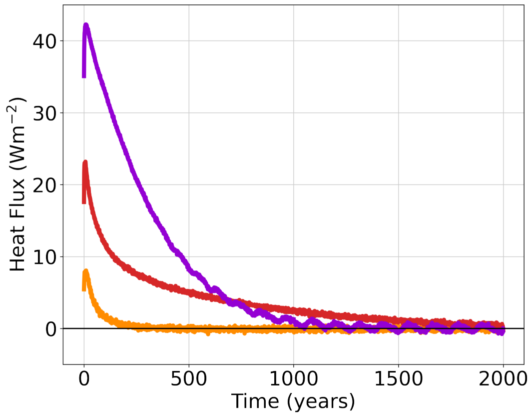

(b)

Figure 3.7.1: Time series of the annual mean heat flux into the ocean for different values of κ: (a) warm start, (b) cold start.

elevated high-latitude temperatures. The climatic impact of this mode is modest at the global scale: the maximum variation in globally averaged surface temperature is approximately 0.15°C. The largest temperature variability occurs at high latitudes, where the amplitude reaches 2.06°C, whereas variability in the equatorial band remains comparatively small, with a maximum of 0.33°C.

The volume-averaged ocean temperature shows only marginal, slow variation at the end of the simulations, remaining comparable between warm and cold start cases. For $\kappa = 5.0$ and 50×10^{-4} m^2 s^{-1}, the cold start exhibits a warming trend at the end of the runs, whereas for $\kappa = 0.5 \times 10^{-4}$ m^2 s^{-1} the warm start shows a cooling trend (Figure 3.7.2). If given the time to further evolve, it is reasonable to assume that both cold and warm start simulations would reach nearly identical volume-averaged temperatures.

The overturning circulation (Figure 3.7.3) exhibits a broadly similar structure in both cold and warm start cases, with enhanced intensity at higher latitudes for increasing values of κ in the cold start with respect to the warm start. This trend is reflected in Figure 3.7.4b, which highlights the difference in ocean meridional heat transport between cold and warm starts. Heat transport is consistently larger in the cold start case, particularly at high latitudes, and the contrast grows with increasing κ. Such differences can be attributed to larger meridional temperature gradients for the cold start cases - still warming at the end of the runs - as opposed to their warm start counterparts. Cold start scenarios yield marginally colder climates overall, with lower average temperatures both at the surface (Figure 3.7.5) and at depth (Figure 3.7.3), reflecting the system's slow adjustment from the initial conditions. An exception occurs at high latitudes ($\gtrsim 60°$), where for large κ values the cold start produces slightly higher temperatures than the warm start, due to the overturning cell extending further poleward.

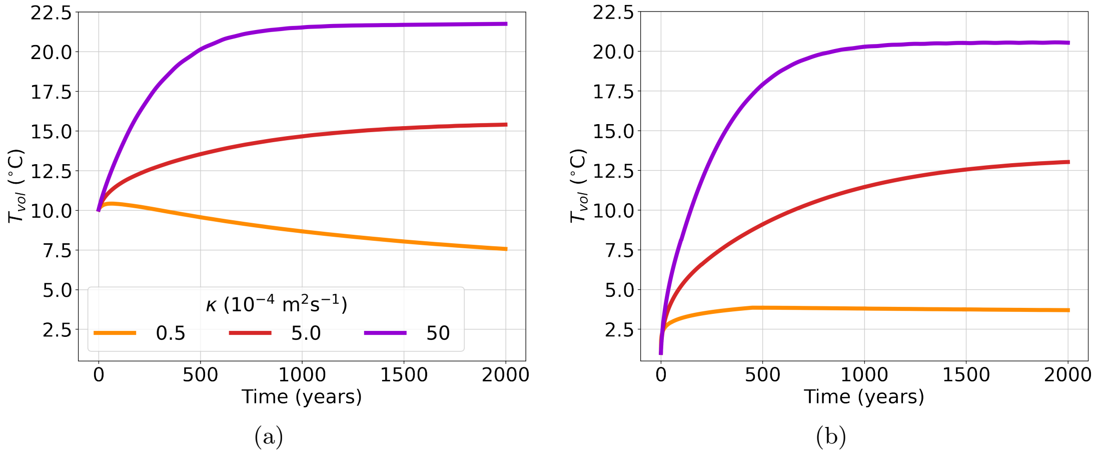

Figure 3.7.2: Time series of the volume-averaged annual mean ocean temperature for different values of κ: (a) warm start, (b) cold start.

Overall, no AQMOC bistability is found with respect to initial ocean temperature conditions. The meridional overturning circulation shows no distinct regimes, and heat is consistently transported poleward. It is reasonable to expect that differences in the volume-averaged temperature and in the strength of the AQMOC between cold and warm start runs, although present here, would diminish if the simulations were allowed to evolve beyond 2000 years; however, confirming this may require tens to hundreds of thousands of years of integration. All simulations begin without ice and with isothermal latitudinal ocean profiles at temperatures above the freezing point of seawater. As the AQMOC transports heat poleward, ice formation does not occur, thereby preventing activation of the ice-albedo feedback, a potential source of bistability. Consequently, the quasi-steady state solutions obtained from different initial ocean temperatures lead to comparable climate conditions, indicating that the scenarios investigated in Di Paolo et al. [2025] are independent of initial temperature conditions.

3.7.2 Alternative land configurations

When modelling exoplanetary climates, a critical assumption concerns the configuration of continental land masses. The distribution and extent of land relative to oceans exerts a fundamental influence on climate regulation, operating through mechanisms that include the modification of the planetary energy balance via surface albedo, the regulation of the carbon cycle, and the shaping of ocean circulation governing the transport of heat and nutrients [Guimond et al., 2026].

The number of known exoplanets continues to grow along with advances in observational techniques and instrumentation, yet probing the surface characteristics of Earth-sized worlds remains beyond current capabilities, as such worlds are typically too faint and

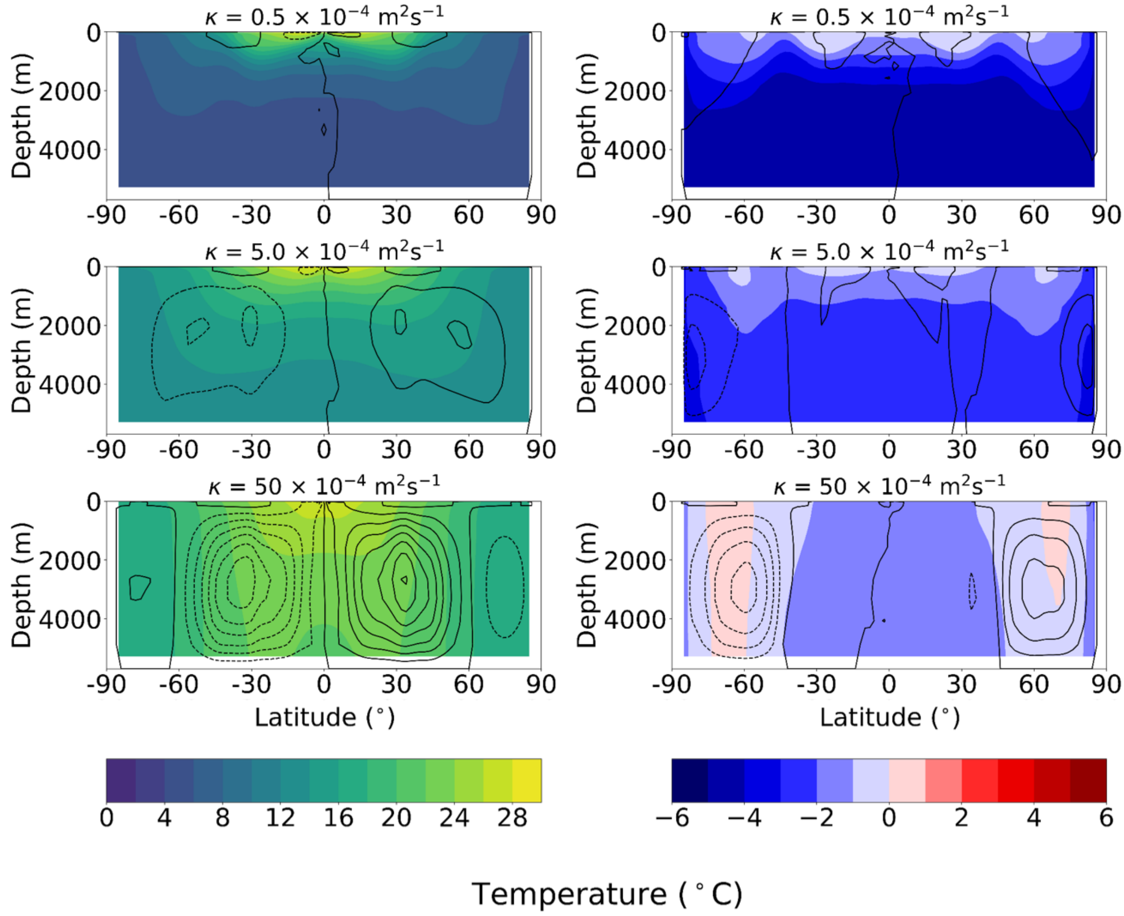

Figure 3.7.3: Shading shows zonally averaged values of ocean temperature, black contours show the meridional overturning streamfunction. Contour interval is 50 Sv. Clockwise circulation is depicted by solid lines, anticlockwise circulation is depicted by dashed lines. Warm start simulations (left panel) and difference between cold and warm start simulations (right panel). Quantities are averaged over the last simulated 100 years for each case. The analogous plot for the cold start simulations is depicted in Figure 3.4.1.

distant to be spatially resolved. Future developments, however, may enable the detection of surface features through a range of approaches. For instance, variations in transit depth caused by changes in the observed planetary silhouette due to surface "bumpiness" could provide constraints on exotopography [McTier & Kipping, 2018], although refraction effects introduce additional complexity [Macdonald & Cowan, 2019]. Another promising avenue involves reflected light-curve inversions: since dry land generally exhibits higher albedo than ocean surfaces, and terrestrial vegetation displays distinctive spectral and polarised reflectance, such techniques could reveal land-water ratios and even continental boundaries, provided that cloud variability and seasonal changes are properly accounted for [Kawahara & Fujii, 2011; Berdyugina & Kuhn, 2019; Kawahara & Masuda, 2020; Ramos & Pallé, 2021]. A fundamentally different strategy exploits the optical properties of the solar gravitational lens (SGL), which focus light from a source on the opposite side of the Sun onto a telescope positioned in the SGL focal region, well beyond the

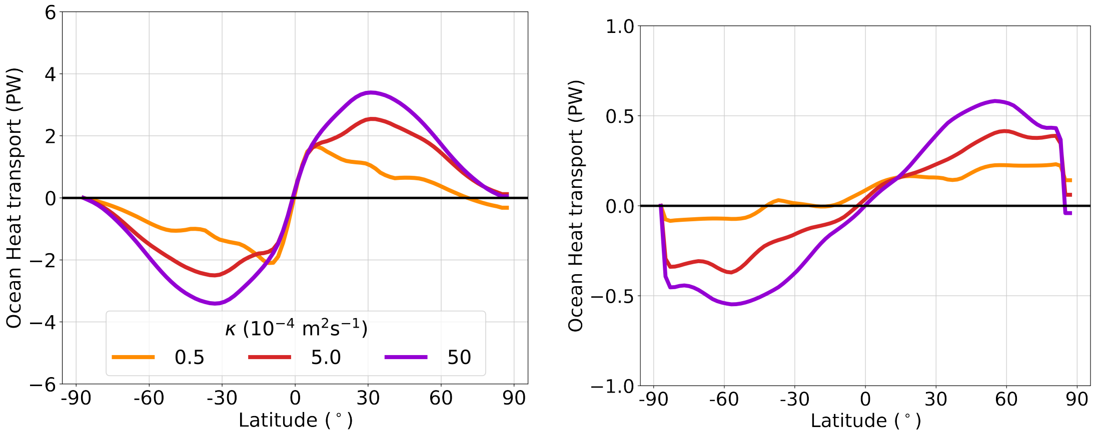

(a) (b)

Figure 3.7.4: Zonal mean of the ocean heat transport as a function of latitude and κ: (a) warm start simulations, (b) difference between cold and warm start simulations. Ocean heat transport for cold start simulations is depicted in Figure 3.6.5.

Solar System, and may potentially deliver unprecedented high-resolution imaging of rocky exoplanets [Turyshev & Toth, 2022; Turyshev & Toth, 2023].

In Section 3.3.3, we noted that two common continental configurations employed in exoclimate models are either a fully ocean-covered planet or one characterised by meridional barriers that may include gaps at different latitudes. While Di Paolo et al. [2025] examined a specific ridgeworld configuration consisting of a single pole-to-pole barrier, additional idealised setups consisting of vast ocean basins of uniform depth with only limited land masses are explored here. Such configurations serve as simplified representations of both ocean-covered planets and planets with varying land distributions but remain more generic than assuming specific continents (e.g. Earth's continents [Del Genio et al., 2019b]).

It is therefore important to clarify the terminology used to describe these configurations, as ambiguity persists in the literature. Following the definitions of Smith et al. [2006] and Marshall et al. [2007], the term "aquaplanet" refers to terrestrial planets with atmosphere and ocean similar to Earth's, but with highly schematized land distributions (including ridges) or no land at all (commonly termed "Waterworld" or "Aqua"). Meridional barrier configurations may include, for example, a single barrier extending from pole to pole (the "Ridgeworld" of Di Paolo et al. [2025]), a "Drake" configuration with one barrier interrupted by a gap in the Southern Hemisphere, a "DoubleDrake" with two such barriers joined at the North Pole, or an "Equatorial Passage" with a barrier interrupted in the tropics [Smith et al., 2004; Smith et al., 2006; Enderton & Marshall, 2009; Ferreira et al., 2010; van de Velde et al., 2021]. Beyond these configurations, typically used in studies of exoclimates with dynamical oceans, other continental configurations have been investigated, including polar and equatorial

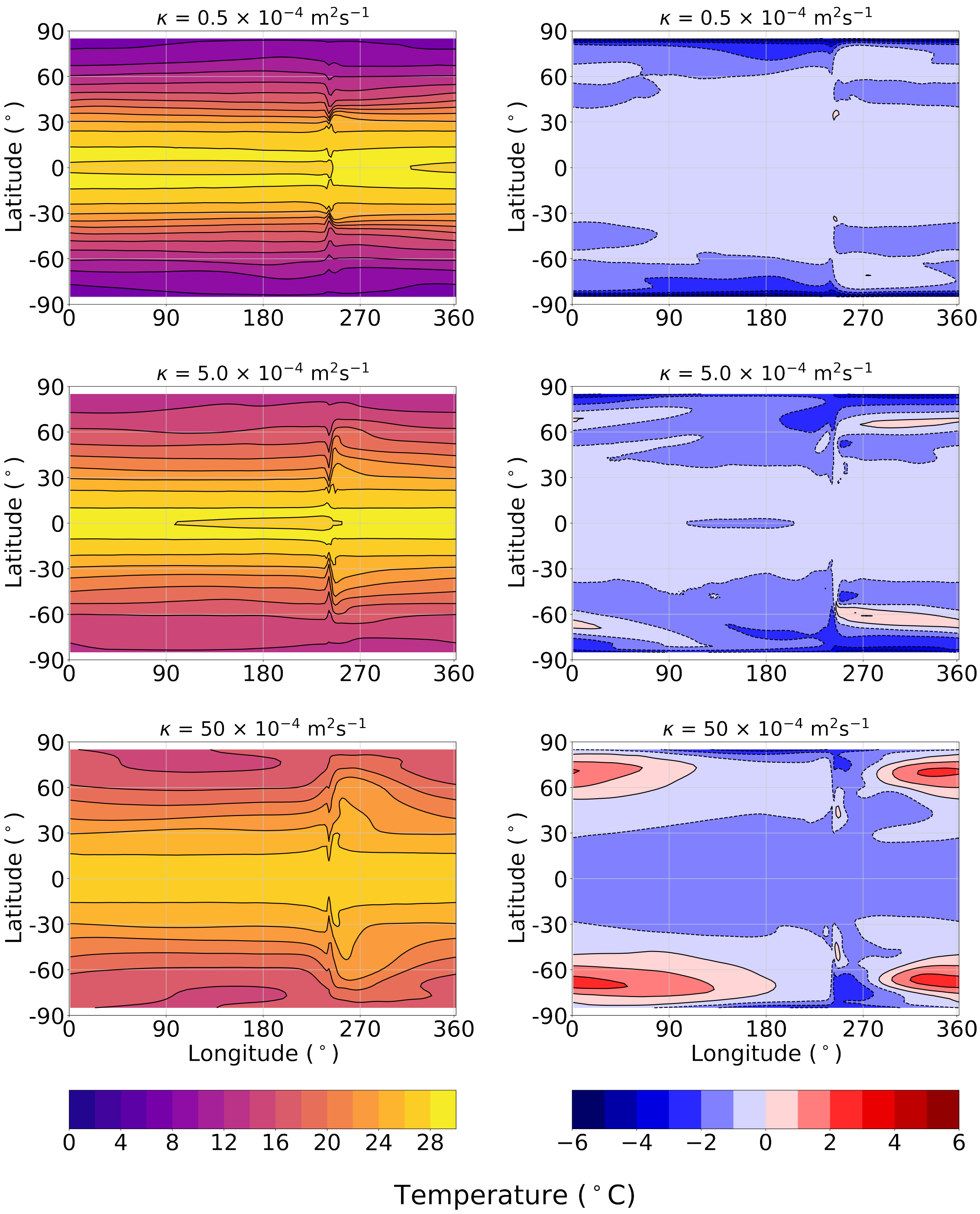

Figure 3.7.5: Surface temperature averaged over the last simulated 100 years for each case. Warm start simulations (left panel) and difference between cold and warm start simulations (right panel). Cold start simulations are depicted in Figure 3.6.4.

continents [Biasiotti et al., 2022], land-dominated planets [Glaser et al., 2025], and supercontinents [Way et al., 2021]. In addition, studies of synchronously rotating exoplanets have examined the effects of varying continental and barrier distributions relative to the substellar point [Lewis et al., 2018; Yang et al., 2019; Zhao et al., 2021; Macdonald et al., 2022].

The "Ridgeworld" configuration of Di Paolo et al. [2025], consisting of a single, 2°-wide submerged meridional barrier connecting two polar islands that extend to 86°N/S (Figure 3.7.6a), is compared to a "Waterworld" configuration (following the nomenclature of Smith et al. [2006]), in which the only land masses are the two polar islands (Figure 3.7.6b). The model setup is identical to that employed in Di Paolo et al. [2025], and the vertical diffusion coefficient is fixed at $\kappa = 5.0 \times 10^{-4}$ m^2s^{-1}. For reference in the longitude-latitude maps, the meridional ridge is placed at longitude 240°; however, its exact position is inconsequential, since under the Earth-like rotation scenario the planet is evenly illuminated across all longitudes.

In the Waterworld configuration (right panel of Figure 3.7.7a), the absence of barriers to zonal flow, together with the predominantly zonal surface wind field, generates strong currents that encircle the planet at all latitudes, forming a global wind-driven circulation constrained primarily by bottom friction. At low latitudes these currents are westward, with a maximum velocity of 2.29 ms^{-1} at the equator, whereas in Ridgeworld (left panel of Figure 3.7.7a) the equatorial westward current is significantly weaker, peaking at 0.66 ms^{-1}. At higher latitudes the circulation reverses direction, with eastward currents reaching 0.84 ms^{-1} at 40° N/S, compared to only 0.13 ms^{-1} at the same latitude in Ridgeworld.

Because of the absence of barriers to zonal flow in Waterworld, the longitudinal pressure gradient vanishes, and geostrophic balance consequently implies no time-mean meridional flow. The weak poleward transport (right panel of Figure 3.7.7b) observed near the equator, with a maximum velocity of only 0.07 ms^{-1} - approximately thirty times smaller than the zonal component - arises from Ekman currents driven by surface wind stress. By contrast, in the Ridgeworld configuration (left panel of Figure 3.7.7b), vigorous poleward boundary currents develop along the western margin of the basin,

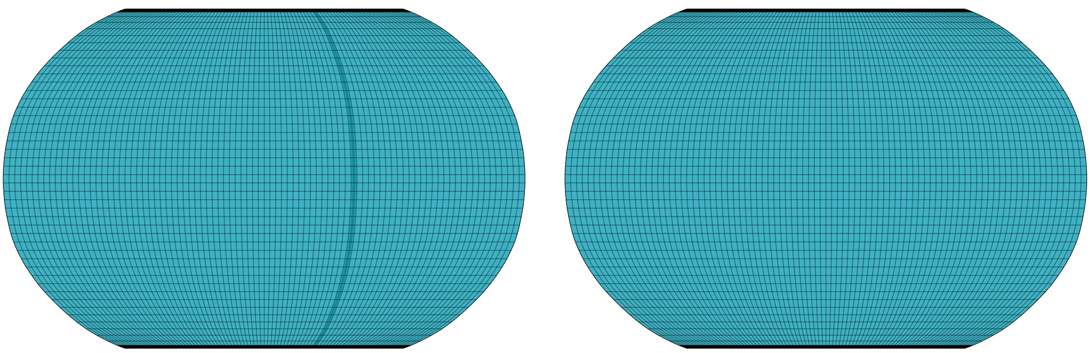

(a) (b)

Figure 3.7.6: Ridgeworld (a) and Waterworld (b) continental configurations. The polar islands (black) entend to 86°N/S to prevent numerical instabilities. The meridional barrier (shaded) starts at a depth of 145 m and reaches the bottom of the basin (5700 m), and is positioned at longitude 240°.

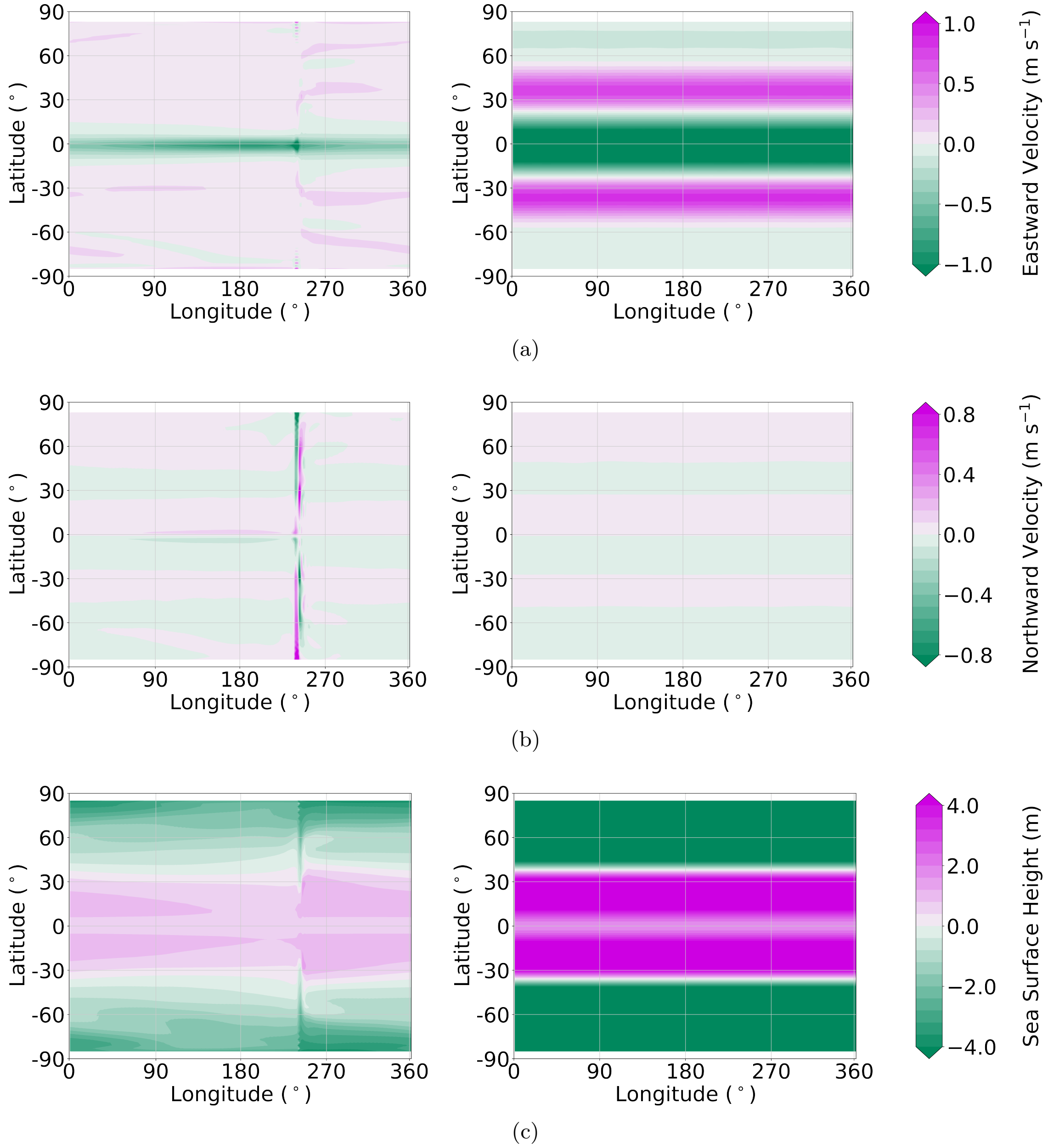

Figure 3.7.7: Eastward ocean surface velocity (a), northward ocean surface velocity (b) and sea surface height above the reference geoid (c) for Ridgeworld (left panel) and Waterworld (right panel) configurations. Quantities are averaged over the last 100 years for each case.

with average velocities of 0.43 ms^{-1}. The associated equatorward return flow on the eastern side of the ridge is an order of magnitude weaker, about 0.042 ms^{-1}, a ratio consistent with that found for subtropical gyres on Earth [Pedlosky, 1987].

In the Waterworld configuration, the sea surface height (right panel of Figure 3.7.7c) reflects the dominant zonal structure of the ocean currents. Sea surface height is elevated relative to the reference geoid within the convergence zone at low latitudes, reaching maxima of 6.57 m at 25° N/S where the zonal currents reverse direction. Poleward of

40° N/S, sea surface height falls below the reference geoid, with a minimum of -9.18 m at 60° N/S, coincident with another reversal of the zonal currents. In contrast, the Ridgeworld configuration (left panel of Figure 3.7.7c) exhibits clear low-latitude gyres in both hemispheres. Here, sea surface height is elevated by approximately 1 m east of the meridional barrier, accompanied by strong poleward-flowing geostrophic western boundary currents, with a pattern consistent with those observed in subtropical gyres on Earth [Fu & Chelton, 1984].

In the Waterworld configuration, surface winds drive Ekman transport that produces convergence in the subtropics and divergence at the equator and mid-latitudes, leading to downwelling and upwelling, respectively. This forcing supports two deep overturning cells of alternating circulation direction in each hemisphere, extending nearly to the ocean floor (left panel of Figure 3.7.8). The effect of the associated circulation is evident in the zonally averaged temperature field, with Ekman suction bringing cooler waters to the surface at the equator and mid-latitudes, and Ekman pumping subducting warm surface waters in the subtropics. Overall, the AQMOC is concentrated in the mid-latitudes and reaches its maximum strength just off the equator at the surface, with a transport of ~90 Sv. In the Ridgeworld configuration, the thermohaline meridional overturning circulation (case $\kappa = 5.0 \times 10^{-4}$ m^{2}s^{-1} in Figure 3.4.1, with streamfunction contours at 50 Sv intervals instead of 20 Sv) is dominated by a single, large cell in each hemisphere. This circulation is characterised by intense deep-water formation at the highest latitudes and compensating upwelling in the equatorial region. The AQMOC reaches a maximum transport of 140 Sv near 3000 m depth at high latitudes. Ridgeworld supports geostrophic meridional flow across the ocean, producing a hemispherically symmetric overturning pattern that encompasses the full meridional extent of each hemisphere. Warm, saline surface waters is advected poleward, cools and sinks at the poles, and returns equatorward at depth before upwelling back to the surface. In addition, a few weak, shallow cells appear in the upper ocean, likely wind-driven, but ultimately are negligible in terms of global AQMOC. The thermocline is significantly shallower with respect to the Waterworld configuration, with colder tropics and warmer mid- and high- latitudes both at depth (right panel of Figure 3.7.8) and at the surface (right panel of Figuree 3.7.9).

The similarity of the circulation and ocean heat transport in a Ridgeworld configuration to that of Earth, and its marked contrast with a Waterworld configuration, has been demonstrated in coupled AOGCM studies [Smith et al., 2006; Enderton & Marshall, 2009]. Consequently, Ridgeworld can be regarded as a general representation of a terrestrial aquaplanet whose ocean dynamics resemble those of Earth. Beyond the case of a single pole-to-pole meridional barrier, alternative meridional barrier configurations have also been investigated. A wider meridional ridge yields circulation qualitatively similar to Ridgeworld, but produces a stronger, hemispherically symmetric overturning

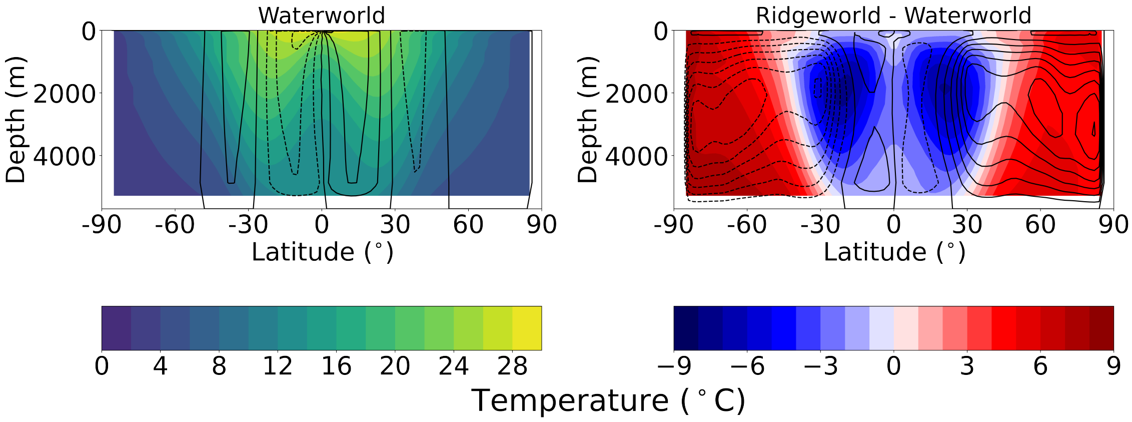

Figure 3.7.8: Left: shading shows zonally averaged values of temperature for the ocean, black contours show the meridional overturning streamfunction with 20 Sv contour interval. An analogous plot for the Ridgeworld configuration is shown in Figure 3.4.1. Right: difference between Ridgeworld and Waterworld configurations, with 20 Sv contour interval. Quantities are averaged over the last simulated 100 years for each case.

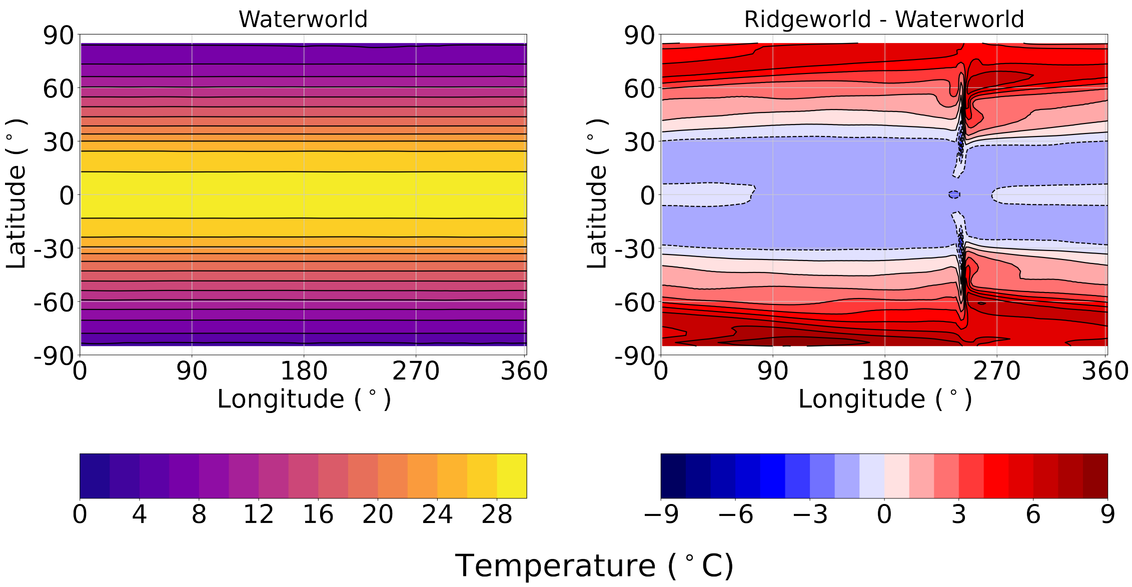

Figure 3.7.9: Left: sea surface temperature for the Waterworld configuration. An analogous plot for the Ridgeworld configuration is shown in Figure 3.6.4. Right: difference between Ridgeworld and Waterworld configurations. Quantities are averaged over the last simulated 100 years for each case.

circulation [Smith et al., 2004]. A Drake configuration produces hemispherically asymmetric circulation with Waterworld (Ridgeworld) features at gap (barrier) latitudes, enhanced deep-water formation in the north but reduced poleward heat transport in the south [Smith et al., 2006; Enderton & Marshall, 2009]. Configurations with multiple meridional barriers with circumpolar gaps, such as such as DoubleDrake, simulate multiple ocean basins of varying width [Marotzke & Willebrand, 1991; Nilsson et al., 2013]. An Equatorial Passage produces strong zonal currents across the gap and gyres at the western boundaries at mid- and high- latitudes. Circulation lacks cross-equatorial flow, with deep water forming at the poles and upwelling in the mid-latitudes within the same hemisphere, while deep overturning and the absence of equatorial gyres enhance heat transport at all latitudes [Enderton & Marshall, 2009].

We consider two alternative barrier configurations to assess whether the simulated circulation differs substantially from the Ridgeworld case. The first, termed "Splitridge" (Figure 3.7.10a), presents a gap in the meridional barrier between 30°S and 30° N. Two additional meridional barriers are positioned at the same latitudes of the gap, with a longitudinal offset of 120° relative to the original barrier in each direction. In this setup, the polar barriers and equatorial barriers do not overlap latitudinally. The second configuration, "Fourridges" (Figure 3.7.10b), presents four 45° meridional barriers. Two segments connect to the polar islands at longitude 240°, while the other two are shifted by 120° in each direction. One of these spans from the northern barrier to just south of the equator, and the other extends from the southern barrier to just north of the equator. In this case, the barriers exhibit slight overlaps of 2° between equatorial and polar barriers, and 4° between equatorial barriers.

Both configurations exhibit distinct circulation patterns within the three "basins" formed by the four meridional barriers. In Splitridge, circulation in each basin remains hemispherically symmetric, whereas in Fourridges asymmetries develop due to the uneven placement of the low-latitude barriers relative to the equator (Figure 3.7.10b). Despite these differences within the basins, the zonally integrated overturning circulation (Figure 3.7.11) is broadly symmetric about the equator in both configurations, as the opposing displacements of the low-latitude barriers in Fourridges compensate when averaged zonally. In both cases, the large-scale AQMOC consists of clockwise

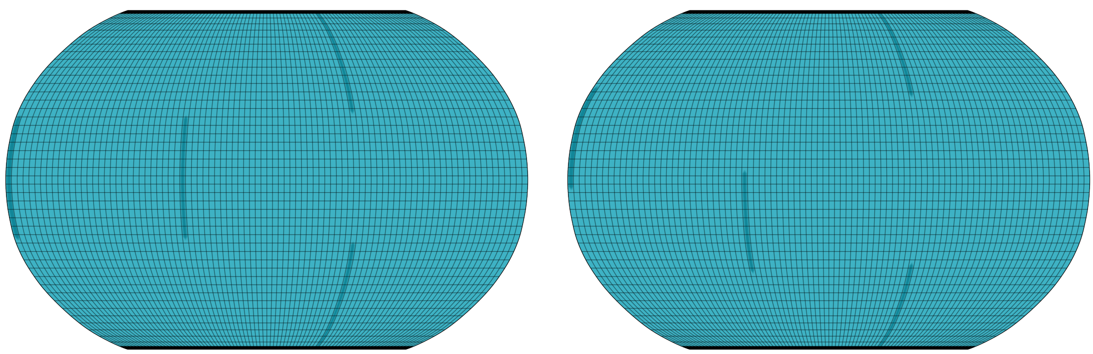

(a) (b)

Figure 3.7.10: Splitridge (a) and Fourridges (b) continental configurations. The polar islands (black) entend to 86°N/S to prevent numerical instabilities. The meridional barriers (shaded) start at a depth of 145 m and reaches the bottom of the basin (5700 m). All ridges are offset by 120°, with the barriers connected to the poles positioned at longitude 240°.

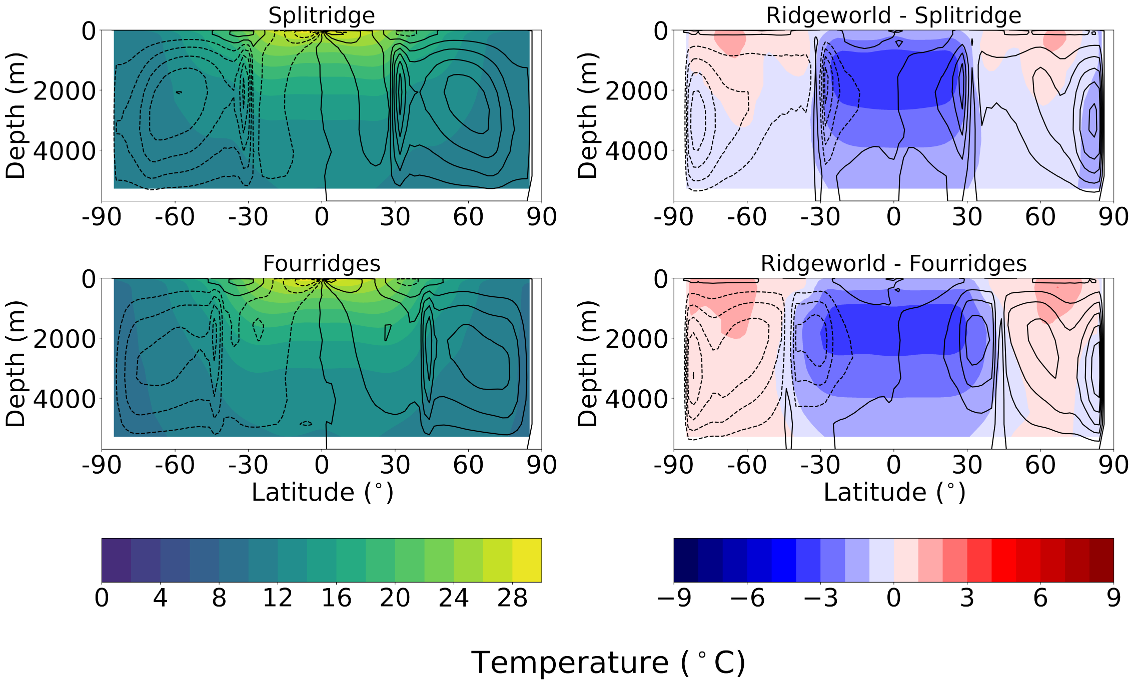

Figure 3.7.11: Left: shading shows zonally averaged values of temperature for the ocean, black contours show the meridional overturning streamfunction with 20 Sv contour interval. An analogous plot for the Ridgeworld configuration is shown in Figure 3.4.1. Right: difference between Ridgeworld and Splitridge/Fourridges configurations, with 20 Sv contour interval. Quantities are averaged over the last simulated 100 years for each case.

overturning in the northern hemisphere and anticlockwise overturning in the southern hemisphere, extending across the full meridional range, including high latitudes. Within the latitude band of the equatorial gap (30° N/S in Splitridge and 45° N/S in Fourridges), the overturning structure somewhat resembles the deep, more vertically oriented cells of Waterworld, albeit the circulation here is weaker. Unlike Waterworld, both configurations maintain overturning that reaches the poles, similar to Ridgeworld. The AQMOC attains maximum transports of ∼110 Sv in Splitridge and ∼100 Sv in Fourridges, in both cases near 2500 m depth and located at the edges of the equatorial gap. The location of these maxima, at depth and offset with respect to the equator, resemble Ridgeworld and contrast with Waterworld, where the strongest overturning occurs at the surface at the equator. In general, the circulation structure of both Splitridge and Fourridges resembles that of Ridgeworld, though with reduced strength overall.

In both Splitridge and Fourridges, the thermocline is substantially shallower than in Waterworld (Figure 3.7.11), closely resembling the structure in Ridgeworld. Within the latitude band of the equatorial gap, zonally averaged temperatures are warmer than in Ridgeworld at all depths. Surface temperatures are comparable to those of Waterworld

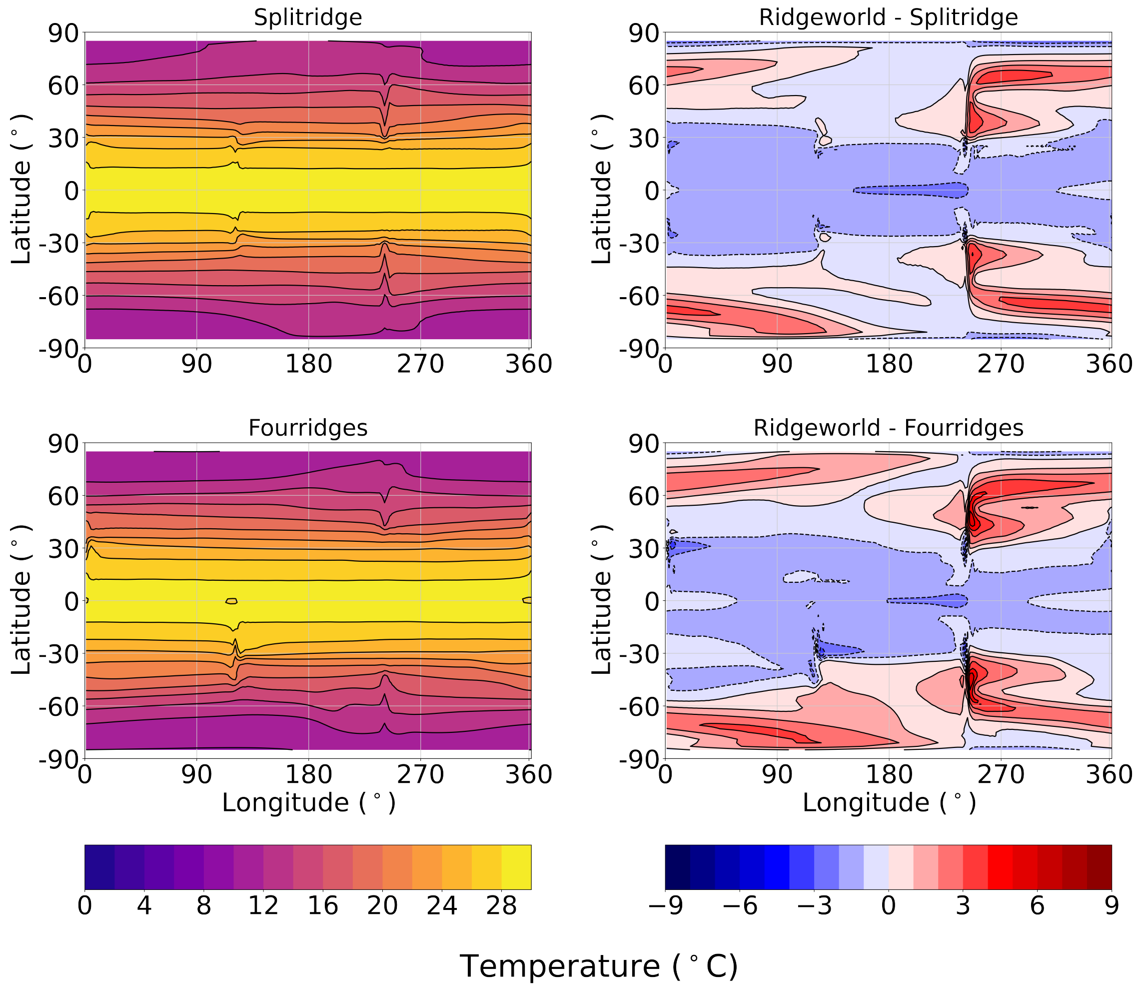

Figure 3.7.12: Left: sea surface temperature for the Splitridge and Fourridges configurations. An analogous plot for the Ridgeworld configuration is shown in Figure 3.6.4. Right: difference between Ridgeworld and Splitridge/Fourridges configurations. Quantities are averaged over the last simulated 100 years for each case.

(Figures 3.7.12 and 3.7.9), whereas subsurface waters remain considerably cooler than in Waterworld (Figure 3.7.11 and 3.7.8), and closer to the temperatures of Ridgeworld. Poleward of the gap, surface waters are colder than in Ridgeworld in both configurations, whereas temperatures at depth for Splitridge (Fourridges) are warmer (colder) than Ridgeworld (Figure 3.7.11). Overall, zonally averaged temperature anomalies relative to Ridgeworld are modest, especially when contrasted with the much larger deviations in Waterworld (Figure 3.7.8). Maximum differences reach 3.7°C in Splitridge and 3.5°C in Fourridges, compared with 7.9°C in Waterworld. At the surface (Figures 3.7.12), the largest departures from Ridgeworld occur just east of 240° longitude, where the Ridgeworld barrier lies, and near the latitudes of the equatorial gaps (30° N/S in Splitridge and 45° N/S in Fourridges), with peak anomalies of 4.1°C and 5.9°C, respectively. Anomalies in Waterworld compared to Ridgeworld (Figures 3.7.9) reach 8.9°C at high southern latitudes, due to the meridional overturning circulation in

Waterworld being confined to lower latitudes.

Zonally averaged quantities for all analysed continental configurations are shown in Figure 3.7.13. Ridgeworld exhibits the strongest ocean heat transport across all latitudes among the configurations, consistent with its more vigorous overturning circulation, whereas Waterworld shows the weakest transport. Splitridge and Fourridges lie between these two extremes, with stronger heat transport than Waterworld, particularly at mid and high latitudes, attained by overturning cells extending to the poles rather than remaining confined to low latitudes (Figure 3.7.13a).

Surface temperatures in Waterworld, Splitridge, and Fourridges are warmer and broadly comparable within the tropics relative to Ridgeworld, whereas at mid and high latitudes Ridgeworld, Splitridge, and Fourridges are similarly warmer than Waterworld (Figure 3.7.13b). High-latitude differences are substantially larger than tropical differences: Waterworld is markedly colder near the poles because its overturning circulation does not extend to high latitudes. This also produces hemispheric asymmetries in Waterworld, with the southern hemisphere colder than the northern hemisphere, a consequence of adopting Earth's orbital configuration in which the planet is at periapsis during northern winter/southern summer and at apoapsis during northern summer/southern winter. In all other configurations, the overturning circulation reaches the poles and largely suppresses such asymmetries. The surface meridional temperature gradient is therefore largest in Waterworld and smallest in Ridgeworld, with Splitridge and Fourridges exhibiting intermediate gradients due to their comparatively warm polar regions. As a result, zonal wind patterns are similar among Ridgeworld, Splitridge, and Fourridges. The global mean surface temperature is highest in Splitridge and Fourridges (approximately 22.0°C), slightly lower in Ridgeworld (21.6°C), and lowest in Waterworld (21.1°C).

Because of its overturning circulation structure, Waterworld shows the largest departures from Ridgeworld in both volume-averaged temperature and salinity (Figures 3.7.13c and 3.7.13d). In Waterworld, tropical waters are warmer and saltier than in the other configurations, accompanied by strong upwelling of cold, fresh water at the equator and a sharp decrease in both quantities poleward of the tropics. In contrast, Splitridge, Fourridges, and Ridgeworld exhibit significantly reduced meridional gradients, with cooler and fresher tropical waters, weaker equatorial upwelling, and warmer, saltier waters at mid and high latitudes. Relative to the Ridgeworld scenarios analysed in Di Paolo et al. [2025], Waterworld behaves more similarly to simulations with reduced values of κ, which are characterised by weaker ocean heat transport and consequently larger meridional temperature gradients, than to its counterpart with the same κ.

Overall, all land configurations that include a meridional barrier exhibit enhanced ocean heat transport at mid and high latitudes compared with configurations lacking such

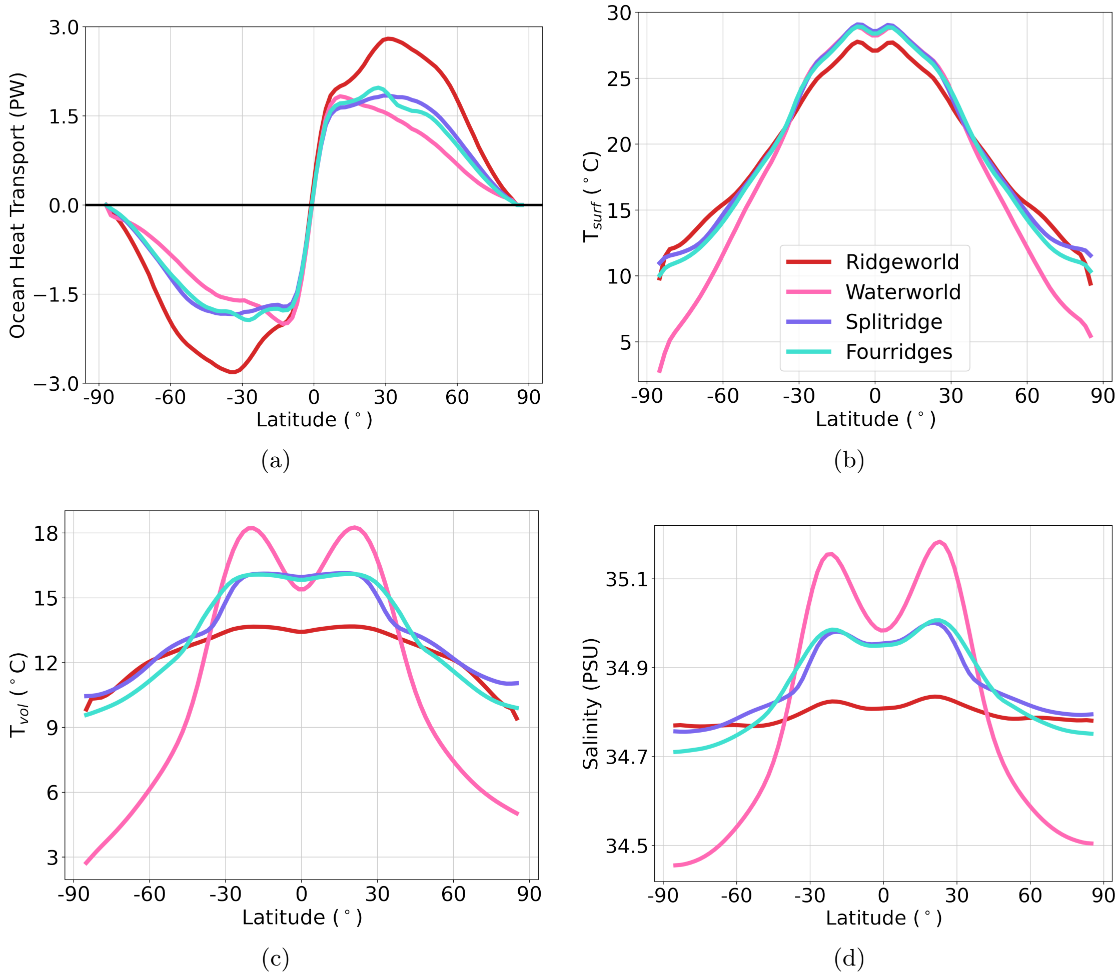

Figure 3.7.13: Latitudinal profiles of ocean heat transport (a), surface temperature (b), volume-averaged temperature (c), and volume-averaged salinity (d) for all analysed configurations. Quantities are averaged over the last 100 years for each case.

barriers. This result is demonstrated here across three distinct barrier geometries and is consistent with previous studies employing Drake, DoubleDrake, or Equatorial Passage configurations, even when using different models and parametrisations [Marotzke, 1997; Smith et al., 2006]. While Di Paolo et al. [2025] focused on Ridgeworld configurations, the substantially weaker mid- and high-latitude heat transport in Waterworld would hypothetically lead to more rapid glaciation under reduced instellation scenarios, and potentially amplify the contrast between low and high vertical diffusion cases. Notably, although the Waterworld configuration examined here does not form any sea-ice despite cold polar temperatures, other studies have shown that the vanishingly small ocean heat transport at high latitudes in such a configuration can generate polar ice caps, in stark contrast to a warmer resulting climate of a Ridgeworld configuration [Marotzke, 1997]. The circulation structure in all barrier configurations more closely resembles that of an Earth-like climate, with overturning cells extending into high latitudes, and differs fundamentally from that of an aquaplanet lacking meridional barriers. The strong similarities among barrier configurations, together with their pronounced contrast to Waterworld, support the use of Ridgeworld as a simple and generalised framework for studying terrestrial climates without prescribing Earth-specific continents.

3.8 Concluding remarks and motivation for Chapter 4

This chapter investigated how tidally driven ocean mixing shapes the climate states and potential habitability of terrestrial exoplanets. Using a coupled AOGCM, the analysis demonstrated that the climatic response to tidal mixing is nonlinear and nonmonotonic: moderately high values of ocean vertical diffusivity enhance poleward heat transport and reduce meridional temperature gradients, with the strongest response occurring for diffusivities approximately two orders of magnitude larger than Earth's. In contrast, both very low and excessively high diffusivities weaken the overturning circulation and yield sharper meridional temperature gradients. Further investigation confirmed the overall validity of these results across different initial conditions and across alternative continental configurations incorporating different meridional barriers.

The chapter therefore provides insight into how enhanced ocean vertical diffusivity, associated with a stronger tidal forcing, affects planetary climate and habitability. Strong tidal forcing can occur in scenarios in which the modelled planet resides in close orbits around a low-mass star, but it may also result from planets orbited by close and/or massive satellites. Intending to present a comparison of high diffusivity results and scenarios characterised by diffusivity of the same order of magnitude of $\kappa_\oplus$, this idealised study focused on varying a single parameter, the ocean vertical diffusion coefficient κ, within an otherwise multidimensional parameter space. Notably, the planetary rotation rate was fixed to be equal to that of Earth. This choice allows a more direct comparison with an Earth-like reference case.

For planets orbiting low-mass stars, a particularly relevant scenario for the search and characterisation of potentially habitable environments, several planetary properties are expected to differ from those examined here. Among these, the planetary rotation rate in such systems is likely affected through different mechanisms linked to the intense tidal torques exerted by the host star on the planetary body. One of these mechanisms is tidal locking, briefly discussed in Section 1.2.5, which can significantly alter the planetary rotation rate leading to different possible outcomes. Spin-orbit resonances occur when the planetary rotation period is locked into a simple integer ratio with the planetary orbital period. The most commonly studied case is synchronous rotation, a special case of spin-orbit resonances in which the same hemisphere of the planet permanently faces the star, producing fixed dayside and nightside regions and stationary stellar tides. Higher-order resonances, however, allow the tidal bulge raised by the host star to travel across the planetary body as the planet moves along its orbit, potentially leading to enhanced ocean vertical mixing. This latter scenario, generally underexplored relative to synchronous rotation, is the focus of Chapter 4.

4

Climate Patterns of Spin-Orbit Resonant Exoplanets Around Low-Mass Stars

---

This study was submitted to *The Astrophysical Journal* (manuscript #: AAS72428) in December 2025 under the same title by Maria Di Paolo, David P. Stevens and Manoj Joshi. The text in this chapter is unchanged compared with the article, except for the section "Supplementary material" (4.6) included at the end of the chapter, which provides additional commentary, extended discussion, and supplementary figures that were omitted from the article. The research presented in this chapter was carried out on the High-Performance Computing clusters supported by the Research and Specialist Computing Support service at the University of East Anglia. Simulations and initial analyses were performed on the UEA cluster ADA, while subsequent analyses were carried out on the UEA cluster HALI following the migration and decommissioning of ADA commenced in Summer 2025. M.D.P., D.S., and M.J. conceived the study. M.D.P. conducted the experiments. All authors contributed to the analysis and reviewed the paper manuscript. The FORTE 2.0 Blaker et al. [2021] code, compilation instructions and example run scripts, together with all necessary ancillary files, are accessible at `doi.org/10.5281/zenodo.4108373`. The data that support the findings of this study are accessible at `doi.org/10.5281/zenodo.17885048`.

4.1 Abstract

M dwarfs are the most promising candidates for finding habitable worlds through atmospheric characterisation. Planets in the habitable zone of low-mass stars experience intense tidal forcings and often become tidally locked. Despite the majority of research being centered on the climate dynamics of synchronously rotating planets in this scenario, synchronous rotation is not an inevitable outcome of tidal locking. Several different circumstances can result in an asynchronous rotation, and in some instances can lead to spin-orbit resonances (SORs). We explore the climates of two different spin-orbit resonant scenarios with a coupled atmosphere-ocean general circulation climate model. Given the crucial role played by the oceans in shaping planetary climate, we adopt two different ocean tidal forcing parameterizations for each SOR scenario. Each of these cases are simulated with both a dynamic ocean and a thermodynamic ocean. Our findings reveal striking differences between the analysed resonant case and the commonly studied synchronous rotation case. Periodic climate patterns are observed, with climatic features such as clouds and rainfall exhibiting a 60° longitudinal shift relative to the substellar point. The evolution of quantities such as thermal emission and reflected light during a stellar period is noteworthy from the observational point of view, showing appreciable differences compared to the synchronous rotation scenario.

4.2 Introduction

Planets orbiting M- and K- dwarf stars represent the best candidates for detailed characterisations of potentially habitable terrestrial exoplanetary atmospheres using next-generation observatories. Planets orbiting cool stars offer multiple observational benefits, stemming both from the high occurrence rate of these stars and their orbiting planets [Dressing & Charbonneau, 2013, 2015; Cloutier & Menou, 2020; Ment & Charbonneau, 2023] as well as from inherent observational advantages [Scalo et al., 2007; Charbonneau & Deming, 2007; Shields et al., 2016]. The interest in these systems has catalyzed the development of novel observational techniques and steered mission concepts designed for the forthcoming decade [Kasper et al., 2021; Quanz et al., 2022a; Harada et al., 2024; Zúñiga-Fernández et al., 2024; Angerhausen et al., 2024]. It is therefore imperative to prioritize the integration and application of climate modelling studies to effectively support the observational community in the characterisation of potentially habitable exoplanets.

Climate modelling studies of potentially habitable exoplanets have predominantly employed general circulation models (GCMs) with simplified ocean representations, such as slab oceans [Kopparapu et al., 2016, 2017; Boutle et al., 2017; Hammond & Komacek, 2024]. Thanks to their computational efficiency, these approaches have provided valuable insights into planetary habitability, atmospheric processes and surface characteristics through parameter sweeps [Kopparapu et al., 2017; Kilic et al., 2017; Nowajewski et al., 2018; Komacek & Abbot, 2019]. However, these studies inherently limit the accuracy of climate and habitability assessments, as they do not account for the complex interactions and feedbacks associated with fully dynamic oceans. The crucial role of ocean circulation, and therefore ocean heat transport, in stabilizing Earth's climate by mitigating geographic, seasonal, and diurnal temperature extremes is well studied [Trenberth & Caron, 2001; Winton, 2003; Herweijer et al., 2005]. Studies conducted over the last fifteen years substantiate that ocean dynamics constitute a significant contribution to climate studies across a variety of planetary contexts, encompassing Earth's paleoclimates [Yang et al., 2012a,b; Kienert et al., 2012; Ragon et al., 2024], climate simulations of planets orbiting in the early Solar System [Way & Del Genio, 2020; Schmidt et al., 2022], and exoclimes [Hu & Yang, 2014; Cullum et al., 2014; Kilic et al., 2018; Olson et al., 2020]. In general, although the assumption of a simplified ocean is certainly computationally convenient, the potential underestimation/misrepresentation of certain processes and feedbacks can lead to a failure to capture key climatic features, hence why fully coupled AOGCMs represent the most physically comprehensive tools for fully characterising terrestrial climate [Yang et al., 2013; Hu & Yang, 2014; Ferreira et al., 2014; Kilic et al., 2018; Yang et al., 2019; Di Paolo et al., 2025].

The interest in characterising habitable planets around cool stars is long-standing, but poses several challenges from both the observational and the theoretical point of view. The prospect of building accurate climate models is hindered by the fact that many characteristics of planets in this configuration are ultimately unknown, such as their spin state. Due to the low luminosity of cool dwarfs, the circumstellar habitable zone in such systems is located relatively close to the host star [Kasting et al., 1993; Kopparapu et al., 2013]. Consequently, potentially habitable planets orbiting in these systems experience strong tidal interactions, which can alter the planet's rotational angular momentum through a process known as tidal locking [Murray & Dermott, 1999]. While tidal locking and its possible outcomes have been studied since the 1960s in the context of Solar System planets and satellites [MacDonald, 1964; Goldreich, 1965; Goldreich & Peale, 1966a,b; Goldreich, 1966], tidal studies for exoplanets are challenging due to a combination of observational limitations - such as sparse constraints on the orbital architecture of the system and the presence of companions - and uncertainties in planetary properties - such as atmospheric structure, internal and rheological variables, tidal deformation and dissipation parameters.

Possible outcomes of such tidal evolution in this scenario seem to be manifold, ranging from spin-orbit resonances (SORs) to librations of different amplitude and even chaotic behaviour [Dobrovolskis, 2007; Leconte et al., 2015; Vinson & Hansen, 2017; Barnes, 2017;

Renaud et al., 2021; Chen et al., 2023; Valente et al., 2024; Yuan et al., 2025]. Furthermore, the tidal response of a free-surface ocean differs markedly from that of a solid body, and accounting for oceanic tides - which exhibit strong frequency-resonant behaviour - in addition to solid-body tides can stabilise asynchronous equilibrium rotation states [Auclair-Desrotour et al., 2019]. The most commonly studied scenario is a special case of tidal locking: the 1:1 SOR, or synchronous rotation, where the periods for the planet to complete one rotation on its spin axis and one orbit around the host star are identical, giving a permanent dayside and nightside. Atmospheric heat transport can prevent nightside volatile trapping for reasonable values of surface pressure [Joshi et al., 1997], while ocean heat transport can extend an "eyeball" state, with a pool of open water centered on the substellar point [Pierrehumbert, 2011], into a "lobster" [Hu & Yang, 2014]. Several studies have analysed different aspects of climates in this scenario, focusing mainly on distinct regimes of atmospheric circulation depending on the planetary rotation period, atmospheric composition, surface pressure, incident stellar flux, surface gravity, planetary radius, and cloud particle size (e.g., Kopparapu et al. [2017]; Haqq-Misra et al. [2018]; Komacek & Abbot [2019]).

Only a few studies have focused on higher order resonances, among which the 3:2 SOR is the lowest order non-synchronous resonance and the most likely to occur for low values of orbital eccentricity [Correia & Laskar, 2009]. In this case, the planet rotates three times on its spin axis for every two orbits it completes around its host star, meaning that the substellar point shifts by 180° in longitude for every completed orbit (see Figure 4.2.1).

Climate simulations of GJ 667Cc for an orbit with eccentricity 0.4 and several SORs, assuming a slab ocean and thermodynamic sea ice, found two distinct patterns of the mean state climate: an "eyeball" exoplanet with a substellar warm region (1:1, 2:1 SORs) and a "waterbelt" exoplanet with zonally uniform temperature decreasing with latitude (3:2, 5:2 SORs) [Wang et al., 2014]. Thermal phase curves can be used to distinguish between these two climate patterns, with the former presenting significantly stronger variations than the latter during an orbital period. However, Dobrovolskis [2015] later proved that they used incorrect spatial insolation functions for the 3:2 and 5:2 resonances, and that for an eccentric orbit these SORs would result in a "double-eyeball" pattern rather a "waterbelt" exoplanet.

The climate of Proxima b has been the subject of several investigations that compare the 1:1 and 3:2 scenarios in the case of circular and/or eccentric orbits with either a static ocean [Turbet et al., 2016; Boutle et al., 2017] or a shallow dynamic ocean [Del Genio et al., 2019a]. The results are generally similar, with the 3:2 SOR climates exhibiting large meridional temperature gradients, with an equatorial "waterbelt" configuration that can transition to a "double-eyeball" configuration with increasing eccentricity. These results are highly sensitive to the choice of parameters such as the instellation and the chosen albedo, which ultimately determine the presence of open-water regions as opposed to a "slushball"

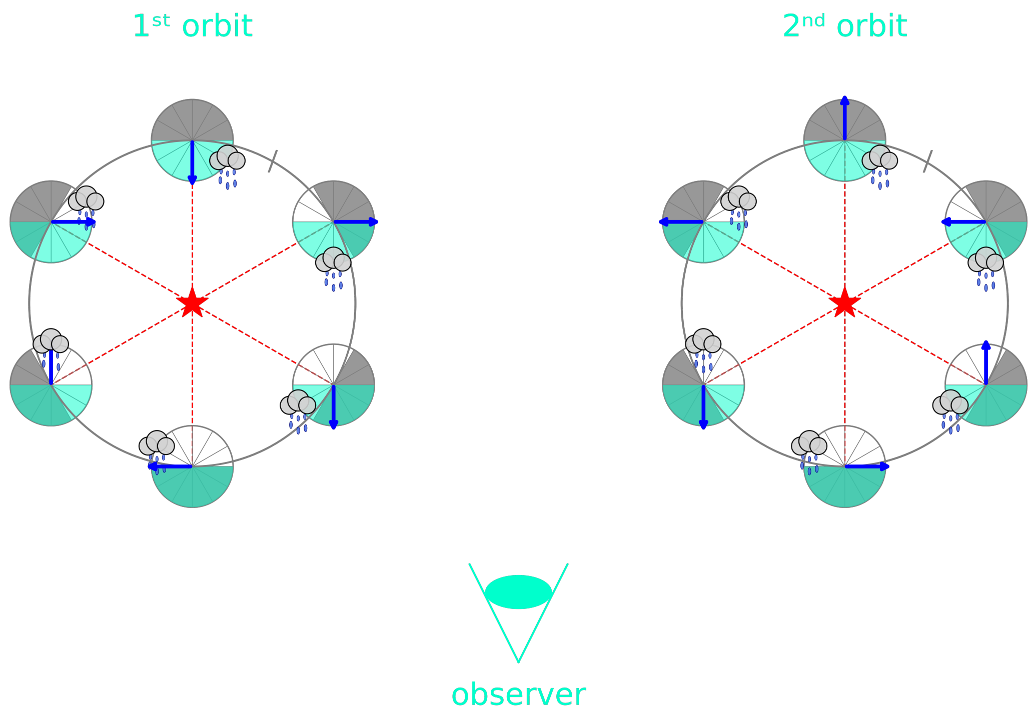

Figure 4.2.1: Observing configuration, assuming both an anticlockwise orbit and an anticlockwise spin rotation. White/gray hemispheres represent the day/night sides at each point of the orbit. The turquoise hemispheres represent the observable portion of the planet. The blue arrow is a reference meridian. The substellar point, positioned in correspondence of the red dashed line on the planetary surface, shifts 180° in longitude for every completed orbit, realigning with its initial location after two full orbits (or one stellar period).

planet. When a dynamic ocean is considered, the peak ocean surface temperature occurs slightly downstream with respect to the substellar point, due to modest eastward ocean heat transport at this location [Del Genio et al., 2019a]. Moreover, the atmospheric circulation in the null eccentricity case is similar to that of a moderately slowly rotating Earth, with Hadley cells extending to the poles, westerly jets in the midlatitudes, easterly trade winds at low latitudes and a very weak westerly equatorial surface ocean current [Del Genio et al., 2019a]. More recently, Braam et al. [2025] used a 3D coupled climate-chemistry model to study Proxima b for circular 1:1 and eccentric 3:2 SORs. Synthetic mid-infrared spectra showed that the severe zonal asymmetries of the 1:1 SOR case lead to spectral fluctuations as a function of orbital phase, which are dampened in the 3:2 SOR case because of the more homogeneous atmosphere.

More general results, not tied to a specific exoplanet, include a study of the effect of sea ice drift on snowball transitions at the outer edge of the habitable zone, performed with a fully coupled atmosphere-ocean-sea ice model for a sample of nine exoplanets [Yang et al., 2020]. By conducting an array of sensitivity tests for a range of parameters, they found that sea-ice drift is efficient in shrinking the open ocean and leading the system to a snowball state. Another more generalized study employed a 3D GCM with a shallow dynamic ocean and incorporated tidal heating to model SOR exoplanets at the inner edge of the habitable zone, showing that internal heating drives a rapid transition from temperate to moist greenhouse states, with only minor effects on upper atmospheric water mixing ratios [Colose et al., 2021]. To date, 3:2 SOR climate studies have primarily focused on the mean climate state, and, to our knowledge, no AOGCM investigation of climate pattern variability over a stellar period has yet been conducted.

In this study, we investigate the climate of ocean worlds in 3:2 SORs orbiting cool host stars with the FORTE 2.0 AOGCM [Blaker et al., 2021]. Differently from previously published studies, we use a custom continental "Ridgeworld" configuration (see Methods). Rather than concentrating on a single, specific exoplanet, our goal is to conduct a broadly applicable study, providing insights into potentially common features of exoclimes in this scenario. Accordingly, we investigate two different rotation and orbital periods, and consider two different ocean tidal scenarios, since both of these phenomena have significant effects on planetary climate [Cullum et al., 2014; Di Paolo et al., 2025]. We present an in-depth analysis of several climate features in this scenarios, both for the ocean and the atmosphere. We finally present simulated phase curves of planetary thermal emission, which reveal a potential discriminant to determine whether a planet is characterised by either a 1:1 or a 3:2 SOR state.

4.3 Methods

4.3.1 Model description

FORTE 2.0 [Blaker et al., 2021] is a fast and flexible coupled AOGCM of intermediate-resolution. The ocean general circulation model (Modular Ocean Model – Array Processor, or MOMA) [Webb, 1996] is coupled once per model day to the atmospheric general circulation model (Intermediate Global Circulation Model version 4, or IGCM4) [Joshi et al., 2015].

In the MOMA setup adopted here, horizontal resolution is $2^\circ \times 2^\circ$, with 15 vertical z-layer levels. Level thickness increases progressively with depth, from 30 m at the surface to 836.10 m at depth. Overall, the ocean extends to a maximum depth of 5700 m.

The IGCM4 setup is characterised by a T42 spectral resolution, a grid spacing of $\sim 2.8^\circ$, and a troposphere-only atmosphere, extending to about 25 km in altitude, subdivided into 20σ levels.

The convection scheme and stratiform precipitation in the IGCM4 are mostly based on

Forster et al. [2000], with a few additional parameterisations and adjustments to better match observations of Earth [Joshi et al., 2015].

4.3.2 System architecture

We choose two representative M stars in the range of masses of the spectral class, $M_\star \approx (0.08 - 0.6)\, M_\odot$, where $M_\odot$ is the solar mass (see Table 4.1). We assume an Earthlike stellar radiation forcing at the top of the atmosphere, with $S_\odot = 1365$ Wm^{-2}. For simplicity, the planetary orbit is modeled to be circular, with null orbital inclination, thus edge-on with respect to the hypothetical observer, and the planetary axial tilt is zero.

The choice of a null eccentricity is motivated by a number of reasons. While equilibrium tide theory states that a non-zero orbital eccentricity is required for a planet not to be captured into 1:1 SOR, but rather into higher order resonances, theoretical studies are usually limited to considering tidal interactions between a planet and its host star, neglecting the possibility of additional forcings due to planetary companions or satellites, or even disturbances linked to impacts, and generally have a restricted treatment of rheology and planetary triaxiality.

Planetary systems around M dwarfs are often multiple and tightly dynamically packed [Fang & Margot, 2013; Ballard & Johnson, 2016]. Thus, planetary spin states might be significantly influenced by gravitational interactions between neighbouring planets. Provided a companion is present in the system, asynchronous SORs are possible even when the eccentricity is nearly zero [Correia & Delisle, 2019]. For instance, Vinson & Hansen [2017] demonstrated that interactions between Earth-sized planets near a mean motion resonance are strong enough to lead to high amplitude librations of the spin state, or even complete circulation, instead of 1:1 SORs.

Moreover, a number of transit timing variations studies estimate small eccentricities ranging from 0.01 to 0.1 for the majority of low-mass planetary systems [Wu & Lithwick, 2013; Van Eylen & Albrecht, 2015; Hadden & Lithwick, 2017]. Multiple investigations of the climate of Proxima b in a 3:2 SOR state assumed a null orbital eccentricity, justifying this choice on the fact that an eccentricity of about ~ 0.06 would be sufficient to capture the planet into a 3:2 SOR [Ribas et al., 2016].

In order to determine the orbital radius in each case, and therefore the orbital period, we express the instellation received by the modeled exoplanet $S_\star$ in terms of $L_\star$, the luminosity of the host star in solar units ($L_\odot$), and $r_{p,\star}$, the planetary orbital radius in au units. Adopting a traditional parametrization of the luminosity-mass relationship [Harwit, 1998] yields:

$$S_\star = \frac{L_\star}{{r_{p,\star}}^2} = \frac{{M_\star}^{3.5}}{{r_{p,\star}}^2} \quad . \tag{4.3.1}$$

We require the instellation received by the modelled exoplanet $S_\star$ to be equal to the insolation that Earth receives, determining the distance between the exoplanet and its host star:

$$\begin{aligned} r_{p,\star} = \sqrt{\frac{{M_\star}^{3.5}}{S_\star}} \approx (0.05 - 0.13) \sqrt{\frac{{M_\odot}^{3.5}}{S_\odot}} \quad , \\ \approx (0.05 - 0.13) \ \text{au} \quad , \end{aligned} \tag{4.3.2}$$

where we substituted the chosen values of the M star mass (see Table 4.1). Kepler's third law yields the planetary orbital period $T_{orbital}$ in both cases, and by using the values for the host star mass and the planetary orbital radius we obtain:

$$\begin{aligned} T_{orbital} = \sqrt{\frac{4\pi^2 {r_{p,\star}}^3}{GM_\star}} \approx (0.025 - 0.083) \sqrt{\frac{4\pi^2 {r_{\oplus,\odot}}^3}{GM_\odot}} \quad , \\ \approx (9 - 30) \ \text{days} \quad , \end{aligned} \tag{4.3.3}$$

with the subscript $\oplus$ denoting quantities referring to Earth (e.g., $r_{\oplus,\odot}$ for the average orbital radius). We note that, throughout this work, the unit of measure "day" refers to an Earth day.

Since we are modelling 3:2 SOR asynchronously rotating planets, this means that the length of an exoplanet day $T_{rotation}$ can be determined from its orbital period:

$$T_{rotation} = 2/3 \ T_{orbital} = (6 - 20) \ \text{days} \quad . \tag{4.3.4}$$

The stellar day, equivalent of the solar day on Earth, can be computed according to:

$$T_{stellar} = \left(\frac{1}{T_{rotation}} - \frac{1}{T_{orbital}} \right)^{-1} = (18 - 60) \ \text{days} \quad , \tag{4.3.5}$$

and corresponds to the interval of time between two successive transits of the star across the same reference meridian on the planet.

A simple rendition of this configuration is presented in Figure 4.2.1. The reference meridian (blue arrow) realigns with the host star after completing two full orbits, or equivalently after completing three full rotations with respect to the planetary spin axis. Spin-orbit resonance states affect the orbital spatial distribution of incident stellar flux: given that we chose to adopt a null eccentricity all longitudes receive the same amount of stellar flux during a stellar period, unlike the 1:1 SOR and the 3:2 eccentric cases [Dobrovolskis, 2015].

	$M_\star$ ($M_\odot$)	$a_{p,\star}$ (au)	$T_{orbital}$ (day)	$T_{rotation}$ (day)	$T_{stellar}$ (day)
Case 1	0.18	0.05	9	6	18
Case 2	0.31	0.13	30	20	60

Table 4.1: SORs scenarios (the unit of measure "day" is an Earth day).

The simulated climates reach a quasi steady state after 2500 years. The analysis focuses on the last 100 stellar periods after a 2500 year run.

4.3.3 Planet configuration

We consider an Earth-sized ocean planet, covered by a single, global-scale ocean basin of uniform depth (5700 m). We adopt a "Ridgeworld" configuration (e.g. Smith et al. [2006]; Ferreira et al. [2010]; Yang et al. [2019]; van de Velde et al. [2021]): a single, 2° wide, meridional ridge 145 m below the surface connects two polar islands that extend to 86°N/S. This continental configuration, more general than assuming a specific land mask, importantly allows the formation of ocean gyres, prevents the formation of unrealistically large zonal oceanic jets that occur in "Aquaplanet", while at the same time supporting a large-scale overturning circulation and heat redistribution. The atmospheric composition is Earth-like, characterised by pre-industrial atmospheric concentrations of CO_2.

Asynchronously rotating potentially habitable planets reside in close orbit round their low-mass host stars, experiencing strong tidal interactions. Therefore, they are subjected to large travelling tides. These tidal effects can be parameterized with an enhanced oceanic vertical diffusivity κ [Di Paolo et al., 2025]. We choose to analyse SOR scenarios in two different tidal regimes: a low vertical diffusivity regime with $\kappa = 1.5 \times 10^{-4}\mathrm{m}^2\mathrm{s}^{-1}$, similar to the one estimated for Earth $\kappa_\oplus = 1 \times 10^{-4}\mathrm{m}^2\mathrm{s}^{-1}$ [Munk & Wunsch, 1998], and a high vertical diffusivity regime with $\kappa = 150 \times 10^{-4}\mathrm{m}^2\mathrm{s}^{-1}$, that corresponds to a maximised total and oceanic heat transport [Di Paolo et al., 2025].

Simulating exoplanetary climate using both a dynamic and a thermodynamic ocean provides critical insight into the role of oceanic processes in regulating planetary climates. For the former, we employ the default setting of MOMA, which is inclusive of both diffusive and advective processes at play in determining the state of the ocean, while for the latter we adapt MOMA to exclude advection. Therefore, for the thermodynamic configuration, we modify MOMA to suppress advection by setting all ocean velocities to zero and prescribe a globally uniform salinity. This choice not only removes advective salinity transport but also effectively eliminates salinity diffusion, which operates on timescales roughly two orders of magnitude longer than thermal diffusion. Neglecting salinity as an active tracer is a common simplification in idealised ocean models, as reducing the number of prognostic tracers substantially decreases model complexity [Codron, 2012; Bhatnagar et al., 2025]. The thermodynamic configuration retains the full 15-level vertical structure of the ocean and therefore does not constitute a slab ocean; rather, it represents a vertically resolved diffusive ocean in which heat transport is governed solely by prescribed diffusion in the absence of fluid dynamical processes.

The albedos of snow and ice decrease progressively at longer wavelengths, especially beyond 1 μm, due to their optical properties. Low-mass stars emit a substantial portion of their radiation in this longer-wavelength range. The resulting albedos of snow and ice on planets orbiting M-stars are significantly lower than those observed on Earth [Joshi & Haberle, 2012]. In order to take this into account, we use 0.4 as the maximum value for the ice and snow albedo, consistent with a mean value of calculated albedos for different mixtures of ice and snow [Shields et al., 2013].

4.4 Results

4.4.1 Ocean

The thermal inertia of the ocean causes the location of the warmest water in the upper layers to be shifted away from the substellar point (Figure 4.4.1). At any fixed location, there is a temporal lag between the star's transit overhead and the peak in sea surface temperature. Differently from the synchronous rotation scenario, where the hot spot is fixed on the planetary surface with respect to the substellar point, in this scenario the hot spot travels across the planetary surface following the passage of the star overhead.

The ocean state is tightly linked to the value of κ. As oceanic diffusion becomes more important, the thermocline deepens. Figure 4.4.1 shows how, for both rotational states, the signal travels to greater depths in the cases of enhanced κ with respect to their counterparts. This is evident in Figure 4.4.2, which shows the temperature profiles in the equatorial band (between latitudes of 5°S and 5°N) at the longitude 120°, with the spread in the upper ocean representing the variability of temperature due to the transient signal. Both the dynamic and the thermodynamic ocean models simulate less stratified profiles in the cases of high κ. In general, the thermodynamic ocean runs exhibit warmer temperatures than the dynamic ocean runs at this location, as when ocean dynamics are active cold water is advected at depth from high latitudes. This has a less evident effect on near surface temperatures, given that the stellar forcing dominates, resulting in generally similar temperatures for both types of ocean model. Only the $T_{orbital}$ = 30 days, κ = 1.5 $\kappa_{\oplus}$ scenario presents marginally warmer

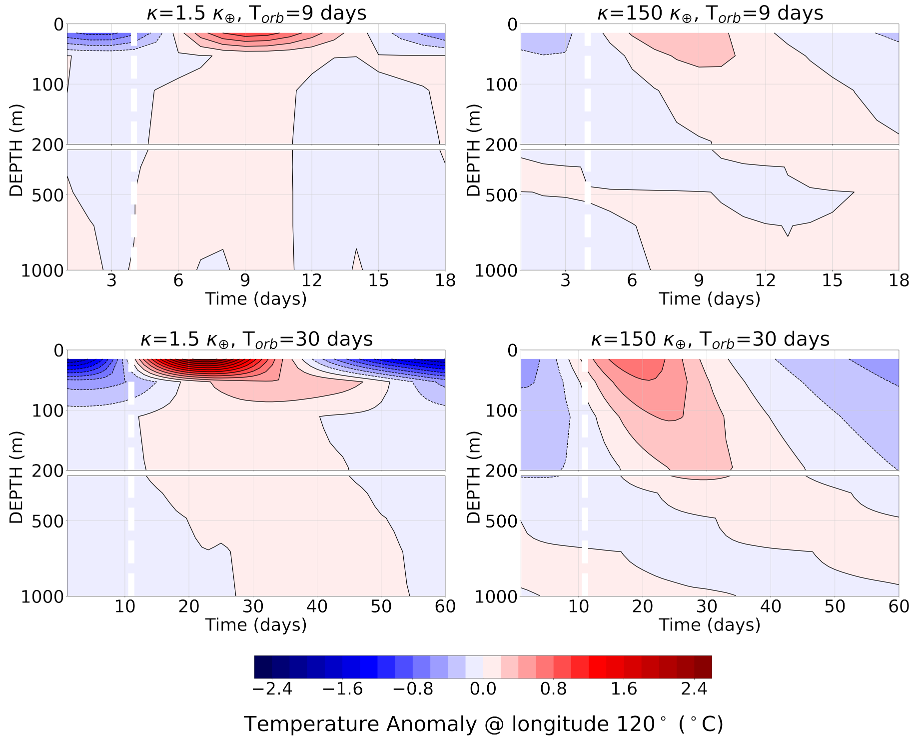

Figure 4.4.1: Cross section of the upper dynamic ocean layers, at longitude 120° and between latitudes of 5°S and 5°N, showing temperature anomaly. White dashed lines represent the location of the substellar point. Composite quantities have been averaged over the last 100 stellar periods.

temperatures near the surface in the case of the dynamic ocean. This is caused by downwelling occurring at the equator which warms the upper ocean layers.

In the case of the dynamic ocean, the ocean response is a combination of a downward propagating signal and dynamical waves that depend on boundary conditions. Figure 4.4.3 shows the density anomaly at a depth of about 500 m in the case of the dynamic ocean. The plots on the right are obtained by compositing over one hundred stellar periods in each case. In the high κ cases, the effect of vertical diffusion clearly dominates, resulting in an evident downward propagating signal that is linked to, but lags, the location of the substellar point in time. Taking as a reference the longitude 120°, the position of less/more dense water roughly corresponds to the position of the warmer/colder water depicted in Figure 4.4.1 at the same depth.

In the faster rotation case, the temperature anomalies propagate downward at depth more quickly than in the slower rotation case, which is indicated by the inclination of the black contours in Figure 4.4.1. This explains why the density anomalies depicted in Figure 4.4.3 seem to be in opposite phases in the two high diffusion cases with different rotation period.

In the low κ cases the downward propagating signal is weaker and shallower, and dynamical features can dominate. In the $T_{orbital}$ = 9 days scenario, the very weak

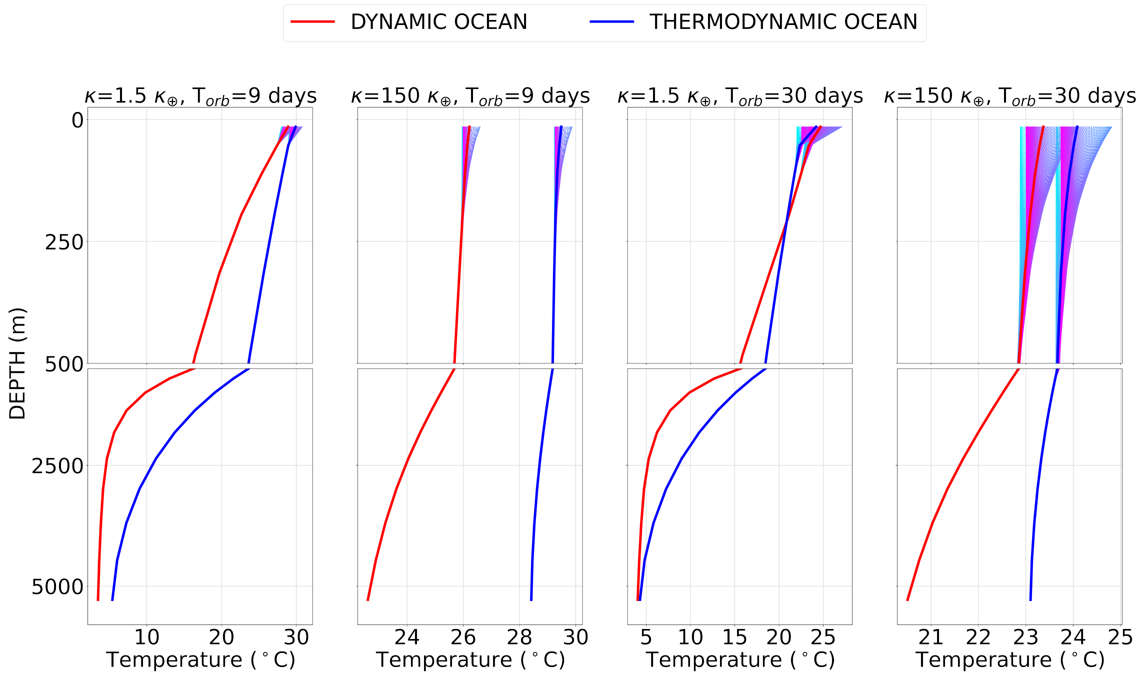

Figure 4.4.2: Temperature profiles of dynamic vs thermodynamic ocean at longitude 120° and between latitudes of 5°S and 5°N. For each profile, a spread of daily averaged temperatures is plotted, showcasing the variability of the temperature in the upper ocean layers with the shifting position of the substellar point.

intermittent wave-like pattern depicted in Figure 4.4.3 appears only after compositing over one hundred stellar periods, but is absent when averaging over shorter intervals of time, and does not appear to be phase-locked with the forcing. Conversely, the larger anomalies associated with stronger forcing in the $T_{orbital} = 30$ days scenario are westward propagating equatorial Rossby waves and eastward propagating Kelvin waves. These waves originate at the barrier, positioned at longitude 240°, and are triggered by alternating zonal wind patterns that periodically reverse direction: associated Ekman convergence forces equatorial downwelling of lighter water, while Ekman divergence forces equatorial upwelling of denser water. The patterns of winds are described in more detail in the next section (Atmosphere). We further investigate this case by spreading the composited stellar period, obtained by compositing over 100 stellar periods, into 10 stellar periods obtained by compositing over 10 stellar periods (plot on the left of Figure 4.4.3). The Rossby waves, spanning the planet with a velocity of about 2 ms^{-1}, are still clearly visible. Multiple and frequent Kelvin waves with a velocity of about 6 ms^{-1} - about three times the Rossby wave speed - are possibly triggered by stochastic forcings such as random weather events. Phase-locked Kelvin waves are more evident east of the barrier when averaging over longer periods of time.

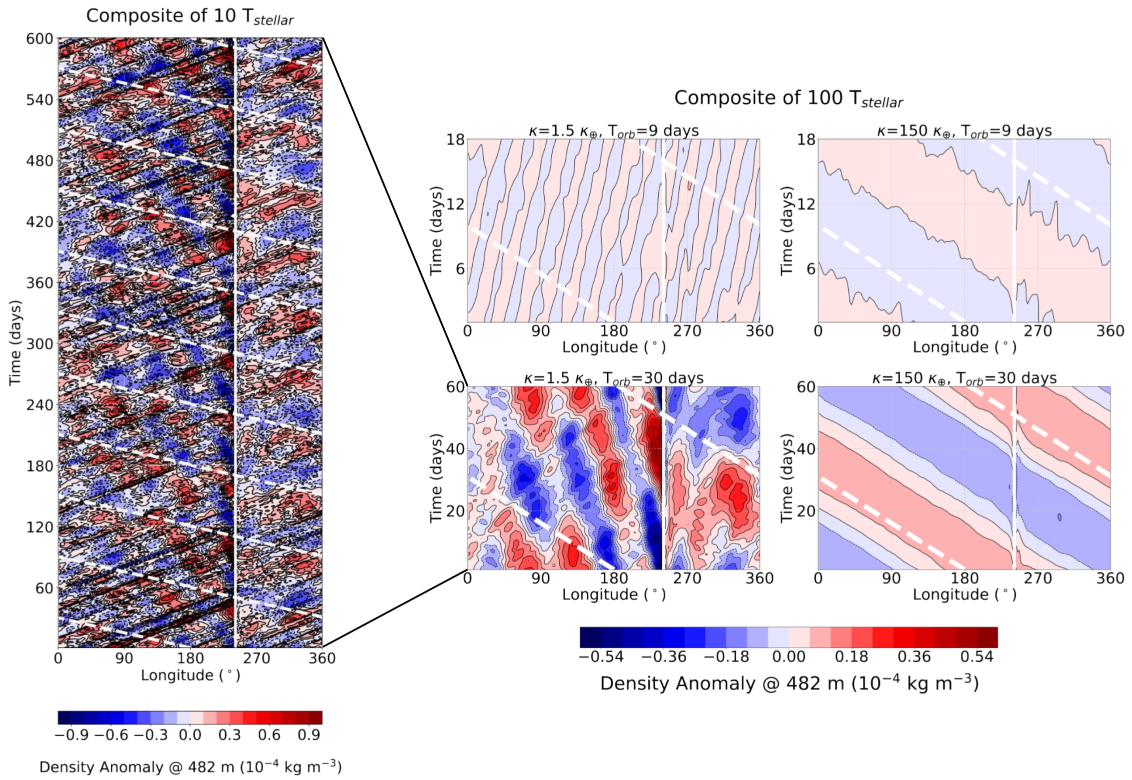

Figure 4.4.3: Hovmöller diagram showing density anomaly at 482 m of depth, between latitudes of 5°S and 5°N. White dashed lines represent the location of the substellar point. Composite quantities at the equator have been averaged over the last 100 stellar periods either into one composited stellar period (plots on the right) or into ten composited stellar periods (plot on the left).

4.4.2 Atmosphere

Figure 4.4.4a clearly shows that at all times, the surface temperature peaks with a longitudinal shift of about $\sim 60°$ eastward with respect to the location of the substellar point on the planetary surface, consistent with Figure 4.4.1. The most prominent features are observed in the case $T_{orbital} = 30$ days with $\kappa = 1.5\ \kappa_{\oplus}$, with a higher surface temperature range. In general, scenarios characterised by the same value of the vertical diffusion coefficient will present a stronger signal for the slow rotation scenario (Figure 4.4.1 and Figure 4.4.4a). In these scenarios, the stellar forcing travels slowly across the surface, the host star illuminates the same spot on the planet for longer periods of time, and the effect of stellar forcing dominates. Scenarios characterised by the same rotation period will present a stronger signal for the low diffusion scenario, as warm water at the surface is not rapidly diffused downwards, and more heat is retained in the upper ocean.

In all scenarios, the effect of surface heating dominates, with moisture building up in the lower atmosphere and condensing into clouds, triggering rainfall. Rainfall peaks with a $\sim 60°$ longitudinal shift with respect to the substellar point (see Figure 4.4.4b), coincident

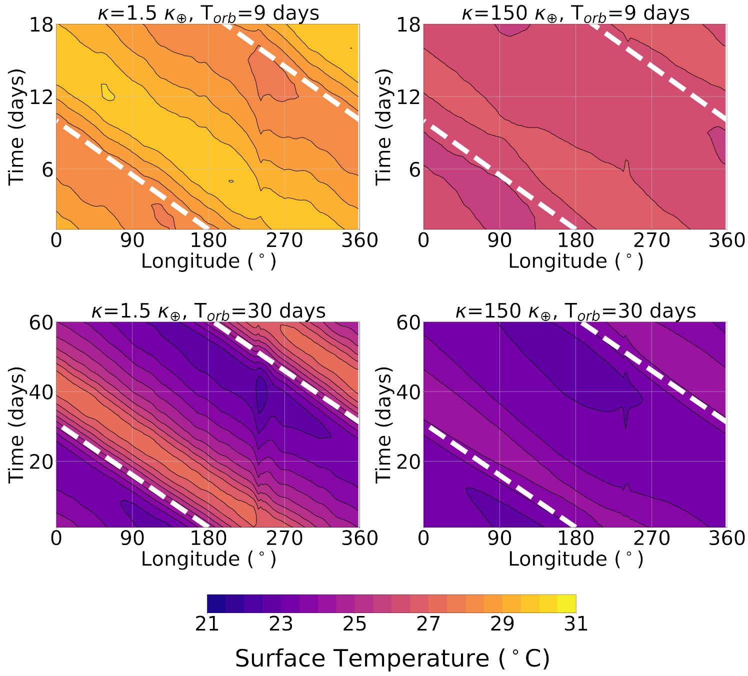

(a)

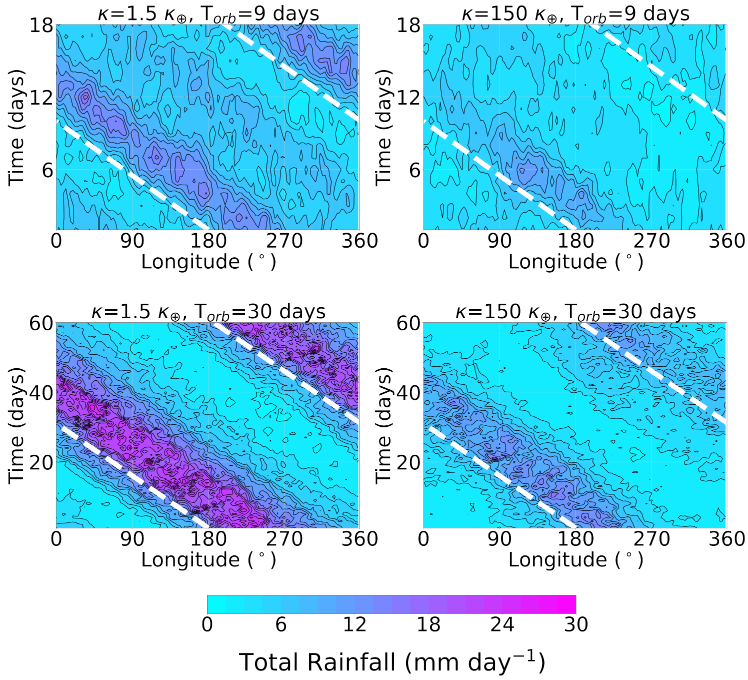

(b)

Figure 4.4.4: Hovmöller diagram showing composite quantities averaged over the equatorial band (5°S - 5°N) and over the last 100 stellar periods for the dynamic ocean scenarios. White dashed lines represent the location of the substellar point. (a) Surface temperature, (b) total rainfall.

with the highest surface temperature. The rainfall is significantly more intense in the case $T_{orbital} = 30$ days with $\kappa = 1.5\ \kappa_{\oplus}$, associated with the stronger temperature forcing, reaching a maximum of $\sim$ 30 mm day^{-1} over the equatorial band. Rainfall exhibits significant variability over each stellar period. At any fixed location, while the passage of the star overhead is followed by a clear maximum in the signal averaged in time, the non-composited signal is noisy. An example of this is shown in Figure 4.4.5, for the longitude $\sim 120° \pm 10°$ in the equatorial band. As expected, the signal to noise ratio increases for slower rotations, where a general similar behaviour is maintained even for the non-averaged signal. The case $T_{orbital} = 30$ days with $\kappa = 1.5\ \kappa_{\oplus}$ presents the most consistent peak in rainfall for each stellar period, with an average maximum value of $\sim$ 22 mm day^{-1} at this specific location, as expected from the biggest temperature contrast observed in this scenario. The above shift in surface temperature, and consequently in rainfall, is generally observed with both the dynamic and the thermodynamic ocean models.

The surface temperature in the equatorial band is higher in the thermodynamic ocean scenario for all cases except the $T_{orbital} = 30$ days with $\kappa = 1.5\ \kappa_{\oplus}$ case, which exhibits slightly warmer temperatures in the dynamic ocean scenario, associated with more abundant rainfall. The peak in total rainfall is generally sharper in the case of the thermodynamic ocean than in that of the dynamic ocean. In particular, the higher diffusion scenarios show a bigger relative increase in the maximum value of total rainfall, in accordance with a bigger relative increase in surface temperature (see Figure 4.4.2). In general, the signal still exhibits significant variability with time even in the thermodynamic ocean cases. The distribution of clouds, not shown here, does not perfectly correspond to the rainfall pattern. This is due to a delay between the formation of clouds and highest precipitation. At any instant, significant shallow convection is present westward of the substellar point.

Figure 4.4.6a depicts the convergence/divergence of equatorial zonal winds through the alternating bands of easterly and westerly winds. As mentioned in the previous section, equatorial zonal winds at 850 hPa generally converge towards the hot spot on the planetary surface, and diverge from the diametrically opposite point. This pattern is evident for the slow rotation cases, while is less demarcated in the faster rotation cases, as a consequence of the weaker surface temperature gradients associated with the position of the substellar point.

Interactions between zonal wind patterns and the barrier generate equatorial Rossby and Kelvin waves that propagate westward and eastward, respectively, at depth (Figure 4.4.3). In the case with $T_{\mathrm{orbital}} = 30$ days and $\kappa = 1.5\,\kappa_{\oplus}$, on either side of the location of the barrier (longitude 240°), Ekman convergence and divergence associated with alternating eastward and westward zonal winds (Figure 4.4.6a) result in oceanic equatorial downwelling and upwelling. For instance, at the beginning of the stellar period, the barrier lies at the transition between opposing zonal wind directions, creating a zone of wind convergence. West of the barrier, Ekman convergence induced by the eastward winds that this region has been experiencing up to this point forces warm,

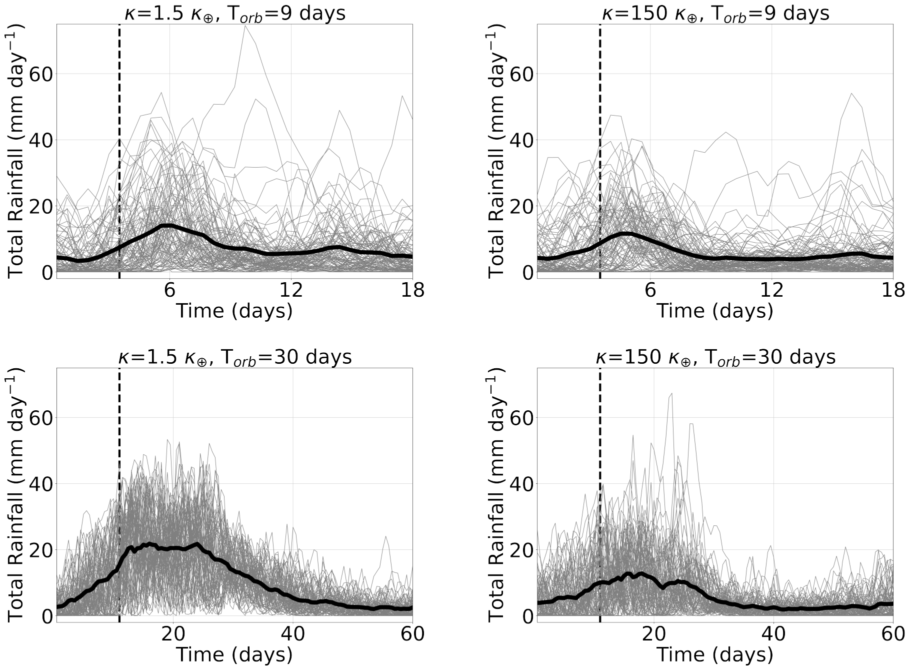

Figure 4.4.5: Variability of total rainfall at longitude 120° and averaged between latitudes of 5°S and 5°N. For each case, the thick black solid line represent the composited average over the last 100 stellar periods, while light gray solid lines represent rainfall during each of these stellar periods. Black dashed lines represent the instant that corresponds to the passage of the star overhead at this location.

buoyant surface water downward, producing the negative density anomaly seen in Figure 4.4.3. East of the barrier, the onset of westward winds generates Ekman divergence and upwelling, bringing colder, denser water upward and creating a positive anomaly. These anomalies then propagate away from the barrier: the downwelling signal to the east is carried rapidly by the Kelvin wave, while the corresponding downwelling response to the west travels more slowly as a Rossby wave. Their differing propagation speeds produce the observed phase offset between the anomalies on either side of the barrier. At the same location, about halfway through the stellar period, the divergence of westward and eastward zonal winds (Figure 4.4.6a) produces mirrored density anomalies through the same mechanism.

Figure 4.4.6b depicts the zonal wind at 850 hPa at the fixed location of 120° as a function of latitude. As expected, the wind at the equator exhibits alternating eastward and westward directions depending on the time during the stellar period. The pattern is more latitudinally extended in the slow rotation scenarios, while it is constrained to lower latitudes in the fast rotation cases owing to weaker divergence associated with a smaller heating anomaly. For the same rotation rate, $\kappa = 150\ \kappa_{\oplus}$ cases exhibit weaker high-latitude westerlies than $\kappa = 1.5\ \kappa_{\oplus}$ cases, due to reduced meridional temperature gradients. This behaviour can be described as a moving Walker circulation that follows the shifting position of the peak surface temperature. Similarly, in the case of slowly

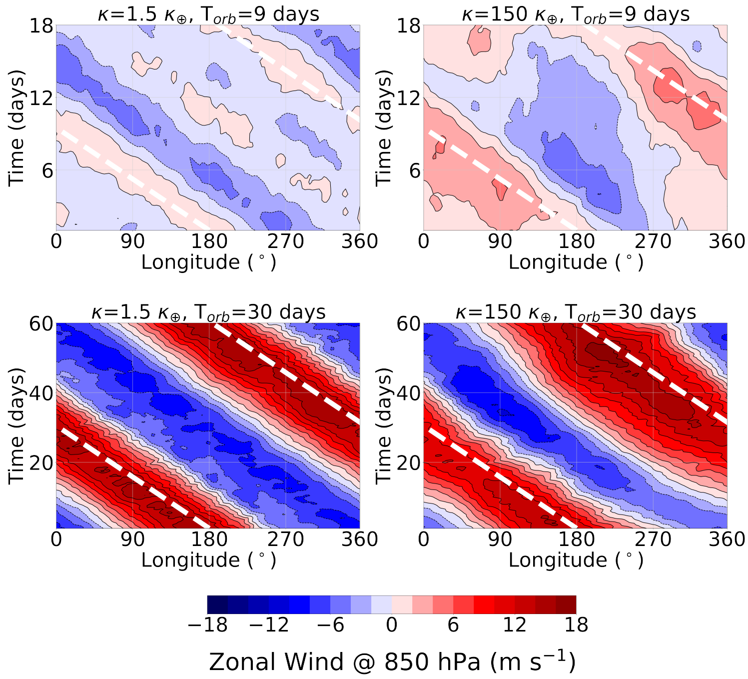

(a)

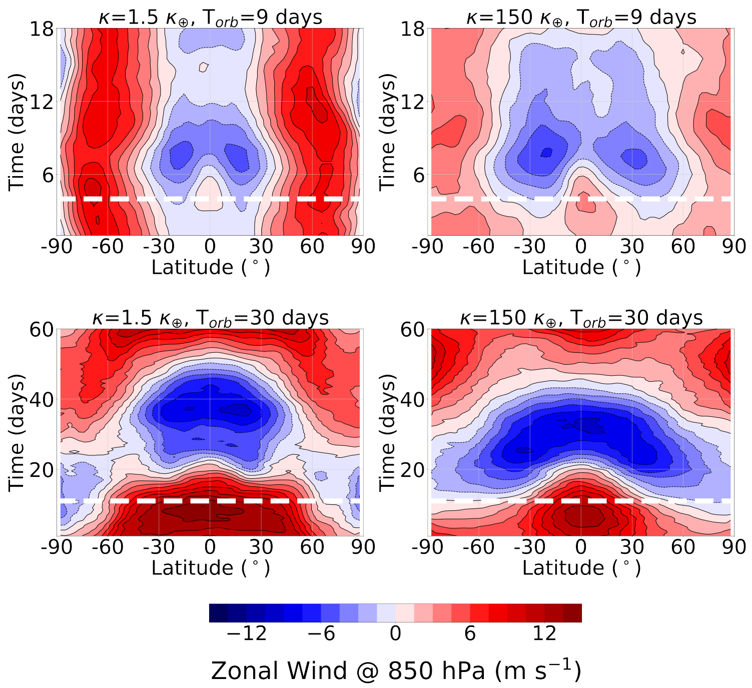

(b)

Figure 4.4.6: Hovmöller diagram showing composite quantities averaged over the last 100 stellar periods. White dashed lines represent the location of the substellar point. (a) Zonal wind at 850 hPa, averaged over the equatorial band (5°S - 5°N), as a function of longitude. (b) Zonal wind at 850 hPa, at longitude 120°, as a function of latitude.

rotating 1:1 SOR exoplanets, atmospheric circulation models predict a global overturning circulation centered on the substellar point; air rises at the substellar point in the permanent day hemisphere, travels towards the colder night hemisphere in the upper atmosphere, and sinks at a location that depends on the strength of the circulation [Hammond & Lewis, 2021]. Equatorial zonal winds at 250 hPa (not shown) have a superrotating westerly wind jet in all scenarios. In general, the results of the thermodynamic ocean simulations show a similar behaviour. However, asymmetries with respect to the equator and/or with respect to the position of the substellar point depicted in Figure 4.4.6 are introduced by dynamical features that are obviously absent in the case of the thermodynamic ocean.

In slow rotation cases, the meridional circulation in the hemisphere centered on the hot spot on the planetary surface consists of a single Hadley cell extending from the equator to the poles [Haqq-Misra et al., 2018], whereas in fast rotation cases the Hadley circulation is restricted to low latitudes.

4.4.3 Observables

Mapping terrestrial exoplanets involves constraining temporal and spatial properties in order to gain further insight into the planetary characteristics, therefore allowing us to develop an understanding of their climate dynamics. Possible photometric signals are the planetary top-of-atmosphere outgoing longwave radiation, or thermal emission, and the top-of-atmosphere outgoing shortwave radiation, or reflected light. Thermal orbital phase curves are a simple method to infer information regarding the planetary temperature and heat transport efficiency from the disk-integrated emitted thermal flux. On the other hand, reflected light orbital phase curves provide crucial insight into surface composition and cloud coverage. Together, photometric phase curves are crucial for understanding exoplanetary climate dynamics and potential habitability.

The planet top-of-atmosphere outgoing radiation is split into longwave ($> 4\ \mu$m) and shortwave (UV-VIS-NIR between 0.12 - 4 μm) in the atmospheric model output. We assume an edge-on orientation, so that orbital phases of ± 0.5 correspond to secondary eclipses, where only the day hemisphere of the planet is visible to the observer, and orbital phases of $\pm 0, 1$ are transit events, where only the night hemisphere of the planet is visible to the observer. In order to focus on the climatic features of each case, we exclude the contribution of the star to the total observed flux in each orbital configuration, effectively separating the planetary signal. The light curves depicted in this section in Figure 4.4.9 simulate daily observations for a total of 1800 days, corresponding to 100 stellar periods for the faster rotation cases, and 30 stellar periods for the slow rotation scenario. Each plot shows the daily visible hemisphere integrated flux, the 10th and 90th percentile and the composited signal.

Previous studies of 3:2 SORs circular orbits scenarios adopted an “Aquaplanet” setup with no meridional barriers, which is completely zonally uniform. Observing different areas of the planet would not imply any longitude-specific feature: excluding transient events, the potential observables would not exhibit any variability between consecutive orbits. In our modelling configuration, it is crucial to consider the full orbital phase curves over two consecutive orbits, or equivalently over one full stellar period. This is because in two consecutive orbits, the same orbital configuration is associated with different portions of the planet in the field of view of the observer. The configuration depicted in Figure 4.2.1 shows how the position of a reference meridian (blue arrow) with respect to the observer changes in time: when considering equivalent orbital phases for consecutive orbits, the observed signal originates from different portions of the planet. The white transparent bands in Figures 4.4.7 highlight the planetary hemisphere that is visible to the observer at all times during a stellar period.

The top-of-atmosphere shortwave radiation represented in Figure 4.4.7a exhibits a slight asymmetry with respect to the substellar point (white dashed line) in all cases: the signal peaks eastward from the position of the substellar point, as we would expect from the previous considerations regarding the rainfall longitudinal shift. The first reason for the small amount of asymmetry is attributable to the fact that the amount of reflected light is highly dependent on the cloud amount. As mentioned in the previous section (see Atmosphere), the significant asymmetry in the rainfall signal with respect to the substellar point does not necessarily correspond to an equally evident asymmetry in the cloud coverage. The second reason stems from system geometry: incoming stellar flux scales with the cosine of the zenith angle, so the amount of potentially reflected light decreases moving longitudinally away from the substellar point. Although the precipitation peak is evident, its $\sim 60^\circ$ offset implies a reduced reflected flux. Consequently, while Figure 4.4.7a shows slight asymmetry, the disc-integrated signal in Figure 4.4.9 remains largely symmetric about transits/secondary eclipses midpoints, with only minor deviations in slow rotation cases.

Although most precipitation in the model arises from convective processes, this does not imply a strong spatial correspondence between the diagnosed convective-cloud field and the rainfall pattern. The model convective-cloud diagnostic aggregates both shallow and deep convection, whereas only deep convection produces substantial precipitation. As shown in Figure 4.4.8, the resulting convective cloud distribution does not correlate with the rainfall pattern in Figure 4.4.4b, as extensive shallow convection occurs west of the substellar point, rains out slowly, and contributes little to total rainfall. In FORTE 2.0, precipitation is therefore a more reliable indicator of deep convective activity. It serves as a good proxy for cumulonimbus clouds [Joshi et al., 2015], whose distribution shapes the top-of-atmosphere outgoing longwave radiation shown in Figure 4.4.7b. This motivates the use of tropical precipitation - rather than total or convective cloud cover - to characterise the spatial and temporal structure of deep convection and its imprint on planetary thermal

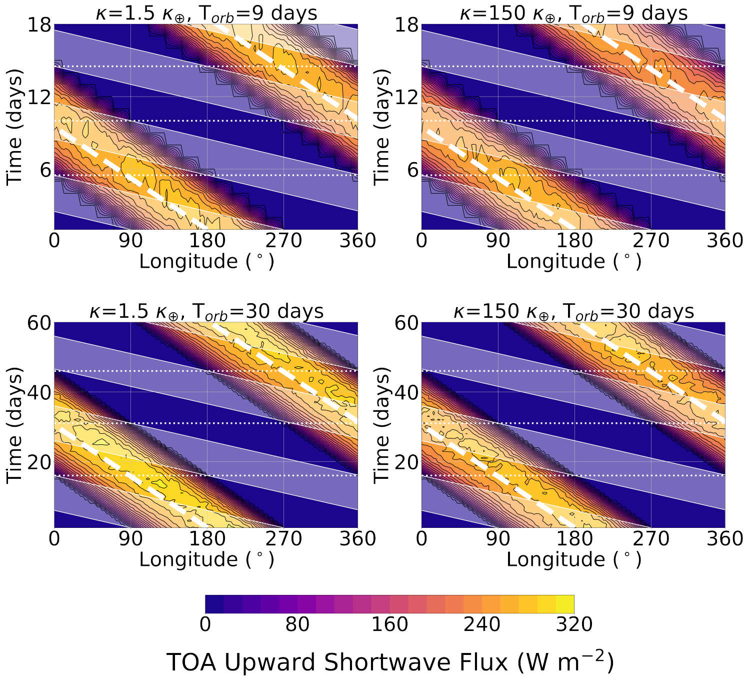

(a)

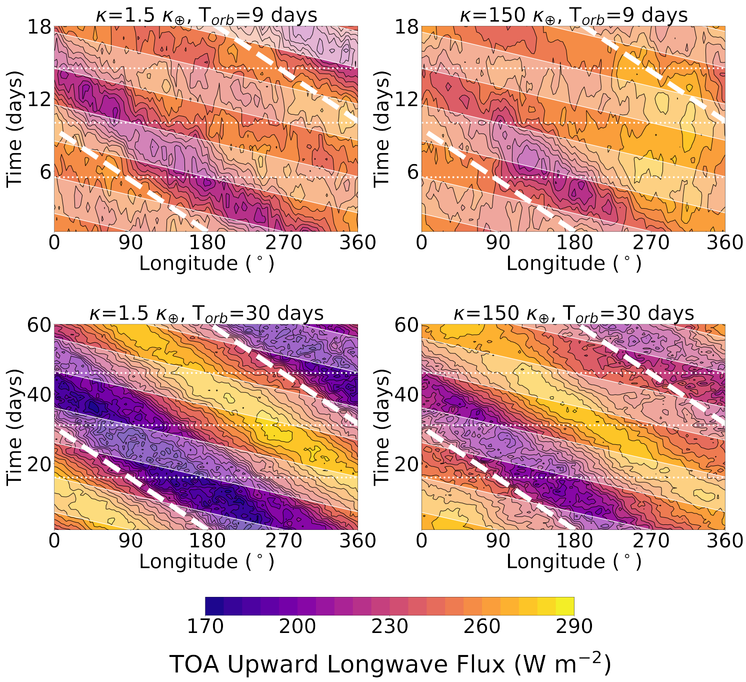

(b)

Figure 4.4.7: Hovmöller diagram showing composite quantities averaged over the equatorial band (5°S - 5°N) and over the last 100 stellar periods. White dashed lines represent the location of the substellar point, transparent white stripes correspond to the portion of planet that is theoretically observable, thin dotted lines correspond to the main phases of transits and secondary eclipses, starting with the first secondary eclipse in all cases. (a) Outgoing shortwave radiation at the top of the atmosphere. (b) outgoing longwave radiation at the top of the atmosphere.

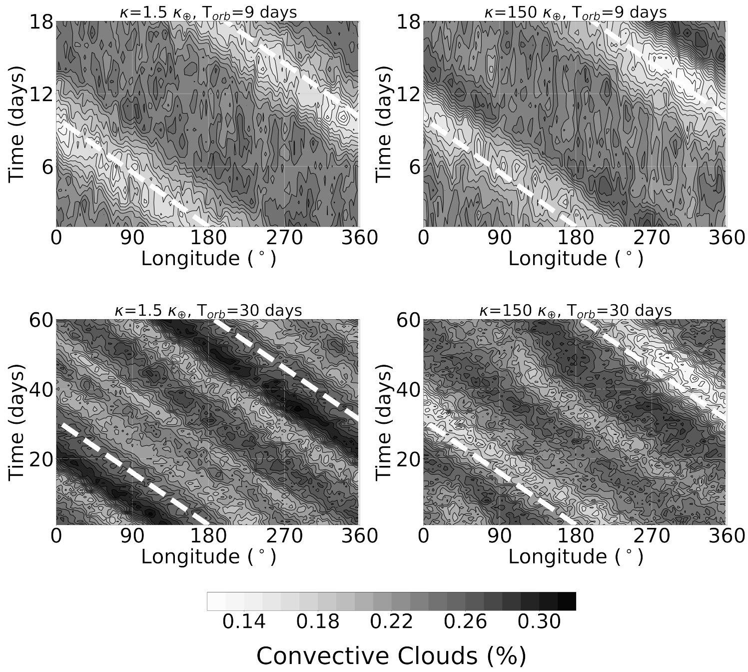

Figure 4.4.8: Hovmöller diagram showing composite convective cloud amount averaged over the equatorial band (5°S - 5°N) and over the last 100 stellar periods. White dashed lines represent the location of the substellar point.

emission.

The top-of-atmosphere longwave radiation represented in Figure 4.4.7b clearly shows that the minimum thermal emission to space is co-located with the maximum rainfall, as the latter is associated with deep convective cloud having cold cloud tops. As expected, the equatorial band signal is more prominent for the $T_{orbital} = 30$ days with $\kappa = 1.5\ \kappa_{\oplus}$ case, that exhibits the strongest rainfall signal. The thermal emission appears to be generally more muted and less spatially constrained for the $T_{orbital} = 9$ days cases that exhibit the noisiest rainfall signal. In these cases, the hemisphere-integrated top-of-atmosphere outgoing longwave radiation depicted in the phase curves shows no strong correlation with different orbital phases, as shown by the top panels of Figure 4.4.9a. This is the result of a more zonally uniform thermal emission from the planet, yielding a more homogeneous signal. In the cases of slower rotation, the disc-integrated top-of-atmosphere outgoing longwave radiation depicted in the light curves show evident asymmetries with respect to the transits/secondary eclipses midpoints. A sinusoidal curve is clearly identifiable, with evident peaks occurring before the transit phase, during which the entirety of the dark hemisphere is facing the observer. Both emitted light curves shown in the bottom panels of Figure 4.4.9a are negatively shifted as a result of the longitudinal asymmetry introduced by the rainfall signal. This negative shift appears to be smaller for the high diffusion case with respect to the low diffusion case, as a consequence of the weaker asymmetry in outgoing longwave radiation at the top of the atmosphere in this scenario due to a weaker rainfall signal (as mentioned in Atmosphere).

Figure 4.4.9 highlights the reflected and emitted light variability, by specifically showcasing the 10th and 90th percentiles of the distribution of data from each stellar period, as well as the composite average. As expected, cases of fast rotation present bigger uncertainties, with a significant spread for the thermal emission phase curve. Between the two cases characterised by slow rotation, the low diffusion case is noticeably less noisy, as a consequence of the previously mentioned stronger rainfall signal.

The results relative to the thermodynamic ocean simulations, depicted in Figure 4.4.9b, show comparable results regarding the reflected light curve. The emitted light curves present asymmetry with respect to the midpoint of the transit, with a comparable shift than their counterparts in Figure 4.4.9a. The similarity of these feature indicates that the general climate response is not especially affected by ocean dynamics, and that the surface temperature offset - and therefore rainfall and thermal emission offsets - are a direct consequence of the thermal inertia of the ocean and not a result of horizontal ocean heat transport.

Ocean dynamics plays a role in determining the amplitude of the thermal emission phase curve. In the slow rotation case, the thermodynamic ocean emission phase curve has a slightly larger amplitude with respect to its dynamical counterpart. Compared to the dynamic ocean, the thermodynamical scenario, in which circulation is absent, presents higher temperatures at the equator, but significantly lower temperature at mid- and high- latitudes. This results in lower rainfall and generally more abundant thermal emission. This is especially evident for the higher diffusion case, in which meridional surface temperature gradients are starker.

An additional interesting feature of the emitted light curves depicted in the bottom panels of Figure 4.4.9a is the unequal magnitude of successive maxima and minima, as most evidently shown for the case κ=150 $\kappa_{\oplus}$, $T_{orbital}$ = 30 days. This is a direct consequence of how ocean dynamics interact with the barrier, as this feature is non existent in the thermodynamical counterpart.

More specifically, taking as an example the consecutive maxima of the dynamical case κ=150 $\kappa_{\oplus}$, $T_{orbital}$ = 30 days, it is evident that the first peak is marginally smaller than the second. Given our observational configuration set up, the orbital phase associated with the first peak corresponds to observing the hemisphere east of the barrier, while the second peak corresponds to observing the hemisphere west of the barrier, with the barrier having just crossed the eastern terminator. The visible hemisphere associated with the first peak exhibits warmer temperatures, a more prominent rainfall and consequently a smaller amount of thermal emission. This is due to the fact that the barrier allows the formation of gyres, that transport heat from the equator to the mid latitudes, analogous to what happens with western boundary currents on Earth [Atkinson, 2010].

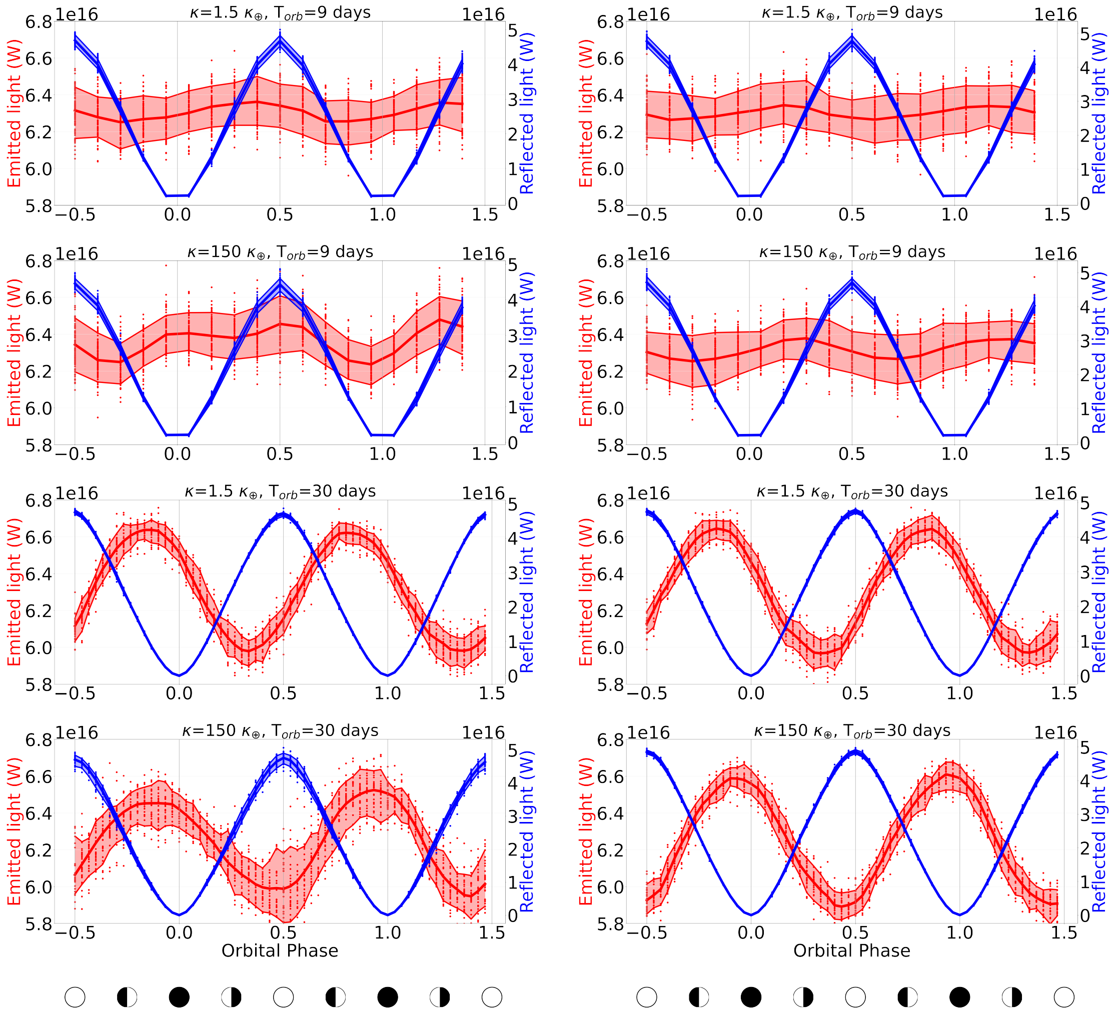

(a) (b)

Figure 4.4.9: Emitted and reflected light phase curves for the dynamic ocean scenario (a) and the thermodynamic ocean scenario (b). Scatter plot: daily hemisphere integrated emitted (red) and reflected (blue) flux. Thick line plot: composited emitted (red) and reflected (blue) signal. Shaded region: 10th to 90th percentile range of the emitted (red) and reflected (blue) signal.

The time-dependency of the curve amplitude is more evident in the high diffusion case, because the enhanced ocean circulation results in higher mid- and high- latitude surface temperatures compared to the low diffusion scenario, exacerbating the zonal asymmetry introduced by the barrier.

For both the reflected and emitted light, the thermodynamic ocean simulations present a slightly smaller spread of the 80th percentile compared to the dynamic ocean simulations, consistent with the muted rainfall variability observed in these scenarios, as mentioned in the Atmosphere section.

4.5 Discussion and Conclusions

In this paper we employ a 3D coupled atmosphere-ocean general circulation climate model to investigate climate features of water-rich terrestrial exoplanets captured into 3:2 SORs in the habitable zone of low-mass stars. We explore the interplay between climate, orbital configuration, and therefore rotation regime, and oceanic tidal regime. We address the issue of estimating potential observational characteristics of such planets by analysing reflectance and thermal emission phase curves, in an effort to establish a criterion that would allow us to discriminate between two possible outcomes of tidal locking - 1:1 and 3:2 SORs - for potentially habitable planets orbiting low-mass stars. This work is primarily motivated by the lack of previous research using a climate model with a dynamic ocean to focus on the evolution of climatic features during a stellar period for planets captured into higher order SORs. While the 1:1 SOR scenario has been extensively studied, 3:2 SOR cases are still relatively unexplored.

The aim of our study is to offer an insight on how both atmosphere and ocean dynamics shape planetary climate and affect potentially observable quantities for the duration of a stellar period in this scenario. In order to present a valuable tool of comparison between two possible SOR scenarios we conducted an idealised study, focusing on varying two parameters - associated with rotation and tidal regimes - of the multidimensional parameter space. This choice resulted in fixing other parameters, such as the stellar radiation forcing at the top of the atmosphere and the orbital eccentricity, to specific values. For instance, the instellation is assumed to be Earth-like, and the orbit is presumed to be circular. While exploring other values of the parameter space would be interesting, it would also be computationally expensive and would introduce multiple degeneracies that would render a direct comparison of different scenarios more complicated. The choice of a null orbital eccentricity, even if idealised, is particularly convenient, as non-null values would introduce the question of having to additionally establish the planet's longitude at perihelion, introducing yet another dimension to the parameter space. Moreover, the specific choice of adopting a "Ridgeworld" configuration is motivated by the intent of representing a continental setup that would allow a more Earth-like ocean circulation compared to an "Aquaplanet" configuration, while being as general as possible at the same time.

The ocean response is a combination of downward propagating signals and dynamical waves that depend on boundary conditions. Due to the thermal inertia of the ocean, the surface temperature exhibits a 60° longitudinal shift with respect to the position of the substellar point. This results in a similar shift of the position of the maximum rainfall on the planetary surface, with a consequent asymmetry of the thermal emission of the planet, which instead of being centered on the substellar point is shifted westward. This pattern, although present in all analysed scenarios, is more evident for the slow rotation regime, as the ocean - and consequently the atmosphere - have more time to respond to the heating caused by the slowly shifting stellar forcing. For the same rotation case, tidal scenarios characterised by weaker ocean vertical diffusion present clearer climate patterns, as the temperature signal resulting from the stellar forcing is not efficiently mixed in the vertical but persists strongly in the upper ocean layers.

In order to fully characterise exoplanetary properties, a combination of thermal emission and reflected light observations would be necessary [Cowan et al., 2012]. We simulate phase curves for both emitted and reflected light for all analysed scenarios, assuming the orbit to be edge-on with respect to a potential observer. Reflected light phase curves do not present any substantial asymmetry with respect to the midpoint of the transit, in any of the analysed scenarios. Therefore, there is no discernible difference between a 1:1 and a 3:2 scenario, as observed reflected light would peak at full phase (during secondary eclipses) and drop to minima at transits, with no noticeable offset or asymmetry in both cases.

Thermal emission phase curves present more interesting features. The top-of-atmosphere outgoing thermal radiation is a result of the interplay between surface temperature, cloud formation and atmospheric dynamics. In the case of a 1:1 SOR dry exoplanet, with no thick atmosphere, the planet would be characterised by stark thermal contrast between its permanent day and night sides. This would result in a sharp thermal emission peak near secondary eclipse and minimal thermal emission near transit [Koll & Abbot, 2015]. In the case of a simulated 1:1 SOR exoplanet with a coupled slab ocean, the amplitude of the phase curve would be reduced, as the temperature contrast between the day and the night side would be less stark with respect to the dry case. While the maximum surface temperature coincides with the substellar point, the day hemisphere is shrouded in thick symmetric clouds, which would cause reduced observed thermal emission at the top of the atmosphere. This results in peaks corresponding to transits and troughs corresponding to secondary eclipses (for instance, broadband thermal emission phase curves calculated for temperate aquaplanets shown in Wolf et al. [2019]). These simplified examples of phase curves, shown in the top panels of Figure 4.5.1, assume no significant horizontal heat transport - simulated in coarse GCMs with no meridional barriers by unrealistically strong equatorial jets - and no appreciable cloud advection due to strong atmospheric circulation. These would result in a longitudinal shift of the planetary outgoing longwave emission. Moreover, we assume a temperate mean state of the climate, comparable to the one simulated in our cases, and associated with a planet orbiting in the middle range of the habitable zone.

We compare our results, obtained for a 3:2 SOR scenario by employing a coupled atmosphere-ocean general circulation model equipped with a full-depth dynamic ocean, to 1:1 SOR idealised results in Figure 4.5.1. We find that both a fast and a slow rotation regime result in phase curves characterised by significantly different features compared

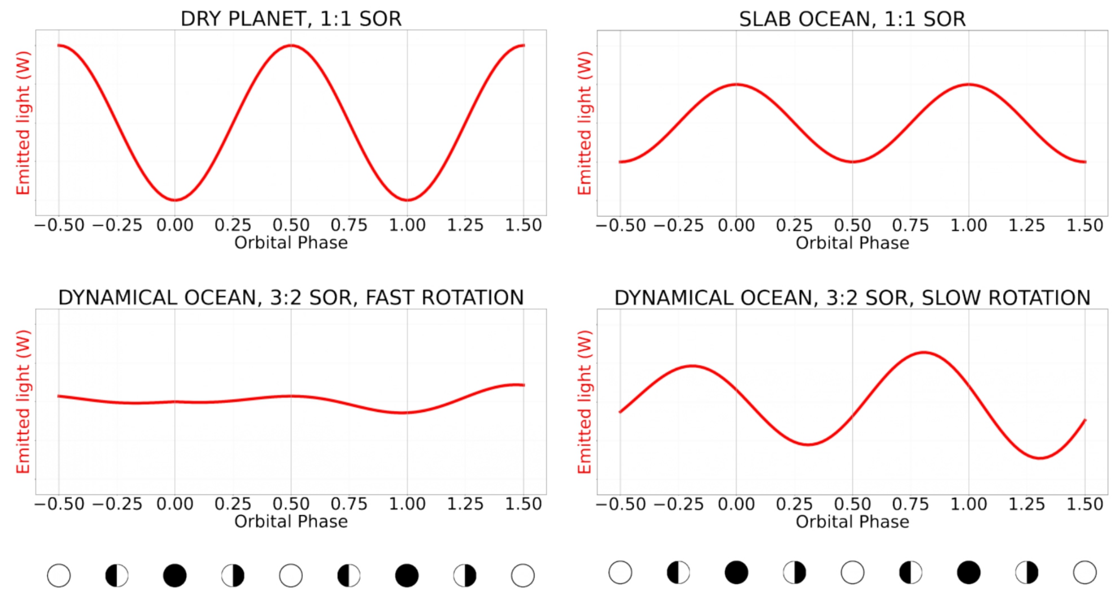

Figure 4.5.1: Thermal emission phase curve schematics for idealised 1:1 SOR and our 3:2 SOR scenarios.

with the synchronous rotation scenario, meaning that discerning between the two SORs might be possible from thermal emission observations. In the case of a fast rotation regime, the more homogeneous atmosphere results in a smoother phase curve, with little evidence of peak and troughs. In the case of a slow rotation regime, the longitudinal shift of outgoing longwave radiation as a consequence of the shifted position of the peak in rainfall results in an offset of the thermal emission phase curve. With respect to the 1:1 SOR slab ocean scenario, the phase curve in this case presents a negative shift, with an evident asymmetry with respect to the mid point of the transit. Moreover, the impact of ocean dynamics in combination with a “Ridgeworld” continental configuration results in an orbital phase-dependent amplitude of the curve. The importance of ocean circulation in shaping planetary climates, and therefore potential observables, is evident: this appreciable effect is triggered by a submerged continental barrier, and would undoubtedly be even more pronounced for actual continents, that could introduce an additional longitudinal asymmetry linked to different surface types.

Climate simulations of similar scenarios differing exclusively for the initial position of the barrier with respect to the substellar point would present the same longitudinal shift in maximum surface temperature, peak rainfall and minimum outgoing longwave radiation. The initial position of the barrier with respect to the observer would influence the shape of the thermal emission phase curve (for instance, the amplitude of consecutive peaks and troughs), but not its offset. This is a consequence of different portions of the planetary surface being in the field of view of the observer. As mentioned in the Observables section, the longitude specific feature of the barrier introduces asymmetries in the planetary thermal emission associated with the same orbital configuration during consecutive orbits.

We note that, although several climate studies regarding 1:1 SOR exoplanets simulate the position of the surface temperature maximum to roughly correspond to the substellar point location, numerous papers have demonstrated how a hot spot offset is highly sensitive to several different factors. Efficient atmospheric/oceanic horizontal heat transport and robust equatorial jet streams can cause an eastward shift of the hot spot with respect to the substellar point (for instance, Showman & Polvani [2011]; Hammond & Pierrehumbert [2018]; Hammond & Lewis [2021]). Ocean dynamics influences surface temperatures and atmospheric patterns, and can result in lobster-like spatial pattern instead of eyeball configurations (for instance, [Del Genio et al., 2019a]). Various other parameters play an important role in determining climate patterns in this scenario, such as stellar flux, atmospheric composition, planetary rotation rate, surface gravity, planetary radius, and cloud particle size (for instance, Komacek & Abbot [2019]). The extreme sensitivity not only to the choice of parameter values, but also to physical parameterizations and model architecture complexity and resolution, warrant a vast range of further study of planetary climate states. This issue has prompted the development of a model intercomparison study specifically for synchronous planets orbiting low-mass stars [Haqq-Misra et al., 2022], in an ongoing effort to systematically evaluate model performance and achieve a consistent framework that would allow a realistic interpretation of planetary environments from future observational data.

The feasibility of relying on this kind of study to infer information from observational data is still currently under development and is subject to continuous and further refinement. Theoretically, variations in reflectivity and outgoing longwave radiation may be leveraged to distinguish between different orbital configurations. However, for the case of temperate Earth-sized planets orbiting low-mass stars, this will require the capabilities of the next generation of observatories including the Large Interferometer For Exoplanets (LIFE) [Quanz et al., 2022b] and the Planetary Camera and Spectrograph (PCS) for the Extremely Large Telescope (ELT) [Kasper et al., 2021]. We estimate the photometric flux ratio between our simulated planets and an M host star to be $\sim 10^{-8}$, which is above the threshold contrast that the PCS can achieve for hypothetical exo-Earths orbiting nearby M-stars, assuming an adequate angular separation.

The next generation of ground- and space-based observatories have the potential to directly image nearby terrestrial exoplanets residing in the habitable zone of their host star through both thermal emission and reflected light, enabling their characterisation. This will allow the atmospheric characterisation of a statistically relevant sample of potentially habitable world candidates, which will require the implementation of realistic climate models in order to correctly interpret observational data. In this context, modelling studies such as the one presented in this paper will represent a useful tool develop a theoretical understanding of what future observations might be able to constrain.

4.6 Supplementary material

4.6.1 Phase curves computation

In order to compute the planet's thermal emission and reflected light phase curves from the model's top-of-atmosphere radiative fluxes, an evaluation of how both the visible and the illuminated hemispheres evolve with orbital phase is necessary. At each model output time t, the substellar point is determined from the orbital geometry, with the substellar longitude advancing according to the planet's rotation and orbital motion. Both an anticlockwise orbit and an anticlockwise spin rotation are assumed, the initial substellar longitude is fixed at 180° during the first secondary eclipse phase. The illuminated hemisphere is centered on the substellar point. Any point on the planetary surface can be formally classified as "illuminated" if the cosine of the stellar zenith angle $z_\star$, i.e. the angle between the local zenith direction and the host star, is such that $\cos z_\star > 0$. Assuming an edge-on orientation, the initial system configuration, i.e. the first secondary eclipse, is such that the visible hemisphere corresponds to the dayside of the planet. The center of the visible hemisphere in the initial configuration coincides with the initial position of the substellar point, with longitude 180°. Any point on the planetary surface can be formally classified as part of the visible hemisphere if the cosine of the observer zenith angle for an observer on Earth $z_\oplus$, i.e. the angle between the local surface normal and the observer, is such that $\cos z_\oplus > 0$. Figure 4.6.1 illustrates the system geometry as viewed from Earth, whereas Figure 4.6.2 shows the temporal evolution of the position of the illuminated and visible hemispheres for the $T_{\text{orb}} = 9$ day case.

In a 3:2 SOR, the substellar point shifts by 180° in longitude for every orbital period, and realigns with its initial position after a whole stellar period has passed. After a stellar period, the initial configuration is reinstated, with the substellar point and centre of the visible hemisphere aligned at longitude 180°. The orbital phase, defined by the star-planet-observer geometry, determines the overlap between the illuminated and visible hemispheres. During secondary eclipses (phases $n \pm 0.5$, with n integer), the observer views the fully illuminated dayside, whereas during transits (phases n) only the nightside is visible. Intermediate phases reveal varying fractions of the dayside and nightside.

The thermal emission phase curve is obtained by integrating the model's TOA upward longwave flux, $F_{\text{LW}}(\theta, \lambda, t)$, over the visible hemisphere. Each grid cell contributes in proportion to its projected area, equal to the area of the grid cell weighted by $\cos z_\oplus$, to take into account the viewing geometry. The disc-integrated thermal flux at time t is therefore:

$$F_{\text{thermal}}(t) = \iint_{\cos z_\oplus > 0} F_{\text{LW}}(\theta, \lambda, t) \cos z_\oplus \, a^2 \cos\theta \, d\theta \, d\lambda \quad . \tag{4.6.1}$$

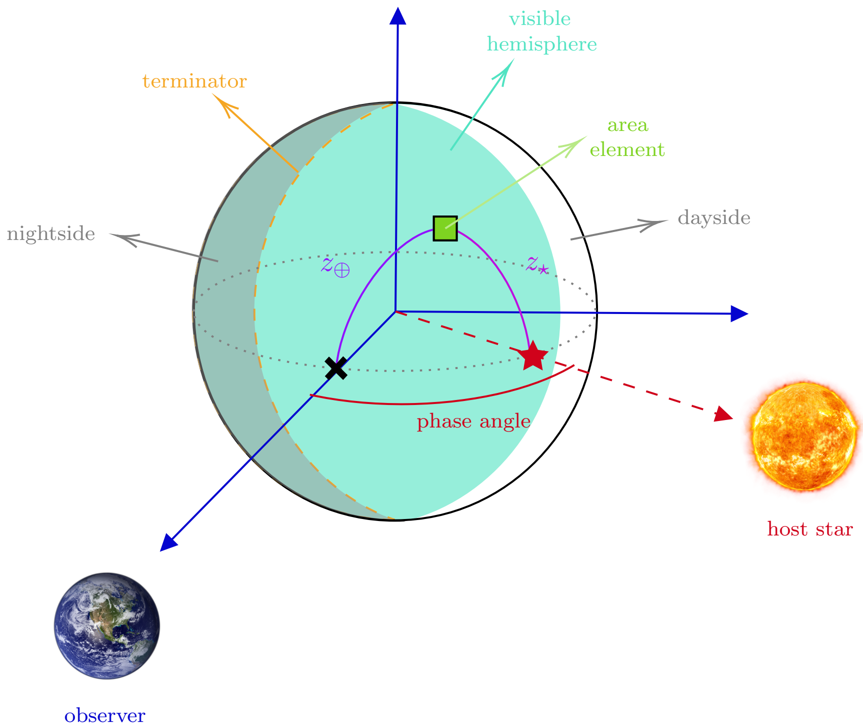

Figure 4.6.1: Geometry of the system for an exoplanet observed from Earth. The visible hemisphere (turquoise) is centred on the sub-Earth point (black cross), i.e. the location on the exoplanet closest to Earth. The illuminated hemisphere (white) is centred on the substellar point (red star). The observer and the stellar zenith angles (purple) describe the location of a grid cell (green).

The reflected-light phase curve was computed analogously, using the model's TOA upward shortwave flux, $F_{\mathrm{SW}}(\theta, \lambda, t)$. Only grid cells that were both illuminated and visible contributed to the reflected signal. The reflected flux at time t is thus:

$$F_{\text{reflected}}(t) = \iint_{\substack{\cos z_\oplus > 0 \\ \cos z_\star > 0}} F_{\mathrm{SW}}(\theta, \lambda, t) \cos z_\oplus \, a^2 \cos\theta \, d\theta \, d\lambda \quad . \tag{4.6.2}$$

Such disc-integrated quantities describe the variation of emitted and reflected light at any time t by capturing the evolution of the shape of the illuminated and visible crescents as the planet moves through its orbit, as well as any spatial variation or pattern of the fluxes in time. In order to obtain the phase curves, the integrations are repeated for a fixed time of 1800 days, corresponding to 100 stellar periods for the fast rotation case and 30 stellar periods for the slow rotation case, across all orbital phases.

To obtain an averaged phase curve from multiple simulated observations that span multiple stellar periods, disc-integrated quantities for each model output time, $F(t)$, are composited as a function of orbital phase. Each time t is associated with a discrete orbital phase $\alpha(t)$. Because the model samples the same discrete set of orbital phases in each stellar period,

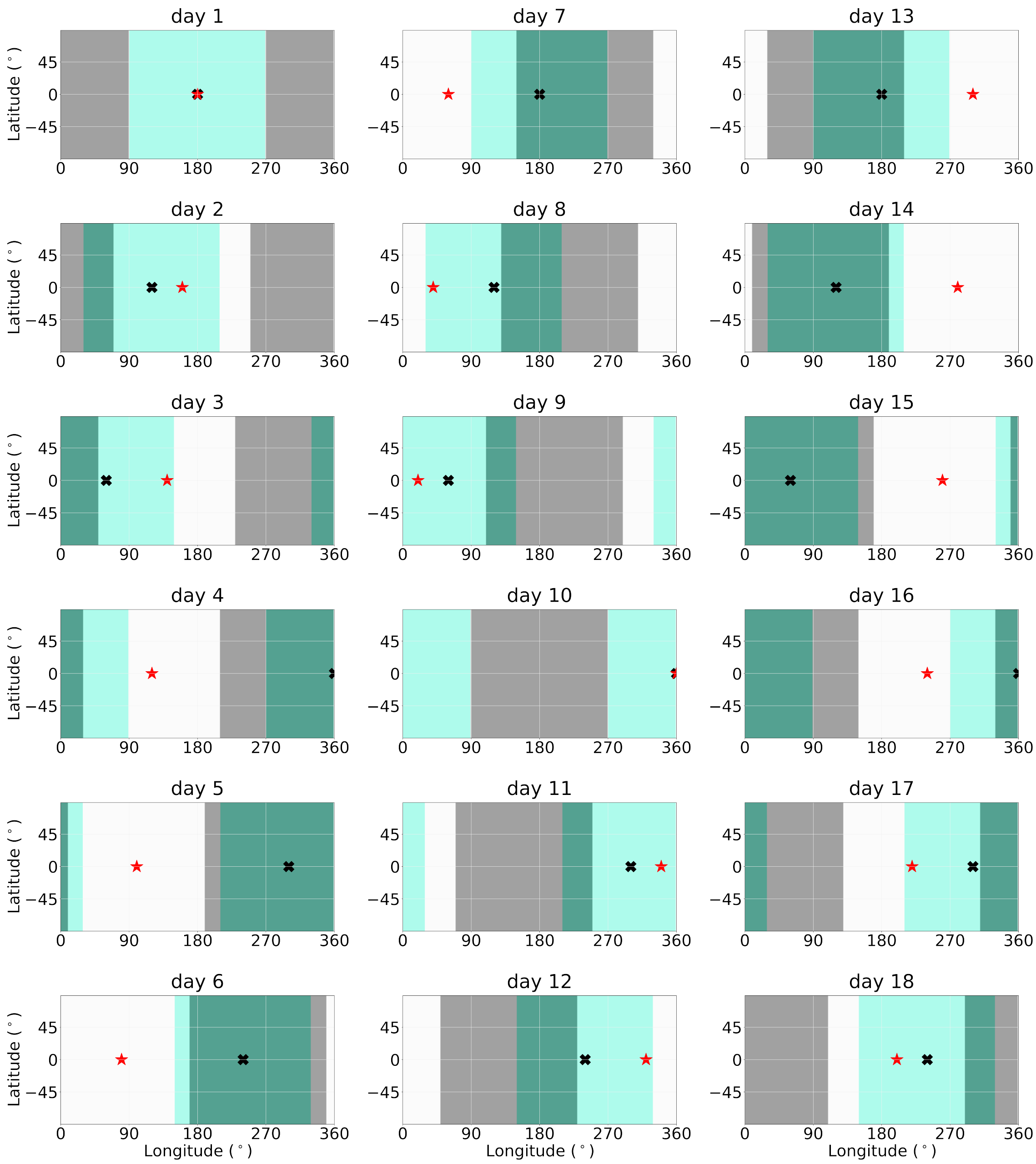

Figure 4.6.2: Observing geometry, assuming both an anticlockwise orbit and an anticlockwise spin rotation, as well as an edge-on orientation for the $T_{orb} = 9$ days scenario. White/gray hemispheres represent the day/night sides at each point of the orbit. The substellar point is represented by the red star, centred on the dayside. The turquoise hemispheres represent the observable portion of the planet, centred on the black cross. The three columns represent three separate rotation periods, or one single stellar period. Secondary eclipses correspond to phases in which the illuminated (white) and observed (turquoise) hemispheres fully overlap, while transits correspond to phases in which the dark (grey) and observable (turquoise) hemispheres fully overlap, with the illuminated (white) hemisphere being completely disjointed.

every phase α_i occurs multiple times. The composited signal is therefore obtained by averaging all $F(t)$ corresponding to the same α_i:

$$\bar{F}(\alpha_i) = \frac{1}{N_i} \sum_{\{t:\alpha(t)=\alpha_i\}} F(t) \quad , \tag{4.6.3}$$

where N_i is the number of occurrences of phase α_i in the selected temporal interval. Thus, the obtained phase curve represents the mean disc-integrated flux as a function of orbital phase. A larger number of samples at each phase angle, N_i, is desirable to improve the statistical robustness of the composite phase curve, as it allows to reduce the influence of transient features that are not phase-locked, therefore ensuring that the resulting phase curve reflects the underlying behaviour of the model rather than stochastic fluctuations. In the limit of large N_i, the composite phase curve converges toward the true phase-dependent signal predicted by the model. Similar compositing calculations were carried out to obtain averaged quantities (such as surface temperature or total rainfall) as a function of stellar day.

Long, continuous phase-curve observations of exoplanets remain challenging because they require uninterrupted monitoring over one or more full orbits, which is often limited by spacecraft scheduling, visibility windows, and instrumental stability. As a result, the longest continuous phase-curve sequences of specific exoplanets to date span a few orbits at most with JWST (e.g. 59 hours for Gillon et al. [2025]), while the largest number of orbits composited into a phase curve comes from long-baseline photometry missions such as Kepler, which monitored the same field for years and enabled phase-curve analyses built from hundreds of repeated orbits [Angerhausen et al., 2015]. Therefore, short-period planets are inherently easier to characterise, allowing full-orbit coverage within a single observing window and reducing susceptibility to long-term drifts. However, in a scenario such as the one analysed here, shorter period exoplanets may exhibit higher climatic variability and therefore yield noisier signals. Future facilities are expected to improve phase-curve capabilities, potentially enabling higher-precision characterisation of planetary signals over many orbits.

4.6.2 Ocean-driven modulation of phase curves

Figures 4.4.4 and 4.4.7 show climate patterns averaged over the equatorial band (5°S - 5°N), where the heating forcing is strongest owing to the system's geometry. Considering latitude-integrated quantities provides a means to determine whether longitude-dependent features persist at higher latitudes and therefore can manifest as observable imprints. Such an analysis may uncover additional patterns emerging away from the equator, such as the ones linked to the western boundary currents at mid and high latitudes. Alternatively, it can indicate that the equatorial patterns may be localized (for instance, equatorial upwelling is specific to 5°S - 5°N latitudes) and become effectively muted in the disc-integrated signal, despite the equatorial band contributing the largest projected area in the viewing geometry.

Section 4.4.3 briefly notes that ocean circulation influences the time dependence of the thermal emission light curve amplitude. Figure 4.6.3a illustrates this effect clearly: in addition to the heating signature associated with the substellar point, a persistent surface-temperature anomaly appears near the longitude of the meridional barrier (240°). This feature arises from the heat transport from the equator toward higher latitudes, driven by the gyre circulation that develops in the presence of the barrier. As a result, the temperature averaged over all latitudes is systematically elevated at this longitude, independent of orbital phase. This longitudinally fixed structure becomes more pronounced in the high-diffusion simulations due to the enhanced circulation and associated heat transport compared to the low-diffusion simulations, as discussed in Di Paolo et al. [2025].

In contrast, no such feature is present in the thermodynamic ocean configuration (Figure 4.6.3b). Regarding the surface temperature averaged over the equatorial band, the latitude-averaged surface temperature is dominated almost entirely by the substellar heating pattern. A comparable behaviour would also likely be expected for a "Waterworld" configuration under the same 3:2 SOR scenario. As discussed in Section 3.7.2, heat transport into mid and high latitudes is strongly suppressed in this case. The absence of meridional barriers to zonal flow yields negligible mean meridional circulation and only weak poleward heat transport from the equator compared to the Ridgeworld configuration. Consequently, the surface temperature field, and the associated climate patterns, would primarily scale with the imposed heating distribution, with a longitudinal shift due to the thermal inertia of the ocean.

As noted in Section 4.4.3, the thermal-emission light curve for the dynamical case with $\kappa = 150\,\kappa_{\oplus}$ and $T_{\mathrm{orbital}} = 30$ days exhibits a first peak that is marginally smaller than the second. The top-of-atmosphere upward longwave flux on the visible hemispheres corresponding approximately to the orbital phases of the two consecutive peaks are shown in Figure 4.6.4 for both the dynamic ocean and thermodynamic ocean simulations. Near the first peak, the meridional barrier lies close to the western edge of the visible hemisphere. In the dynamic ocean case (Figure 4.6.4a), the visible portion of the planet therefore includes the region east of the barrier that is influenced by the ocean-driven climate patterns. Conversely, during the second peak, the visible hemisphere encompasses the region west of the barrier.

The difference between the top-of-atmosphere upward longwave flux at the two peaks reveals a systematically weaker signal - particularly at higher latitudes - during the first peak in the region east of the barrier (Figure 4.6.4b). As a result, the disc integrated

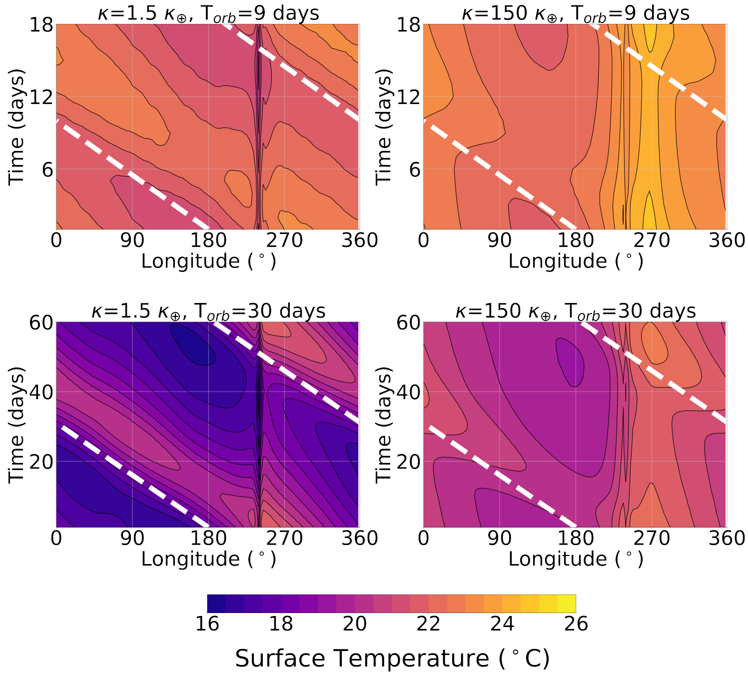

(a)

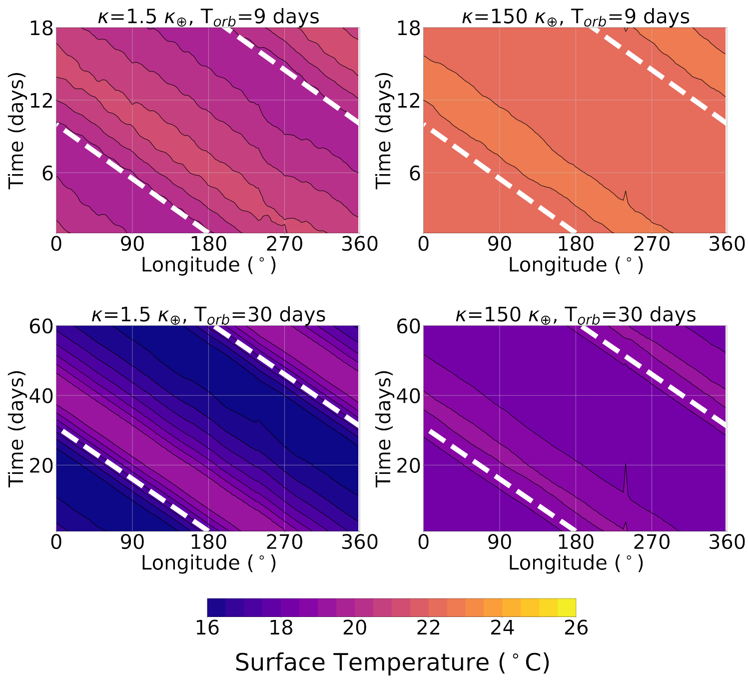

(b)

Figure 4.6.3: Hovmöller diagram showing composite surface temperature averaged over all latitudes and over the last 100 stellar periods. White dashed lines represent the location of the substellar point. (a) Dynamic ocean simulations, (b) thermodynamic ocean simulations.

top-of-atmosphere longwave flux is smaller for the first peak. In the thermodynamic ocean simulation (Figure 4.6.4c), no comparable longitudinal contrast is present: the two distributions of upward longwave flux are nearly indistinguishable (Figure 4.6.4d), and the corresponding light-curve peaks have essentially the same amplitude.

Similarly to the behaviour described for the light-curve peaks, the amplitudes of the troughs are also influenced by ocean gyres. The top-of-atmosphere upward longwave flux on the visible hemispheres corresponding approximately to the orbital phases of two consecutive troughs is shown in Figure 4.6.5 for both the dynamic ocean and thermodynamic ocean simulations. During the orbital phase associated with the first trough, the meridional barrier lies nearly diametrically opposite the sub-observer point, roughly at the centre of the unobservable hemisphere. By the time of the second trough,

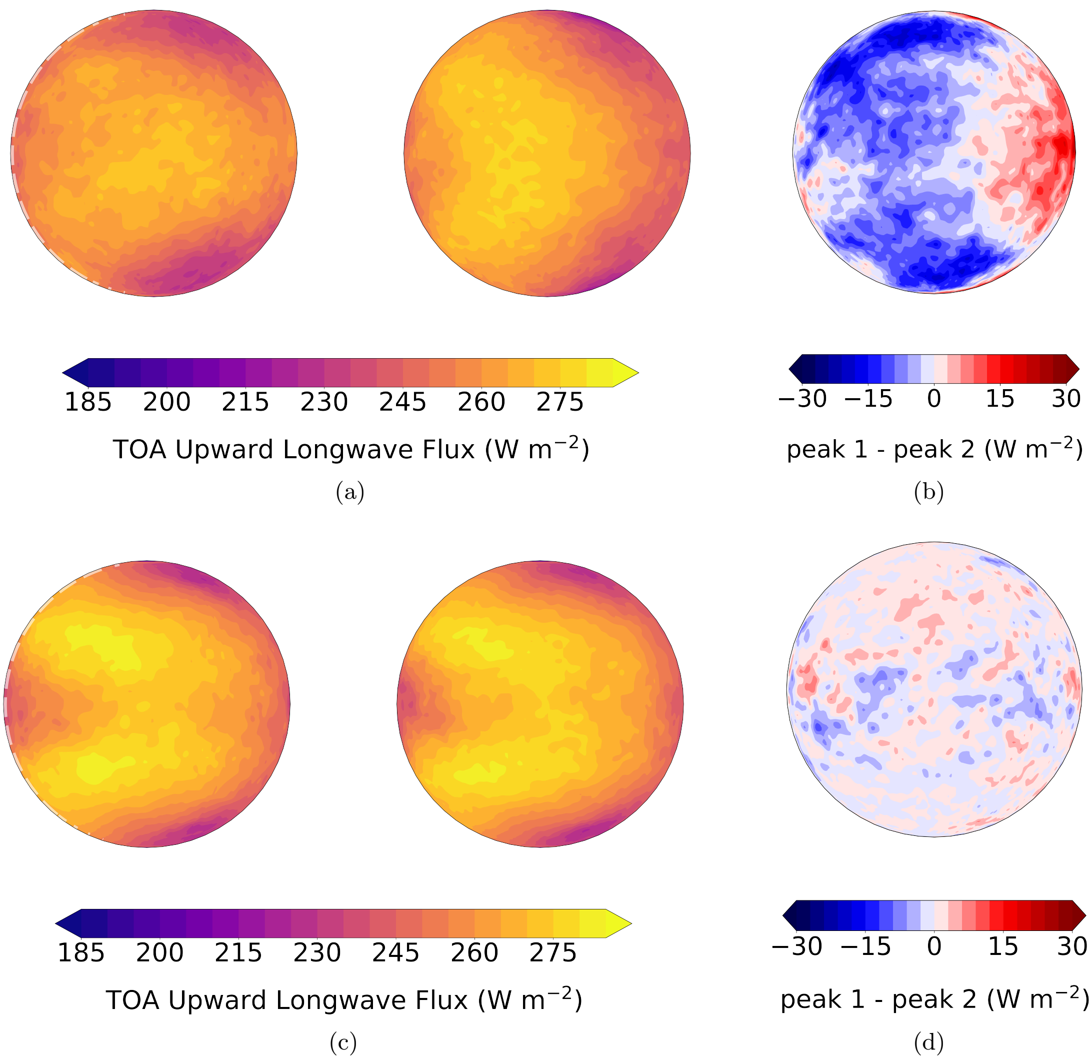

Figure 4.6.4: Top-of-atmosphere upward longwave flux of the the $\kappa = 150\ \kappa_{\oplus}$, $T_{orb} = 30$ days scenario. Visible hemisphere at the phases corresponding to the first and second peaks of the light curve for the dynamic ocean simulations (a) and the thermodynamic ocean simulations (c). Difference between the two fields for the dynamic ocean simulations (b) and the thermodynamic ocean simulations (d). The position of the barrier is represented by the white dashed lines.

the barrier has rotated to a position just east of the sub-observer point.

In the dynamic ocean simulation, the flux distribution during the second trough exhibits reduced emission at mid and high latitudes east of the barrier compared with the corresponding visible regions during the first trough (Figure 4.6.5b). At low latitudes, however, the signal is enhanced during the second trough: the strong heating associated with the substellar point west of the barrier is redistributed by the ocean circulation, leading to comparatively lower temperatures and reduced precipitation east of the barrier, and therefore a larger upward longwave flux than in the first trough

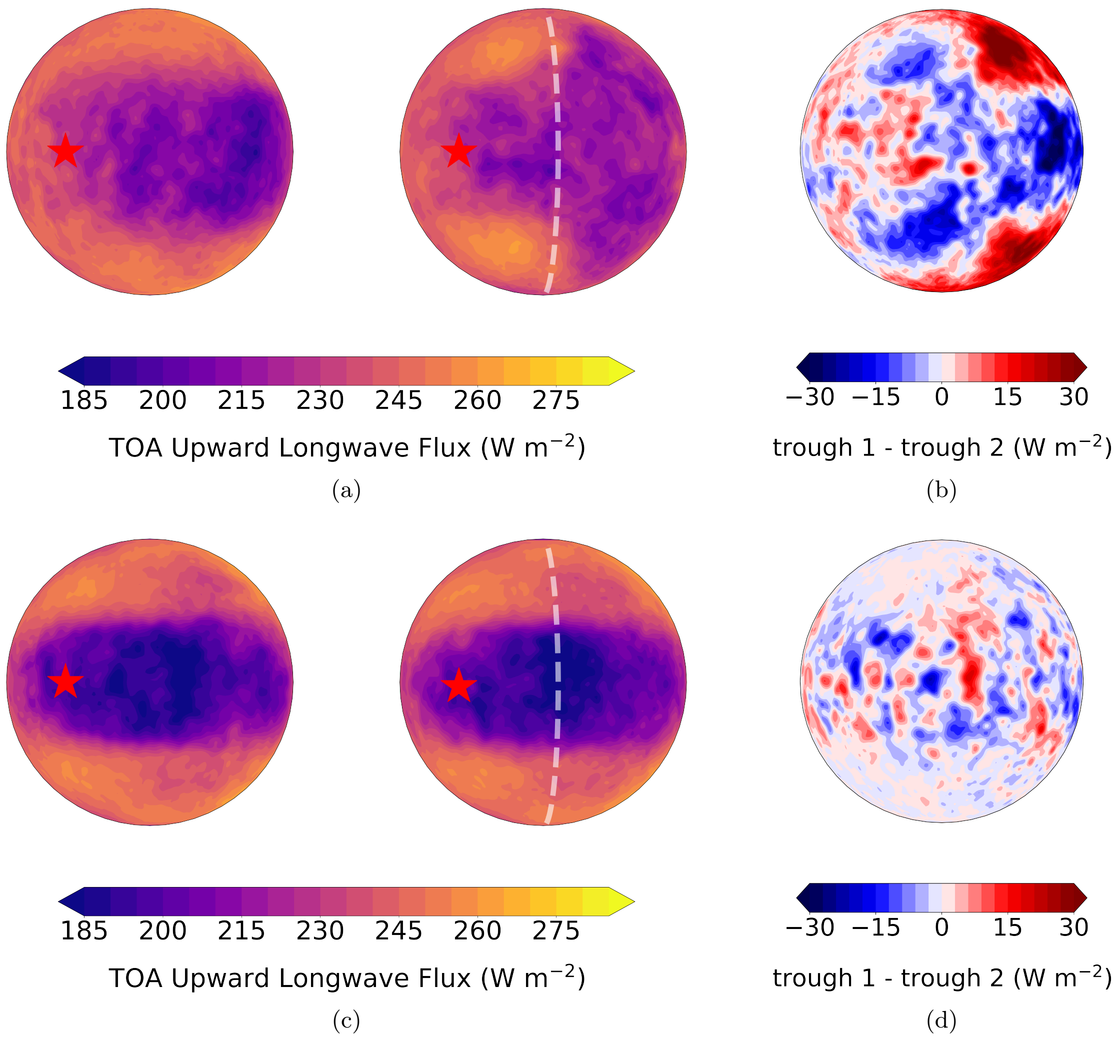

Figure 4.6.5: Top-of-atmosphere upward longwave flux of the the $\kappa = 150\ \kappa_{\oplus}$, $T_{orb} =$ 30 days scenario. Visible hemisphere at the phases corresponding to the first and second troughs of the light curve for the dynamic ocean simulations (a) and the thermodynamic ocean simulations (c). Difference between the two fields for the dynamic ocean simulations (b) and the thermodynamic ocean simulations (d). The position of the barrier is represented by the white dashed lines. The substellar point is represented by the red star.

configuration, where the substellar heating remains confined to lower latitudes. The resulting disc-integrated flux produces a deeper second trough.

In the thermodynamic ocean case, the flux patterns are significantly more uniform between the two troughs. The dominant feature is a region of reduced thermal emission at low latitudes trailing the substellar point, and the difference field shows no longitude-dependent structure associated with the position of the barrier (Figure 4.6.5d). Consequently, the two troughs have nearly identical amplitudes.

The fact that the top-of-atmosphere upward longwave flux differs at the same phase angle - that is, for the same relative position between planet, star, and observer - demonstrates that compositing observations over multiple orbits, instead of over stellar periods, would potentially obscure zonal asymmetries in the planetary climate. Here, the asymmetries linked to the position of the meridional barrier are associated with regions of elevated surface temperature and enhanced precipitation, but more pronounced spatial contrasts could arise on planets with significantly different regional climates, such as the coexistence of glaciated and thawed regions in a “double-eyeball” configuration, which would rotate into and out of view at different orbital phases. Moreover, the configuration explored here includes a submerged meridional barrier, and thus zonally symmetric surface albedo - as aside from the polar islands, the planet is entirely ocean-covered - meaning that zonal asymmetries near the barrier are directly ascribable to ocean circulation. Alternative continental geometries, however, could introduce much stronger longitudinal contrasts in both thermal emission and reflected light.

These considerations are also relevant regarding spectral observations. Braam et al. [2025] generated synthetic emission spectra across the wavelength range of the Large Interferometer for Exoplanets for Proxima b in both 1:1 and 3:2 SORs, finding spectral fluctuations up to 36 ppm (i.e. a fractional deviation of 36×10^{-6} relative to the stellar flux) over an orbit in the 1:1 case due to strong spatial and temporal asymmetries, whereas comparatively constant spectra in the 3:2 configuration due to largely suppressed dayside-nightside contrast yielding a more zonally homogeneous atmosphere. On this basis, they proposed that spectral variability may serve as an observational discriminant between 1:1 and 3:2 SORs. As shown here, phase-dependent zonal asymmetries can arise in 3:2 SORs scenarios, potentially introducing time-dependent spectral fluctuations that could complicate or weaken this diagnostic.

Overall, the dynamical features identified in these simulations are likely to manifest in the corresponding synthetic transmission spectra. Ocean circulation and the associated climate patterns can modify the structure of the terminator region, particularly at high latitudes and in the region east of the barrier. When this portion of the planet is probed during transit, the resulting circulation patterns can generate regions of reduced top-of-atmosphere upward longwave radiation at high-latitudes, as well as differences between the morning and evening limbs arising from zonal asymmetries. Such features could imprint on the transmission spectra, with especially cloudy terminator regions producing flattened spectra and suppressed molecular absorption features. As for the modulation of the thermal emission light curve amplitude, the magnitude of these effects depends on the initial position of the barrier relative to the substellar point.

4.6.3 Mean climate state

All simulated configurations, spanning both low and high ocean vertical diffusivities and both fast and slow rotation rates, produce temperate climates. Earth-like rotation scenarios ($T_{\rm orb}$ = 360 days, $T_{\rm rot}$ = 1 day) discussed in Chapter 3 yield mean climate states that more closely resemble the faster-rotation case ($T_{\rm orb}$ = 9 days, $T_{\rm rot}$ = 6 days) than the slower-rotation case ($T_{\rm orb}$ = 30 days, $T_{\rm rot}$ = 20 days). Faster rotation generally results in overall warmer mean surface temperatures than slower rotation (left panel of Figure 4.6.6). In all scenarios, surface temperatures peak at low latitudes, with the warmest values occurring under low-diffusion conditions, while high-latitude temperatures remain substantially colder than in the corresponding high-diffusion cases. Meridional gradients are substantially reduced under high vertical diffusion due to enhanced ocean circulation (consistent with the analysis presented in Chapter 3): from 24.9°C (19.4°C) in the fast (slow) rotation under low-diffusion to 12.4°C (10.9°C) in the corresponding high-diffusion case. Overall, climates with the same diffusivity but different rotation periods remain more similar to one another than climates with different diffusivities under the same rotation rate.

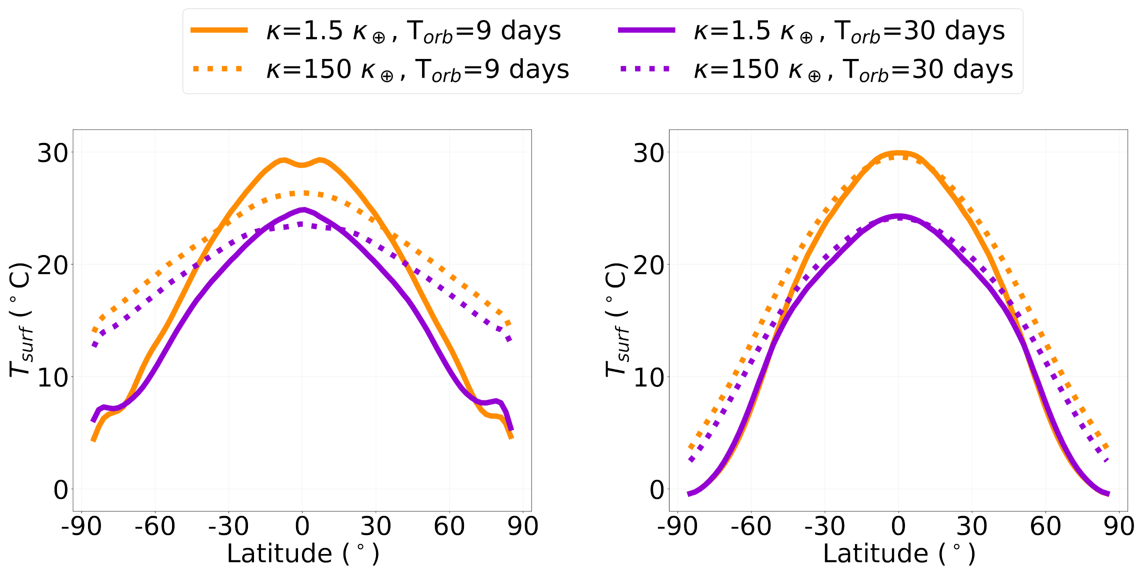

Figure 4.6.6: Surface temperature as a function of latitude for different SOR scenarios. Dynamic ocean simulations (left), thermodynamic ocean simulations (right). Quantities are averaged over the last 100 stellar periods for each simulation.

Adopting a thermodynamic ocean model produces larger meridional temperature gradients compared to the dynamic ocean simulations, with systematically warmer equatorial regions and colder polar regions across all scenarios (right panel of Figure 4.6.6). Variations in vertical diffusivity have only a minor influence on the zonally averaged surface temperature compared with the dynamic ocean simulations; instead, the rotation period exerts the dominant control on the resulting climate. At low latitudes (∼45°S-45°N), simulations with the same rotation period exhibit similar temperature regardless of diffusivity. Divergences emerge only poleward of ∼45°, where simulations with the same diffusivity exhibit similar temperature despite different rotational scenarios. In these high-latitude regions, increased vertical diffusion produces only modest warming.

Across all scenarios and with both ocean model versions, faster rotation consistently produces overall warmer surface temperatures than slower rotation, with the largest differences occurring at low latitudes. This warming arises from a weaker dayside cloud-albedo feedback in the fast-rotation regime, associated with a weaker rainfall signal as discussed in 4.4.2, which allows bigger heat flux into the ocean (Figure 4.6.7). At higher latitudes, a more efficient poleward heat transport in high diffusion cases leads to higher surface temperatures, enhanced precipitation and reduced heat flux compared to the low diffusion scenarios.

Consistent with the Earth-like rotation experiments discussed in Chapter 3, volume-averaged temperatures are substantially warmer at all latitudes in the high-diffusion cases compared with the low-diffusion cases, reflecting the enhanced

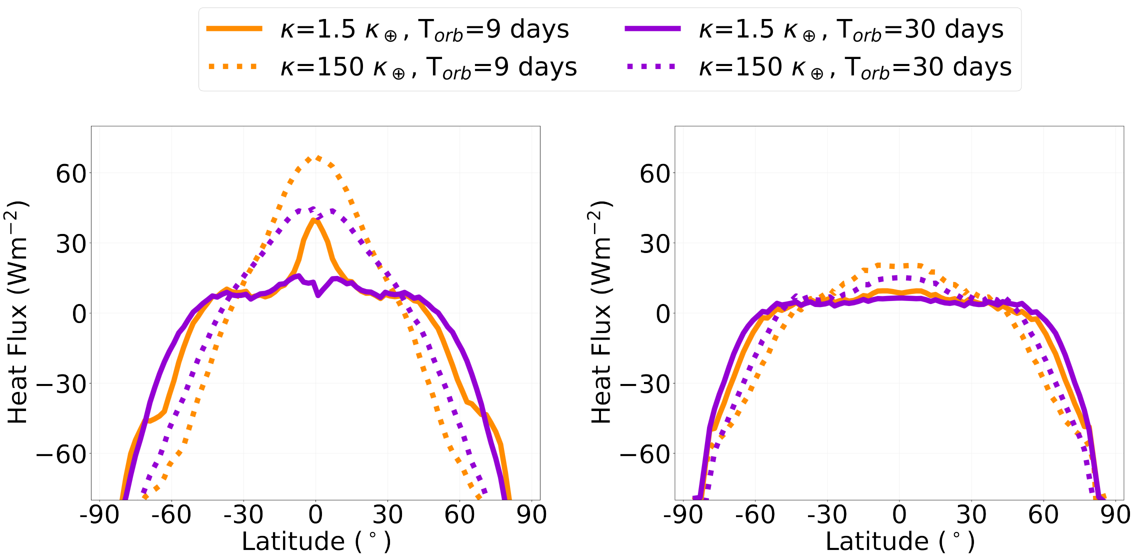

Figure 4.6.7: Heat flux into the ocean as a function of latitude for different SOR scenarios. Dynamic ocean simulations (left), thermodynamic ocean simulations (right). Quantities are averaged over the last 100 stellar periods for each simulation.

oceanic circulation (Figure 4.6.8). Both global averages and latitudinal profiles of volume-averaged ocean temperature in the Earth-like rotation scenario (Figure 3.6.3b) are marginally more similar to those of the corresponding fast rotation simulations than to those of the slow rotation simulations. The global volume-mean temperature is ∼ 8.3°C (∼ 21.6°C) for low (high) diffusion under Earth-like rotation, ∼ 6.6°C (∼ 22.0°C) for fast rotating 3:2 SOR configurations, and ∼ 6.6°C (∼ 19.9°C) for slow rotating 3:2 SOR scenarios. Because strong vertical diffusion efficiently warms the deep ocean, the latitudinal profiles of volume-averaged temperature in the high-diffusion cases closely resemble the corresponding surface-temperature profiles. In contrast, low-diffusion cases exhibit colder and flatter profiles, reflecting the persistence of low temperatures at depth. Simulations employing a thermodynamic ocean (right panel of Figure 4.6.8), in which poleward ocean heat transport is strongly suppressed, exhibit markedly larger meridional temperature gradients across all rotation scenarios compared with the dynamic ocean simulations, with comparatively warmer low latitudes and colder high latitudes.

Ocean heat transport increases systematically with vertical diffusivity across all dynamic ocean simulations, ranging from 2.19 PW (1.96 PW) in the fast (slow) rotation, low-diffusion cases to 5.31 PW (4.04 PW) in the corresponding high-diffusion cases (left panel of Figure 4.6.9a). Ocean heat transport is substantially weaker in the thermodynamic ocean simulations, where increasing vertical diffusivity produces only a modest enhancement of poleward heat transport, with a maximum of 2.13 PW attained under fast rotation. Scaling arguments for the dependence of ocean heat transport on rotation rate generally predict stronger transport under slower rotation [Vallis & Farneti,

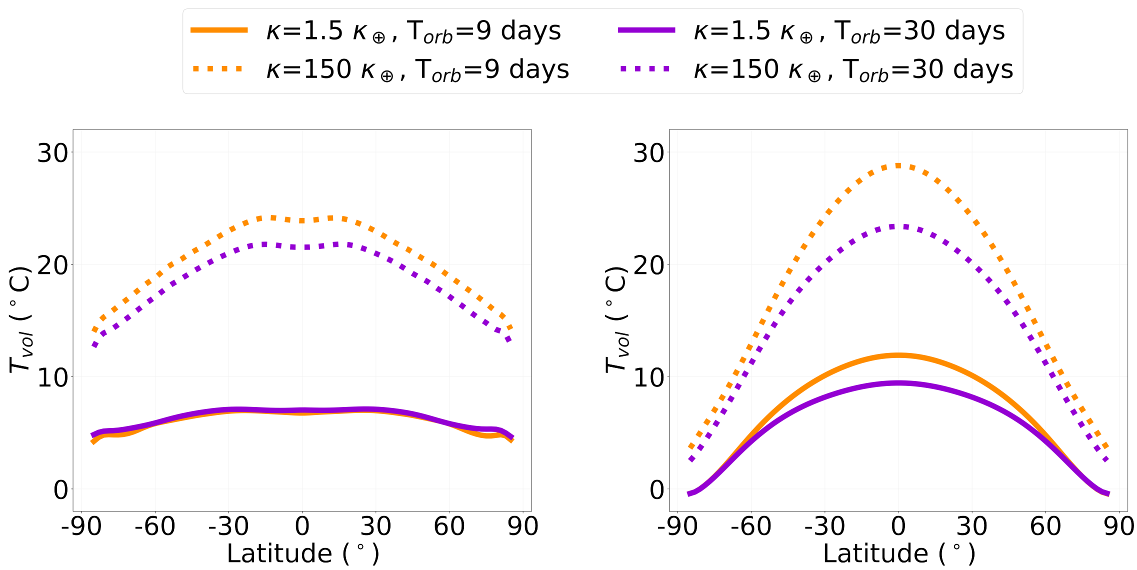

Figure 4.6.8: Volume-averaged temperature as a function of latitude for different SOR scenarios. Dynamic ocean simulations (left), thermodynamic ocean simulations (right). Quantities are averaged over the last 100 stellar periods for each simulation.

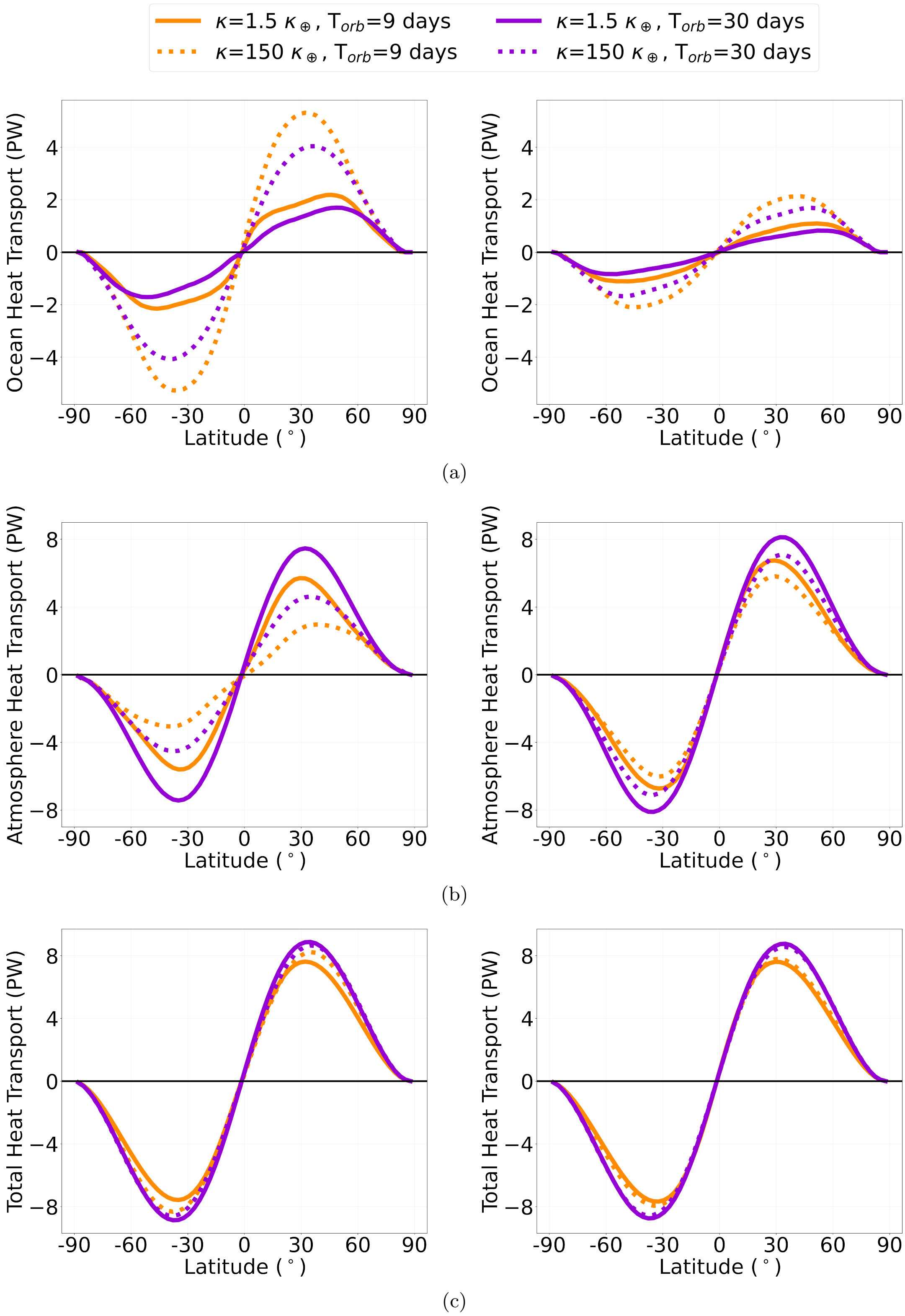

Figure 4.6.9: Ocean (a), atmosphere (b), and total (c) heat transport as a function of latitude for different SOR scenarios. Dynamic ocean simulations (left), thermodynamic ocean simulations (right). Quantities are averaged over the last 100 stellar periods for each simulation.

2009; Cullum et al., 2014]. However, applying these scalings directly to our experiments is not straightforward, as different scenarios are accompanied by changes in the forcing. Overall, ocean heat transport is largest in simulations where the net heat flux into the ocean is maximised, which occurs under fast rotation in these simulations.

Conversely, atmospheric heat transport is minimised in the faster rotation scenarios (Figure 4.6.9b), consistent with studies showing that rapidly rotating planets exhibit increasingly less efficient meridional heat transport due to smaller and weaker Hadley cells and smaller eddy length scales as rotation period shortens [Kaspi & Showman, 2015; Liu et al., 2017; Guendelman & Kaspi, 2019]. Here, atmospheric heat transport peaks at 5.70 PW (2.96 PW) in the low (high) diffusion fast rotation cases, compared with 7.46 PW (4.61 PW) in the corresponding slow rotation cases. In all cases, atmospheric heat transport exceeds that of the Earth-like rotation experiments, which reach only 3.34 PW (1.50 PW) in the low (high) diffusion configurations. Thermodynamic ocean simulations yield even larger atmospheric heat transport across all rotation rates, with a maximum of 8.12 PW occurring in the slow rotation, low diffusion case.

An imperfect compensation between oceanic and atmospheric heat transport leads to broadly similar total heat transport profiles across all scenarios (Figure 4.6.9c). Planets captured in spin-orbit resonances constitute another case in which Bjerknes compensation [Bjerknes, 1964], though not complete, appears to hold. Reduced ocean heat transport at slower rotation rates is compensated by enhanced atmospheric heat transport, and vice versa for faster rotation rates. As a result, total heat transport varies only modestly among the simulations, with maximum values differing by approximately 1.27 PW. Overall, slower rotation rates tend to produce slightly stronger total heat transport in both the dynamic and thermodynamic ocean configurations. Total heat transport in the Earth-like rotation case reaches a maximum of 5.67 PW in the high diffusion scenario, a value about a third lower than those obtained in any of the SOR simulations.

The crucial role of ocean dynamics in shaping planetary climate is illustrated by the surface temperature maps in Figure 4.6.10. In both the dynamic and thermodynamic ocean simulations, enhanced vertical diffusion reduces meridional temperature gradients, warming the high latitudes and cooling the tropics. This effect is only marginal in the thermodynamic ocean case, with equatorial temperatures maintaining virtually unchanged temperatures across different diffusion scenarios. The dynamic ocean simulations exhibit features reminiscent of the Earth-like rotation experiments (Figure 3.6.4), including the formation of clear gyre structures east of the barrier, which are responsible for amplitude modulation of thermal emission phase curves. In contrast, surface temperatures in the thermodynamic ocean simulations are nearly zonally symmetric, similar to the "Waterworld" configuration discussed in Section 3.7.2. Notably, thermodynamic ocean cases with low diffusion, characterised by minimised poleward heat transport, develop sub-zero polar temperatures.

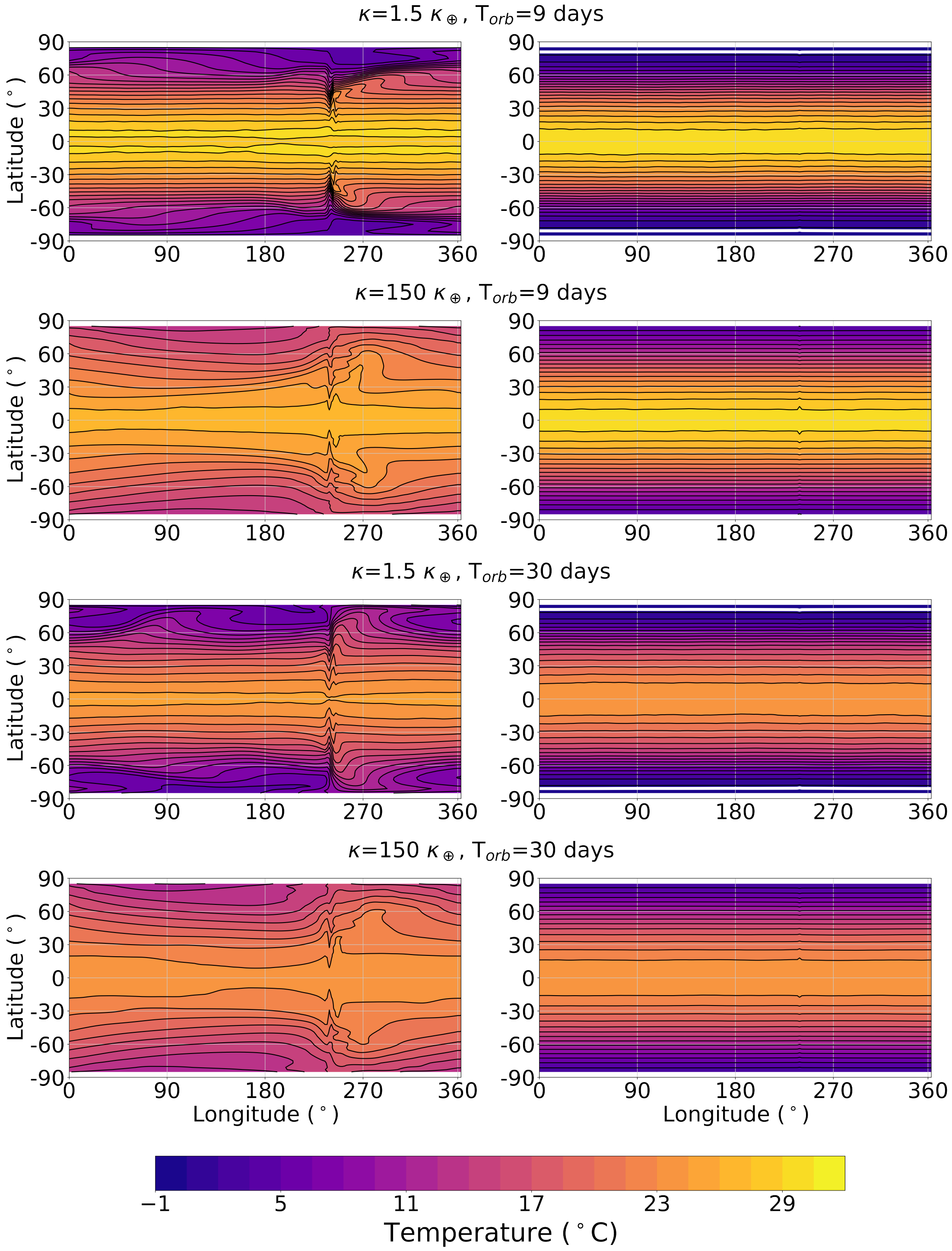

Figure 4.6.10: Sea surface temperature maps for dynamic ocean simulations (left) and thermodynamic ocean simulations (right). White lines demarcate the sub-zero temperatures. An analogous plot for the Earth-like rotation configuration is shown in Figure 3.6.4. Quantities are averaged over the last 100 stellar periods for each simulation.

4.6.4 Ocean dynamical waves

As discussed in Section 4.4.1, oceanic waves develop at depth as a consequence of the phase-locked pattern of alternating westerlies and easterlies. In the case with $\kappa = 1.5\,\kappa_\oplus$ and $T_{\rm orb} = 30$ days, these phase-locked dynamical waves persist regardless of the number of stellar periods over which the fields are composited.

The simulation with $\kappa = 1.5\,\kappa_\oplus$ and $T_{\rm orb} = 9$ days exhibits features that warrant further investigation (right panel of Figure 4.6.11). This scenario is characterised by low vertical diffusivity, which allows stratification, and should in principle permit the development of density anomalies, in contrast to the high-diffusion cases where surface heating is efficiently mixed downward and vertical stratification is weakened. However, relative to the slow rotation case, the zonal wind phase-locked signature is substantially weaker and less defined, and the surface temperature signal is reduced, because of the rapidly moving stellar forcing across the planetary surface. These factors together lead to weaker upwelling and downwelling and consequently smaller density anomalies. When averaging over the equatorial band (5°S–5°N) and compositing over 100 stellar periods, a sequence

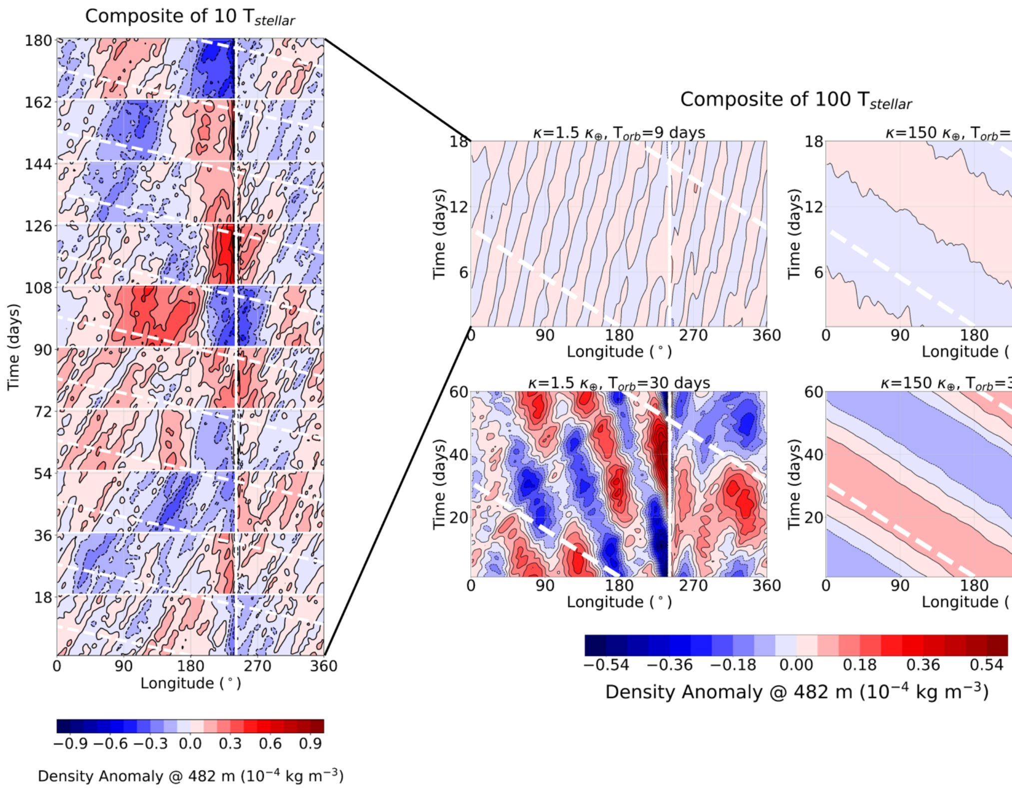

Figure 4.6.11: Hovmöller diagram showing density anomaly at 482 m of depth, between latitudes of 5°S and 5°N. White dashed lines represent the location of the substellar point. Composite quantities at the equator have been averaged over the last 100 stellar periods either into one composited stellar period (plots on the right) or into ten composited stellar periods (plot on the left).

of evenly spaced, frequently occurring eastward-propagating anomalies becomes apparent. Away from the longitudes immediately adjacent to the meridional barrier, the density anomalies peak at ~3 - 6 $\times 10^{-6}$ kgm^{-3}, approximately an order of magnitude smaller than those found in the $\kappa = 1.5\,\kappa_{\oplus}$, $T_{\text{orb}} = 30$ days case. Even near the barrier, their peak values remain roughly six times weaker than in the slower-rotation simulation. These slowly propagating anomalies appear too frequent to be directly linked to the stellar forcing, and consequently to the associated wind response. When compositing over only 10 stellar periods (left panel of Figure 4.6.11), these signals largely disappear.

To better characterise their nature, future work includes conducting a Wheeler-Kiladis analysis [Wheeler & Kiladis, 1999] by projecting the longitude-time density field onto wavenumber-frequency space, enabling equatorial wave modes to be isolated through their characteristic dispersion relationships. Such spectral decomposition would help filter and separate overlapping signals and identify distinct forms of propagating tropical variability differing in direction and frequency.

While such analysis may offer valuable insight into the dynamical processes operating within the ocean interior, it is important to emphasize that these features arise at depths greater than ~300 m and are entirely absent at the surface, where the signal is dominated by the stellar heating in all scenarios (Figure 4.6.12). Dynamical structures

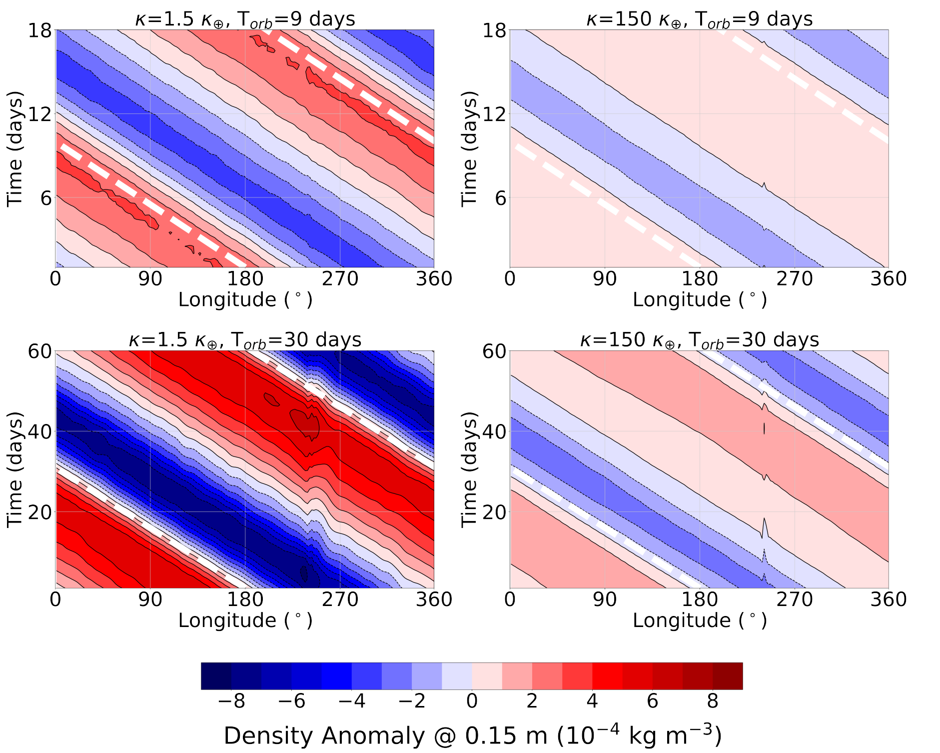

Figure 4.6.12: Hovmöller diagram showing density anomaly at 0.15 m of depth, between latitudes of 5°S and 5°N. White dashed lines represent the location of the substellar point. Composite quantities at the equator have been averaged over the last 100 stellar periods.

confined to deep ocean layers and not expressed at the surface produce no discernible signatures in either surface temperature or total rainfall (Figure 4.4.4). Consequently, they are effectively undetectable and do not contribute to the simulated phase curves (Figure 4.4.9a). Analyses of rainfall anomalies in time-longitude space, constructed analogously to the ocean density-anomaly diagnostics, do not reveal clear signatures of atmospheric wave propagation. This absence of coherent eastward- or westward-moving structures is consistent with the dominance of the stellar-heating pattern at the surface, which overwhelms any weaker dynamical variability. However, conducting a Wheeler-Kiladis spectral analysis in this case as well may uncover dynamical features that remain hidden in the simpler time-longitude composite representation, which can obscure variability that is intermittent, overlapping, or only weakly coherent in longitude.

The behaviour of the ocean dynamical waves in these simulations depends on the geometry of the imposed meridional ridge. Altering the ridge structure would modify the circulation. A ridge submerged to substantially greater depth would allow strong zonal currents to dominate, producing a dynamical scenario similar to that expected on an ocean world without a meridional barrier; in such a case, strong zonal flow may suppress density anomalies and associated dynamical waves. In contrast, extending the ridge to the ocean surface is not expected to produce qualitatively different dynamics from those obtained here, although some variation in signal amplitude may occur due to mild adjustments in the upper ocean. As in the present configuration - with the ridge submerged to 145 m - dynamical waves would still be expected to develop well below the barrier, where their signal becomes sufficiently strong to appear in longitude-time composites, while the surface remains dominated by the imposed stellar-heating pattern.

Changing the planetary rotation rate alters both the Coriolis parameter and its meridional gradient, which together govern the behaviour of equatorial Kelvin and Rossby waves. Faster rotation strengthens the meridional gradient of the Coriolis effect, narrowing the equatorial waveguide and producing tighter meridional trapping, while the stronger rotational restoring mechanisms can increase the westward phase speed of Rossby waves. As rotation slows and this restoring mechanism weakens, equatorial Rossby waves propagate more slowly, broaden meridionally, and become less distinct as a dynamical mode. Kelvin waves likewise exhibit reduced equatorial confinement, though they retain their phase speed, allowing the mode to persist even as it spreads meridionally.

4.7 Concluding remarks

This chapter has explored the climate dynamics of terrestrial exoplanets captured in 3:2 spin-orbit resonances around low-mass stars using a coupled AOGCM. By examining two distinct rotation periods and two tidal regimes, and by contrasting dynamic and thermodynamic ocean configurations, a range of processes, triggered by characteristic instellation patterns and shaping distinct climate features across the planetary surface, have been explored.

The longitudinal migration of the substellar point produces temperature and precipitation structures, with characteristic offsets of approximately 60° relative to the substellar point. These migrating features produce offsets in the planet's thermal emission phase curves, offering a potential observational discriminant between synchronous and resonant rotation states. Ocean dynamical processes produce potentially detectable signatures in such phase curves by modulating their amplitude in time. Although observationally inconsequential, deep-ocean dynamical processes substantially differ in each of the analysed scenarios, and offer opportunities to conduct further investigations.

Although a wide range of rotation rates and vertical diffusivities could in principle be investigated, the scenarios examined here were selected to provide a representative sampling of the parameter space. Having already thoroughly examined the role of ocean vertical diffusion in shaping the climate of planets characterised by Earth-like rotation rates, varying it alongside the rotation/orbital rate does not introduce a degeneracy in the interpretation of the results. However, such degeneracies could arise if additional parameters were varied simultaneously. As in the case of Chapter 3, this study could naturally be extended, as a wide range of additional parameters such as resonance states, orbital parameters and instellations, may be varied.

The findings presented here provide a framework for interpreting future observations of terrestrial exoplanets orbiting cool stars. As demonstrated by the results in this chapter, together with the extended diagnostics in the supplementary material, the complexity of these systems - arising from nonlinear feedbacks and dynamical processes that are dependent on model parametrisations - suggests that expanding this line of investigation using a broader suite of climate models would be highly valuable. As observational capabilities continue to advance, characterising the diversity of climates permitted by different spin-orbit resonant states will become increasingly important for assessing the habitability and climate properties of observable rocky exoplanets.

5

Conclusions and Perspectives

The main conclusions of this thesis concern the climatic impact of tidal-driven ocean mixing and the climate state of terrestrial exoplanets in 3:2 spin-orbit resonances. Across both contexts, the results demonstrate that ocean dynamics exerts a decisive influence on planetary climate, shaping heat redistribution, shifting habitability boundaries, and imprinting detectable signatures on potential observables. These findings underscore the limitations of simplified ocean treatments for evaluating habitability and interpreting observations of terrestrial exoplanets. The research presented here opens several promising avenues for future work. These include incorporating additional physical processes to achieve a more comprehensive representation of exoplanet climates, applying diagnostic tools to better interpret unresolved dynamical features, and exploring a broader range of configurations. The current limitations of FORTE 2.0 - the atmosphere-ocean general circulation model used in this study - can also be addressed by coupling the model to a flexible radiative-transfer scheme, enabling participation in community model-intercomparison projects and contributing to the broader effort to develop a physically grounded, generalisable framework for exoplanet climate modelling.

5.1 Conclusions

As the search for habitable worlds progresses and exoplanet characterisation continues to advance, understanding the physical mechanisms that govern planetary climates, particularly for worlds considered the most promising detectable hosts of life-supporting environments, has become increasingly important. In this context, terrestrial planets orbiting low-mass stars have become a central focus of exoclimate modelling efforts. These systems offer both unique opportunities and significant challenges: their close proximity to a small host star improves observational prospects, yet such configuration not only induces strong tidal interactions that can produce a multitude of spin states, but can also result in complex atmosphere-ocean feedbacks and dynamical mechanisms that cannot be assumed to resemble those of Earth.

The results obtained in this thesis contribute to the broader effort to develop a comprehensive understanding of the processes that shape exoplanet climates in different configurations. This work has examined the climate dynamics of terrestrial exoplanets using a fully coupled atmosphere-ocean general circulation model, with particular emphasis on asynchronous rotation and tidal-driven ocean mixing scenarios in which ocean dynamical processes exert a fundamental influence on both climatic and observational properties. The study was deliberately designed to evaluate the climatic impact of ocean processes, differently from the common approach adopted in this field, where the vast majority of previous investigations have relied on slab-ocean or thermodynamic-ocean approximations that cannot capture the full complexity of ocean circulation. Such simplified treatments are typically adopted because they are computationally inexpensive and because exoplanet characterisation is currently dominated by atmospheric observations, leading to the assumption that atmospheric modelling should be prioritised while ocean processes are of secondary importance. However, the approach taken here is motivated by well-established insights from the only fully characterised ocean - Earth's. Observational and modelling studies of Earth demonstrate that dynamical processes redistribute heat, modulating surface temperatures and therefore interacting with the atmosphere through nonlinear feedbacks. This thesis addresses these considerations by systematically providing a physically consistent investigation of scenarios in which ocean processes significantly influence the climate state of the simulated exoplanet.

The research first examines how tidal-driven ocean vertical mixing shapes the climates and potential habitability of terrestrial exoplanets. Though especially relevant for planets in the habitable zones of low-mass stars, the examined mechanisms are applicable to other cases characterised by strong tidal forcing, such as planets orbited by massive and/or nearby satellites. Such process has received only limited attention in the literature and is generally not included in studies employing dynamical ocean models.

Assuming an Earth-like rotation, tidal forcing is represented through the ocean vertical diffusion coefficient, which is varied over four orders of magnitude, demonstrating that ocean tidal processes exert a nonlinear and nonmonotonic influence on planetary climate. Tidal mixing fundamentally shapes ocean circulation, altering both its strength and the dominant heat-transport mechanism, with a transition from overturning-dominated to gyre-dominated regimes. As a consequence, it modifies the magnitude of the total meridional heat transport and its partitioning between the ocean and the atmosphere. Increasing vertical diffusivity initially strengthens overturning circulation and enhances poleward heat transport, but beyond a threshold roughly two orders of magnitude larger than Earth's value this trend reverses, revealing an optimal tidal-mixing regime that maximises heat redistribution and minimises surface temperature gradients. Only planets within this regime remain temperate under simulated reduced instellation, while those with weaker or stronger mixing rapidly enter glaciated states once a critical ice-line latitude is crossed. Such changes effectively shift the outer edge of the habitable zone and expand the stellar-flux range that permits habitable conditions in ways that cannot be captured by simplified or atmosphere-only models.

Further investigations test the robustness and generality of the main findings, confirming that the simulated climate states are not tied to a specific setup but reflect broader dynamical behaviour. Simulations with modified ridge geometries - where the meridional barrier is divided into multiple segments - produce climate states qualitatively similar to the standard ridgeworld configuration, while additional experiments exploring different initial thermal states converge to the same qualitative outcome. These additional analyses broaden the applicability of the main findings and demonstrate that they reflect dynamical processes relevant across a wide range of exoplanetary environments.

Together, the results underscore that ocean dynamics is indispensable for assessing the climates of potentially habitable exoplanets. The common assumption that exoplanet oceans behave similarly to Earth's is not generally valid. Climate models that employ simplified ocean treatments cannot reliably depend on Earth-based parametrisations of dynamical processes. These findings therefore highlight the need for habitability assessments that incorporate fully coupled atmosphere-ocean dynamics, rather than relying solely on atmospheric models or slab-ocean approaches that omit the complexity of ocean circulation.

The second part of the thesis focuses specifically on modelling the climate of terrestrial planets orbiting low-mass stars. Although most previous studies have focused on synchronous rotation, tidal theory predicts that a variety of asynchronous states - including higher-order spin-orbit resonances - are plausible. This part of the thesis addresses these scenarios by systematically exploring the combined effects of rotation, tidal regime, and ocean dynamics in the understudied context of 3:2 spin-orbit resonances.

Two rotation and two tidal regimes are simulated with both dynamic and thermodynamic ocean model configurations that allow the assessment of the ocean's role in modulating climate. The simulations show that the periodic stellar forcing associated with the 3:2 resonance, combined with the ocean's thermal inertia, displaces the warmest surface waters away from the substellar point, producing a migrating hotspot that travels across the planetary surface over the course of a stellar period. The depth of the thermocline is strongly controlled by the vertical diffusivity: higher diffusivities generate deeper, less stratified profiles and allow periodic heating to penetrate further into the ocean interior. Dynamic ocean simulations introduce additional complexity, most notably enabling efficient poleward heat transport and the formation of pronounced gyre structures east of the meridional barrier. The atmospheric response exhibits a systematic longitudinal shift of rainfall of roughly 60° relative to the substellar point, determining reduced thermal emission in the same region. This behaviour differs fundamentally from the synchronous rotation case, in which the substellar point is fixed on the planetary surface and climate patterns remain largely stationary.

The periodic climate patterns identified in the simulations translate into distinctive thermal emission phase curves. In the slow rotation scenario, the slowly migrating stellar forcing produces stark and defined temperature and rainfall patterns, which imprint on the phase curve as a clear offset relative to the midpoint of the transits. The dynamic ocean configuration introduces additional complexity: western boundary currents determine increased rainfall at higher latitudes, generating a phase-dependent modulation in the amplitude of the phase curve. In contrast, the fast rotation scenario exhibits weaker and less defined climatic patterns, yielding a more homogeneous thermal emission across longitudes and a correspondingly flatter, almost featureless phase curve. These signatures provide a potential observational discriminant between synchronous and asynchronous rotation states. The results therefore highlight the importance of accounting for spin-orbit resonances, and for possible ocean-driven signatures imprinted on phase curves, when interpreting future observations of terrestrial exoplanets orbiting low-mass stars. The interplay between periodic stellar forcing, atmospheric dynamics, and ocean circulation generates diverse yet physically interpretable patterns that may be detectable with next-generation observatories.

This thesis contributes to clarifying the complexity of exoplanet climates in asynchronous states subjected to a range of tidal forcings and underscores the need for physically comprehensive models when assessing the habitability and observational properties of terrestrial planets around cool stars. As the characterisation of terrestrial exoplanets continues to advance, understanding the diversity of climates permitted by different configurations will be essential for developing a unified climate modelling framework capable of both interpreting observational data and guiding future observational efforts.

5.2 Perspectives

Several avenues for extending the research presented in this thesis were briefly outlined in Chapters 3 and 4. Future investigations could incorporate physical processes not included in the present model but likely to influence the climate of tidally forced planets. Although the analysis in Chapter 3 considers strong tidal forcing in a broad sense - relevant both for planets in the habitable zones of low-mass stars and for planets orbited by massive and/or nearby satellites - additional processes become particularly important in the specific case of low-mass stellar hosts. For example, the spectral dependence of snow and ice albedo, which is not included in the current simulations, can substantially weaken the ice-albedo feedback. In scenarios where the planet undergoes global glaciation under reduced instellation, a weaker feedback could delay or even prevent full glaciation, allowing the formation of stable ice caps that do not reach the critical ice-line latitude. Moreover, in regimes where tidal forcing is strong, internal tidal heating may provide an additional energy source capable of delaying or preventing global glaciation. Variations in atmospheric CO_2 or other greenhouse gases would likewise influence the mean climate state, particularly under reduced instellation, and could lead to different climatic outcomes than those obtained here. The implications of deep-ocean warming for long-term climate stability through seafloor weathering feedbacks could also be explored. Incorporating these processes would introduce an interplay among multiple feedbacks and heating sources, likely producing shifts in the outer edge of the habitable zone that differ from those predicted in this study.

In the case of 3:2 spin-orbit resonance simulations, the additional complexity exhibited by the dynamic ocean configuration includes equatorial Kelvin and Rossby waves in the low diffusivity, slow rotation regime and frequent eastward propagating density anomalies in the low diffusivity fast rotation regime. Although dynamically significant, these waves do not affect surface temperatures and therefore leave no imprint on observable quantities. As discussed in Chapter 4, a valuable direction for future work is the application of Wheeler-Kiladis analysis, which decomposes equatorial variability into characteristic wavenumber-frequency components. This approach would enable a clear separation of dynamical modes and strengthen the interpretation of the oceanic processes emerging in the simulations. Moreover, while the present study examines two rotation rates, extending the analysis to both slower and faster rotations would help determine whether the trends identified here - particularly those related to atmospheric and oceanic heat transport - persist or whether new nonlinear behaviour emerges under potentially progressively different forcing. Another promising avenue is the exploration of additional higher-order spin-orbit resonances, such as 2:1 or 5:2 states. Although less likely than the 1:1 and 3:2 configurations, these resonances would impose distinct instellation patterns on the planetary surface and could yield a broader range of thermal-emission phase-curve behaviours within a single stellar period, offering a more comprehensive understanding of asynchronous climate regimes.

In principle, the vast number of unknown parameters governing exoplanetary systems means that climate modelling studies could be expanded indefinitely to incorporate additional physical processes, explore parameter dependencies, and examine alternative configurations. This vast parameter space, combined with the computational cost of fully coupled atmosphere-ocean general circulation models, necessitates a series of assumptions in the research presented in this thesis. One particularly relevant parameter not explored here is orbital eccentricity. In Chapter 4, a circular orbit was assumed, yet even moderate eccentricity would alter the spatial and temporal distribution of instellation across the planetary surface. Under the zonally asymmetric configuration adopted in this work - featuring a meridional barrier fixed at a specific longitude - introducing eccentricity would also require specifying the longitude of perihelion, thereby adding another dimension to an already large parameter space.

It is important to note that FORTE 2.0 is designed to model the climate of planets with oceans comparable in depth to Earth's, whose global mean ocean depth is approximately $\sim$4 km. Because the ocean model is designed around terrestrial conditions, it relies on several assumptions - such as the incompressibility assumption and the thin-shell approximation - that hold only for relatively shallow oceans, for which ocean depth is negligible compared to the planetary radius. For significantly deeper oceans, which may be hundreds of times deeper than Earth's and reach GPa-level pressures at their bottom, these assumptions break down: water compressibility becomes relevant, and high-pressure ice phases are expected to form at depth [Nixon & Madhusudhan, 2021]. Therefore, although exploring the climatic impact of tidal mixing on a population of super-Earths and mini-Neptunes - planets with masses ranging from 1 to 20 $M_\oplus$, up to $\sim$0.06 M_J in Figure 1.1.4 - and potentially characterised by deep liquid water oceans, is certainly of interest, FORTE 2.0 is not suited for modelling such regimes.

In the broader context of climatic impacts of tidal forcing, planets orbiting multiple-star systems represent an especially compelling avenue for future study. Notably, the nearest confirmed exoplanet to the Solar System, Proxima Centauri b, resides in the habitable zone of the M-dwarf Proxima Centauri, itself a member of a triple-star system. A substantial fraction of stars in the Galaxy belong to binary, triple, or higher-order stellar systems, and consequently many known exoplanets also reside in such environments; in the solar neighbourhood, an estimated 20-25% of exoplanet systems have stellar companions [González-Payo et al., 2024]. Double-star planetary systems can host dynamically stable and suitably irradiated habitable zones in both circumstellar (S-type) and circumbinary (P-type) configurations [Simonetti et al., 2020]. Climate simulations of these planets that aim to include ocean tide-induced mixing would require not only a treatment of the time-varying incident stellar flux from each star, but also a representation of the tidal forcing generated by each stellar component. This, in turn, would necessitate formulating a vertical diffusion coefficient that depends explicitly on the evolving orbital configuration.

Accounting for the influence of the host star's spectral energy distribution was addressed in Chapter 4 through a modified treatment of snow and ice albedo for low-mass stars. However, a key limitation of FORTE 2.0 is its reliance on a modified version of the Morcrette radiation scheme [Joshi et al., 2015], whose radiative-transfer parametrisations were developed for Earth's atmosphere and are therefore tuned to terrestrial gas compositions and the solar spectrum. The fact that the experiments presented here are idealised, and do not aim to simulate specific planets, as well as the wide range of possible atmospheric compositions for terrestrial exoplanets introducing substantial uncertainty into radiative-transfer parametrisations, justifies the solar stellar flux adopted in this study. However, coupling the model to a more flexible radiative-transfer code would be advantageous and would render FORTE 2.0 employable when simulating specific scenarios. As future work, the model can be coupled to SOCRATES (Suite of Community RAdiative Transfer codes based on Edwards and Slingo), a modular radiative-transfer framework developed by the UK Met Office that offers greater flexibility in atmospheric composition and spectral resolution [Manners et al., 2015]. Access to the SOCRATES code repository has already been granted by its developers, enabling this integration in subsequent stages of the project.

Enhancing the model's flexibility - particularly its ability to simulate a wider range of atmospheric compositions and stellar spectra - would enable participation in model-intercomparison efforts such as the CUISINES framework, a community-driven methodology for designing, running, and analysing exoplanet model intercomparison projects [Sohl et al., 2024]. Within this framework, the CRÈME intercomparison focuses on benchmarking exoplanet climate models predictions of Earth against observed data. Experiments performed with the current version of FORTE 2.0 can contribute to the CRÈME "core experiments", as these require a solar stellar spectrum and pre-industrial CO_2 concentrations, fully reproducible with FORTE 2.0. The "ideal experiments", however, would require fully dynamic sea ice, which is not supported in FORTE 2.0, where sea ice is represented as a fixed barrier to ocean-atmosphere heat exchange imposed when sea-surface temperatures fall below 271 K.

The SAMOSA intercomparison aims to sample the climate of a synchronously rotating planet across a wide grid of surface pressures and instellation values, using GCM simulations to reconstruct the full parameter space through interpolation. Differences among models at the sampled points can substantially alter the resulting climate maps. The SAMOSA protocol specifies a hypothetical planet with a 15-day synchronous rotation period orbiting a 3000 K blackbody star, an aquaplanet surface configuration, and an atmosphere containing 400 ppm CO_2 with no ozone. While FORTE 2.0 can reproduce the required atmospheric composition, the spectral energy distribution of a

3000 K blackbody, in the mid-range of M dwarfs, differs markedly from the solar spectrum, making coupling to SOCRATES essential for meaningful comparison across models. Importantly, the only published SAMOSA results to date employ thermodynamic slab-ocean models with no dynamic heat transport [Haqq-Misra et al., 2022], so comparison with a fully dynamic ocean model such as FORTE 2.0 would provide particularly valuable insight. Potential collaborations for participation in both CRÈME and SAMOSA have already been established.

In this context, an intercomparison project focused on exoplanetary oceans would provide a systematic framework for assessing how different ocean models influence exoplanetary climates. Key aspects to investigate include the strength and structure of ocean heat transport and the sensitivity of ocean circulation to parameters such as instellation, planetary rotation rate, ocean salinity, surface pressure, freshwater fluxes, tidal forcing, and the representation of turbulence and mixing. Comparing models with varying levels of complexity - from slab oceans to fully dynamic three-dimensional oceans - would clarify how ocean dynamics shape surface and atmospheric properties, and therefore the resulting photometric and spectral signatures, substantially enriching current exoplanet climate research. Establishing a coordinated intercomparison would therefore provide a critical foundation for evaluating the role of oceans in the climates and potential habitability of terrestrial exoplanets. A particularly valuable extension would involve applying this framework across a diverse range of planetary types. Sub-Neptunes, which dominate the known exoplanet population and represent compelling astrobiological targets [Bean et al., 2021], are especially interesting in this regard. Their interiors may host multiple layers of water, different ice types, or supercritical fluids arranged at different depths, underscoring the need to investigate dynamic ocean–ice coupling in such environments. An ocean intercomparison applied to such planets would help bridge the gap between current observations of sub-Neptunes and the highly degenerate interior structures inferred from theory.

A further implication of coupling FORTE 2.0 to SOCRATES is the possibility to generate synthetic planetary spectra for simulated planets orbiting low-mass stars. This would require radiative-transfer suites capable of producing simulated observations of synthetic spectra across a broad wavelength range. Such tools typically rely on detailed atmospheric inputs - including temperature-pressure profiles, gas abundances, aerosol and cloud optical properties and their vertical distributions - along with the observing geometry, instrument configuration, and the host star spectrum. Several of these radiative-transfer instruments are currently available and are already widely used in exoplanet research. Given the growing emphasis on spectral characterisation, producing synthetic spectra for the simulations presented in this thesis would provide an additional observational diagnostic that complements the thermal emission phase curves analysed here.

Bibliography

Abbot, D. S. Analytical Investigation of the Decrease in the Size of the Habitable Zone Due to a Limited CO_2 Outgassing Rate. *ApJ*, 827(2):117, 2016. doi: 10.3847/0004-637X/827/2/117.

Adams, A. D., Boos, W. R., and Wolf, E. T. Aquaplanet Models on Eccentric Orbits: Effects of the Rotation Rate on Observables. *AJ*, 157(5):189, 2019. doi: 10.3847/1538-3881/ab107f.

Adams, J. C. Explanation of the observed irregularities in the motion of Uranus, on the hypothesis of disturbance by a more distant planet; with a determination of the mass, orbit, and position of the disturbing body. *MNRAS*, 7:149–152, 1846. doi: 10.1093/mnras/7.9.149.

Airapetian, V. S., Glocer, A., Khazanov, G. V., et al. How Hospitable Are Space Weather Affected Habitable Zones? The Role of Ion Escape. *ApJL*, 836(1):L3, 2017. doi: 10.3847/2041-8213/836/1/L3.

Airapetian, V. S., Barnes, R., Cohen, O., et al. Impact of space weather on climate and habitability of terrestrial-type exoplanets. *International Journal of Astrobiology*, 19(2):136–194, 2020. doi: 10.1017/S1473550419000132.

Aleina, F. C., Baudena, M., D'Andrea, F., et al. Multiple equilibria on planet Dune: climate–vegetation dynamics on a sandy planet. *Tellus B: Chemical and Physical Meteorology*, 2013. doi: 10.3402/tellusb.v65i0.17662.

Ames, F., Ferreira, D., Czaja, A., et al. Ocean stratification impedes particulate transport to the plumes of Enceladus. *Communications Earth and Environment*, 6(1):63, 2025. doi: 10.1038/s43247-025-02036-3.

Angerhausen, D., DeLarme, E., and Morse, J. A. A Comprehensive Study of Kepler Phase Curves and Secondary Eclipses: Temperatures and Albedos of Confirmed Kepler Giant Planets. *PASP*, 127(957):1113, 2015. doi: 10.1086/683797.

Angerhausen, D., Pidhorodetska, D., Leung, M., et al. Large Interferometer For Exoplanets (LIFE). XII. The Detectability of Capstone Biosignatures in the Mid-infrared—Sniffing Exoplanetary Laughing Gas and Methylated Halogens. *AJ*, 167(3): 128, 2024. doi: 10.3847/1538-3881/ad1f4b.

Anglada-Escudé, G., Amado, P. J., Barnes, J., et al. A terrestrial planet candidate in a temperate orbit around Proxima Centauri. *Nature*, 536(7617):437–440, 2016. doi: 10.1038/nature19106.

Arakawa, A. Computational design for long-term numerical integration of the equations of fluid motion: Two-dimensional incompressible flow. Part I. *Journal of Computational Physics*, 1(1):119–143, 1966. ISSN 0021-9991. doi: 10.1016/0021-9991(66)90015-5.

Aristotle. *On the Heavens*, volume 191 of *Loeb Classical Library*. Harvard University Press, Cambridge, MA, 1939.

Arnold, N. P., Tziperman, E., and Farrell, B. Abrupt Transition to Strong Superrotation Driven by Equatorial Wave Resonance in an Idealized GCM. *Journal of the Atmospheric Sciences*, 69(2):626–640, 2012. doi: 10.1175/JAS-D-11-0136.1.

Arnscheidt, C. W. and Rothman, D. H. Routes to global glaciation. *Proceedings of the Royal Society A: Mathematical, Physical and Engineering Sciences*, 476(2239):20200303, 2020. ISSN 1364-5021. doi: 10.1098/rspa.2020.0303.

Ashkenazy, Y. and Tziperman, E. Dynamic Europa ocean shows transient Taylor columns and convection driven by ice melting and salinity. *Nature Communications*, 12:6376, 2021. doi: 10.1038/s41467-021-26710-0.

Atkinson, A. S., Alexander, D., and Farrish, A. O. Exploring the Effects of Stellar Magnetism on the Potential Habitability of Exoplanets. *ApJ*, 969(2):147, 2024. doi: 10.3847/1538-4357/ad4605.

Atkinson, L. P. *Western Boundary Currents*, pages 121–169. Springer Berlin Heidelberg, Berlin, Heidelberg, 2010. ISBN 978-3-540-92735-8. doi: 10.1007/978-3-540-92735-8_3.

Auclair-Desrotour, P., Leconte, J., Bolmont, E., et al. Final spin states of eccentric ocean planets. *A&A*, 629:A132, 2019. doi: 10.1051/0004-6361/201935905.

Ballard, S. and Johnson, J. A. The Kepler Dichotomy among the M Dwarfs: Half of Systems Contain Five or More Coplanar Planets. *ApJ*, 816(2):66, 2016. doi: 10.3847/0004-637X/816/2/66.

Barnes, J. R., Jeffers, S. V., and Jones, H. R. A. The effect of M dwarf starspot activity on low-mass planet detection thresholds. *MNRAS*, 412(3):1599–1610, 2011. doi: 10.1111/j.1365-2966.2010.17979.x.

Barnes, R. Tidal locking of habitable exoplanets. *Celestial Mechanics and Dynamical Astronomy*, 129(4):509–536, 2017. doi: 10.1007/s10569-017-9783-7.

Basant, R., Luque, R., Bean, J. L., et al. Four Sub-Earth Planets Orbiting Barnard's Star from MAROON-X and ESPRESSO. *ApJL*, 982(1):L1, 2025. doi: 10.3847/2041-8213/adb8d5.

Bathiany, S., Claussen, M., and Fraedrich, K. Implications of climate variability for the detection of multiple equilibria and for rapid transitions in the atmosphere-vegetation system. *Climate Dynamics*, 38(9-10):1775–1790, 2012. doi: 10.1007/s00382-011-1037-x.

Batra, K. and Olson, S. L. Climatic Effects of Ocean Salinity on M Dwarf Exoplanets. *ApJL*, 971(1):L11, 2024. doi: 10.3847/2041-8213/ad63a5.

Baum, S. K. and Crowley, T. J. GCM simulations of snowball Earth conditions during the late Proterozoic. *Palaeogeography, Palaeoclimatology, Palaeoecology*, 167(1-2):331–355, 2001. doi: 10.1016/S0031-0182(00)00242-7.

Bean, J. L., Raymond, S. N., and Owen, J. E. The Nature and Origins of Sub-Neptune Size Planets. *Journal of Geophysical Research (Planets)*, 126(1):e06639, 2021. doi: 10.1029/2020JE006639.

Belorizky, D. Le Soleil, Etoile Variable. *L'Astronomie*, 52:359–361, 1938.

Berdyugina, S. V. and Kuhn, J. R. Surface Imaging of Proxima b and Other Exoplanets: Albedo Maps, Biosignatures, and Technosignatures. *The Astronomical Journal*, 158(6): 246, 2019. doi: 10.3847/1538-3881/ab2df3.

Bergsten, G. J., Pascucci, I., Mulders, G. D., et al. The Demographics of Kepler's Earths and Super-Earths into the Habitable Zone. *The Astronomical Journal*, 164(5):190, 2022. ISSN 1538-3881. doi: 10.3847/1538-3881/ac8fea.

Bergsten, G. J., Pascucci, I., Hardegree-Ullman, K. K., et al. No Evidence for More Earth-sized Planets in the Habitable Zone of Kepler's M versus FGK Stars. *AJ*, 166(6):234, 2023. doi: 10.3847/1538-3881/ad03ea.

Berman, L. 70 Ophiuchi as a triple system. *Lick Observatory Bulletin*, 443:24–30, 1932. doi: 10.5479/ADS/bib/1932LicOB.16.24B.

Berner, R. GEOCARB II: A revised model of atmospheric CO2 over Phanerozoic time. *American Journal of Science*, 294:56–91, 1994. doi: 10.2475/ajs.294.1.56.

Bhatnagar, S., Codron, F., Millour, E., Bolmont, E., Brunetti, M., Kasparian, J., Turbet, M., and Chaverot, G. Fast and physically grounded ocean model for gcms: The dynamical slab ocean model of the generic-pcm. *EGUsphere*, 2025. doi: 10.5194/egusphere-2025-3786.

Biasiotti, L., Simonetti, P., Vladilo, G., et al. EOS-ESTM: a flexible climate model for habitable exoplanets. *MNRAS*, 514(4):5105–5125, 2022. doi: 10.1093/mnras/stac1642.

Birkby, J. L. *Spectroscopic Direct Detection of Exoplanets*, pages 1485–1508. Springer International Publishing, Cham, 2018. ISBN 978-3-319-55333-7. doi: 10.1007/978-3-319-55333-7_16.

Bjerknes, J. Atlantic Air-Sea Interaction. *Advances in Geophysics*, 10:1–82, 1964. doi: 10.1016/S0065-2687(08)60005-9.

Blaker, A. T., Joshi, M., Sinha, B., et al. FORTE 2.0: a fast, parallel and flexible coupled climate model. *Geoscientific Model Development*, 14(1):275–293, 2021. doi: 10.5194/gmd-14-275-2021.

Bochanski, J. J., Hawley, S. L., Covey, K. R., et al. The Luminosity and Mass Functions of Low-mass Stars in the Galactic Disk. II. The Field. *AJ*, 139(6):2679–2699, 2010. doi: 10.1088/0004-6256/139/6/2679.

Bohl, A., Lawrence, L., Lowry, G., et al. Probing the Limits of Habitability: A Catalog of Rocky Exoplanets in the Habitable Zone. *arXiv e-prints*, art. arXiv:2501.14054, 2025. doi: 10.48550/arXiv.2501.14054.

Bonfils, X., Astudillo-Defru, N., Díaz, R., et al. A temperate exo-Earth around a quiet M dwarf at 3.4 parsec. *A&A*, 613:A25, 2018. doi: 10.1051/0004-6361/201731973.

Borucki, W. J. and Summers, A. L. The photometric method of detecting other planetary systems. *Icarus*, 58(1):121–134, 1984. ISSN 0019-1035. doi: 10.1016/0019-1035(84)90102-7.

Boss, A. P., Basri, G., Kumar, S. S., et al. Nomenclature: Brown Dwarfs, Gas Giant Planets, and ? In Martín, E., editor, *Brown Dwarfs*, volume 211 of *IAU Symposium*, page 529, 2003.

Boutle, I. A., Mayne, N. J., Drummond, B., et al. Exploring the climate of Proxima B with the Met Office Unified Model. *A&A*, 601:A120, 2017. doi: 10.1051/0004-6361/201630020.

Boutle, I. A., Joshi, M., Lambert, F. H., et al. Mineral dust increases the habitability of terrestrial planets but confounds biomarker detection. *Nature Communications*, 11:2731, 2020. doi: 10.1038/s41467-020-16543-8.

Bowler, B. P., Liu, M. C., Dupuy, T. J., et al. Near-infrared Spectroscopy of the Extrasolar Planet HR 8799 b. *ApJ*, 723(1):850–868, 2010. doi: 10.1088/0004-637X/723/1/850.

Braam, M., Palmer, P. I., Decin, L., et al. Earth-like Exoplanets in Spin–Orbit Resonances: Climate Dynamics, 3D Atmospheric Chemistry, and Observational Signatures. *PSJ*, 6(1):5, 2025. doi: 10.3847/PSJ/ad9565.

Broecker, W. S. The Great Ocean Conveyor. *Oceanography*, 4(2), 1991. doi: 10.5670/oceanog.1991.07.

Broecker, W. S., Peteet, D. M., and Rind, D. Does the ocean-atmosphere system have more than one stable mode of operation? *Nature*, 315:21–26, 1985. doi: 10.1038/315021a0.

Brown, J. L., Hill, D. J., Dolan, A. M., et al. PaleoClim, high spatial resolution paleoclimate surfaces for global land areas. *Nature Scientific Data*, 5:180254, 2018. doi: 10.1038/sdata.2018.254.

Bruno, G. *Opere di Giordano Bruno Nolano, ora per la prima volta raccolte e pubblicate*. Tipografia di G. Antonelli, Napoli, 1830.

Bryan, F. Parameter Sensitivity of Primitive Equation Ocean General Circulation Models. *Journal of Physical Oceanography*, 17(7):970–986, 1987. doi: 10.1175/1520-0485(1987)017⟨0970:PSOPEO⟩2.0.CO;2.

Bryan, K. A numerical method for the study of the circulation of the world ocean. *Journal of Computational Physics*, 4(3):347–376, 1969. doi: 10.1016/0021-9991(69)90004-7.

Buckley, M. W. and Marshall, J. Observations, inferences, and mechanisms of the Atlantic Meridional Overturning Circulation: A review. *Reviews of Geophysics*, 54(1):5–63, 2016. doi: 10.1002/2015RG000493.

Böning, C. W. and Herrmann, P. Annual cycle of poleward heat transport in the ocean: Results from high-resolution modeling of the north and equatorial atlantic. *Journal of Physical Oceanography*, 24(1):91 – 107, 1994. doi: 10.1175/1520-0485(1994)024⟨0091:ACOPHT⟩2.0.CO;2.

Cael, B. B. and Ferrari, R. The ocean's saltiness and its overturning. *Geophys. Res. Lett.*, 44(4):1886–1891, 2017. doi: 10.1002/2016GL072223.

Caldeira, K. and Kasting, J. F. Susceptibility of the early earth to irreversible glaciation caused by carbon dioxide clouds. *Nature*, 359:226–228, 1992. doi: 10.1038/359226a0.

Campbell, B. and Walker, G. A. H. Precision Radial Velocities with an Absorption Cell. *Publications of the Astronomical Society of the Pacific*, 91(542):540, 1979. doi: 10.1086/130535.

Campbell, B., Walker, G. A. H., and Yang, S. A Search for Substellar Companions to Solar-type Stars. *ApJ*, 331:902, 1988. doi: 10.1086/166608.

Cecchi-Pestellini, C., Ciaravella, A., and Micela, G. Stellar X-ray heating of planet atmospheres. *A&A*, 458(2):L13–L16, 2006. doi: 10.1051/0004-6361:20066093.

Chambers, J. The effect of seafloor weathering on planetary habitability. *The Astrophysical Journal*, 896(2):L1–L10, 2020. doi: 10.3847/1538-4357/ab94a4.

Charbonneau, D. and Deming, D. The Dynamics-Based Approach to Studying Terrestrial Exoplanets. *arXiv e-prints*, art. arXiv:0706.1047, 2007. doi: 10.48550/arXiv.0706.1047.

Charbonneau, D., Brown, T. M., Latham, D. W., et al. Detection of Planetary Transits Across a Sun-like Star. *ApJL*, 529(1):L45–L48, 2000. doi: 10.1086/312457.

Charbonneau, D., Brown, T. M., Noyes, R. W., et al. Detection of an Extrasolar Planet Atmosphere. *ApJ*, 568(1):377–384, 2002. doi: 10.1086/338770.

Charnay, B., Forget, F., Wordsworth, R., et al. Exploring the faint young Sun problem and the possible climates of the Archean Earth with a 3-D GCM. *Journal of Geophysical Research (Atmospheres)*, 118(18):10,414–10,431, 2013. doi: 10.1002/jgrd.50808.

Charnay, B., Le Hir, G., Fluteau, F., et al. A warm or a cold early Earth? New insights from a 3-D climate-carbon model. *Earth and Planetary Science Letters*, 474:97–109, 2017. ISSN 0012-821X. doi: 10.1016/j.epsl.2017.06.029.

Charney, J. G. Dynamics of deserts and drought in the Sahel. *Quarterly Journal of the Royal Meteorological Society*, 101(428):193–202, 1975. doi: 10.1002/qj.49710142802.

Checlair, J. H., Olson, S. L., Jansen, M. F., et al. No Snowball on Habitable Tidally Locked Planets with a Dynamic Ocean. *ApJL*, 884(2):L46, 2019. doi: 10.3847/2041-8213/ab487d.

Chen, H., Li, G., Paradise, A., et al. Sporadic Spin-orbit Variations in Compact Multiplanet Systems and Their Influence on Exoplanet Climate. *ApJL*, 946(2):L32, 2023. doi: 10.3847/2041-8213/acbd33.

Christiansen, J. L., McElroy, D. L., Harbut, M., et al. The NASA Exoplanet Archive and Exoplanet Follow-up Observing Program: Data, Tools, and Usage. *PSJ*, 6(8):186, 2025. doi: 10.3847/PSJ/ade3c2.

Cloutier, R. and Menou, K. Evolution of the Radius Valley around Low-mass Stars from Kepler and K2. *AJ*, 159(5):211, 2020. doi: 10.3847/1538-3881/ab8237.

Cochran, W. D., Hatzes, A. P., and Hancock, T. J. Constraints on the Companion Object to HD 114762. *ApJL*, 380:L35, 1991. doi: 10.1086/186167.

Cockell, C. S., Bush, T., Bryce, C., et al. Habitability: A Review. *Astrobiology*, 16(1): 89–117, 2016. doi: 10.1089/ast.2015.1295.

Codron, F. Ekman heat transport for slab oceans. *Climate Dynamics*, 38(1-2):379–389, 2012. doi: 10.1007/s00382-011-1031-3.

Colose, C. M., Haqq-Misra, J., Wolf, E. T., et al. Effects of Spin-Orbit Resonances and Tidal Heating on the Inner Edge of the Habitable Zone. *ApJ*, 921(1):25, 2021. doi: 10.3847/1538-4357/ac135c.

Coogan, L. and Dosso, S. Alteration of ocean crust provides a strong temperature dependent feedback on the geological carbon cycle. *Earth and Planetary Science Letters*, 415:38–46, 2015. doi: 10.1016/j.epsl.2015.01.027.

Coogan, L. and Gillis, K. Temperature dependence of seafloor hydrothermal alteration and the strength of the oceanic crustal carbon sink. *Earth and Planetary Science Letters*, 508:41–49, 2018. doi: 10.1016/j.epsl.2018.01.009.

Correia, A. C. M. and Delisle, J.-B. Spin-orbit coupling for close-in planets. *A&A*, 630: A102, 2019. doi: 10.1051/0004-6361/201936336.

Correia, A. C. M. and Laskar, J. Mercury's capture into the 3/2 spin-orbit resonance as a result of its chaotic dynamics. *Nature*, 429(6994):848–850, 2004. doi: 10.1038/nature02609.

Correia, A. C. M. and Laskar, J. Mercury's capture into the 3/2 spin-orbit resonance including the effect of core-mantle friction. *Icarus*, 201(1):1–11, 2009. doi: 10.1016/j.icarus.2008.12.034.

Correia, A. C. M., Boué, G., Laskar, J., et al. Deformation and tidal evolution of close-in planets and satellites using a Maxwell viscoelastic rheology. *A&A*, 571:A50, 2014. doi: 10.1051/0004-6361/201424211.

Cowan, N. B. and Agol, E. The Statistics of Albedo and Heat Recirculation on Hot Exoplanets. *ApJ*, 729(1):54, 2011. doi: 10.1088/0004-637X/729/1/54.

Cowan, N. B., Voigt, A., and Abbot, D. S. Thermal Phases of Earth-like Planets: Estimating Thermal Inertia from Eccentricity, Obliquity, and Diurnal Forcing. *ApJ*, 757(1):80, 2012. doi: 10.1088/0004-637X/757/1/80.

Cox, M. and Bryan, K. A Numerical Model of the Ventilated Thermocline. *Journal of Physical Oceanography - J PHYS OCEANOGR*, 14:674–687, 1984. doi: 10.1175/1520-0485(1984)014⟨0674:ANMOTV⟩2.0.CO;2.

Crockett, W. W., Shaw, J. O., Simpson, C., et al. Physical constraints during Snowball Earth drive the evolution of multicellularity. *Proceedings of the Royal Society B: Biological Sciences*, 291(2025):20232767, 2024. ISSN 0962-8452. doi: 10.1098/rspb.2023.2767.

Crowe, M. J. and Dowd, M. F. The Extraterrestrial Life Debate from Antiquity to 1900. In Vakoch, D. A., editor, *Astrobiology, History, and Society*, page 3. Springer-Verlag Berlin Heidelberg, 2013. doi: 10.1007/978-3-642-35983-5_1.

Cullum, J., Stevens, D., and Joshi, M. The Importance of Planetary Rotation Period for Ocean Heat Transport. *Astrobiology*, 14(8):645–650, 2014. doi: 10.1089/ast.2014.1171.

Cullum, J., Stevens, D., and Joshi, M. Importance of ocean salinity for climate and habitability. *Proceedings of the National Academy of Science*, 113(16):4278–4283, 2016. doi: 10.1073/pnas.1522034113.

D'Andrea, F., Provenzale, A., Vautard, R., et al. Hot and cool summers: Multiple equilibria of the continental water cycle. *Geophysical Research Letters*, 33(24), 2006. doi: 10.1029/2006GL027972.

de Kok, R. J., Brogi, M., Snellen, I. A. G., et al. Detection of carbon monoxide in the high-resolution day-side spectrum of the exoplanet HD 189733b. *A&A*, 554:A82, 2013. doi: 10.1051/0004-6361/201321381.

Del Genio, A. D., Way, M. J., Amundsen, D. S., et al. Habitable Climate Scenarios for Proxima Centauri b with a Dynamic Ocean. *Astrobiology*, 19(1):99–125, 2019a. doi: 10.1089/ast.2017.1760.

Del Genio, A. D., Way, M. J., Kiang, N. Y., et al. Climates of Warm Earth-like Planets. III. Fractional Habitability from a Water Cycle Perspective. *ApJ*, 887(2):197, 2019b. doi: 10.3847/1538-4357/ab57fd.

Demory, B.-O., de Wit, J., Lewis, N., et al. Inference of Inhomogeneous Clouds in an Exoplanet Atmosphere. *ApJL*, 776(2):L25, 2013. doi: 10.1088/2041-8205/776/2/L25.

Di Paolo, M., Stevens, D., Joshi, M., et al. Nonlinear and Nonmonotonic Effect of Ocean Tidal Mixing on Exoplanet Climates and Habitability. *ApJL*, 982(2):L48, 2025. doi: 10.3847/2041-8213/adbca3.

Di Stefano, R., Berndtsson, J., Urquhart, R., et al. A possible planet candidate in an external galaxy detected through X-ray transit. *Nature Astronomy*, 5:1297–1307, 2021. doi: 10.1038/s41550-021-01495-w.

Dobos, V., Heller, R., and Turner, E. L. The effect of multiple heat sources on exomoon habitable zones. *A&A*, 601:A91, 2017. doi: 10.1051/0004-6361/201730541.

Dobrovolskis, A. R. Atmospheric tides and the rotation of Venus II. Spin evolution. *Icarus*, 41(1):18–35, 1980. doi: 10.1016/0019-1035(80)90157-8.

Dobrovolskis, A. R. Spin states and climates of eccentric exoplanets. *Icarus*, 192(1):1–23, 2007. doi: 10.1016/j.icarus.2007.07.005.

Dobrovolskis, A. R. Insolation patterns on eccentric exoplanets. *Icarus*, 250:395–399, 2015. doi: 10.1016/j.icarus.2014.12.017.

Dobrovolskis, A. R. and Ingersoll, A. P. Atmospheric tides and the rotation of Venus I. Tidal theory and the balance of torques. *Icarus*, 41(1):1–17, 1980. doi: 10.1016/0019-1035(80)90156-6.

Dole, S. H. *Habitable planets for man.* Blaisdell Publishing Company, 1964.

Dressing, C. D. and Charbonneau, D. The Occurrence Rate of Small Planets around Small Stars. *ApJ*, 767(1):95, 2013. doi: 10.1088/0004-637X/767/1/95.

Dressing, C. D. and Charbonneau, D. The Occurrence of Potentially Habitable Planets Orbiting M Dwarfs Estimated from the Full Kepler Dataset and an Empirical Measurement of the Detection Sensitivity. *ApJ*, 807(1):45, 2015. doi: 10.1088/0004-637X/807/1/45.

Dressing, C. D., Spiegel, D. S., Scharf, C. A., et al. Habitable Climates: The Influence of Eccentricity. *ApJ*, 721(2):1295–1307, 2010. doi: 10.1088/0004-637X/721/2/1295.

Dutkiewicz, A., Merdith, A. S., Collins, A. S., et al. Duration of Sturtian "Snowball Earth" glaciation linked to exceptionally low mid-ocean ridge outgassing. *Geology*, 52 (4):292–296, 2024. ISSN 0091-7613. doi: 10.1130/G51669.1.

Eberhard, J., Bevan, O. E., Feulner, G., et al. Sensitivity of Neoproterozoic snowball-Earth inceptions to continental configuration, orbital geometry, and volcanism. *Climate of the Past*, 19(11):2203–2235, 2023. doi: 10.5194/cp-19-2203-2023.

Edson, A., Lee, S., Bannon, P., et al. Atmospheric circulations of terrestrial planets orbiting low-mass stars. *Icarus*, 212(1):1–13, 2011. doi: 10.1016/j.icarus.2010.11.023.

Eggl, S., Georgakarakos, N., and Pilat-Lohinger, E. Habitable Zones in Binary Star Systems: A Zoology. *Galaxies*, 8(3):65, 2020. doi: 10.3390/galaxies8030065.

Enderton, D. and Marshall, J. Explorations of Atmosphere-Ocean-Ice Climates on an Aquaplanet and Their Meridional Energy Transports. *Journal of the Atmospheric Sciences*, 66(6):1593–1611, 2009. doi: 10.1175/2008JAS2680.1.

Fang, J. and Margot, J.-L. Are Planetary Systems Filled to Capacity? A Study Based on Kepler Results. *ApJ*, 767(2):115, 2013. doi: 10.1088/0004-637X/767/2/115.

Farneti, R. and Vallis, G. K. Meridional energy transport in the coupled atmosphere–ocean system: Compensation and partitioning. *Journal of Climate*, 26(18):7151 – 7166, 2013. doi: 10.1175/JCLI-D-12-00133.1.

Ferrari, R. and Ferreira, D. What processes drive the ocean heat transport? *Ocean Modelling*, 38(3):171–186, 2011. doi: 10.1016/j.ocemod.2011.02.013.

Ferreira, D., Marshall, J., and Campin, J.-M. Localization of Deep Water Formation: Role of Atmospheric Moisture Transport and Geometrical Constraints on Ocean Circulation. *Journal of Climate*, 23(6):1456, 2010. doi: 10.1175/2009JCLI3197.1.

Ferreira, D., Marshall, J., and Rose, B. Climate Determinism Revisited: Multiple Equilibria in a Complex Climate Model. *Journal of Climate*, 24(4):992–1012, 2011. doi: 10.1175/2010JCLI3580.1.

Ferreira, D., Marshall, J., O'Gorman, P. A., et al. Climate at high-obliquity. *Icarus*, 243: 236–248, 2014. doi: 10.1016/j.icarus.2014.09.015.

Fischer, H., Schmitt, J., Lüthi, D., et al. The role of Southern Ocean processes in orbital and millennial CO2 variations – A synthesis. *Quaternary Science Reviews*, 29(1):193–205, 2010. ISSN 0277-3791. doi: 10.1016/j.quascirev.2009.06.007.

Fofonoff, N. P. and Millard, R. C. Algorithms for the computation of fundamental properties of seawater. Technical Report 44, UNESCO, Paris, 1983.

Forgan, D. and Kipping, D. Dynamical effects on the habitable zone for Earth-like exomoons. *MNRAS*, 432(4):2994–3004, 2013. doi: 10.1093/mnras/stt662.

Forgan, D. H. The habitable zone for Earth-like exomoons orbiting Kepler-1625b. *International Journal of Astrobiology*, 18(6):510–517, 2019. doi: 10.1017/S1473550418000514.

Forster, P. M., Blackburn, M., Glover, R., et al. An examination of climate sensitivity for idealised climate change experiments in an intermediate general circulation model. *Climate Dynamics*, 16(10-11):833–849, 2000. doi: 10.1007/s003820000083.

Fu, L.-L. and Chelton, D. B. Large-scale ocean circulation revealed by satellite altimetry. *Nature*, 308:148–150, 1984. doi: 10.1038/308148a0.

Fu, M., Abbot, D. S., Koeberl, C., et al. Impact-induced initiation of Snowball Earth: A model study. *Science Advances*, 10(6):eadk5489, 2024. doi: 10.1126/sciadv.adk5489.

Gaia Collaboration et al. The Gaia mission. *A&A*, 595:A1, 2016. doi: 10.1051/0004-6361/201629272.

Galilei, G. *Sidereus nuncius*. Tommaso Baglioni, Venice, 1610. First edition.

Galilei, G. *Istoria e dimostrazioni intorno alle macchie solari e loro accidenti*. Giacomo Mascardi, Rome, 1613. First edition.

Galilei, G. *Dialogo sopra i due massimi sistemi del mondo*. Giovan Battista Landini, Florence, 1632. First edition.

Galle, J. G. Account of the discovery of Le Verrier's planet Neptune, at Berlin, Sept. 23, 1846. *MNRAS*, 7:153, 1846. doi: 10.1093/mnras/7.9.153.

Gallet, F., Charbonnel, C., Amard, L., et al. Impacts of stellar evolution and dynamics on the habitable zone: The role of rotation and magnetic activity. *A&A*, 597:A14, 2017. doi: 10.1051/0004-6361/201629034.

Gargett, A. E. Vertical eddy diffusivity in the ocean interior. *Journal of Marine Research*, 42(2):359–393, 1984. doi: 10.1357/002224084788502756.

Gatewood, G. An astrometric study of Lalande 21185. *AJ*, 79:52–53, 1974. doi: 10.1086/111530.

Geist, A., Beguelin, A., Dongarra, J., et al. *PVM: Parallel Virtual Machine — A User's Guide and Tutorial for Networked Parallel Computing.* MIT Press, Cambridge, Massachusetts, 1994. doi: 10.7551/mitpress/5712.001.0001.

Ghil, M. and Lucarini, V. The physics of climate variability and climate change. *Reviews of Modern Physics*, 92(3):035002, 2020. doi: 10.1103/RevModPhys.92.035002.

Giacalone, S. and Dressing, C. Small and Close-in Planets are Uncommon Around A-type Stars. *The Astronomical Journal*, 169:45, 2024. doi: 10.3847/1538-3881/ad9587.

Gillon, M., Triaud, A. H. M. J., Demory, B.-O., et al. Seven temperate terrestrial planets around the nearby ultracool dwarf star TRAPPIST-1. *Nature*, 542(7642):456–460, 2017. doi: 10.1038/nature21360.

Gillon, M., Ducrot, E., Bell, T. J., et al. First JWST thermal phase curves of temperate terrestrial exoplanets reveal no thick atmosphere around TRAPPIST-1 b and c. *arXiv e-prints*, art. arXiv:2509.02128, 2025. doi: 10.48550/arXiv.2509.02128.

Glaser, D. M., Aleinov, I., Leboissetier, A., et al. Continental orientation and the climate of land-dominated, arid planets. *The Planetary Science Journal*, 6(5):111, 2025. doi: 10.3847/PSJ/adccb6.

Goldreich, P. Tidal De-spin of Planets and Satellites. *Nature*, 208(5008):375–376, 1965. doi: 10.1038/208375b0.

Goldreich, P. Final spin states of planets and satellites. *AJ*, 71:1, 1966. doi: 10.1086/109844.

Goldreich, P. and Peale, S. Spin-orbit coupling in the solar system. *AJ*, 71:425, 1966a. doi: 10.1086/109947.

Goldreich, P. and Peale, S. J. Resonant Rotation for Venus? *Nature*, 209(5028):1117–1118, 1966b. doi: 10.1038/2091117a0.

González-Payo, J., Caballero, J. A., Gorgas, J., et al. Multiplicity of stars with planets in the solar neighbourhood. *A&A*, 689:A302, 2024. doi: 10.1051/0004-6361/202450048.

Gould, A. and Loeb, A. Discovering Planetary Systems through Gravitational Microlenses. *ApJ*, 396:104, 1992. doi: 10.1086/171700.

Griffies, S. M., Biastoch, A., Böning, C., et al. Coordinated Ocean-ice Reference Experiments (COREs). *Ocean Modelling*, 26(1):1–46, 2009. ISSN 1463-5003. doi: 10.1016/j.ocemod.2008.08.007.

Guendelman, I. and Kaspi, Y. Atmospheric Dynamics on Terrestrial Planets: The Seasonal Response to Changes in Orbital, Rotational, and Radiative Timescales. *ApJ*, 881(1):67, 2019. doi: 10.3847/1538-4357/ab2a06.

Guimond, C. M., Spohn, T., Berdyugina, S., et al. Water Versus Land on Temperate Rocky Planets. *SSRv*, 222(1):8, 2026. doi: 10.1007/s11214-025-01264-5.

Guzewich, S. D., Lustig-Yaeger, J., Davis, C. E., et al. The Impact of Planetary Rotation Rate on the Reflectance and Thermal Emission Spectrum of Terrestrial Exoplanets around Sunlike Stars. *ApJ*, 893(2):140, 2020. doi: 10.3847/1538-4357/ab83ec.

Hadden, S. and Lithwick, Y. Kepler Planet Masses and Eccentricities from TTV Analysis. *AJ*, 154(1):5, 2017. doi: 10.3847/1538-3881/aa71ef.

Hall, C., Stancil, P. C., Terry, J. P., et al. A New Definition of Exoplanet Habitability: Introducing the Photosynthetic Habitable Zone. *ApJL*, 948(2):L26, 2023. doi: 10.3847/2041-8213/acccfb.

Hall, M. M. and Bryden, H. L. Direct estimates and mechanisms of ocean heat transport. *Deep Sea Research A*, 29(3):339–359, 1982. doi: 10.1016/0198-0149(82)90099-1.

Hammond, M. and Lewis, N. T. The rotational and divergent components of atmospheric circulation on tidally locked planets. *Proceedings of the National Academy of Science*, 118(13):e2022705118, 2021. doi: 10.1073/pnas.2022705118.

Hammond, M. and Pierrehumbert, R. T. Wave-mean Flow Interactions in the Atmospheric Circulation of Tidally Locked Planets. *ApJ*, 869(1):65, 2018. doi: 10.3847/1538-4357/aaec03.

Hammond, T. and Komacek, T. D. The Coupled Impacts of Atmospheric Composition and Obliquity on the Climate Dynamics of TRAPPIST-1e. *ApJ*, 968(1):43, 2024. doi: 10.3847/1538-4357/ad4a59.

Haqq-Misra, J., Wolf, E. T., Joshi, M., et al. Demarcating Circulation Regimes of Synchronously Rotating Terrestrial Planets within the Habitable Zone. *ApJ*, 852(2):67, 2018. doi: 10.3847/1538-4357/aa9f1f.

Haqq-Misra, J., Wolf, E. T., Fauchez, T. J., et al. The Sparse Atmospheric Model Sampling Analysis (SAMOSA) Intercomparison: Motivations and Protocol Version 1.0: A CUISINES Model Intercomparison Project. *PSJ*, 3(11):260, 2022. doi: 10.3847/PSJ/ac9479.

Harada, C. K., Dressing, C. D., Kane, S. R., et al. Setting the Stage for the Search for Life with the Habitable Worlds Observatory: Properties of 164 Promising Planet-survey Targets. *ApJS*, 272(2):30, 2024. doi: 10.3847/1538-4365/ad3e81.

Harrington, J., Hansen, B. M., Luszcz, S. H., et al. The Phase-Dependent Infrared Brightness of the Extrasolar Planet υ Andromedae b. *Science*, 314(5799):623–626, 2006. doi: 10.1126/science.1133904.

Hart, M. H. Habitable Zones about Main Sequence Stars. *Icarus*, 37(1):351–357, 1979. doi: 10.1016/0019-1035(79)90141-6.

Harwit, M. Stars. In *Astrophysical Concepts*, Astronomy and Astrophysics Library, pages 287–349. Springer, New York, NY, 1998.

Hatzes, A. P., Cochran, W. D., Endl, M., et al. A Planetary Companion to γ Cephei A. *ApJ*, 599(2):1383–1394, 2003. doi: 10.1086/379281.

Hawkins, E., Smith, R. S., Allison, L. C., et al. Bistability of the Atlantic overturning circulation in a global climate model and links to ocean freshwater transport. *Geophysical Research Letters*, 38(10), 2011. doi: 10.1029/2011GL047208.

Hays, L. E., New, M. H., and Voytek, M. A. 2015 NASA Astrobiology Strategy Document and the Vision for Solar System Exploration. In LPI Editorial Board, editor, *Planetary Science Vision 2050 Workshop*, volume 1989 of *LPI Contributions*, page 8141, 2017.

Heath, M. J., Doyle, L. R., Joshi, M. M., et al. Habitability of Planets Around Red Dwarf Stars. *Origins of Life and Evolution of the Biosphere*, 29(4):405–424, 1999. doi: 10.1023/A:1006596718708.

Heintz, W. D. Reexamination of suspected unresolved binaries. *ApJ*, 220:931–934, 1978. doi: 10.1086/155982.

Heller, R. and Barnes, R. Exomoon Habitability Constrained by Illumination and Tidal Heating. *Astrobiology*, 13(1):18–46, 2013. doi: 10.1089/ast.2012.0859.

Hellerman, S. and Rosenstein, M. Normal monthly wind stress over the world ocean with error estimates. *Journal of Physical Oceanography*, 13(7):1093 – 1104, 1983. doi: 10.1175/1520-0485(1983)013⟨1093:NMWSOT⟩2.0.CO;2.

Henry, G. W., Marcy, G. W., Butler, R. P., et al. A Transiting "51 Peg-like" Planet. *ApJL*, 529(1):L41–L44, 2000. doi: 10.1086/312458.

Herschel, W. *The Scientific Papers of Sir William Herschel, Volume I.* Royal Society and Royal Astronomical Society, London, 1912.

Hershey, J. L. Astrometric analysis of the field of AC +65 6955 from plates taken with the Sproul 24-inch refractor. *AJ*, 78:421–425, 1973. doi: 10.1086/111436.

Herweijer, C., Seager, R., Winton, M., et al. Why ocean heat transport warms the global mean climate. *Tellus Series A*, 57(4):662, 2005. doi: 10.3402/tellusa.v57i4.14708.

Hoffman, P. F. and Schrag, D. P. The snowball Earth hypothesis: testing the limits of global change. *Terra Nova*, 14(3):129–155, 2002. doi: 10.1046/j.1365-3121.2002.00408.x.

Horneck, G., Walter, N., Westall, F., et al. AstRoMap European Astrobiology Roadmap. *Astrobiology*, 16(3):201–243, 2016. doi: 10.1089/ast.2015.1441.

Hsu, D. C., Ford, E. B., and Terrien, R. Occurrence rates of planets orbiting M Stars: applying ABC to Kepler DR25, Gaia DR2, and 2MASS data. *Monthly Notices of the Royal Astronomical Society*, 498(2):2249–2262, 2020. ISSN 0035-8711. doi: 10.1093/mnras/staa2391.

Hu, Y. and Yang, J. Role of ocean heat transport in climates of tidally locked exoplanets around M dwarf stars. *Proceedings of the National Academy of Science*, 111(2):629–634, 2014. doi: 10.1073/pnas.1315215111.

Huang, S.-S. Occurrence of Life in the Universe. *American Scientist*, 47(3):397–402, 1959.

Huygens, C. *The Cosmotheoros*. Timothy Childe, London, 1698. English translation of *Cosmotheoros*.

Hyde, W. T., Crowley, T. J., Baum, S. K., et al. Neoproterozoic 'snowball earth' simulations with a coupled climate/ice-sheet model. *Journal of Geophysical Research: Atmospheres*, 105(D23):1575–1593, 2000. doi: 10.1029/1999JD900537.

Jackson, B., Barnes, R., and Greenberg, R. Tidal heating of terrestrial extrasolar planets and implications for their habitability. *MNRAS*, 391(1):237–245, 2008a. doi: 10.1111/j.1365-2966.2008.13868.x.

Jackson, B., Greenberg, R., and Barnes, R. Tidal Evolution of Close-in Extrasolar Planets. *ApJ*, 678(2):1396–1406, 2008b. doi: 10.1086/529187.

Jacob, W. S. On certain Anomalies presented by the Binary Star 70 Ophiuchi. *MNRAS*, 15:228, 1855. doi: 10.1093/mnras/15.9.228.

Janson, M., Bergfors, C., Goto, M., et al. Spatially Resolved Spectroscopy of the Exoplanet HR 8799 c. *ApJL*, 710(1):L35–L38, 2010. doi: 10.1088/2041-8205/710/1/L35.

Janssen, R. H. H., Meinders, M. B. J., Van Nes, E. H., et al. Microscale vegetation-soil feedback boosts hysteresis in a regional vegetation–climate system. *Global Change Biology*, 14(5):1104–1112, 2008. doi: 10.1111/j.1365-2486.2008.01540.x.

Ji, X. and Abbot, D. S. Snowball Bistability Vanishes at Moderate Orbital Eccentricity. *PSJ*, 6(12):296, 2025. doi: 10.3847/PSJ/ae201c.

Johns, W. E., Baringer, M. O., Beal, L. M., et al. Continuous, Array-Based Estimates of Atlantic Ocean Heat Transport at 26.5°N. *Journal of Climate*, 24(10):2429–2449, 2011. doi: 10.1175/2010JCLI3997.1.

Johns, W. E., Elipot, S., Smeed, D. A., et al. Towards two decades of Atlantic Ocean mass and heat transports at 26.5° N. *Philosophical Transactions of the Royal Society A: Mathematical, Physical and Engineering Sciences*, 381(2262):20220188, 2023. doi: 10.1098/rsta.2022.0188.

Jones, B. W., Sleep, P. N., and Underwood, D. R. Habitability of Known Exoplanetary Systems Based on Measured Stellar Properties. *ApJ*, 649(2):1010–1019, 2006. doi: 10.1086/506557.

Joshi, M., Stringer, M., van der Wiel, K., et al. IGCM4: a fast, parallel and flexible intermediate climate model. *Geoscientific Model Development*, 8(4):1157–1167, 2015. doi: 10.5194/gmd-8-1157-201510.5194/gmdd-7-5517-2014.

Joshi, M. M. and Haberle, R. M. Suppression of the Water Ice and Snow Albedo Feedback on Planets Orbiting Red Dwarf Stars and the Subsequent Widening of the Habitable Zone. *Astrobiology*, 12(1):3–8, 2012. doi: 10.1089/ast.2011.0668.

Joshi, M. M., Haberle, R. M., and Reynolds, R. T. Simulations of the Atmospheres of Synchronously Rotating Terrestrial Planets Orbiting M Dwarfs: Conditions for Atmospheric Collapse and the Implications for Habitability. *Icarus*, 129(2):450–465, 1997. doi: 10.1006/icar.1997.5793.

Kant, I. Untersuchung der Frage, ob die Erde in ihrer Umdrehung um die Achse eine Veränderung erlitten habe. *Wöchentliche Königsbergische Frag- und Anzeigungs-Nachrichten*, 1754. Original newspaper publication.

Kasper, M., Cerpa Urra, N., Pathak, P., et al. PCS — A Roadmap for Exoearth Imaging with the ELT. *The Messenger*, 182:38–43, 2021. doi: 10.18727/0722-6691/5221.

Kaspi, Y. and Showman, A. P. Atmospheric Dynamics of Terrestrial Exoplanets over a Wide Range of Orbital and Atmospheric Parameters. *ApJ*, 804(1):60, 2015. doi: 10.1088/0004-637X/804/1/60.

Kasting, J. F., Whitmire, D. P., and Reynolds, R. T. Habitable Zones around Main Sequence Stars. *Icarus*, 101(1):108–128, 1993. doi: 10.1006/icar.1993.1010.

Kaula, W. M. Tidal Dissipation by Solid Friction and the Resulting Orbital Evolution. *Reviews of Geophysics and Space Physics*, 2:661–685, 1964. doi: 10.1029/RG002i004p00661.

Kawahara, H. and Fujii, Y. Mapping clouds and terrain of earth-like planets from photometric variability. *The Astrophysical Journal Letters*, 739(2):L62, 2011. doi: 10.1088/2041-8205/739/2/L62.

Kawahara, H. and Masuda, K. Bayesian dynamic mapping of an exo-earth from photometric variability. *The Astronomical Journal*, 160(5):242, 2020. doi: 10.3847/1538-3881/abae63.

Kay, C., Opher, M., and Kornbleuth, M. Probability of CME Impact on Exoplanets Orbiting M Dwarfs and Solar-like Stars. *ApJ*, 826(2):195, 2016. doi: 10.3847/0004-637X/826/2/195.

Kiefer, F. Determining the mass of the planetary candidate HD 114762 b using Gaia. *A&A*, 632:L9, 2019. doi: 10.1051/0004-6361/201936942.

Kienert, H., Feulner, G., and Petoukhov, V. Faint young Sun problem more severe due to ice-albedo feedback and higher rotation rate of the early Earth. *Geophys. Res. Lett.*, 39 (23):L23710, 2012. doi: 10.1029/2012GL054381.

Kilic, C., Raible, C. C., and Stocker, T. F. Multiple Climate States of Habitable Exoplanets: The Role of Obliquity and Irradiance. *ApJ*, 844(2):147, 2017. doi: 10.3847/1538-4357/aa7a03.

Kilic, C., Lunkeit, F., Raible, C. C., et al. Stable Equatorial Ice Belts at High Obliquity in a Coupled Atmosphere-Ocean Model. *ApJ*, 864(2):106, 2018. doi: 10.3847/1538-4357/aad5eb.

Kite, E. S., Gaidos, E., and Manga, M. Climate Instability on Tidally Locked Exoplanets. *ApJ*, 743(1):41, 2011. doi: 10.1088/0004-637X/743/1/41.

Kitzmann, D., Patzer, A. B. C., von Paris, P., et al. Clouds in the atmospheres of extrasolar planets. I. Climatic effects of multi-layered clouds for Earth-like planets and implications for habitable zones. *A&A*, 511:A66, 2010. doi: 10.1051/0004-6361/200913491.

Knutson, H. A., Charbonneau, D., Allen, L. E., et al. A map of the day-night contrast of the extrasolar planet HD 189733b. *Nature*, 447(7141):183–186, 2007. doi: 10.1038/nature05782.

Knutson, H. A., Charbonneau, D., Allen, L. E., et al. The 3.6-8.0 μm Broadband Emission Spectrum of HD 209458b: Evidence for an Atmospheric Temperature Inversion. *ApJ*, 673(1):526–531, 2008. doi: 10.1086/523894.

Koch, D. G., Borucki, W. J., Basri, G., et al. Kepler Mission Design, Realized Photometric Performance, and Early Science. *ApJL*, 713(2):L79–L86, 2010. doi: 10.1088/2041-8205/713/2/L79.

Kodama, T., Genda, H., O'ishi, R., et al. Inner Edge of Habitable Zones for Earth-Sized Planets With Various Surface Water Distributions. *Journal of Geophysical Research (Planets)*, 124(8):2306–2324, 2019. doi: 10.1029/2019JE006037.

Koll, D. D. B. and Abbot, D. S. Deciphering Thermal Phase Curves of Dry, Tidally Locked Terrestrial Planets. *ApJ*, 802(1):21, 2015. doi: 10.1088/0004-637X/802/1/21.

Komacek, T. D. and Abbot, D. S. The Atmospheric Circulation and Climate of Terrestrial Planets Orbiting Sun-like and M Dwarf Stars over a Broad Range of Planetary Parameters. *ApJ*, 871(2):245, 2019. doi: 10.3847/1538-4357/aafb33.

Komacek, T. D., Showman, A. P., and Tan, X. Atmospheric Circulation of Hot Jupiters: Dayside-Nightside Temperature Differences. II. Comparison with Observations. *ApJ*, 835(2):198, 2017. doi: 10.3847/1538-4357/835/2/198.

Kopp, R. E., Kirschvink, J. L., Hilburn, I. A., et al. The Paleoproterozoic snowball Earth: A climate disaster triggered by the evolution of oxygenic photosynthesis. *Proceedings of the National Academy of Sciences*, 102(32):11131–11136, 2005. doi: 10.1073/pnas.0504878102.

Kopparapu, R. K., Ramirez, R., Kasting, J. F., et al. Habitable Zones around Main-sequence Stars: New Estimates. *ApJ*, 765(2):131, 2013. doi: 10.1088/0004-637X/765/2/131.

Kopparapu, R. K., Ramirez, R. M., SchottelKotte, J., et al. Habitable Zones around Main-sequence Stars: Dependence on Planetary Mass. *ApJL*, 787(2):L29, 2014. doi: 10.1088/2041-8205/787/2/L29.

Kopparapu, R. K., Wolf, E. T., Haqq-Misra, J., et al. The Inner Edge of the Habitable Zone for Synchronously Rotating Planets around Low-mass Stars Using General Circulation Models. *ApJ*, 819(1):84, 2016. doi: 10.3847/0004-637X/819/1/84.

Kopparapu, R. K., Wolf, E. T., Arney, G., et al. Habitable Moist Atmospheres on Terrestrial Planets near the Inner Edge of the Habitable Zone around M Dwarfs. *ApJ*, 845(1):5, 2017. doi: 10.3847/1538-4357/aa7cf9.

Kossakowski, D., Kürster, M., Trifonov, T., et al. The CARMENES search for exoplanets around M dwarfs. Wolf 1069 b: Earth-mass planet in the habitable zone of a nearby, very low-mass star. *A&A*, 670:A84, 2023. doi: 10.1051/0004-6361/202245322.

Kočandrle, R. Infinite Worlds in the Thought of Anaximander. *The Classical Quarterly*, 69(2):483–500, 2019. doi: 10.1017/S000983882000004X.

Kreidberg, L. Exoplanet Atmosphere Measurements from Transmission Spectroscopy and Other Planet Star Combined Light Observations. In Deeg, H. J. and Belmonte, J. A., editors, *Handbook of Exoplanets*, page 100. Springer International Publishing, 2018. doi: 10.1007/978-3-319-55333-7_100.

Krissansen-Totton, J. and Catling, D. Constraining climate sensitivity and continental versus seafloor weathering using an inverse geological carbon cycle model. *Nature Communications*, 8:15423, 2017. doi: 10.1038/ncomms15423.

Laertius, D. *Lives of Eminent Philosophers, Volume II.* Loeb Classical Library, Harvard University Press, Cambridge, MA, 1925.

Landais, F., Schmidt, F., and Lovejoy, S. Topography of (exo)planets. *MNRAS*, 484(1): 787–793, 2019. doi: 10.1093/mnras/sty3253.

Lardner, D. *Handbook of Natural Philosophy and Astronomy.* Taylor, Walton, and Maberly, London, 1851.

Latham, D. W., Mazeh, T., Stefanik, R. P., et al. The unseen companion of HD114762: a probable brown dwarf. *Nature*, 339(6219):38–40, 1989. doi: 10.1038/339038a0.

Le Hir, G., Goddéris, Y., Donnadieu, Y., et al. A geochemical modelling study of the evolution of seawater composition linked to a “snowball” glaciation. *Biogeosciences*, 5: 253–267, 2008. doi: 10.5194/bg-5-253-2008.

Le Verrier, U. J. J. *Recherches sur les mouvements de la planète Herschel.* Connaissance des temps. Bachelier, Paris, 1846.

Lecavelier des Etangs, A. and Lissauer, J. J. The IAU working definition of an exoplanet. *NewAR*, 94:101641, 2022. doi: 10.1016/j.newar.2022.101641.

Leconte, J., Forget, F., Charnay, B., et al. 3D climate modeling of close-in land planets: Circulation patterns, climate moist bistability, and habitability. *A&A*, 554:A69, 2013. doi: 10.1051/0004-6361/201321042.

Leconte, J., Wu, H., Menou, K., et al. Asynchronous rotation of Earth-mass planets in the habitable zone of lower-mass stars. *Science*, 347(6222):632–635, 2015. doi: 10.1126/science.1258686.

Lenton, T., Daines, S., and Mills, B. COPSE reloaded: An improved model of biogeochemical cycling over Phanerozoic time. *Earth-Science Reviews*, 178:1–28, 2018. doi: 10.1016/j.earscirev.2017.12.004.

Lerner, P., Romanou, A., Way, M., et al. Obliquity Dependence of Ocean Productivity and Atmospheric CO_2 on Earth-like Worlds. *ApJ*, 979(2):234, 2025. doi: 10.3847/1538-4357/ada277.

Levitus, S. *Climatological Atlas of the World Ocean.* NOAA Professional Paper 13. U.S. Government Printing Office, Washington, D.C., 1982.

Lewis, N. T., Lambert, F. H., Boutle, I. A., et al. The Influence of a Substellar Continent on the Climate of a Tidally Locked Exoplanet. *ApJ*, 854(2):171, 2018. doi: 10.3847/1538-4357/aaad0a.

Li, Y. and Yang, H. A Theory for Self-Sustained Multicentennial Oscillation of the Atlantic Meridional Overturning Circulation. *Journal of Climate*, 35(18):5883 – 5896, 2022. doi: 10.1175/JCLI-D-21-0685.1.

Lineweaver, C. H., Fenner, Y., and Gibson, B. K. The Galactic Habitable Zone and the Age Distribution of Complex Life in the Milky Way. *Science*, 303(5654):59–62, 2004. doi: 10.1126/science.1092322.

Lingam, M. and Loeb, A. On the Habitable Lifetime of Terrestrial Worlds with High Radionuclide Abundances. *ApJL*, 889(1):L20, 2020. doi: 10.3847/2041-8213/ab68e5.

Linsenmeier, M., Pascale, S., and Lucarini, V. Climate of Earth-like planets with high obliquity and eccentric orbits: Implications for habitability conditions. *Planet. Space Sci.*, 105:43–59, 2015. doi: 10.1016/j.pss.2014.11.003.

Liu, X., Battisti, D. S., and Roe, G. H. The Effect of Cloud Cover on the Meridional Heat Transport: Lessons from Variable Rotation Experiments. *Journal of Climate*, 30(18): 7465–7479, 2017. doi: 10.1175/JCLI-D-16-0745.1.

Lobo, A. H., Shields, A. L., Palubski, I. Z., et al. Terminator Habitability: The Case for Limited Water Availability on M-dwarf Planets. *ApJ*, 945(2):161, 2023. doi: 10.3847/1538-4357/aca970.

Lucretius. *De Rerum Natura.* Loeb Classical Library. Harvard University Press, Cambridge, MA, 1924. Revised edition by Martin F. Smith.

Luger, R. and Barnes, R. Extreme Water Loss and Abiotic O2Buildup on Planets Throughout the Habitable Zones of M Dwarfs. *Astrobiology*, 15(2):119–143, 2015. doi: 10.1089/ast.2014.1231.

Macdonald, E., Paradise, A., Menou, K., et al. Climate uncertainties caused by unknown land distribution on habitable M-Earths. *MNRAS*, 513(2):2761–2769, 2022. doi: 10.1093/mnras/stac1040.

Macdonald, E. J. R. and Cowan, N. B. An empirical infrared transit spectrum of Earth: opacity windows and biosignatures. *MNRAS*, 489(1):196–204, 2019. doi: 10.1093/mnras/stz2047.

Macdonald, F. A. and Swanson-Hysell, N. L. The franklin large igneous province and snowball earth initiation. *Elements*, 19(5):296–301, 2023. doi: 10.2138/gselements.19.5.296.

MacDonald, G. J. F. Tidal Friction. *Reviews of Geophysics and Space Physics*, 2:467–541, 1964. doi: 10.1029/RG002i003p00467.

MacLeod, K. G., Huber, B. T., Berrocoso, J., et al. A stable and hot Turonian without glacial 18O excursions is indicated by exquisitely preserved Tanzanian foraminifera. *Geology*, 41(10):1083–1086, 2013. ISSN 0091-7613. doi: 10.1130/G34510.1.

Madden, J. and Kaltenegger, L. How surfaces shape the climate of habitable exoplanets. *MNRAS*, 495(1):1–11, 2020. doi: 10.1093/mnras/staa387.

Madhusudhan, N. Exoplanetary Atmospheres: Key Insights, Challenges, and Prospects. *ARA&A*, 57:617–663, 2019. doi: 10.1146/annurev-astro-081817-051846.

Manabe, S. Climate and the Ocean Circulation. II. The Atmospheric Circulation and the Effect of Heat Transfer by Ocean Currents. *Monthly Weather Review*, 97(11):775 – 805, 1969. doi: 10.1175/1520-0493(1969)097⟨0775:CATOC⟩2.3.CO;2.

Manners, J., Edwards, J., Hill, P., et al. Socrates: Suite of community radiative transfer codes based on edwards and slingo. Technical Report Met Office Technical Report, UK Met Office, 2015. URL https://github.com/MetOffice/socrates. Access to full documentation available via the Met Office Science Repository Service.

Mao, S. and Paczynski, B. Gravitational Microlensing by Double Stars and Planetary Systems. *ApJL*, 374:L37, 1991. doi: 10.1086/186066.

Marley, M. S., Ackerman, A. S., Cuzzi, J. N., et al. Clouds and Hazes in Exoplanet Atmospheres. In Mackwell, S. J., Simon-Miller, A. A., Harder, J. W., and Bullock, M. A., editors, *Comparative Climatology of Terrestrial Planets*, pages 367–392. University pf Arizona Press, 2013. doi: 10.2458/azu_uapress_9780816530595-ch015.

Marotzke, J. Boundary mixing and the dynamics of three-dimensional thermohaline circulations. *Journal of Physical Oceanography*, 27(8):1713 – 1728, 1997. doi: 10.1175/1520-0485(1997)027⟨1713:BMATDO⟩2.0.CO;2.

Marotzke, J. and Willebrand, J. Multiple equilibria of the global thermohaline circulation. *Journal of Physical Oceanography*, 21(9):1372–1385, 1991. doi: 10.1175/1520-0485(1991)021⟨1372:MEOGTC⟩2.0.CO;2.

Marshall, H., Walker, J., and Kuhn, W. Long-term climate change and the geochemical cycle of carbon. *Journal of Geophysical Research*, 93:791–801, 1988. doi: 10.1029/88JD01568.

Marshall, J., Ferreira, D., Campin, J.-M., et al. Mean Climate and Variability of the Atmosphere and Ocean on an Aquaplanet. *Journal of the Atmospheric Sciences*, 64 (12):4270, 2007. doi: 10.1175/2007JAS2226.1.

Martínez-Rodríguez, H., Caballero, J. A., Cifuentes, C., et al. Exomoons in the Habitable Zones of M Dwarfs. *ApJ*, 887(2):261, 2019. doi: 10.3847/1538-4357/ab5640.

Mayor, M. and Queloz, D. A Jupiter-mass companion to a solar-type star. *Nature*, 378 (6555):355–359, 1995. doi: 10.1038/378355a0.

McCarthy, G. D., Smeed, D. A., Johns, W. E., et al. Measuring the Atlantic Meridional Overturning Circulation at 26°N. *Progress in Oceanography*, 130:91–111, 2015. doi: 10.1016/j.pocean.2014.10.006.

McMahon, S. and Parnell, J. Weighing the deep continental biosphere. *FEMS Microbiology Ecology*, 87(1):113–120, 2014. doi: 10.1111/1574-6941.12196.

McTier, M. A. S. and Kipping, D. M. Finding mountains with molehills: The detectability of exotopography. *Monthly Notices of the Royal Astronomical Society*, 475(4):4978–4985, 2018. doi: 10.1093/mnras/sty143.

Meadows, V. S. and Barnes, R. K. Factors Affecting Exoplanet Habitability. In Deeg, H. J. and Belmonte, J. A., editors, *Handbook of Exoplanets*, page 57. Springer, 2018. doi: 10.1007/978-3-319-55333-7_57.

Menou, K. and Tabachnik, S. Dynamical Habitability of Known Extrasolar Planetary Systems. *ApJ*, 583(1):473–488, 2003. doi: 10.1086/345359.

Ment, K. and Charbonneau, D. The Occurrence Rate of Terrestrial Planets Orbiting Nearby Mid-to-late M Dwarfs from TESS Sectors 1-42. *AJ*, 165(6):265, 2023. doi: 10.3847/1538-3881/acd175.

Möhlmann, D. Widen the Belt of Habitability! *Origins of Life and Evolution of the Biosphere*, 42(2-3):93–100, 2012. doi: 10.1007/s11084-012-9278-1.

Mol Lous, M., Helled, R., and Mordasini, C. Potential long-term habitable conditions on planets with primordial H-He atmospheres. *Nature Astronomy*, 6:819–827, 2022. doi: 10.1038/s41550-022-01699-8.

Moulton, F. R. The limits of temporary stability of satellite motion, with an application to the question of the existence of an unseen body in the binary system 70 Ophiuchi. *AJ*, 20:33–37, 1899. doi: 10.1086/103096.

Mousis, O., Deleuil, M., Aguichine, A., et al. Irradiated Ocean Planets Bridge Super-Earth and Sub-Neptune Populations. *ApJL*, 896(2):L22, 2020. doi: 10.3847/2041-8213/ab9530.

Mróz, P., Udalski, A., Bennett, D. P., et al. Two new free-floating or wide-orbit planets from microlensing. *A&A*, 622:A201, 2019. doi: 10.1051/0004-6361/201834557.

Mulders, G., Pascucci, I., and Apai, D. A Stellar-mass-dependent Drop in Planet Occurrence Rates. *The Astrophysical Journal*, 798, 2014. doi: 10.1088/0004-637X/798/2/112.

Munk, W. and Wunsch, C. Abyssal recipes II: energetics of tidal and wind mixing. *Deep Sea Research Part I: Oceanographic Research*, 45(12):1977–2010, 1998. doi: 10.1016/S0967-0637(98)00070-3.

Murante, G., Provenzale, A., Vladilo, G., et al. Climate bistability of Earth-like exoplanets. *MNRAS*, 492(2):2638–2650, 2020. doi: 10.1093/mnras/stz3529.

Murphy, M. This Nobel Prize Winner Explains Why You Need A Dose Of 'Soft Insanity' To Be Successful. *Forbes*, 2022.

Murray, C. D. and Dermott, S. F. Tides, Rotation, and Shape. In *Solar System Dynamics*, pages 130–135. Cambridge University Press, 1999. doi: 10.1017/CBO9781139174817.

Musgrave, R. The Lifecycle of Topographically-Generated Internal Waves. In Garrett, C., Naveira Garabato, A., and Sutherland, B., editors, *Ocean Mixing: Drivers, Mechanisms and Impacts*, pages 117–144. Elsevier, 2021. doi: 10.1016/C2019-0-03674-6.

Nakayama, A., Kodama, T., Ikoma, M., et al. Runaway climate cooling of ocean planets in the habitable zone: a consequence of seafloor weathering enhanced by melting of high-pressure ice. *Monthly Notices of the Royal Astronomical Society*, 488(2):1580–1596, 2019. doi: 10.1093/mnras/stz1812.

NASA - Jet Propulsion Laboratory, California Institute of Technology. Visions of the Future Poster Series - 51 Pegasi b. NASA's Image and Video Library, 2020. Accessed: 2025-12-04.

Netto, Y., Lorenzo-Oliveira, D., Meléndez, J., et al. Radial-velocity Precision of ESPRESSO Through the Analysis of the Solar Twin HIP 11915. *AJ*, 162(4):160, 2021. doi: 10.3847/1538-3881/ac1bb5.

Newton, I. *The Mathematical Principles of Natural Philosophy*. Benjamin Motte, London, 1729. First English translation.

Nilsson, J., Langen, P. L., Ferreira, D., et al. Ocean basin geometry and the thermohaline circulation. *Journal of Physical Oceanography*, 43(3):610–626, 2013. doi: 10.1175/JPO-D-12-0132.1.

Nixon, M. C. and Madhusudhan, N. How deep is the ocean? Exploring the phase structure of water-rich sub-Neptunes. *MNRAS*, 505(3):3414–3432, 2021. doi: 10.1093/mnras/stab1500.

Noda, S., Ishiwatari, M., Nakajima, K., et al. The circulation pattern and day-night heat transport in the atmosphere of a synchronously rotating aquaplanet: Dependence on planetary rotation rate. *Icarus*, 282:1–18, 2017. doi: 10.1016/j.icarus.2016.09.004.

Nowajewski, P., Rojas, M., Rojo, P., et al. Atmospheric dynamics and habitability range in Earth-like aquaplanets obliquity simulations. *Icarus*, 305:84–90, 2018. doi: 10.1016/j.icarus.2018.01.002.

Olson, S., Jansen, M. F., Abbot, D. S., et al. The Effect of Ocean Salinity on Climate and Its Implications for Earth's Habitability. *Geophys. Res. Lett.*, 49(10):e95748, 2022. doi: 10.1029/2021GL095748.

Olson, S. L., Jansen, M., and Abbot, D. S. Oceanographic Considerations for Exoplanet Life Detection. *ApJ*, 895(1):19, 2020. doi: 10.3847/1538-4357/ab88c9.

Pacanowski, R. C., Dixon, K. W., and Rosati, A. The GFDL Modular Ocean Model User's Guide: Version 1.0. Technical Report GFDL Ocean Group Technical Report No. 2, Geophysical Fluid Dynamics Laboratory, Princeton, NJ, 1991.

Palubski, I. Z., Shields, A. L., and Deitrick, R. Habitability and Water Loss Limits on Eccentric Planets Orbiting Main-sequence Stars. *ApJ*, 890(1):30, 2020. doi: 10.3847/1538-4357/ab66b2.

Parmentier, V. and Crossfield, I. J. M. *Exoplanet Phase Curves: Observations and Theory*, pages 1419–1440. Springer International Publishing, Cham, 2018. ISBN 978-3-319-55333-7. doi: 10.1007/978-3-319-55333-7_116.

Pecaut, M. J. and Mamajek, E. E. Intrinsic Colors, Temperatures, and Bolometric Corrections of Pre-main-sequence Stars. *ApJS*, 208(1):9, 2013. doi: 10.1088/0067-0049/208/1/9.

Pedlosky, J. *Geophysical Fluid Dynamics*. Springer, New York, 2nd edition, 1987. doi: 10.1007/978-1-4612-4650-3.

Pepe, F., Molaro, P., Cristiani, S., et al. ESPRESSO: The next European exoplanet hunter. *Astronomische Nachrichten*, 335(1):8, 2014. doi: 12.1002/asna.201312004.

Perryman, M. *The Exoplanet Handbook*. Cambridge University Press, 2 edition, 2018. doi: 10.1017/9781108304160.

Perryman, M. A. C. Extra-solar planets. *Reports on Progress in Physics*, 63(8):1209–1272, 2000. doi: 10.1088/0034-4885/63/8/202.

Perryman, M. A. C. Perryman Tree, 2024. URL https://www.michaelperryman.co.uk/exoplanets.

Petigura, E. A., Rogers, J. G., Isaacson, H., et al. The California-Kepler Survey. X. The Radius Gap as a Function of Stellar Mass, Metallicity, and Age. *The Astronomical Journal*, 163(4):179, 2022. ISSN 1538-3881. doi: 10.3847/1538-3881/ac51e3.

Pierrehumbert, R. T. A Palette of Climates for Gliese 581g. *ApJL*, 726(1):L8, 2011. doi: 10.1088/2041-8205/726/1/L8.

Planetary Habitability Laboratory. Habitable Worlds Catalog, 2024. URL https://phl.upr.edu/hwc. University of Puerto Rico at Arecibo.

Pollack, J. B., Kasting, J. F., Richardson, S. M., et al. The case for a wet, warm climate on early Mars. *Icarus*, 71(2):203–224, 1987. doi: 10.1016/0019-1035(87)90147-3.

Quanz, S. P., Absil, O., Benz, W., et al. Atmospheric characterization of terrestrial exoplanets in the mid-infrared: biosignatures, habitability, and diversity. *Experimental Astronomy*, 54(2-3):1197–1221, 2022a. doi: 10.1007/s10686-021-09791-z.

Quanz, S. P., Ottiger, M., Fontanet, E., et al. Large Interferometer For Exoplanets (LIFE). I. Improved exoplanet detection yield estimates for a large mid-infrared space-interferometer mission. *A&A*, 664:A21, 2022b. doi: 10.1051/0004-6361/202140366.

Quick, L. C., Roberge, A., Mendoza, G. T., et al. Prospects for Cryovolcanic Activity on Cold Ocean Planets. *ApJ*, 956(1):29, 2023. doi: 10.3847/1538-4357/ace9b6.

Ragon, C., Vérard, C., Kasparian, J., et al. Alternative climatic steady states near the Permian–Triassic Boundary. *Scientific Reports*, 14(1):26136, 2024. doi: 10.1038/s41598-024-76432-8.

Rahmstorf, S., Crucifix, M., Ganopolski, A., et al. Thermohaline circulation hysteresis: A model intercomparison. *Geophysical Research Letters*, 32(23), 2005. doi: 10.1029/2005GL023655.

Ramirez, R. M. and Kaltenegger, L. A Volcanic Hydrogen Habitable Zone. *ApJL*, 837(1):L4, 2017. doi: 10.3847/2041-8213/aa60c8.

Ramirez, R. M. and Kaltenegger, L. A Methane Extension to the Classical Habitable Zone. *ApJ*, 858(2):72, 2018. doi: 10.3847/1538-4357/aab8fa.

Ramos, A. A. and Pallé, E. Planet cartography with neural learned regularization. *Astronomy & Astrophysics*, 645:A90, 2021. doi: 10.1051/0004-6361/202039460.

Rauer, H., Aerts, C., Cabrera, J., et al. The PLATO mission. *Experimental Astronomy*, 59(3):26, 2025. doi: 10.1007/s10686-025-09985-9.

Read, P. L. A Sea Change in Exoplanet Climate Models? *Astrobiology*, 14(8):627–628, 2014. doi: 10.1089/ast.2014.1404.

Renaud, J. P., Henning, W. G., Saxena, P., et al. Tidal Dissipation in Dual-body, Highly Eccentric, and Nonsynchronously Rotating Systems: Applications to Pluto-Charon and the Exoplanet TRAPPIST-1e. *PSJ*, 2(1):4, 2021. doi: 10.3847/PSJ/abc0f3.

Rencurrel, M. C. and Rose, B. E. J. Exploring the Climatic Response to Wide Variations in Ocean Heat Transport on an Aquaplanet. *Journal of Climate*, 31(16):6299–6318, 2018. doi: 10.1175/JCLI-D-17-0856.1.

Reuyl, D. and Holmberg, E. On the Existence of a Third Component in the System 70 Ophiuchi. *ApJ*, 97:41, 1943. doi: 10.1086/144489.

Ribas, I., Bolmont, E., Selsis, F., et al. The habitability of Proxima Centauri b. I. Irradiation, rotation and volatile inventory from formation to the present. *A&A*, 596:A111, 2016. doi: 10.1051/0004-6361/201629576.

Ridgway, R. J., Zamyatina, M., Mayne, N. J., et al. 3D modelling of the impact of stellar activity on tidally locked terrestrial exoplanets: atmospheric composition and habitability. *MNRAS*, 518(2):2472–2496, 2023. doi: 10.1093/mnras/stac3105.

Robertson, P., Roy, A., and Mahadevan, S. Stellar Activity Mimics a Habitable-zone Planet around Kapteyn's Star. *ApJL*, 805(2):L22, 2015. doi: 10.1088/2041-8205/805/2/L22.

Rodríguez-Mozos, J. M. and Moya, A. Erosion of an exoplanetary atmosphere caused by stellar winds. *A&A*, 630:A52, 2019. doi: 10.1051/0004-6361/201935543.

Rose, B. E. J. and Marshall, J. Ocean Heat Transport, Sea Ice, and Multiple Climate States: Insights from Energy Balance Models. *Journal of the Atmospheric Sciences*, 66 (9):2828, 2009. doi: 10.1175/2009JAS3039.1.

Rosenblatt, F. A Two-Color Photometric Method for Detection of Extra solar Planetary Systems. *Icarus*, 14(1):71–93, 1971. doi: 10.1016/0019-1035(71)90103-5.

Rushby, A. J., Claire, M. W., Osborn, H., et al. Habitable Zone Lifetimes of Exoplanets around Main Sequence Stars. *Astrobiology*, 13(9):833–849, 2013. doi: 10.1089/ast.2012.0938.

Salazar, A. M., Olson, S. L., Komacek, T. D., et al. The Effect of Substellar Continent Size on Ocean Dynamics of Proxima Centauri b. *ApJL*, 896(1):L16, 2020. doi: 10.3847/2041-8213/ab94c1.

Scalo, J., Kaltenegger, L., Segura, A., et al. M Stars as Targets for Terrestrial Exoplanet Searches And Biosignature Detection. *Astrobiology*, 7(1):85–166, 2007. doi: 10.1089/ast.2006.0125.

Schmidt, F., Way, M. J., Costard, F., et al. Circumpolar ocean stability on Mars 3 Gy ago. *Proceedings of the National Academy of Science*, 119(4):e2112930118, 2022. doi: 10.1073/pnas.2112930118.

Schmitt, R. W. The Ocean's Role in Climate. *Oceanography*, 2018. doi: 10.5670/oceanog.2018.225.

Schneider, J. On the Search for O_2 in Extrasolar Planets. *Ap&SS*, 212(1-2):321–325, 1994. doi: 10.1007/BF00984535.

Schulze-Makuch, D. and Irwin, L. N. The prospect of alien life in exotic forms on other worlds. *Naturwissenschaften*, 93(4):155–172, 2006. doi: 10.1007/s00114-005-0078-6.

Seager, S., Petkowski, J. J., Günther, M. N., et al. Possibilities for an Aerial Biosphere in Temperate Sub Neptune-Sized Exoplanet Atmospheres. *Universe*, 7(6):172, 2021. doi: 10.3390/universe7060172.

See, T. J. J. Researches on the orbit of 70 Ophiuchi, and on a periodic perturbation in the motion of the system arising from the action of an unseen body. *AJ*, 16:17–23, 1896. doi: 10.1086/102368.

Segura, A., Walkowicz, L. M., Meadows, V., et al. The Effect of a Strong Stellar Flare on the Atmospheric Chemistry of an Earth-like Planet Orbiting an M Dwarf. *Astrobiology*, 10(7):751–771, 2010. doi: 10.1089/ast.2009.0376.

Sergeev, D. E., Lambert, F. H., Mayne, N. J., et al. Atmospheric Convection Plays a Key Role in the Climate of Tidally Locked Terrestrial Exoplanets: Insights from High-resolution Simulations. *ApJ*, 894(2):84, 2020. doi: 10.3847/1538-4357/ab8882.

Sergeev, D. E., Lewis, N. T., Lambert, F. H., et al. Bistability of the Atmospheric Circulation on TRAPPIST-1e. *PSJ*, 3(9):214, 2022. doi: 10.3847/PSJ/ac83be.

Shields, A. L. and Carns, R. C. Hydrohalite Salt-albedo Feedback Could Cool M-dwarf Planets. *ApJ*, 867(1):11, 2018. doi: 10.3847/1538-4357/aadcaa.

Shields, A. L., Meadows, V. S., Bitz, C. M., et al. The Effect of Host Star Spectral Energy Distribution and Ice-Albedo Feedback on the Climate of Extrasolar Planets. *Astrobiology*, 13(8):715–739, 2013. doi: 10.1089/ast.2012.0961.

Shields, A. L., Ballard, S., and Johnson, J. A. The habitability of planets orbiting M-dwarf stars. *PhR*, 663:1, 2016. doi: 10.1016/j.physrep.2016.10.003.

Showman, A. P. and Polvani, L. M. Equatorial Superrotation on Tidally Locked Exoplanets. *ApJ*, 738(1):71, 2011. doi: 10.1088/0004-637X/738/1/71.

Showman, A. P., Lewis, N. K., and Fortney, J. J. 3D Atmospheric Circulation of Warm and Hot Jupiters. *ApJ*, 801(2):95, 2015. doi: 10.1088/0004-637X/801/2/95.

Si, Y., Yang, J., and Liu, Y. Planetary climate under extremely high vertical diffusivity. *A&A*, 658:A33, 2022. doi: 10.1051/0004-6361/202140778.

Siegfried, T. *The Number of the Heavens: A History of the Multiverse and the Quest to Understand the Cosmos*. Harvard University Press, Cambridge, MA, 2019. ISBN 9780674975880.

Silva, L., Vladilo, G., Schulte, P. M., et al. From climate models to planetary habitability: temperature constraints for complex life. *International Journal of Astrobiology*, 16(3): 244–265, 2017. doi: 10.1017/S1473550416000215.

Simonetti, P., Vladilo, G., Silva, L., et al. Statistical Properties of Habitable Zones in Stellar Binary Systems. *ApJ*, 903(2):141, 2020. doi: 10.3847/1538-4357/abc074.

Singh, H., Feldl, N., Kay, J. E., et al. Climate sensitivity is sensitive to changes in ocean heat transport. *Journal of Climate*, 35(9):2653 – 2674, 2022. doi: 10.1175/JCLI-D-21-0674.1.

Sinha, B. and Smith, R. Development of a Fast Coupled General Circulation Model (FORTE) for Climate Studies, Implemented Using the OASIS Coupler. Technical

Report Internal Document 81, Southampton Oceanography Centre, Southampton, UK, 2002.

Smith, R. S., Dubois, C., and Marotzke, J. Ocean circulation and climate in an idealised pangean oagcm. *Geophysical Research Letters*, 31(18):L18207, 2004. doi: 10.1029/2004GL020643.

Smith, R. S., Dubois, C., and Marotzke, J. Global Climate and Ocean Circulation on an Aquaplanet Ocean Atmosphere General Circulation Model. *Journal of Climate*, 19(18): 4719, 2006. doi: 10.1175/JCLI3874.1.

Snellen, I. A. G. and Brown, A. G. A. The mass of the young planet Beta Pictoris b through the astrometric motion of its host star. *Nature Astronomy*, 2:883–886, 2018. doi: 10.1038/s41550-018-0561-6.

Snellen, I. A. G., de Mooij, E. J. W., and Albrecht, S. The changing phases of extrasolar planet CoRoT-1b. *Nature*, 459(7246):543–545, 2009. doi: 10.1038/nature08045.

Snellen, I. A. G., de Kok, R. J., de Mooij, E. J. W., et al. The orbital motion, absolute mass and high-altitude winds of exoplanet HD209458b. *Nature*, 465(7301):1049–1051, 2010. doi: 10.1038/nature09111.

Snellen, I. A. G., Brandl, B. R., de Kok, R. J., et al. Fast spin of the young extrasolar planet β Pictoris b. *Nature*, 509(7498):63–65, 2014. doi: 10.1038/nature13253.

Sohl, L. E., Fauchez, T. J., Domagal-Goldman, S., et al. The CUISINES Framework for Conducting Exoplanet Model Intercomparison Projects, Version 1.0. *PSJ*, 5(8):175, 2024. doi: 10.3847/PSJ/ad5830.

Solomon, S. C. and Head, J. W. Fundamental Issues in the Geology and Geophysics of Venus. *Science*, 252(5003):252–260, 1991. doi: 10.1126/science.252.5003.252.

Spiegel, D. S., Menou, K., and Scharf, C. A. Habitable Climates: The Influence of Obliquity. *ApJ*, 691(1):596–610, 2009. doi: 10.1088/0004-637X/691/1/596.

Spiegel, D. S., Raymond, S. N., Dressing, C. D., et al. Generalized Milankovitch Cycles and Long-Term Climatic Habitability. *ApJ*, 721(2):1308–1318, 2010. doi: 10.1088/0004-637X/721/2/1308.

Spinelli, R., Borsa, F., Ghirlanda, G., et al. The ultraviolet habitable zone of exoplanets. *MNRAS*, 522(1):1411–1418, 2023. doi: 10.1093/mnras/stad928.

Stark, C. R., Helling, C., Diver, D. A., et al. Electrostatic activation of prebiotic chemistry in substellar atmospheres. *International Journal of Astrobiology*, 13(2):165–172, 2014. doi: 10.1017/S1473550413000475.

Stevenson, K. B., Désert, J.-M., Line, M. R., et al. Thermal structure of an exoplanet atmosphere from phase-resolved emission spectroscopy. *Science*, 346(6211):838–841, 2014. doi: 10.1126/science.1256758.

Stommel, H. Thermohaline Convection with Two Stable Regimes of Flow. *Tellus*, 13(2): 224–230, 1961. doi: 10.1111/j.2153-3490.1961.tb00079.x.

Stone, P. H. Constraints on dynamical transports of energy on a spherical planet. *Dynamics of Atmospheres and Oceans*, 2(2):123–139, 1978. ISSN 0377-0265. doi: 10.1016/0377-0265(78)90006-4.

Strand, K. A. 61 Cygni as a Triple System. *PASP*, 55(322):29–32, 1943. doi: 10.1086/125484.

Struve, O. Proposal for a project of high-precision stellar radial velocity work. *The Observatory*, 72:199–200, 1952.

Suárez Mascareño, A., Rebolo, R., González Hernández, J. I., et al. Characterization of the radial velocity signal induced by rotation in late-type dwarfs. *MNRAS*, 468(4): 4772–4781, 2017. doi: 10.1093/mnras/stx771.

Sumi, T., Bennett, D. P., Bond, I. A., et al. A Cold Neptune-Mass Planet OGLE-2007-BLG-368Lb: Cold Neptunes Are Common. *ApJ*, 710(2):1641–1653, 2010. doi: 10.1088/0004-637X/710/2/1641.

Talley, L. D., Reid, J. L., and Robbins, P. E. Data-Based Meridional Overturning Streamfunctions for the Global Ocean. *Journal of Climate*, 16(19):3213–3226, 2003. doi: 10.1175/1520-0442(2003)016⟨3213:DMOSFT⟩2.0.CO;2.

Terray, L., Valcke, S., and Piacentini, A. The OASIS Coupler User Guide, Version 2.3. Technical Report TR/CMGC/99-37, CERFACS, Toulouse, France, 1999.

Tilley, M. A., Segura, A., Meadows, V., et al. Modeling Repeated M Dwarf Flaring at an Earth-like Planet in the Habitable Zone: Atmospheric Effects for an Unmagnetized Planet. *Astrobiology*, 19(1):64–86, 2019. doi: 10.1089/ast.2017.1794.

Trenberth, K. E. and Caron, J. M. Estimates of Meridional Atmosphere and Ocean Heat Transports. *Journal of Climate*, 14(16):3433–3443, 2001. doi: 10.1175/1520-0442(2001)014⟨3433:EOMAAO⟩2.0.CO;2.

Turbet, M., Leconte, J., Selsis, F., et al. The habitability of Proxima Centauri b. II. Possible climates and observability. *A&A*, 596:A112, 2016. doi: 10.1051/0004-6361/201629577.

Turyshev, S. G. and Toth, V. T. Resolved imaging of exoplanets with the solar gravitational lens. *MNRAS*, 515(4):6122–6132, 2022. doi: 10.1093/mnras/stac2130.

Turyshev, S. G. and Toth, V. T. Imaging faint sources with the extended solar gravitational lens. *Physical Review D*, 107(10):104063, 2023. doi: 10.1103/PhysRevD.107.104063.

Valente, E. F. S., Correia, A. C. M., Auclair-Desrotour, P., et al. Tidal evolution of Earth-like planets in the habitable zone of low-mass stars. *A&A*, 687:A47, 2024. doi: 10.1051/0004-6361/202348450.

Vallis, G. K. and Farneti, R. Meridional energy transport in the coupled atmosphere-ocean system: scaling and numerical experiments. *Quarterly Journal of the Royal Meteorological Society*, 135(644):1643–1660, 2009. doi: 10.1002/qj.498.

van de Kamp, P. Astrometric study of Barnard's star from plates taken with the 24-inch Sproul refractor. *AJ*, 68:515–521, 1963. doi: 10.1086/109001.

van de Kamp, P. and Lippincott, S. L. Astrometric study of Lalande 21185. *AJ*, 56:49, 1951. doi: 10.1086/106503.

van de Velde, S. J., Hülse, D., Reinhard, C. T., et al. Iron and sulfur cycling in the cGENIE.muffin Earth system model (v0.9.21). *Geoscientific Model Development*, 14(5): 2713–2745, 2021. doi: 10.5194/gmd-14-2713-2021.

Van Eylen, V. and Albrecht, S. Eccentricity from Transit Photometry: Small Planets in Kepler Multi-planet Systems Have Low Eccentricities. *ApJ*, 808(2):126, 2015. doi: 10.1088/0004-637X/808/2/126.

Vandorou, A., Dang, L., Bennett, D. P., et al. OGLE-2016-BLG-1195Lb: A Sub-Neptune Beyond the Snow Line of an M-dwarf Confirmed by Keck Adaptive Optics. *AJ*, 169(6): 319, 2025. doi: 10.3847/1538-3881/adcec2.

Vervoort, P., Horner, J., Kane, S. R., et al. System Architecture and Planetary Obliquity: Implications for Long-term Habitability. *AJ*, 164(4):130, 2022. doi: 10.3847/1538-3881/ac87fd.

Vinson, A. M. and Hansen, B. M. S. On the spin states of habitable zone exoplanets around M dwarfs: the effect of a near-resonant companion. *MNRAS*, 472(3):3217–3229, 2017. doi: 10.1093/mnras/stx2100.

Vladilo, G., Murante, G., Silva, L., et al. The Habitable Zone of Earth-like Planets with Different Levels of Atmospheric Pressure. *ApJ*, 767(1):65, 2013. doi: 10.1088/0004-637X/767/1/65.

Walker, J., Hays, P., and Kasting, J. A negative feedback mechanism for the long-term stabilization of Earth's surface temperature. *Journal of Geophysical Research*, 86(C10): 9776–9782, 1981. doi: 10.1029/JC086iC10p09776.

Wallace, A. L., Casey, A. R., Brown, A. G. A., et al. Detection and characterization of giant planets with Gaia astrometry. *MNRAS*, 536(3):2485–2495, 2025. doi: 10.1093/mnras/stae2769.

Wang, Y., Tian, F., and Hu, Y. Climate Patterns of Habitable Exoplanets in Eccentric Orbits Around M Dwarfs. *ApJL*, 791(1):L12, 2014. doi: 10.1088/2041-8205/791/1/L12.

Wang, Y., Liu, Y., Tian, F., et al. Effects of Obliquity on the Habitability of Exoplanets around M Dwarfs. *ApJL*, 823(1):L20, 2016. doi: 10.3847/2041-8205/823/1/L20.

Ward, P. and Brownlee, D. E. *The Enigma of the Cambrian Explosion*, pages 125–156. Springer New York, New York, NY, 2000. ISBN 978-0-387-21848-9. doi: 10.1007/0-387-21848-3_7.

Way, M. J. TRAPPIST-1 d: Exo-Venus, Exo-Earth, or Exo-Dead? *ApJL*, 980(1):L7, 2025. doi: 10.3847/2041-8213/adace0.

Way, M. J. and Del Genio, A. D. Venusian Habitable Climate Scenarios: Modeling Venus Through Time and Applications to Slowly Rotating Venus-Like Exoplanets. *Journal of Geophysical Research (Planets)*, 125(5):e06276, 2020. doi: 10.1029/2019JE00627610.1002/essoar.10501118.3.

Way, M. J. and Georgakarakos, N. Effects of Variable Eccentricity on the Climate of an Earth-like World. *ApJL*, 835(1):L1, 2017. doi: 10.3847/2041-8213/835/1/L1.

Way, M. J., Del Genio, A. D., Aleinov, I., et al. Climates of Warm Earth-like Planets. I. 3D Model Simulations. *ApJS*, 239(2):24, 2018. doi: 10.3847/1538-4365/aae9e1.

Way, M. J., Davies, H. S., Duarte, J. C., et al. The Climates of Earth's Next Supercontinent: Effects of Tectonics, Rotation Rate, and Insolation. *Geochemistry, Geophysics, Geosystems*, 22(8):e09983, 2021. doi: 10.1029/2021GC00998310.1002/essoar.10507331.1.

Webb, D. J. An ocean model code for array processor computers. *Computers and Geosciences*, 22(5):569–578, 1996. doi: 10.1016/0098-3004(95)00133-6.

Werlen, A., Dorn, C., Burn, R., et al. Sub-Neptunes Are Drier than They Seem: Rethinking the Origins of Water-rich Worlds. *ApJL*, 991(1):L16, 2025. doi: 10.3847/2041-8213/adff73.

Wheeler, M. and Kiladis, G. N. Convectively coupled equatorial waves: Analysis of clouds and temperature in the wavenumber–frequency domain. *Journal of the Atmospheric Sciences*, 56(3):374 – 399, 1999. doi: 10.1175/1520-0469(1999)056⟨0374:CCEWAO⟩2.0.CO;2.

Wieczorek, M. A., Correia, A. C. M., Le Feuvre, M., et al. Mercury's spin-orbit resonance explained by initial retrograde and subsequent synchronous rotation. *Nature Geoscience*, 5(1):18–21, 2012. doi: 10.1038/ngeo1350.

Williams, D. M. and Pollard, D. Earth-like worlds on eccentric orbits: excursions beyond the habitable zone. *International Journal of Astrobiology*, 1(1):61–69, 2002. doi: 10.1017/S1473550402001064.

Winn, J. N. Joint Constraints on Exoplanetary Orbits from Gaia DR3 and Doppler Data. *The Astronomical Journal*, 164(5):196, 2022. doi: 10.3847/1538-3881/ac9126.

Winton, M. On the Climatic Impact of Ocean Circulation. *Journal of Climate*, 16(17): 2875–2889, 2003. doi: 10.1175/1520-0442(2003)016⟨2875:OTCIOO⟩2.0.CO;2.

Wolf, E. T., Kopparapu, R. K., and Haqq-Misra, J. Simulated Phase-dependent Spectra of Terrestrial Aquaplanets in M Dwarf Systems. *ApJ*, 877(1):35, 2019. doi: 10.3847/1538-4357/ab184a.

Wolszczan, A. and Frail, D. A. A planetary system around the millisecond pulsar PSR1257 + 12. *Nature*, 355(6356):145–147, 1992. doi: 10.1038/355145a0.

Woodward, H. L., Rushby, A. J., and Mayne, N. J. A Novel Metric for Assessing Climatological Surface Habitability. *PSJ*, 6(8):206, 2025. doi: 10.3847/PSJ/adf3ab.

Wu, Y. and Lithwick, Y. Density and Eccentricity of Kepler Planets. *ApJ*, 772(1):74, 2013. doi: 10.1088/0004-637X/772/1/74.

Yang, H., Zhao, Y., Liu, Z., et al. Heat Transport Compensation in Atmosphere and Ocean over the Past 22,000 Years. *Scientific Reports*, 5, 2015. doi: 10.1038/srep16661.

Yang, J., Peltier, W. R., and Hu, Y. The Initiation of Modern "Soft Snowball" and "Hard Snowball" Climates in CCSM3. Part I: The Influences of Solar Luminosity, CO_2 Concentration, and the Sea Ice/Snow Albedo Parameterization. *Journal of Climate*, 25 (8):2711–2736, 2012a. doi: 10.1175/JCLI-D-11-00189.1.

Yang, J., Peltier, W. R., and Hu, Y. The Initiation of Modern "Soft Snowball" and "Hard Snowball" Climates in CCSM3. Part II: Climate Dynamic Feedbacks. *Journal of Climate*, 25(8):2737–2754, 2012b. doi: 10.1175/JCLI-D-11-00190.1.

Yang, J., Cowan, N. B., and Abbot, D. S. Stabilizing Cloud Feedback Dramatically Expands the Habitable Zone of Tidally Locked Planets. *ApJL*, 771(2):L45, 2013. doi: 10.1088/2041-8205/771/2/L45.

Yang, J., Boué, G., Fabrycky, D. C., et al. Strong Dependence of the Inner Edge of the Habitable Zone on Planetary Rotation Rate. *ApJL*, 787(1):L2, 2014a. doi: 10.1088/2041-8205/787/1/L2.

Yang, J., Liu, Y., Hu, Y., et al. Water Trapping on Tidally Locked Terrestrial Planets Requires Special Conditions. *ApJL*, 796(2):L22, 2014b. doi: 10.1088/2041-8205/796/2/L22.

Yang, J., Abbot, D. S., Koll, D. D. B., et al. Ocean Dynamics and the Inner Edge of the Habitable Zone for Tidally Locked Terrestrial Planets. *ApJ*, 871(1):29, 2019. doi: 10.3847/1538-4357/aaf1a8.

Yang, J., Ji, W., and Zeng, Y. Transition from eyeball to snowball driven by sea-ice drift on tidally locked terrestrial planets. *Nature Astronomy*, 4:58–66, 2020. doi: 10.1038/s41550-019-0883-z.

Yaptangco, D. C., Ballard, S., Dittmann, J., et al. Quantifying the Effect of Short-timescale Stellar Activity Upon Transit Detection in M Dwarfs. *AJ*, 169(3):153, 2025. doi: 10.3847/1538-3881/ada898.

Yuan, H. D. A., Su, Y., and Goodman, J. Surprising Spin–Orbit Resonances of Rocky Planets. *ApJ*, 987(1):9, 2025. doi: 10.3847/1538-4357/add2f3.

Zachos, J., Pagani, M., Sloan, L., et al. Trends, Rhythms, and Aberrations in Global Climate 65 Ma to Present. *Science*, 292(5517):686–693, 2001. doi: 10.1126/science.1059412.

Zechmeister, M., Dreizler, S., Ribas, I., et al. The CARMENES search for exoplanets around M dwarfs. Two temperate Earth-mass planet candidates around Teegarden's Star. *A&A*, 627:A49, 2019. doi: 10.1051/0004-6361/201935460.

Zeng, Y. and Jansen, M. F. Ocean Circulation on Enceladus with a High- versus Low-salinity Ocean. *PSJ*, 2(4):151, 2021. doi: 10.3847/PSJ/ac1114.

Zhang, H., Ge, J., Deng, H., et al. Science goals of the Earth 2.0 space mission. In Coyle, L. E., Matsuura, S., and Perrin, M. D., editors, *Space Telescopes and Instrumentation 2022: Optical, Infrared, and Millimeter Wave*, volume 12180, page 1218016. International Society for Optics and Photonics, SPIE, 2022. doi: 10.1117/12.2630151.

Zhao, Z., Liu, Y., Li, W., et al. Climate Change of over 20°C Induced by Continental Movement on a Synchronously Rotating Exoplanet. *ApJL*, 910(1):L8, 2021. doi: 10.3847/2041-8213/abebe6.

Zhong, W. Y. and Haigh, J. D. Improved Broadband Emissivity Parameterization for Water Vapor Cooling Rate Calculations. *Journal of Atmospheric Sciences*, 52:124–138, 1995. doi: 10.1175/1520-0469(1995)052⟨0124:IBEPFW⟩2.0.CO;2.

Zúñiga-Fernández, S., Gillon, M., Pedersen, P. P., et al. SPECULOOS: five years hunting terrestrial planets around ultra-cool dwarfs. In Marshall, H. K., Spyromilio, J., and

Usuda, T., editors, *Ground-based and Airborne Telescopes X*, volume 13094 of *Society of Photo-Optical Instrumentation Engineers (SPIE) Conference Series*, page 1309413, 2024. doi: 10.1117/12.3020550.